The University Of Sheffield.

Development, optimisation and dissolution of glass and ceramic wasteforms for the immobilisation of the UK PuO_2 stockpile

Amber Rose Mason

A thesis submitted in partial fulfilment for the degree of Doctor of Philosophy

NucleUS Immobilisation Science Laboratory
Department of Materials Science and Engineering
The University of Sheffield

September 2021

Abstract

In the UK, there is 140 tHM of PuO_2 stored at the Sellafield site as a zero value asset. This material was generated by nuclear fuel reprocessing in the ThORP and Magnox fuel reprocessing plants, which are due to cease operation by 2021. The current UK government plan is to recycle this material as MOX fuel, however the uptake for this fuel type in the current UK reactor fleet is absent. There is also a significant portion of this waste stream that is contaminated with advanced fission products (e.g. Am-241) and degraded storage materials (e.g. Cl from PVC containment). Therefore, a dual track strategy of immobilisation and MOX fuel research has been suggested for this waste stream, to ensure there is a suitable end state for the stockpile should MOX fuel fabrication not come to fruition.

This thesis presents an investigation of candidate wasteforms which are appropriate for the immobilisation of the UK PuO_2 stockpile, where HIPing was applied as a thermal treatment technology and CeO_2 used as a surrogate for PuO_2 throughout. The key research questions for this thesis were:

1. What are the candidate wasteforms for the immobilisation the UK PuO_2 stockpile given that ~ 5 tHM is degraded/contaminated and MOX fuel is not currently feasible?
2. How do these wasteforms compare in terms of waste loading, technology readiness level and chemical durability?
3. Is hot isostatic pressing a viable thermal treatment method for these wasteforms?
4. Is CeO_2 a suitable surrogate for PuO_2 in each wasteform?

The wasteforms investigated for this thesis were ATS glass and fluorite based ceramics (zirconolite, pyrochlore and cubic zirconia). The results of the studies conducted for each wasteform matrix are presented below.

Chapters 4 and 5 - Alkali tin silicate (ATS) glass: ATS glass is a type of borosilicate glass developed in the US for the immobilisation of excess

weapons plutonium. This composition was modified to include Fe^0 to create a reducing environment within the glass, with the aim of reducing Ce^{4+} to Ce^{3+}, and therefore improving the Ce wasteloading. The matrix of ATS glasses produced were characterised using Ce XANES and Fe EXAFS/Mössbauer spectroscopy to determine the Ce/Fe oxidation state and Fe local coordination environment. Ce was shown to fully reduce to Ce^{3+} and incorporate into the glass upon the addition of Fe^0. Durability tests were completed on the most successful compositions, showing that the addition of Fe improved the short term durability of the glass. HIPing was also shown to be a viable thermal treatment method for ATS glass, producing glass which fully incorporated Ce, with no deleterious effects on the dissolution rate measured.

Chapter 6 - Zirconolite ceramics: Zirconolite ceramics are a proposed wasteform for the immobilisation of PuO_2. A matrix of eight zirconolite formulations was produced using HIPing, assessing two different Ce doping mechanisms, as well as the efficacy of Al, Mg and Fe as charge compensating ions. Secondary phases, including perovskite and trace CeO_2, were observed using XRD and SEM/EDX. A selection of the formulations with the most favourable phase assemblage were subject to durability assessment using aggressive conditions (0.01 M HNO_3 leachant at 90 °C), in order to compare their relative durability as well as comparing their performance to other wasteforms proposed for this waste stream. The secondary Ce-bearing phases were postulated to dominate the dissolution rate measured, with the formulation containing the highest quantity of secondary phases displaying the highest dissolution rate. The Ce dissolution rates were still comparable to others in the literature measured in similar conditions, providing confidence in the long term durability of zirconolite wasteforms despite the heterogeneity in the phase assemblage.

Chapter 7 - Fluorite based ceramics: Ceramic formulations with a fluorite based structure were investigated which included: cubic zirconia, zirconate pyrochlore, and zirconolite. The waste loading of these formulations was previously optimised using CPS, however significant porosity was observed,

hence the application of HIPing in this work to achieve full densification. These formulations included Hf and Gd as neutron absorbing cations, included to observe the effect of these cations on the resulting phase assemblage and relative dissolution rate. Single phase zirconolite was synthesised (with two polytypes observed, 2M and 3T), which proved to be the most durable composition when subject to aggressive PCT-B testing (identical to dissolution conditions implemented in Chapter 6). The least durable formulation was pyrochlore due to the presence of a Ce/Gd fluorite solid solution which was postulated to preferentially dissolve. With the exception of the pyrochlore formulation, the measured dissolution rates of Ce and Gd were within one order of magnitude which is promising for maintaining subcriticality in these wasteforms.

Chapter 8 – Molten salt synthesis of zirconolite ceramics: The molten salt synthesis of zirconolite ceramics was also investigated, for the purposes of selectively immobilising entrained actinides from the legacy and future pyroprocessing of nuclear fuels, using the salt eutectic as a synthesis medium. A self-compensating Ce-doped zirconolite formulation was selected, with several experimental parameters systematically adjusted to observe the effects on the resultant phase assemblage. These experimental parameters included: salt to ceramic ratio, synthesis temperature, duration and atmosphere, as well as reagent excess and surrogate type. An excess of TiO_2 and ZrO_2 reagents was found to produce a wasteform close to single phase, however deleterious Ce-bearing perovskite was still formed. HIPing was not applied in this case since the salt medium must be dissolved post-synthesis, and a second consolidation step for the resulting zirconolite powder must be performed.

In summary, each wasteform investigated was demonstrated to be feasible for the immobilisation of the UK PuO_2 stockpile, when using Ce as a Pu surrogate. Ce was successfully incorporated into the chemical structure of each wasteform studied, with further optimisation of the synthesis parameters required for complete waste incorporation in some instances. The durability of

the ceramic wasteforms was several orders of magnitude greater than the ATS glass wasteforms, when considering the NL_{Ce} and NR_{Ce}. However, it is important to note that the technology readiness level of glass wasteform synthesis in the UK is significantly greater than that of ceramic wasteforms. CeO_2 was demonstrated to be a viable surrogate for PuO_2 but it should be noted that Pu^{4+} has a much greater redox potential that Ce^{4+}, which proved to be problematic for both the glass and ceramic wasteforms studied in this thesis. HIPing was also demonstrated to produce viable wasteforms in Chapters 5 – 7, however the effects of this process on the redox environment requires further consideration.

Acknowledgments

The saying goes that it takes a village to raise a child, and I can safely state that this is also true to graduate a PhD student. This has been the most challenging experience, both personally and professionally, and there are so many people who have helped me to see this project to completion, first and foremost, my supervisor Professor Neil Hyatt. The patience and understanding I have received throughout this project have been outstanding. You have always had faith in me when I had none in myself and I will be forever grateful to you for the opportunities you have given me and the things that I have learned, over and above what is written in this thesis. It has been an absolute privilege!

I am also incredibly thankful to Dr. Laura Gardner, who is my mentor and someone I am also lucky enough to call a great friend; your kindness, enthusiasm and determination are an inspiration every day and I can safely say that I wouldn't have reached the finish line without your unwavering support.

My thanks also go to Dr. Martin Stennett for everything training and XAS related, as well as the hard work you put in to maintaining excellent standards in the labs, this will never not be appreciated.

A huge thank you to Dr. Claire Corkhill, for giving me the opportunity to continue to work in this incredible research group as well as 'lighting a fire in my belly' regarding nuclear materials dissolution. I'm excited to see where the next couple of years takes us.

And to Dr. Colleen Mann, you have been an incredible source of energy, positivity and support, thank you for persevering through those dissolution experiments with me, the results in this thesis are far better thanks to your insightful input!

To my viva examiners Dr. Joe Hriljac and Dr. Hajime Kinoshita, thank you for a really rewarding and challenging discussion, this thesis is much improved thanks to your input.

A big thank you to everyone at the Immobilisation Science Laboratory, past and present, for sharing your knowledge, friendship, support and for making this journey a little easier, as well as to the technicians and support staff throughout the department. My thanks also go to my funding body EPSRC for the financial support in this project, and the NGN CDT Cohort 2 with whom I started this journey, as well as everyone involved in the NGN CDT.

My biggest thanks go to my family, particularly my Mum, for being the best ‘Mum and Dad’ throughout the good and the bad, for encouraging me to keep going when things got tough and for giving me the confidence/stubborn streak to know that I can do anything I set my mind to. I consistently had my doubts but knowing you were always there for me helped me to get through the worst times. And thank you to my Grandma, for instilling a fierce sense of independence in us, it has helped me get to this point today. I would not have reached the end of this process with my sanity in check, especially through the lonely pandemic lockdown days, without the companionship of my cats; Loomis, Rocky, Ada and Eadie, you’re the best.

Last but not least, my sincerest of thanks go to Ashley Sutton, you’ve wiped away more tears that I care to recall, listened to more presentations about zirconolite and ATS glass than any person should, and have been an unfaltering source of love, support, patience and epic food throughout this process, I will never forget it. Now to enjoy reaching the end of this process. Cheers everyone!

Publications

I, the author, confirm that the Thesis is my own work. I am aware of the University's Guidance on the Use of Unfair Means (www.sheffield.ac.uk/ssid/unfair-means). This work has not been previously been presented for an award at this, or any other, university.

Peer review publications

A. R. Mason, F. Y. Tocino, M. C. Stennett, and N. C. Hyatt, "Molten salt synthesis of Ce doped zirconolite for the immobilisation of pyroprocessing wastes and separated plutonium," *Ceram. Int.*, 2020, doi: 10.1016/j.ceramint.2020.08.080.

S. M. Thornber, L. M. Mottram, **A. R. Mason**, P. Thompson, M. C. Stennett, and N. C. Hyatt, "Solubility, speciation and local environment of chlorine in zirconolite glass–ceramics for the immobilisation of plutonium residues," *RSC Adv.*, vol. 10, pp. 32497–32510, 2020, doi: 10.1039/D0RA04938G.

L. M. Mottram, S. Cafferkey, **A. R. Mason**, T. Oulton, S. K. Sun, D. J. Bailey, M. C. Stennett, and N. C. Hyatt, "A feasibility investigation of speciation by Fe K-edge XANES using a laboratory X-ray absorption spectrometer," *J. Geosci.*, vol. 65, no. 1, 2020, doi: 10.3190/jgeosci.299.

A. R. Mason, S. M. Thornber, M. C. Stennett, L. J. Gardner, D. Lützenkirchen-Hecht, and N. C. Hyatt, "Preliminary investigation of chlorine speciation in zirconolite glass-ceramics for plutonium residues by analysis of Cl K-edge XANES," *MRS Advances*, vol. 5, no. 1-2, pp. 37–43, 2020, doi: 10.1557/adv.2019.460.

D. J. Bailey, M. C. Stennett, **A. R. Mason**, and N. C. Hyatt, "Synthesis and characterisation of the hollandite solid solution $Ba_{1.2-x}Cs_xFe_{2.4-x}Ti_{5.6+x}O_{16}$ for partitioning and conditioning of radiocaesium," *J. Nucl. Mater.*, vol. 503, 2018, doi: 10.1016/j.jnucmat.2018.03.005.

Oral Presentations

A. R. Mason, M. C. Stennett, N. C. Hyatt, Hot isostatic pressing and durability testing of alkali tin silicate glass as a wasteform for the immobilisation of plutonium, *International Congress on Glass 2019*, Boston USA, 14th June 2019.

A. R. Mason, M. C. Stennett, N. C. Hyatt, Durability testing of alkali tin silicate glass as a wasteform for the immobilisation of plutonium, *Next Generation Nuclear CDT Winter School*, Solihull, UK, 4th January 2019.

A. R. Mason, M. C. Stennett, N. C. Hyatt, Alkali tin silicate glass as a wasteform for the immobilisation of plutonium, *41st MRS Scientific Basis for Nuclear Waste Management conference*, Sydney, Australia, 1st November, 2017.
Student Scholarship Award winner for this presentation.

A. R. Mason, F. Y. Tocino, M. C. Stennett, N. C. Hyatt, Decontamination and immobilisation of pyroprocessing wastes, *PACIFIC Annual Meeting 2017*, Leeds, UK, 9th May 2017.

A. R. Mason, C. L. Dube, M. C. Stennett, N. C. Hyatt, Immobilisation of actinide wastes using vitreous wasteforms, *Indo-UK Civil Nuclear Network Meeting*, Sheffield, UK, 20th December 2016.

A. R. Mason, C. L. Dube, P. K. Kulriya, M. C. Stennett, N. C. Hyatt, Simulating the radiation damage in vitreous and ceramic nuclear wasteforms, *Inter-University Accelerator Centre Beamline Proposal Defense,* Delhi, India, 6th July 2016.

Abbreviations

AGR	Advanced gas cooled reactor
ANSTO	Australian Nuclear Science and Technology Organisation
ASTM	American Society for Testing and Materials
ATS	Alkali tin silicate glass
BO	Bridging oxygen
BSE	Back scattered electrons
CIP	Cold isostatic pressing
CPS	Cold press and sinter
DIAMEX	Diamide extraction
DIW	Deionised water
EDX	Energy dispersive X-ray spectroscopy
EPR	European pressurised reactor
ESRF	European Synchrotron Radiation Facility
EXAFS	Extended X-ray absorption fine structure
f.u.	Formula unit
FP	Fission product
GANEX	Group actinide extraction
GDF	Geological disposal facility
HIP	Hot isostatic press
HLW	High level waste
ICP-MS	Inductively coupled plasma – mass spectrometry
ICP-OES	Inductively coupled plasma – optical emission spectrometry
ICDD	International Center for Diffraction Data
ICSD	Inorganic Crystal Structure Database
ILW	Intermediate level waste
LLW	Low level waste
MA	Minor actinide
MCC-1	Materials Characterisation Center 1
MOX	Mixed oxide fuel
MW	Mixed windscale
NBO	Non bridging oxygen
NPP	Nuclear power plant

NSLS-II	National Synchrotron Light Source II
PCT-B	Product Consistency Test B
PDF	Powder diffraction file
PUREX	Plutonium uranium reduction extraction
PWR	Pressurised water reactor
SANEX	Selective actinide extraction
SEM	Scanning electron microscopy
SI	Saturation index
SNF	Spent nuclear fuel
SYNROC	SYNthetic ROCk
tHM	Tons of heavy metal
ThORP	Thermal Oxide Reprocessing Plant
UHQ	Ultra high quality water
VLLW	Very low level waste
XANES	X-ray absorption near edge spectroscopy
XAS	X-ray absorption spectroscopy
XRD	X-ray diffraction
XRF	X-ray fluorescence

Contents

1 Introduction

1.1 Radioactive waste in the UK

Radioactive waste is defined as material which is contaminated with radioisotopes that no longer provides a useful function [1]. It has a distinct set of hazards compared to radioactive materials found naturally in the environment since the radioisotopes are accumulated through human activities and therefore have a higher dose rate generally. The hazards are associated with the radiation emitted and the longevity of the radioisotopes themselves. The waste must therefore be processed, treated and conditioned before disposal to prevent environmental contamination and to allow for remote handling. The waste is categorised in the UK based on the heat generation and activity as; very low level waste (VLLW), low level waste (LLW), intermediate level waste (ILW) and high level waste (HLW), each described in Table 1-1. These categories assist in providing guidance as to the appropriate disposal route for each type of waste, as discussed in Section 1.2.

Table 1-1 – Nuclear waste category definitions, along with their relative volume and activity [2].

Category of nuclear waste	Definition	Volume (m^3)	Activity by 2100 (TBq)
VLLW	High volume – maximum concentrations of 4 MBq per tonne can be disposed of in specific landfill sites. Low volume – each 0.1 m^3 with activity < 400 kBq or each single item < 40 kBq. Can be disposed of in any landfill.	2,690,000	11
LLW	Activity < 4 GBq of alpha and < 12 GBq beta/gamma.	1,280,000	140
ILW	Activity > LLW which generates heat < 2 kW m^{-3}	500,000	1,000,000
HLW	Activity > LLW which generates heat > 2 kW m^{-3}.	1,500	12,000,000

In the UK, there is approximately 5.1 million tons of nuclear waste (as of 1st April 2019), originating from civil, medical, defence and industrial uses [2]. This

nuclear waste was, and continues to be, primarily generated in the nuclear fuel cycle, with a significant quantity attributed to the back end of the fuel cycle, and specifically the decommissioning of nuclear reactor sites. It should be noted from Table 1-1 that the category of nuclear waste with the highest activity (HLW) has the smallest volume.

1.2 Nuclear Waste Disposal

The main aims of nuclear waste management and disposal are to ensure that the waste is isolated to prevent migration and dispersion into the environment. Minimising the volume of the waste is also important, as this will minimise the potential costs associated with disposal [3]. The nuclear waste can be encapsulated or immobilised where encapsulation involves entirely surrounding the waste with a stable matrix and therefore isolating it from the environment e.g. cement, and immobilisation is the total incorporation of the waste material into the chemical structure of a matrix.

In the UK, LLW is currently disposed at a shallow engineered repository (Low level waste repository; LLWR) near Drigg. This facility is used for the storage of LLW materials which are not suitable for incineration or treatment. The material is compacted to reduce its overall volume and stored in concreate lined vaults on the site. ILW and LLW is accumulated at all stages of the NFC, whereas HLW is generated from the reprocessing and separation of spent nuclear fuel (SNF). SNF itself is considered to be HLW as well as separated minor actinides (MA) and fission products (FP), however it can be remain in intermediate storage to allow the decay heat from FP to subside [4]. The ILW and HLW will eventually be stored in an underground facility called a geological disposal facility (GDF).

1.2.1 Geological disposal

The method of permanent nuclear waste disposal that has been decided upon in the UK is deep isolation in a geological disposal facility (GDF), illustrated in Figure 1-1. The ILW and HLW will be disposed of in the GDF using a multibarrier method, where each stage of the disposal is carefully engineered

to ensure the long term safety of the facility and the prevention of water ingress. The GDF will be situated 500 – 1000 m underground, at which level the movement of ground water is very slow. The first barrier to water ingress will be the host rock itself, therefore the GDF must be sited to take the hydrogeology into consideration. The second barrier will be the backfill material, used to surround the nuclear waste cannister, with the cannister material itself being the third barrier, which must be produced using a durable material such as stainless steel or copper. The final barrier which will prevent the environmental contamination is the wasteform itself, the material in which the waste is either encapsulated or immobilised, dependent upon the category of waste.

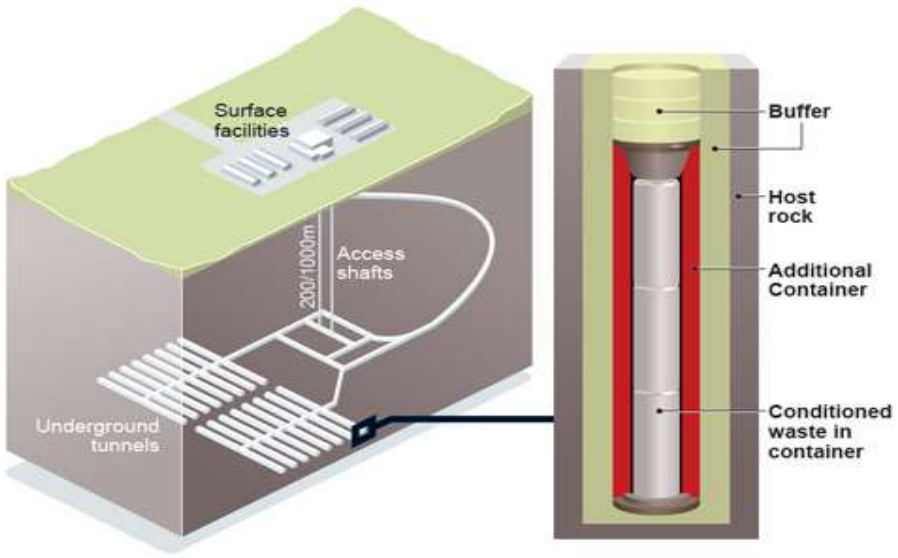

Figure 1-1 - Geological disposal facility diagram displaying multibarrier method. Taken from [5].

This multibarrier engineered disposal facility must be robust enough to withstand at least 100,000 years in this environment since this is the time required for the radiotoxicity of the waste to fall below that of natural U (see Figure 1-2). There is no current agreement upon the position for the UK GDF [6] however Sweden and France are currently in the process of developing their respective sites, with locations having already been selected.

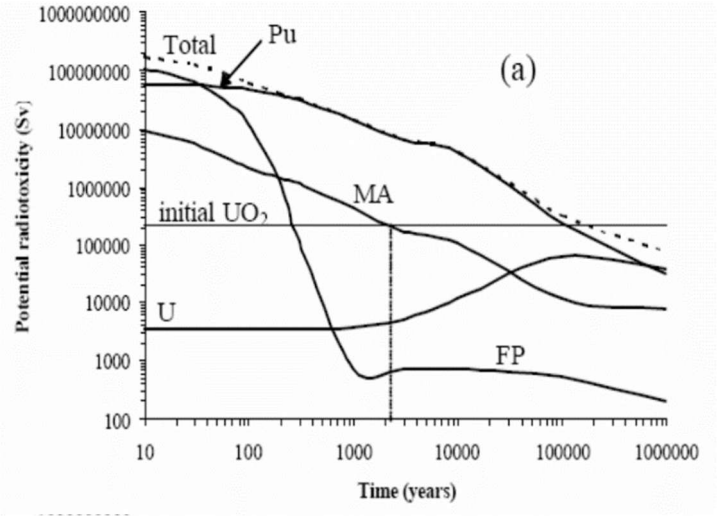

Figure 1-2 - Rate of decay of the components of spent nuclear fuel with time compared to the relative radiotoxicity of each component [7]

1.3 Wasteform requirements

Wasteforms must fulfil certain criteria to be deemed appropriate for geological disposal. These criteria are set out by implementation organisations (e.g. Radioactive Waste Management (RWM)), regulators (e.g. the Environment Agencies) and international organisations (e.g. the International Atomic Energy Agency (IAEA)) [8]–[10]. These criteria and their importance for safe nuclear waste disposal are summarised in Table 1-2.

Table 1-2 – Wasteform acceptance criteria, their definition and explanation of their relative importance.

Criterium	Definition	Importance
Radiation tolerance	Resistance to the loss of durability by radiation effects.	Ensure the long term integrity of the wasteform material.
Waste loading	Quantity of waste immobilised per unit volume.	Reduce the footprint and the cost of the final GDF.
Chemical durability	Resistance to corrosion in groundwater.	Prevent leaching into the environment upon final storage.
Proliferation resistance	Ability of wasteform to suitably contain the waste.	Prevent the theft and subsequent misuse of radioactive waste material.
Process compatibility	Ease of manufacture of the wasteform	Reduce potential cost of immobilisation in wasteform.
Natural analogues	Natural minerals which contain radioactive isotopes	Evidence of ability of the matrix to immobilise radioactive materials for millions of years.

1.4 Plutonium in the UK

Alongside the nuclear waste discussed above, there is approximately 140 tHM of PuO_2 stored as a zero value asset at the Sellafield site, until 2120 which is the planned end date for the site [11]. This is the largest stockpile of civil separated PuO_2 worldwide and originates from the reprocessing of SNF at the Thermal Oxide Reprocessing Plant (ThORP) and Magnox reprocessing plants in the UK [12]. This nuclear fuel reprocessing is due to end in 2021, upon the final closure of the Magnox reprocessing plant. The composition of the PuO_2 stockpile is shown in Table 1-3, of which 23 tHM is foreign-owned material.

Table 1-3 – Inventory of UK civil PuO_2 as of 31 December 2018 [adapted from [13]]. Published by the Office for Nuclear Regulation.

Item	Mass (tHM)
Unirradiated separated plutonium in product stores at reprocessing plants	134.8
Unirradiated separated plutonium in the course of manufacture or fabrication and plutonium contained in unirradiated semi-fabricated or unfinished products at fuel or other fabricating plants or elsewhere	0.7
Plutonium contained in unirradiated MOX fuel or other fabricated products at reactor sites or elsewhere	2.0
Unirradiated separated plutonium held elsewhere.	1.4
Total	**138.9**

The original driver for nuclear fuel reprocessing in the UK was to generate fuel for a fleet of fast-type nuclear reactors, however this program was terminated in 1994 and reprocessing continued, hence generating the majority of the UK PuO_2 stockpile. A 'Credible Options Analysis' was completed by the NDA [14], to aid in the decision of the final fate of the PuO_2 stockpile and reported that there are four main options to be assessed when considering the disposition of the PuO_2 stockpile in the UK:

A. Current baseline strategy - storage at the Sellafield site. Required to convert to a form that is passively safer than PuO_2 powder. No strategy post Sellafield closure in 2120.
B. Immobilisation and disposal – aim to make the material proliferation resistant and passively safe.
C. Reuse as mixed oxide fuel in light water reactors– with ultimate eventual disposal.
D. A combination of the above options.

The Credible Options Analysis states that one of these options must be implemented within 25 years of the report. The Department for Energy and

Climate Change (DECC) published a response to the Credible Options Analysis, stating that mixed oxide (MOX) fuel was the favoured route, with subsequent conditioning of material unsuitable for this route where it will be treated as waste for disposal [15]. The material designated as unsuitable for reuse is identified as Cl contaminated PuO_2, with Cl originating from the radiation degradation of PVC packaging used to surround the material in storage. A small portion of the PuO_2 stockpile is also contaminated with Am-241, generated by the β decay of Pu-241. A dual track research strategy of immobilisation and MOX fabrication has been suggested for PuO_2 [16], which ensure that, if the government were to change its preferred strategy in the future, the subsequent disposition of the stockpile could be implemented more readily. This would also mitigate against the considerable risks associated with MOX implementation. It is generally accepted that interim storage will be a feature of any long term strategy concerning this material since, upon immobilisation, the storage will be required until an ultimate final resting place for nuclear waste is selected.

Immobilisation of the stockpile in a ceramic host phase offers the advantage of a smaller disposal footprint compared to irradiating and immobilisation of MOX fuel due to the heat output of irradiated fuel. Disposal/storage MOX offers another route for immobilisation whereby low specification MOX fuel is produced which may provide a more durable and radiation tolerant wasteform for the long term storage of the stockpile [17]. The immobilisation route also accounts for the stockpile in its entirety.

The stockpile could be used to fuel three European pressurised reactor (EPR) or pressurised water reactor (PWR) reactors for their lifetime [18], however the market for NPP which can burn MOX fuel in the UK and the USA has not reached fruition, with the MOX Fuel Fabrication Facility in the US being scrapped with reasons cited as being the financial and technical implications of such a facility. In the UK, government policy also prevents the MOX (or PuO_2) being shipped to another country. The use of MOX has yet to be shown

as a financially, and therefore commercially viable option for the UK civil nuclear fuel cycle, despite its use being technically plausible.

There is a careful balance required when decided upon the fate of the PuO_2 stockpile, to find the most financially feasible option, since immediate disposal could be securing a precious resource which would then prove to be expensive to return into PuO_2 at a later date. The uncertainty surrounding this issue relates to the cost of each path and the inability of governments to predict the long term fate of this material. The intergenerational burden associated with these materials must also be considered throughout the decision making process.

1.5 Project aims

The central aim of this project was to investigate the suitability of a toolbox of glass and ceramic wasteforms for the immobilisation of the UK PuO_2 stockpile. The viability of thermal treatment of these wasteforms using hot isostatic pressing (HIPing) was also investigated. Their relative suitability is discussed in reference to the wasteform acceptability criteria outlined in Section 1.3, specifically the waste loading achievable, the phase assemblage formed, and the effect of these factors on the chemical durability of the final product. CeO_2 is used as a surrogate for PuO_2 throughout the thesis, with the merits and drawbacks for this choice discussed in Section 3.3, as well as the implications for this selection on each wasteform discussed in the conclusion. A brief outline of the aims of each chapter is presented below along with an assignment of the authors contributions to each chapter, where each draft manuscript was reviewed by Professor Neil Hyatt, Dr. Claire Corkhill and Dr. Laura Gardner:

Chapter 4 – Alkali tin silicate (ATS) glass as a wasteform for the immobilisation of the UK Pu stockpile

ATS glass is a specific formulation of borosilicate glass developed in the US for the immobilisation of wPu, therefore this wasteform was selected for study

in this thesis to investigate its suitability for the immobilisation of the UK PuO_2 stockpile. The aims of this chapter were to:

1. Use CeO_2 as a surrogate for PuO_2 in ATS formulations and maximise the wasteloading by:
    a. observing the effect of processing temperature on Ce solubility in the glass melt.
    b. observing the effect of a reducing agent (Fe^0) on the Ce solubility.
2. Understand the effects of these changes on the resultant glass by fully characterising the wasteforms.
3. Assess the chemical durability of the resulting glass using the ASTM PCT-B and MCC-1 methodologies.

The author's contribution was: all experimental work, data analysis and writing with the exception of performing ICP-OES measurements which were completed by Dr. Claire Corkhill, the collection of Fe EXAFS data which were acquired by Ms. Lucy Mottram, Dr. Dan Bailey and Dr. Martin Stennett, as well as Mössbauer spectra which were acquired by Mr. Dan Austin.

Chapter 5 – Hot isostatic pressing of alkali tin silicate glass as a wasteform for the immobilisation of the UK plutonium stockpile

Using the ATS glass compositions developed in Chapter 4, HIPing was investigated as a method of thermal treatment, with the advantage of this process being the full accountability and criticality control, which are important considerations when designing wasteforms for PuO_2. Each HIPed glass was characterised to understand the effect of HIPing on the wasteform produced. The chemical durability of these wasteforms was investigated and compared to durability of the glasses in Chapter 4, in order to assess whether the effect of HIPing on the dissolution rate of the glass.

The author's contribution was the collection and analysis of all experimental data with the exception of ICP-OES measurements which was completed by Dr. Colleen Mann and Mössbauer spectra were acquired by Mr. Dan Austin.

Chapter 6: The effects of charge compensating ions on the phase assemblage and dissolution behaviour of HIPed Ce-doped zirconolite

Zirconolite is a favourable host phase for actinide waste streams in the multiphase ceramic SYNROC, and is also widely reported in the literature as a potential wasteform for the immobilisation of PuO_2. This phase was therefore selected as a wasteform for investigation in this chapter, with CeO_2 selected as a PuO_2 surrogate. The objectives of this chapter were to:

1. Select formulations of zirconolite using both single site substitution onto the Ca^{2+} site and dual site substitution onto the Ca^{2+} and Zr^{4+} sites, as well as the selection of appropriate Ti^{4+} site charge balancing ions (Al^{3+}, Mg^{2+} and Fe^{3+}).
2. Assess the suitability of using HIPing for the selected formulations.
3. Understand the efficacy of the charge compensating ions by studying the resultant phase assemblage of the wasteform.
4. Assess the effect of the phase assemblage and charge compensating ions on the relative durability of each formulation using an aggressive PCT-B type protocol.

The author's contribution was the collection and analysis of all experimental data with the exception of ICP-MS data which were acquired by Dr. Colleen Mann, as well as the collection of Ce/Fe XANES spectra which were acquired by Dr. Martin Stennett and Mr. Dan Austin. This Chapter also involved considerable method development for the PCT-B experiments and ICP analysis protocol undertaken by the author, but not reported here.

Chapter 7: Hot isostatic pressing and durability assessment of fluorite related ceramic wasteforms containing neutron absorbers for PuO_2 disposition

The HIPing of several types of fluorite based ceramic compositions, including zirconolite, zirconate pyrochlore and cubic zirconia, was investigated. These compositions were selected due to the actinide bearing natural analogues reported along with their ability to accommodate neutron poisons such as Gd

and Hf, as well as the Pu surrogate, Ce. The resulting phase assemblage was analysed and the effect of this on the relative chemical durability of these compositions was investigated using an aggressive PCT-B type protocol. The relative release of the Pu surrogate, Ce, and the neutron poison elements, Gd and Hf, was also investigated to ensure subcriticality of the wasteform and surrounding environment is maintained.

The authors contribution was: all experimental work with the exception of the synthesis of the wasteform materials which was completed by Dr. Martin Stennett, as well as the ICP-MS data acquisition which was completed by Dr. Colleen Mann. This chapter also involved considerable method development for the PCT experiments and ICP analysis protocol undertaken by the author, but not reported here.

Chapter 8: Molten salt synthesis of Ce doped zirconolite for the immobilisation of pyroprocessing wastes and separated plutonium

Pyrochemical reprocessing is an advanced reprocessing technique that generates a salt waste stream which is entrained with MA. The selective immobilisation of these entrained MA pyroprocessing was investigated, with the secondary aim of investigating the separation of Cl from the contaminated portion of the PuO_2 stockpile. Molten salt synthesis was used, with the addition of stoichiometric zirconolite reagents to a chloride salt eutectic, facilitating the selective immobilisation. Several experimental parameters were systematically varied to observe their effect on the phase assemblage produced.

The author's contribution was the completion of all experimental work and data analysis, where Dr. Florent Tocino assisted in experiment design and Dr. Martin Stennett assisted with the acquisition of Ce XANES spectra.

Note to reader

This thesis is presented using the alternative ‘publication’ format, whereby each results chapter was written as a journal article draft (with the exception of Chapter 8 where the published journal article is presented in Appendix A). This format naturally generated some repetition within the Introduction and Experimental sections of Chapters 4 – 8, however this was necessary for the format of draft journal articles. This format also presents some challenges to fully elaborate on the aims and objectives, as well as the motivation of each results chapter, within the results chapters themselves. Please refer to this Introduction chapter for the aims and objectives of the thesis, and the separate results chapters where required.

2 Literature Review

Note to reader: each results Chapter (4 – 8) contains a summary of the literature relevant to the work completed there. This literature review provides relevant background information regarding the generation and subsequent immobilisation of radioactive waste and along with information regarding the durability assessment of the wasteform materials.

2.1 Radioactive decay and nuclear fission

Radioactive decay is the spontaneous emission of radiation caused by unstable nuclei that have an excess of protons or neutrons in the nucleus. There are three main types of radioactive decay:

1. *Alpha decay*

A particle with two protons and two neutrons is emitted from the nucleus as shown in an example of typical alpha decay in Equation (2.1).

$$^{232}_{92}\mathrm{U} \rightarrow {}^{228}_{90}\mathrm{Th} + {}^{4}_{2}\alpha \qquad (2.1)$$

A sheet of paper can prevent penetration of all alpha particles, as will the outer layer of the skin.

2. *Beta decay*

Weak interactions in the nucleus cause either β^+ decay, shown in Equation (2.2) or β^- decay, shown in Equation (2.3).

$$^{14}_{6}\mathrm{C} \rightarrow {}^{14}_{7}\mathrm{N} + \mathrm{e}^- + \bar{\nu}_\mathrm{e} \qquad (2.2)$$

$$^{10}_{6}\mathrm{C} \rightarrow {}^{10}_{5}\mathrm{B} + \mathrm{e}^+ + \nu_\mathrm{e} \qquad (2.3)$$

An excess of neutrons in the nucleus results in β^- decay, whereas an excess of protons results in β^+. A few mm of aluminium or water prevent beta decay products from penetrating a material.

3. Gamma decay

This type of decay involves the emission of a high-energy photon by a nucleus that is in an excited state, and often follows alpha or beta decay. The radiation released has a characteristic energy depending on the nuclei involved and preceding decay route (Figure 2-1). Radiation from gamma decay is stopped by lead or other heavy metals.

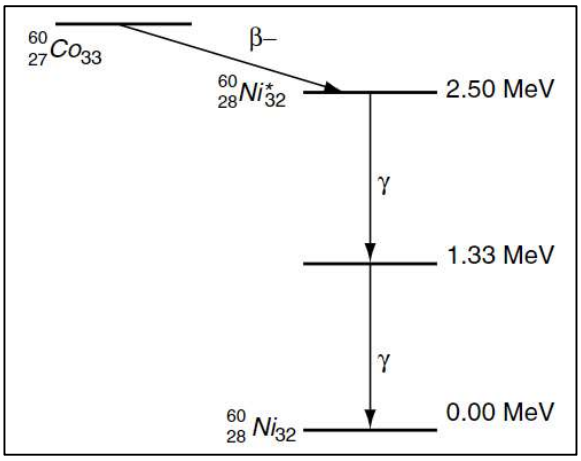

Figure 2-1– Diagram of beta decay and gamma decay of Co-60, showing the release of gamma rays of characterisic energy upon each decay event.

Nuclear fission involves the splitting of a nucleus into two smaller nuclei, known as FPs by the capture of a neutron, as shown in Equation 2.4. This process causes the emission of further neutrons which can help to sustain the reaction. Criticality occurs when one or more the neutrons generated goes on to generate the fission of another atom. There are two types of nuclei which can undergo nuclear fission: fissile nuclei which can maintain a self-sustaining nuclear reaction when bombarded with low energy (thermal) neutrons (e.g. ^{235}U), and fertile nuclei which can be bombarded with high energy neutrons to produce fissile nuclei (e.g. $^{232}Th + n \rightarrow {}^{233}U$).

$$^{235}_{92}\mathrm{U} + {}^{1}_{0}\mathrm{n} \rightarrow \mathrm{A} + \mathrm{B} + \mathrm{x}\,{}^{1}_{0}\mathrm{n} + 200\ \mathrm{MeV} \qquad (2.4)$$

The reaction in Equation 2.4 shows the production of fission products, A and B, with the number of neutrons produced per fission of ^{235}U is denoted by '*x*', where $x \approx 2.5$ per fission of ^{235}U. The percentage yield of FP per mass number for Equation 2.4 is shown in Figure 2-2, where there are two peaks displayed at approximately A = 95 and A = 135, which are the peak in the average mass number of FP. The range of FP produced by nuclear fission is vast, generating elements from approximately 30% of the periodic table [19].

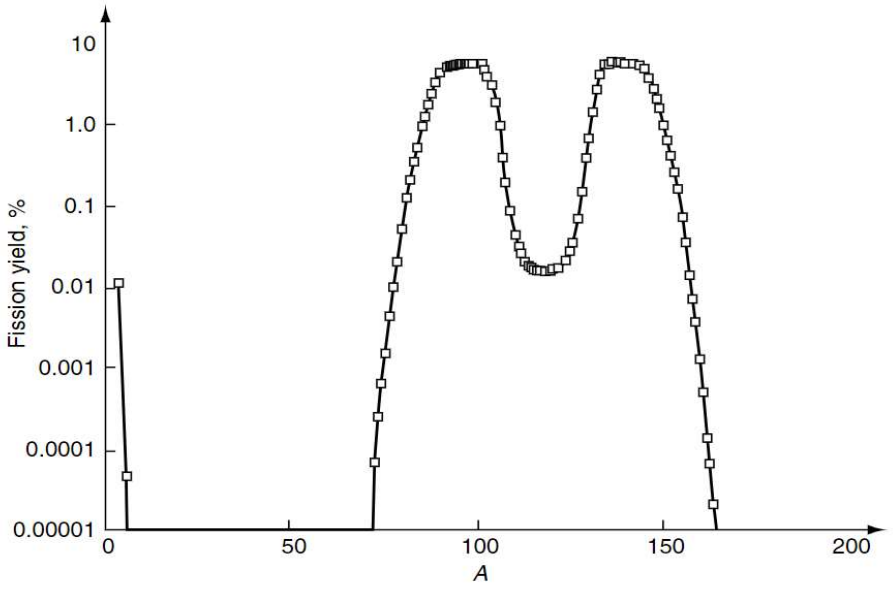

Figure 2-2 - Fission product yield of ^{235}U as a function of mass number. Taken from [1].

2.2 Nuclear power generation

Nuclear power is generated via the nuclear fission of ^{235}U, as described in Equation 2.4, and generates over 10% of the world's electricity. Generating energy using nuclear power plants is particularly of interest in recent years due to the low carbon power generated and the base load addition to the energy mix. The heat produced by nuclear fission is used to heat water to generate steam, which then drives a turbine, a process which is similar to traditional fossil fuel plants. The structure of a nuclear power plant contains the fuel (which can be of several different types such as ceramic UO_2 or metallic U), a moderator and a coolant. The moderator slows the neutron released in fission,

to allow for neutron capture in most types of NPP, however fast reactor types do not require a moderator. The coolant transfers heat arising from fission in the reactor core and usually categorises the reactor type. Water is typically used as a coolant, however there are reactor design which use gases such as He and CO_2, or salts as coolants due to their increased thermal efficiency.

Nuclear power generation produces waste, similarly to other sources of energy generation, however wastes generated from NPPs contains unstable nuclei that are radioactive and is the primary source of nuclear waste generated worldwide. These radioactive waste streams create unique challenges when handling and storing the waste, to ensure that contamination to the environment does not occur and therefore impact human health. However, large amounts of energy are generated from small quantities of nuclear fuel, where the annual output of waste from an average NPP is 4000 m^3 compared to 130,000 m^3 from an average coal power plant [20]. It should also be noted that this hazard will reduce throughout the time that the material is stored/disposed of due to the decay of radioactive elements.

2.3 Nuclear fuel cycle

The nuclear fuel cycle (NFC) is used to describe the steps involved in nuclear power generation and is illustrated in Figure 2-3. There are three main sections of the cycle: the front end, power generation and the back end. The front end of the fuel cycle consists of the mining of uranium ore, through to the enrichment of ^{235}U isotope and subsequent fabrication of nuclear fuel. Nuclear power generation involves the use of the fuel in the nuclear reactor, with the fuel removed from the reactor and replaced when the reactivity has been reduced sufficiently, through a build-up of FPs. Once spent nuclear fuel is removed from the NPP, it can either be stored or reprocessed, with the events occurring at this part of the fuel cycle are known as the back end of the NFC. There are wastes generated at each stage of the fuel cycle. A typical 1 GW NPP generates approximately 100 m^3 of LLW and ILW, and 30 tons of SNF [21], of which 200 kg is PuO_2 [22].

2.3.1 Open and closed fuel cycles

There are two types of NFC, open and closed, which are demonstrated in Figure 2-3, and the type of fuel cycle chosen by a nation will determine the types of wastes generated.

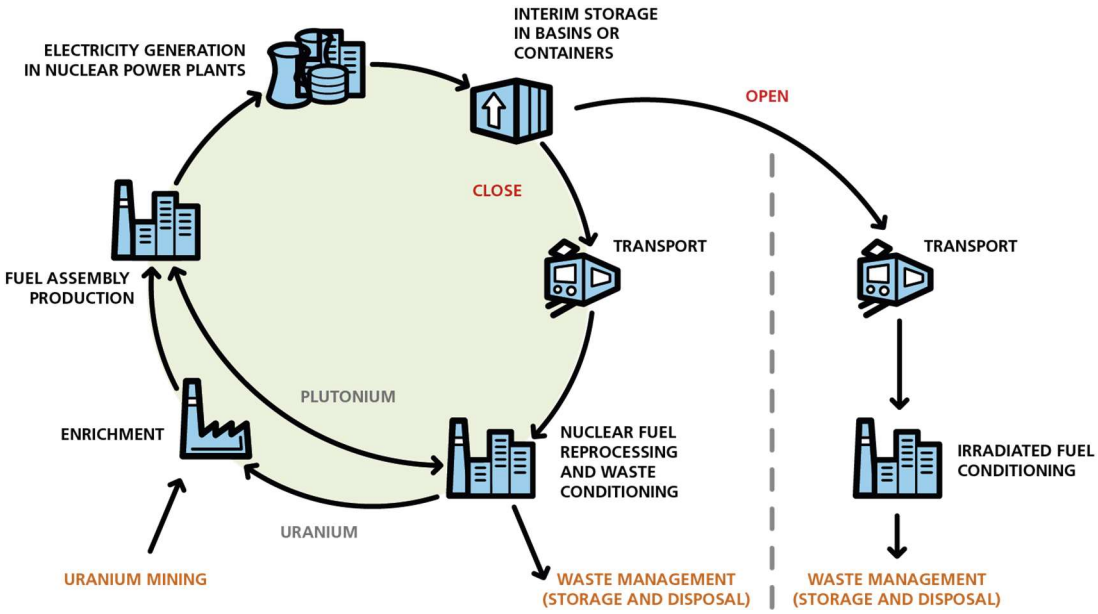

Figure 2-3 - Open and closed fuel cycle flow chart (taken from [23]).

A closed fuel cycle, as shown in Figure 2-3, includes the recycling/reprocessing of SNF to extract the U and Pu that can be reused to produce more fuel, since at least 95% of SNF is composed of UO_2, and 1% PuO_2, both of which are fissile and can be used to further generate nuclear power. However, the remainder of the SNF, the FPs and MAs must first be separated. Aqueous reprocessing of SNF using the PUREX (Plutonium-Uranium-Extraction) process generates large quantities of HLW that comprises MA, FP and corrosion products from activated fuel cladding. These are the most radioactive components of SNF. There are several advantages to closing the nuclear fuel cycle, such as improving the sustainability of the nuclear fuel sources, reducing the requirement for mining, as well as reducing the Pu inventory and addressing the associated proliferation and security risks [24].

The open/once-through fuel cycle involves disposing of SNF directly into a GDF [19], after a period of cooling for several years in cooling ponds. This fuel cycle is implemented by several countries such as Canada, USA, Sweden and Finland. This has the advantage of reducing the processing costs incurred, however the volume of waste to be stored by using this method are much greater, since the cladding and fuel containment are stored with the fuel as a single unit. This will also increase the potential size, and therefore the cost, of a GDF, however the handling and disposal of complex secondary wastes generated from reprocessing are negated.

2.3.2 Nuclear power in the UK

The UK was the first country to produce nuclear power for civil use when the Calder Hall began generating power in 1956 [25]. Since then, nuclear power has continued to provide a significant portion of the energy required in the UK and contributed approximately 19% to the UK energy mix in 2020 [26]. There are two types of nuclear reactor which were first developed in the UK, the Magnox reactor and the advanced gas cooled reactor (AGR), both of which use pressurised gas as a coolant, and only the AGR rectors are currently operational (14 reactors at seven sites across the UK). Sizewell B is the only water cooled/moderated reactor in the UK, which is the pressurised water reactor design (PWR), the most common reactor type in the world (Figure 2-4).

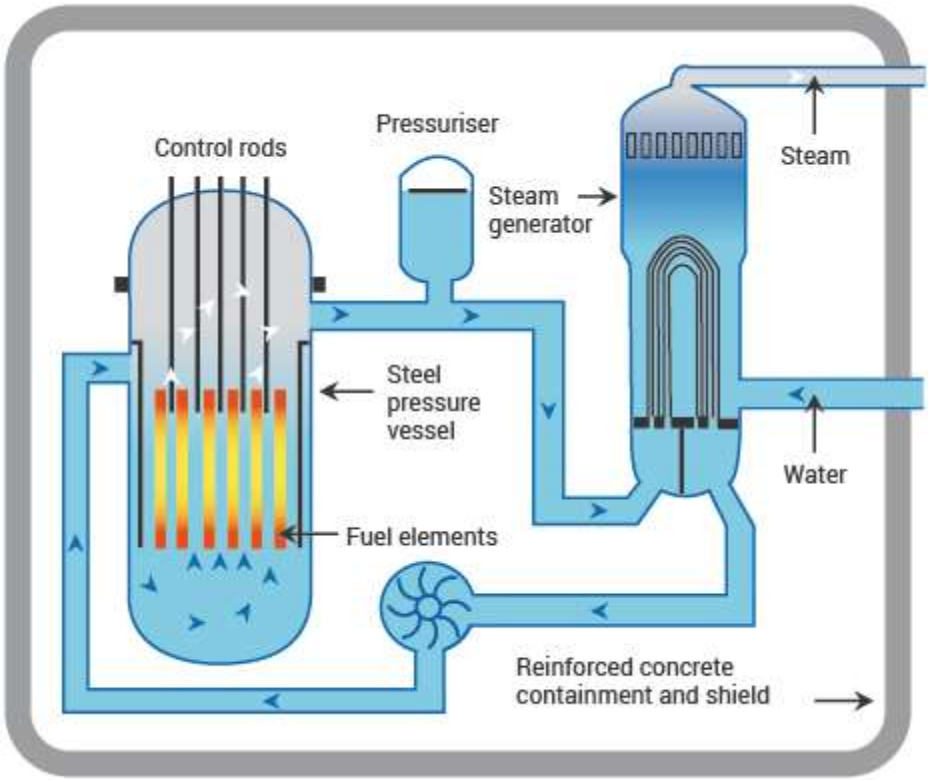

Figure 2-4 – Schematic of a PWR reactor design showing the reactor core, coolant loop, steam generator and control rods. Taken from [27].

2.4 Nuclear fuel reprocessing

The reprocessing of SNF separates the fuel into fissile/fertile material, namely PuO_2 and UO_2 which can be reused in nuclear fuel, and the MA/FP disposed of separately. There are many different methods proposed for the reprocessing of nuclear fuel. The method employed in the UK is PUREX, which is described in detail below.

2.4.1 PUREX process

The method of spent nuclear fuel reprocessing adopted in the UK utilises the PUREX and is the main source of separated Pu in the UK stockpile via the ThORP and Magnox reprocessing plants. This process initially involves the removal of fuel cladding, with the fuel then dissolved in nitric acid. Solvent extraction then takes place where nitric acid solution is mixed with an organic phase, tri-butyl phosphate, which are immiscible. Utilising the range of

oxidation states of U and Pu, they are separated from the FP and MA, and then the U and Pu are separated into separate streams. This process generates separated U and Pu streams in addition to a HLW liquor containing [3]:

1. Fission products – $^{134, 135, 137}Cs$, ^{90}Sr, ^{99}Tc, $^{129, 131}I$,
2. PUREX contaminants,
3. Corrosion products,
4. Minor actinides – ^{237}Np, $^{238, 239}Pu$, ^{241}Am, $^{242, 244}Cm$.

The exact composition and volume of these contaminants in the HLW is dependent upon several factors e.g. reactor type, fuel type, burnup rate.

2.4.2 Advanced extraction methods

There are several advanced aqueous reprocessing techniques which build upon the PUREX process such as GANEX (Grouped Actinide Extraction), DIAMEX (Diamide Extraction) and SANEX (Selective Actinide Extraction). These are all alternative to the PUREX process, using a selection of different organic phases and solvents, as well as buffers to varying the oxidation states of the actinide elements to extract variations of them in each process [28].

An alternative to aqueous reprocessing is pyrochemical reprocessing (pyroprocessing), which is under development at the Korean Atomic Energy Research Institute, South Korea [29] and at Argonne National Laboratory, USA [30], as well as in Russia where pyroprocessing is proposed as the primary method of closing the fuel cycle. Pyroprocessing is a dry process whereby the SNF is electrorefined in a high temperature (500 – 600 °C) salt eutectic, often composed of chloride salts [31], [32]. Uranium is collected at the cathode, leaving behind a salt eutectic with entrained MA and FP. The contamination from the MA and FP in the salt increases the eutectic temperature and therefore must be decontaminated or disposed of periodically. Research is currently being undertaken to selective extract the waste actinides in a ceramic wasteform using the molten salt as a reaction medium [33]–[35], or in a zeolite, which can be heated treated to form a sodalite glass, trapping the waste [36]. Oxygen sparging can also be used to

precipitate the MA and FP chlorides from the salt waste as oxides, which can then be separated from the salt stream and immobilised separately [37], [38]. Pyrochemical reprocessing is advantageous compared to the PUREX process because it ensures proliferation resistance of the end product by recovering U, Pu and MA simultaneously. The salts also have high radiation tolerance compared to the organic compounds used in aqueous extraction processes [39].

2.5 Nuclear waste immobilisation

The immobilisation of waste is defined as the conversion of a waste into a wasteform by chemical incorporation into the structure of the wasteform material [40]. This process reduces the probability of the waste materials to migrate and disperse into the environment. The wastes generated, as specified in Section 1.1, must be conditioned and immobilised using an appropriate material prior to disposal. The desirable characteristics of the wasteform are described in Section 1.3.

2.5.1 Plutonium immobilisation

The immobilisation of PuO_2 must be considered for the end state of the UK PuO_2 stockpile in the event that current policy relating to the status of this material changes (see Section 1.4), and for designing wasteforms that are suitable for the contaminated portion of the stockpile. This research is also of interest for other countries such as Japan, Russia, France and the USA, who also have considerable PuO_2 stockpiles which could require immobilisation in future. There are also several economic and technological challenges associated with the generation of MOX fuel when considering the current state of the UK NFC, since there is a lack of uptake for new build reactors which can utilise this fuel type.

There are several routes for the immobilisation of Pu evaluated in the literature: immobilisation in specially formulated glasses or in to tailored ceramic materials [41]–[46]. Glass-ceramic wasteforms have also been considered for the immobilisation of HLW [47], [48] and Cl contaminated PuO_2

[49]–[53], however these will not be discussed in this thesis. The formulations developed in either route could require consideration to maintaining subcriticality, with the addition of neutron absorber elements into the wasteform to ensure long term integrity of the wasteforms. Accountancy of the Pu throughout the wasteform production process would also need to be addressed. Another route for the immobilisation of PuO_2 is disposal/storage MOX, utilising already operating MOX fuel fabrication plants to generate a low specification MOX fuel for the disposal of PuO_2 [17]. The decision about which type of wasteform should be used are dependent on fulfilling the wasteform acceptance criteria, as discussed in Section 1.3.

2.6 Types of wasteform

There are two key types of wasteform for the disposal of PuO_2 which will be considered in this thesis: glass and ceramics. Details about the types of glass and ceramic composition considered for the immobilisation of PuO_2 and their relative merits can be found in this section.

2.6.1 Glass

Vitrification is considered to be a suitable option for many waste streams, particularly HLW containing FP, MA and activation products, due to the chemical flexibility of the glass structure [3]. Glass formulations have been utilised for this purpose for several decades and vitrification is therefore a well-established technology. However, vitrification is unsuitable for some wastes such as those high in volatile species e.g. Cl, Mo and I, since these are likely to volatilise at typical glass synthesis temperatures (1100 - 1500 °C) and also have low solubility in glass, therefore another type of wasteform must be considered for these waste streams. The solubility of actinide elements, such as Pu, in traditional HLW glasses is also reportedly low (1.5 wt.% in the French R7T7 HLW borosilicate glass composition [54]), however glass formulations can be adapted to allow for increased waste loading of these elements. Vitrification is suitable for the immobilisation of nuclear waste as it fulfils many of the criteria shown in Table 1-2 e.g. there are natural analogues (volcanic glasses, which are approximately 4 million years old with alteration layers of

thickness 200 μm [55]) which provide evidence for chemical durability over geologic time scales [56]. Glasses generally have a flexible network, which can adapt to various waste streams by incorporating many sizes of ions into the chemical structure, including over 30 different elements contained in many HLW streams [21]. Processing efficiency (which is linked to viscosity and melting temperature of the glass) must be considered and therefore a compromise is often made between this and the durability of the glass produced. However, glass wasteforms are intrinsically thermodynamically unstable and their durability is highly dependent upon composition, and crystallisation/elements which remain undissolved in nuclear waste glasses is undesirable. Glass wasteforms are currently being produced on an industrial scale at: La Hague, Sellafield, Savannah River, Karlsruhe, Trombay, West Valley, Hanford, Tokai, Tarapur, Mayak and Rokkasho-Mura [21].

There have been many different glass compositions designed for the immobilisation of different waste streams, however very few are used in practise. There are two main glass compositions which have been considered for nuclear waste immobilisation at present of which the majority of the literature is focussed: borosilicate and phosphate glasses, however others have also been investigated such as aluminosilicate glasses. The formulations in use today have been optimised to achieve the best compromise of the following factors for the target waste stream: operating parameters, waste loading glass properties and long term durability [57].

2.6.1.1 Glass structure

A glass is a material that has a structure which lacks long-range order and can be defined as being X-ray amorphous solid with a time dependent glass transition temperature [11]. The glass structure can be described as a three dimensional network of polyhedral structures, with distorted bond angles that give rise to the random network. Glasses form upon the rapid cooling of liquid which avoids the formation of a crystalline structure. Amorphisation can also occur as a consequence of the radiation damage on crystalline materials.

The Zachariasen model for glass formation is the foundation of many descriptions of glass structure in the literature and proposed a random glass network where silica tetrahedra are connected by bridging oxygens with no ordering at distances > 8 Å. [59]. Zachariasen's rules for the formation of a glass are:

1. An oxygen atom must not be linked to > 2 other atoms.
2. The number of oxygen atoms surrounding an atom must be small.
3. The oxygen polyhedra can only share corners (rather than edges or faces).
4. At least 3 of the corners of any polyhedra must be shared.

The network possesses short range order from the central cation (1.5-2.9 Å), medium range order is also possible (2.9-5.5 Å) which corresponds to the tetrahedra, and long range order (3.5 to ~10 Å), and beyond 10 Å there is no order observed in the network [60]. This is the continuous random network, a model for glass structure which was only applicable to vitreous silica and was modified to better describe alkali silicate glasses with X-ray diffraction studies completed by Warren [61]. This modified model postulates that the addition of an alkali/alkaline earth element, which occupy space between the glass forming tetrahedra, cause a bridging oxygen (Si – O – Si) to become a non-bridging oxygen (Si – O^-) (see Equation 2.5 and Figure 2-5).

$$Si - O - Si + Li_2O \rightarrow 2(Si - O^-) + 2Li^+ \qquad (2.5)$$

Building upon this model further, there is also the modified random network model which was proposed by Greaves [62] who used XAS studies on alkali silicate glasses to further understand the structure of more complex glasses. The model introduces two separate but interlinked regions within the glass network, a network region containing network formers and an internetwork (see Figure 2-5).

Table 2-1 – Examples of elements which correspond to each category of cation in the glass network with associated Dietzel Field Strength range [63].

Cation type	Field strength range	Example elements
Network former	1.4 - 2.0	Si, B, P
Intermediate	0.5 - 1.0	Zr, Ti, Al, Fe
Network modifier	0.1 - 0.4	Li, Na, K, Ca, Mg

Glasses have several components which can be used to describe its structure: network former, intermediate structural elements and network modifiers. Examples of these elements can be found in Table 2-1. It should be noted that it is difficult to confirm whether an element is an intermediate component of the glass without knowledge of the local coordination number of the element in the glass [61].

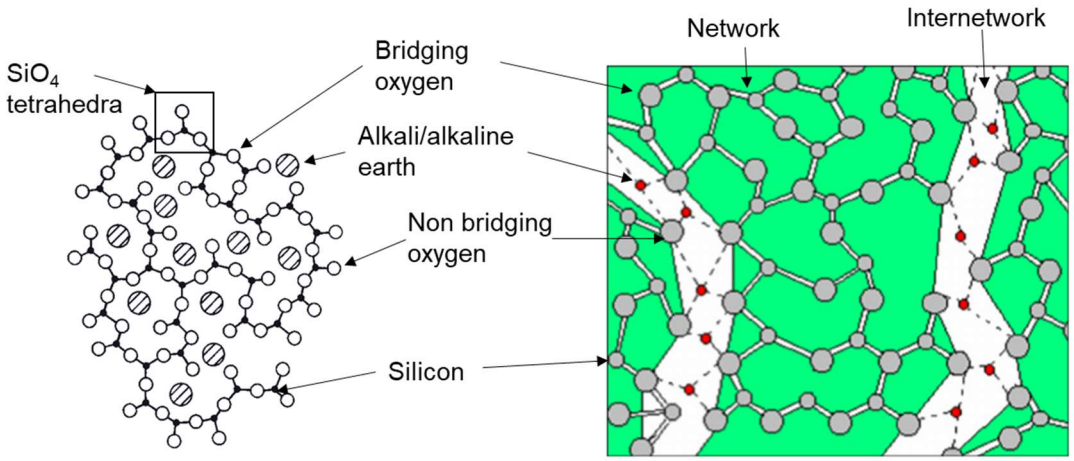

Figure 2-5 – A two dimentional representation of a continuous random network as described by the Zachariasen-Warren model (adapted from [64]) (*left*) and the modified random network (adapted from [1]) (*right*).

A ratio related to the cation-oxygen radius ($d_{C\text{-}O}$) and charge of an cation (Z_c), referred to as the Dietzel field strength, can be used to classify an ion as an intermediate, glass former or network modifier Table 2-1. It is calculated as follows:

$$Dietzel\ field\ strength = \frac{Z_C}{d^2_{(C-O)}} \quad (2.6)$$

The incorporation rate of a radionuclide into the glass depends on the ionic radius/field strength of the radionuclide, the composition and the structural role of each of the elements, and the synthesis conditions

Glasses proposed for nuclear waste immobilisation are typically silica based e.g. borosilicate and aluminosilicate formulations. In silicate glasses, SiO_4 tetrahedra form a disordered network where Si-O-Si bond lengths and angles vary throughout the glass structure. Borosilicate glasses incorporate B as a network forming element, with the addition of B causing a reduction in the melt temperature of the glass. Fe and Al can also behave as network formers in the glass network. Alkali elements can also be added to charge balance the addition of high valence cations, such as Fe and Al into the glass melt, and aid their incorporation as glass network forming elements [65]. The solubility of lanthanide elements in a glass melt is increased with the quantity of alkali elements in excess of Al^{3+} within the melt, ensuring sufficient alkali cations are available for charge balancing.

2.6.1.2 Glasses for Pu immobilisation

Borosilicate glasses have been formulated for the immobilisation of HLW, typically incorporating alkali elements such as Li and Na, for example the MW (Mixed Windscale) glass which is the UK HLW glass formulation. The HLW glass formulations have also been adapted to increase the Pu wasteloading and include: lanthanum borosilicate (LABS), alkali tin silicate (ATS) [66], [67], and aluminoborosilicate glass [68], [69]. These formulations all compromise on either processing temperature, wasteloading or chemical durability, and were compared in a comprehensive study completed by Harrison *et al.* [70]

e.g. lanthanum borosilicate and aluminosilicate compositions are known to have high wasteloading (15 wt.% CeO_2) and good chemical durability (normalised Ce dissolution rate (NR_{Ce}) = 2.92 x 10^{-2} g m^{-2} d^{-1}), however they have a melt temperature of 1500 °C, which can be prohibitive for standard glass melting technologies such as induction melting and Joule heated ceramic melting [71]. This is compared to ATS glass, where a 15 wt.% CeO_2 waste loading was achieved at 1300 °C with NR_{Ce} = 1.21 x 10^{-1} g m^{-2} d^{-1}, which compromises on chemical durability with reduced melt temperature. When considering the MW glass where only 10 wt.% CeO_2 wasteloading was achieved at 1200 °C, with NR_{Ce} = 1.02 g m^{-2} d^{-1} [70], it is clear that the modifications to these compositions can help to achieve a glass suitable for the immobilisation of Pu. Phosphate glasses have also been investigated for HLW immobilisation, with some formulations adapted for Pu immobilisation including iron phosphate, lead iron phosphate and sodium aluminophosphate glasses [72]. These formulations were not considered in this thesis therefore will not be discussed further.

2.6.2 Ceramics

Ceramics are crystalline materials suggested for nuclear waste immobilisation, due to their enhanced chemical durability compared to borosilicate glasses. They can be single phase materials, targeted for the immobilisation of specific elements or multiphase ceramics such as the SYNROC suite of ceramics formulations, each developed to target specific nuclear waste streams. The basic premise for the use of ceramic materials for nuclear waste immobilisation is to target the waste ions onto specific sites of the wasteform. The ceramic formulations are selected based on the wasteform acceptance criteria described in Section 1.3.

There are several different formulations of ceramic material which have been considered in the literature for Pu/actinide immobilisation. These are: SYNROC (specifically SYNROC-C), zirconolite, pyrochlore and zirconia. For pure materials, single phase ceramics are appropriate e.g. the majority of the

Pu stockpile in the UK, with multiphase ceramic materials more appropriate for complex waste streams such as HLW.

2.6.2.1 Ceramics for Pu immobilisation

2.6.2.1.1 Cubic zirconia

Cubic zirconia, ZrO_2, has a fluorite structure, with the general formula MO_{2-x}, where M can accommodate lanthanides, actinides, or neutron absorbers. The structure adopts space group Fm-3m and is described as a face centred cubic array of M cations, with the O anions occupying the tetrahedral interstices. The M cations are often 8-fold co-ordinated at the centre of edge sharing MO_8 cubes. In the case of ZrO_2, the radius Zr^{4+} cation is too small to accommodate 8 O anions in the cubic structure, therefore trivalent cations are readily incorporated to introduce vacancies which stabilise the ZrO_{2-x} structure. Gd is readily incorporated into the cubic zirconia structure for this reason, acting as a neutron absorber, as well as stabilising the chemical structure and reduce the processing temperature required. The chemical structure is highly resistant to radiation damage and subsequent amorphisation [73].

2.6.2.1.2 Pyrochlore

Pyrochlore is a mineral with a fluorite related structure, and has a general formula $A_2B_2X_6Y$, where A and B are 8- and 6-fold coordinated cation sites and X and Y are 4-fold coordinated anions [74]. The pyrochlore structure, in space group Fd-3m, is derived from the fluorite structure by the presence of an ordered (alternating) arrangement of A and B cations on the face centred cubic lattice, coupled with the presence of ordered vacancies on one eighth of the oxygen sites. Actinides and lanthanides are typically targeted for substitution onto the A site, with Zr and/or Ti typically located on the B site. However, increased chemical flexibility is afforded, compared to zirconia, due to the ability to target onto both the A and B site with waste and neutron absorber elements with a variety of ionic radii. There are two types of pyrochlore generally investigated for nuclear waste immobilisation: zirconate and titanate [22], [75]. Zirconate, or ZrO_2 - based pyrochlores are known to

retain their crystalline structure under high levels of radiation damage. However when compared to titanate, or TiO_2-based pyrochlores, they often require sintering at higher temperatures to produce a fully densified material [76].

2.6.2.1.3 Zirconolite

Zirconolite is a titanate ceramic with a fluorite derivative structure and is a member of the pyrochlore mineral family [77]. It has a prototypical formula $CaZr_xTi_{3-x}O_7$ where $0.8 < x < 1.35$ and adopts the C2/c space group [78]. The crystal structure of zirconolite is composed of layers of CaO_8 and ZrO_7 polyhedra interleaved with TiO_6/TiO_5 polyhedra displaying a hexagonal tungsten bronze motif. The repeating unit described above is the structure of the most common polytype, 2M [79], with variations in the stacking sequence contributing to other polytypes such as 3T, 3O and 4M [80]–[84]. The difference in the stacking sequence of these layers results primarily from changes in the cation site occupancy and vacancy distribution [85], however, oxygen fugacity and processing temperature are also contributing factors [86]. Zirconolite 4M is described as layers of zirconolite 2M alternating with pyrochlore structural units, which accommodates greater incorporation of actinide/lanthanide cations into the structure [87], and typically occurs as a result of the substitution of cations with large ionic radius onto the B site (e.g. substitution of Pu^{4+} (0.91 Å) onto Zr^{4+} site (0.78 Å) [88]) [89]. The composition of zirconolite is flexible, allowing the substitution of actinide elements onto both the Ca and Zr sites, dependent upon the valence of the ion, using appropriate charge compensating ions on the Ti site e.g. $Ca_{0.8}Ce_{0.2}ZrTi_{1.8}Al_{0.2}O_7$ [90]. Alternatively, isovalent substitution onto the Zr site can also be targeted [89], e.g. $CaZr_{0.8}Ce_{0.2}Ti_2O_7$ [91], however this substitution mechanism is less common in natural zirconolite specimens. Examples of natural zirconolite exhibit a wide variety of compositions, frequently containing radioactive elements, and are up to 10^9 years old, demonstrating their feasibility for the immobilisation of nuclear waste [77], [92], [93].

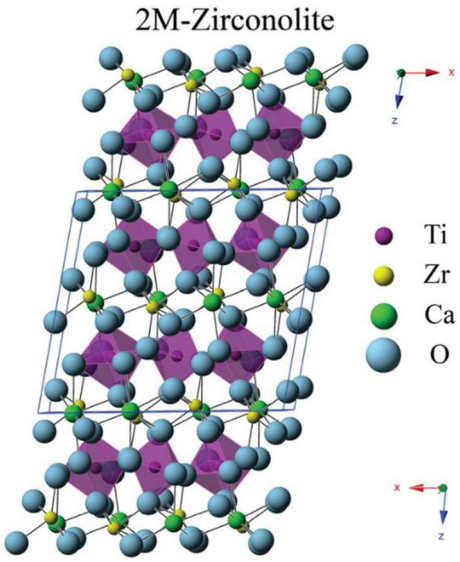

Figure 2-6 – Structure of zirconolite 2M showing the Ca and Zr polyhedra, with alternating layers of Ti polyhedra. Taken from [87].

2.6.2.1.4 Perovskite

Perovskite is a titanate ceramic, with general formula ABX_3, in which the three dimensional network of corner sharing BX_6 polyhedra are occupied by small cations, e.g. Ti, and the cuboctahedra interstices are occupied by the A cation, typically a larger alkali, alkaline earth, actinide or lanthanide cation. The parent structure, in space group Pm-3m, can also be described as close cubic packed AX_3 layers, in which the B cation occupy the octahedral holes. This phase is proposed as part of the SYNROC formulation and is an accessory phase often formed when synthesising zirconolite ceramics [94]. However the durability of perovskite is several orders of magnitude less than other phases in the polyphase ceramic, which contain other titanate ceramic materials such as zirconolite and pyrochlore [95], [96].

2.6.2.1.5 SYNROC

SYNROC, or SYNthetic ROCk, is a multiphase ceramic material first developed at ANSTO by Ringwood *et al.* as an alternative wasteform to borosilicate glass for the immobilisation of HLW [97], [98]. There were several variants of the formulation developed, where SYNROC-C is a variant of the

SYNROC formulation, specifically formulated to immobilise HLW. The formulation contained hollandite ($BaAl_2Ti_6O_{16}$), perovskite, zirconolite and rutile (TiO_2) [99] It was found that actinide elements such as Pu, preferred to partition into the zirconolite phase, therefore this was investigated as a single phase ceramic waste stream as a consequence. SYNROC was also suggested for the immobilisation of Pu, with a pyrochlore rich variant developed to incorporate the Pu stockpile along with feedstock impurities [100]. These formulations were developed based on the behaviour of natural analogue minerals which were found to retain actinide and lanthanide elements for 10^6 - 10^9 years. The formulations can be adapted to accommodate neutron absorbers such as Hf and Gd, which are an important concern for maintaining the subcriticality of elements such as Pu. Pyrochlore and zirconolite are key actinide immobilising phases in this wasteform, leading to the investigation of the feasibility of these single phase wasteforms to be investigated as described above.

2.7 Waste form durability

Chemical durability is arguably one of the most important factors in deciding upon a suitable wasteform for the immobilisation of a specific waste stream. This is to ensure that the wastes immobilised are not released into the environment prematurely. Laboratory tests to assess the chemical durability of wasteforms can provide an insight into their comparative performance against other wasteforms. Some tests can also allow a greater understanding of how the wasteform will perform in an envisaged geological repository environment. The release of radioactive species into the environment must be prevented, hence the importance of dissolution behaviour in contributing to the safety case of the disposal of these wasteforms in a GDF.

2.7.1 Durability test methodologies

Durability/dissolution tests involve the submersion of the wasteform in a solution, with the elemental concentration in solution measured over time. Static dissolution tests are defined by the low leachant renewal rate in the system and can be used to provide a greater understanding of the rate of

saturation of elements in solution, as well as surface effects upon solution saturation. There are two main standard methodologies used for comparing the relative durability of waste, these are PCT-B [101] and MCC-1 [102]. Further information regarding the methodology employed in these standard tests can be found in Section 3.4. In static tests, the dissolution rate reduces over time as the solution reaches saturation of elements. These tests can provide information about the alteration layer formation and subsequent secondary phase precipitation [103]. Dynamic tests, such as single pass flow through tests (SPFT) can also be implemented to gain a greater understanding of the kinetic dissolution behaviour by maintaining dilute conditions [104], however these tests will not be considered in this thesis.

2.7.2 Glass durability

The durability of glass is determined by performing dissolution experiments, completed by submerging the glass in a solution/leachant. HLW borosilicate glasses display three key stages of dissolution, a theory which has been developed over many years, however this process is complex and there are still areas of this process which are still poorly understood. There have been many reviews about the process of glass dissolution, and this represents a condensed version [103], [105]–[108]. There are three stages of glass dissolution, illustrated by the changes in NL in Figure 2-7, and are described as follows.

Stage I: This is the initial rate regime where ion exchange of the alkali ions (network modifiers) in the glass and the H^+ ions in the leachant occurs, as described by Equation 2.7, where A is an alkali/alkaline earth element.

$$\mathrm{Si-O-A + H_2O \rightarrow Si-OH + A^+ + OH^-} \qquad (2.7)$$

This interdiffusion mechanism creates a surface layer depleted in alkali/alkaline earth elements as well as leading to hydrolysis of the network forming species (usually B, Al or Si). Hydrolysis can occur by two different reactions presented in Equation 2.8 and 2.9.

$$\equiv Si - O^- + H_2O \rightarrow \equiv Si - OH + OH^- \quad (2.8)$$

$$\equiv Si - O - Si \equiv + OH^- \rightarrow \equiv Si - OH(S) + \equiv Si - O^- \quad (2.9)$$

This hydrolysis mechanism leads to the formation of an alteration layer on the surface of the glass, consisting of amorphous silica and water. The final stage of hydrolysis occurs with the release of silicilic acid (H_2SiO_4) into solution upon the completion of hydrolysis reactions in a silica tetrahedra. This initial rate of dissolution is the maximum rate of any glass under any particular experimental conditions, particularly for a static dissolution test, before the leachate becomes modified by the release of elements from the glass [109]. The dissolution of glasses can be congruent, where the leaching of elements from the glass is stoichiometric, with incongruent dissolution being related to the selective leaching of elements.

Stage II – This is the residual rate stage which is reached when the solution becomes saturated in glass forming elements, an alteration layer is formed and low dissolution rates are maintained.

Stage III – Rate resumption may occur after the formation of deleterious precipitates in Stage II, which deplete the solution of glass forming elements, triggering the resumption of glass dissolution.

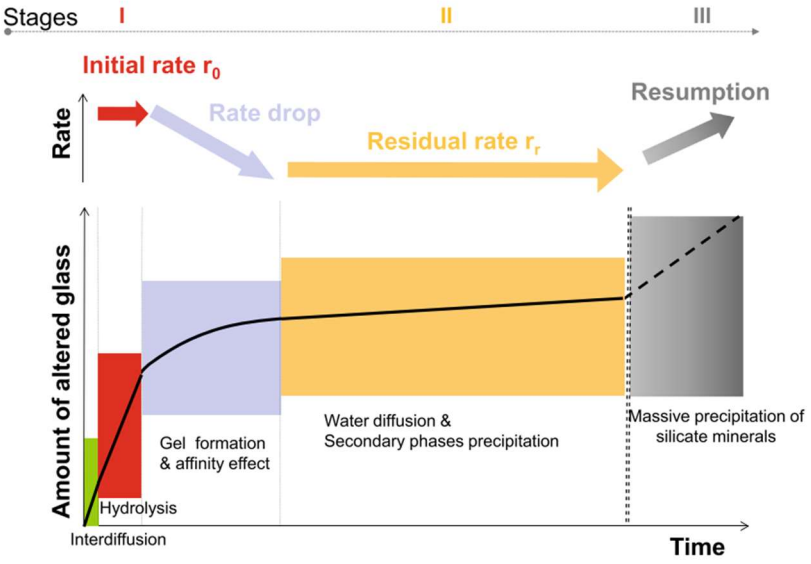

Figure 2-7 – Stages of glass dissolution (taken from [105]).

There are many variables which effect the rate of glass dissolution and the duration of each of the stages discussed above. These are pH, temperature, glass composition, leachant composition and the ratio of surface area of the material to the volume of the leachant [110], [111].

2.7.3 Ceramic durability

During dissolution, ceramic materials can undergo several different reaction such as hydrolysis, hydration, redox reaction and ion exchange, which can lead to the breakage of bonds within the crystal structure, releasing cations into solution [103]. As with glass, dissolution of ceramics can be either congruent or incongruent, with incongruent dissolution indicative of a multiphase system. Literature investigating the durability of ceramic materials is sparse relative to glass durability. This may be due to the challenges in completing dissolution experiments on these largely durable materials, with leach rates several orders of magnitude lower than borosilicate glass compositions. However there have been several PCT-B and MCC-1 tests reported on ceramic materials, particularly SYNROC-C [112], as well as zirconolite [113]–[116], pyrochlore [75], [117], [118] and cubic zirconia [92], [119] compositions developed for Pu/MA disposition.

3 Experimental Techniques

A summary of the techniques used to synthesise the wasteform materials featured in this thesis and characterise them is given in this chapter, as well as details of the experimental parameters used for the techniques corresponding to each results chapter. Details of each dissolution experiment are also included.

3.1 Sample Synthesis and Thermal Treatment Processes

3.1.1 Batching and milling

In order to produce ceramic or glass materials, reagents must first be batched according to a 'recipe' or target stoichiometry. Reagents used are typically metal oxides or carbonates and require drying to remove any absorbed water vapour. In glass melts, reagents which decompose upon heating (e.g. carbonates) are commonly used as this reduces the melting temperature and generates bubbles which aid homogenisation [58].

For ceramic wasteforms, the reagents are batched with a stoichiometric ratio according to a target composition. Milling allows for greater homogenisation of sample powders prior to thermal treatment, as well as reducing particle size. For HIPed ceramics, it is advantageous to use oxide powders as opposed to carbonates since the decomposition of these reagents can lead to unfavourable wasteform microstructures with porosity and lack of densification.

Milling is typically achieved using a planetary mill, where zirconia milling balls are placed into a mill pot with the reagent powders and an appropriate milling fluid e.g. isopropanol, cyclohexane. Using a milling fluid allows particles to move around more freely when milling and ensure even distribution of powder particles. The slurry is milled, dried and sieved to separate the milling balls from the powder.

Experimental Parameters

Chapter 4: Reagents were batched according to the formulation described in Bates *et al.* [66], with the target CeO_2 wasteloading included, and mixed before placing into an alumina crucible in preparation for melting.

Chapter 5: Reagents were also batched as in Chapter 4 with the exclusion of CeO_2. A frit was produced by pouring the glass melt into water and then milled using a Fritsch Planetary Mill (Pulverisette 6) at 500 rpm for 1 min to produce a powder with particle size < 75 µm. This was mixed with CeO_2 and Fe metal to produce a batch suitable for HIPing.

Chapter 6: Oxide reagents were dried in an oven overnight at 180 °C prior to being weighed using a balance with accuracy to 0.0001 g. Reagents were weighed in a stoichiometric ratio to a 50 g batch size and placed into a 250 mL zirconia mill pot with zirconia milling media and 20 mL isopropanol milling fluid to make a slurry. A batch of samples were milled at 500 rpm for 20 min. The slurry was dried overnight at 90 °C and sieved using a 250 µm sieve to separate the powder from the milling media.

Chapter 7: The matrix forming materials and neutron poisons were prepared by weighing out each precursor to 4 d.p, according to the target stoichiometry. The precursors were homogenised in a tumbling ball mill for 16 h, with yttria stabilised zirconia milling media and isopropanol as the milling fluid. The slurries were separated from the media using a sieve and dried overnight at 90 °C. Once dry, the powder batches were passed through a 250 µm mesh sieve and the cerium surrogate was added. Homogenisation of the surrogate and the inert batch was completed using a rotary tumbling mixer for 16 h. This work was completed by Dr. Martin Stennett.

Chapter 8: Oxide and chloride reagents were dried in an oven overnight at 180 °C prior to being weighed using a balance with accuracy to 0.0001 g. Powders were weighed into 1 g batches and milled using a zirconia mill pot and milling media with the Fritsch Mini Mill 6 and isopropanol milling fluid. Salts were also weighed and milled using the same method with the exception of using cyclohexane as a milling fluid since a non-polar solvent was required. Salt and ceramic powders were mixed according to the correct molar ratio and milled once again in cyclohexane

3.1.2 Vitrification

Vitrification involves the mixing of a batched quantity of raw materials which are then melted at an elevated temperature until a liquid is formed. During the cooling process, chemical and physical reactions occur which form an amorphous network at the atomic scale. Melts can either be static or stirred, with stirring aiding the homogenisation of the glass, particularly if there are reagents of high density which may otherwise stratify under gravity. The glass must then be cooled at a rate which is rapid enough to prevent recrystallization in the material. Annealing at a temperature 5 °C above the glass transition temperature and cooling a rate of 1 °C min^{-1} will remove any thermal stresses which may be present in the glass product.

Experimental Parameters

Vitrification is the main material synthesis technique for samples produced in Chapters 4 and 5. The glass precursors were batched and mixed according to Section 3.1.1 and placed into an alumina crucible where it was melted in an electric muffle furnace at a selected temperature between 1100 °C and 1300 °C with a 3 h dwell. They were then cast into a stainless steel mould and annealed at 510 °C.

In the case of materials produced in Chapter 5, a pre-formed glass frit was produced and utilised which was described in Section 3.1.1. The glass batch was melted at 1200 °C for 3 h in an electric muffle furnace. The glass melt was poured into a steel bucket filled with cold water to produce the frit.

3.1.3 Cold pressing and reactive sintering (CPS)

Cold uniaxial pressing and reactive sintering is a method of solid state synthesis, also known as the ‘shake and bake’ method [120], and involves sintering of batched oxide powders to produce dense ceramic bodies. Due to a lack of homogeneity at the atomic scale, producing dense and fully sintered materials using this method requires high temperatures and long furnace dwell durations to provide the thermal energy for the solid state reaction to occur.

The batched oxide powders are milled to improve the homogeneity of the powder and reduce sintering time (see Section 3.1.1) and are pressed into a pellet using a uniaxial hydraulic press and a stainless steel die to form a green body. The green body is sintered in a furnace to form a ceramic body or pellet. This body or pellet may have to be crushed, repressed and sintered once again to produce a fully homogeneous ceramic.

Sintering is the densification of a powder by solid state diffusion between grain boundaries. It is driven by the reduction of the free energy at the surface of the grains (i.e. reducing the total surface area of the particles) by either coarsening, the rearranging of particles, or densification, material moving to fill pores (see Figure 3-1). Coarsening does not lead to the reduction in pore volume therefore does not contribute to the improvement of material properties.

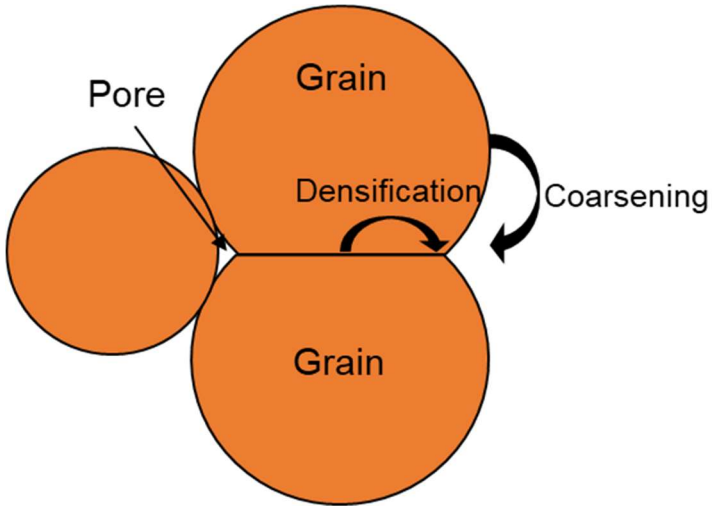

Figure 3-1 – Pathways of solid state diffusion between two idealised spherical particles. Adapted from [121].

Experimental Parameters

Chapter 8: Salt and ceramic powders were milled as in Section 3.1.1 and pressed into a pellet using a hydraulic press and 10 mm hardened stainless steel die applying 2 x 10^5 Pa of pressure. The pellet was sintered in alumina boat crucible at 1200 °C for 2 h in an electric muffle furnace.

3.1.4 Molten salt synthesis

Salts can be used as a liquid diffusion medium in which to synthesise ceramic powders. When heated to, or above, the melting point, the salt acts as a solvent, allowing the ceramic reagents to react more readily with each other to produce a more homogeneous product over shorter time scales and at reduced sintering temperatures when compared to a general solid state synthesis reaction [122]. It is also possible, in principle, to control the particle size and shape using this synthesis method.

The general procedure for the molten salt synthesis of a ceramic material involves mixing the stoichiometric ceramic reagents with the salt, often with an intermediate milling step. The mixture is then uniaxially pressed into a pellet and heated to a temperature greater than the melting point of the salts. Once the pellet has cooled, a solvent (typically water in the case of chloride salts) can be used to dissolve the salt, leaving behind the ceramic powder. The salt used for this process can be a mixture of salts which form a eutectic and reduce the melting temperature e.g. NaCl and KCl.

The particle size and shape can be controlled by taking advantage of two different bounding mechanisms which can occur during molten salt synthesis [123]:

1. Solution precipitation – occurs when the solubility of all reagents within the molten salt are similar and results in product particles which show no obvious similarity in morphology to the reagents (see Figure 3-2(a)).
2. Solution diffusion/templating [124] – one reagent (A) is more soluble that the other (B) resulting in the more soluble reagent dissolving into the molten salt and depositing onto the surface of the less soluble reagent, with subsequent reaction. This produces a product particle with the shape of the less soluble reagent (see Figure 3-2(b)).

Particle shape is highly dependent upon the reagents used and their solubility's in the salt.

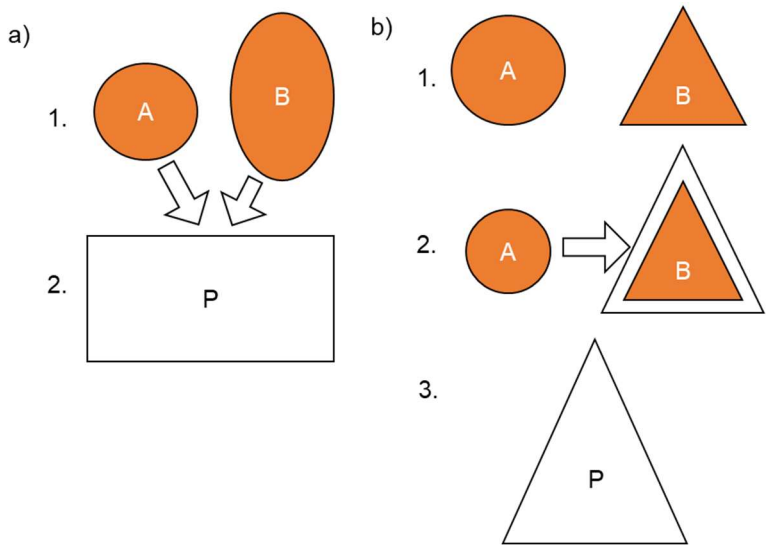

Figure 3-2 – (a) Solution precipitation and (b) solution diffusion (adapted from [122]).

The solution diffusion reaction has two stages: the first is the reaction phase and the second is the particle growth phase. Particle growth does not occur in stage one and this stage concludes once all reagents are consumed. Once stage two begins, particles larger than a critical size continue to grow [121] and smaller particles dissolve into the molten salt and precipitate onto the larger particles.

The molten salt synthesis process is particularly relevant for the immobilisation of radioactive waste from future Generation IV fuel cycles which utilise pyrochemical reprocessing as an option for the reprocessing of SNF (see Section 2.4.2). The salt, which acts as medium for the separation of SNF, into U. Pu, MAs and FPs in pyroprocessing could also act as a wasteform synthesis medium with the addition of ceramic oxide powders. A ceramic nuclear wasteform immobilising the entrained radionuclides could potentially be produced in this way, allowing the salt to be reused in further pyroprocessing and reducing the volume of HLW requiring immobilisation.

Experimental Parameters

Chapter 8: Salt and reagent powders were milled as in Section 3.1.1 and pressed into a pellet using a hydraulic press and 10 mm stainless steel die. The pellet was sintered at 1200 °C for 2 h in an electric muffle furnace. The sintered pellet was crushed using a pestle and mortar and washed with DIW using vacuum filtration to remove the salt.

3.1.5 Hot isostatic pressing

Hot isostatic pressing is a thermal treatment and powder densification process whereby simultaneous isostatic pressure and heat are applied to a material. The material is placed inside an appropriate metal carrier 'can' (which should not interact with the material) and then into pressure vessel where heat is supplied from a furnace. Simultaneously, an inert gas such as Ar surrounds the can, providing the isostatic pressure and densification by increasing the contact stress between the material particles. This results in a product with improved properties such as density at lower temperatures compared to processing using the CPS route.

3.1.5.1 Wasteform preparation and HIPing procedure

The general process for wasteform preparation at The University of Sheffield is as follows:

1. Reagent material is batched, milled and placed into a 600 °C drying oven overnight.
2. Material is then placed into a 316 stainless steel can and pressed using a hydraulic press to ensure the maximum quantity of material is in the can and densification can occur.
3. Can is welded closed and attached to a vacuum pump to remove volatiles.
4. A 'bakeout' at 600 °C while attached to the vacuum to drive away any other volatiles until a vacuum of <50 mTorr is reached.
5. The evacuation tube is then crimped twice with the remainder of the top of the evacuation tube removed and the canister is ready to be HIPed.

6. The canister is placed into the HIP where the maximum temperature, ramp rate and maximum pressure can be controlled.
7. Once the HIP cycle is complete, the canister is removed from the HIP vessel.
8. The stainless steel canister is cut open using an Abrasimet™ 250 saw to reveal the HIPed wasteform inside. This process in described in more detail in [125].

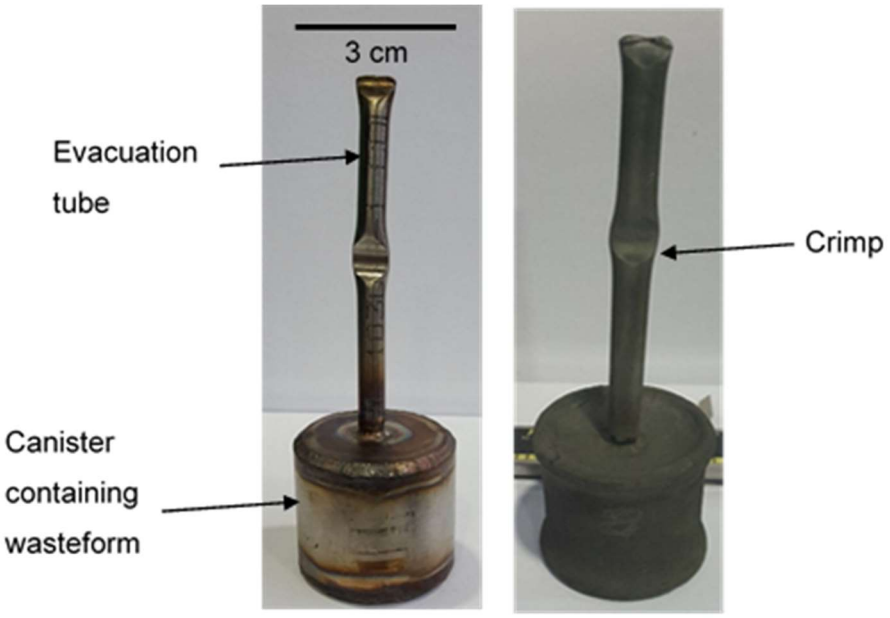

Figure 3-3 – Typical stainless steel HIP cannisters produced at TUoS before HIPing (*left)* and after HIPing (*right*).

3.1.5.2 Advantages of HIPing for nuclear waste applications

HIPing of nuclear wasteforms offers multiple advantages such as accountability throughout the processing of the material. This means that inventories can remain accurately known, and criticality concerns can also be managed, which is especially important for Pu containing materials. Since the canister are hermetically sealed, there are no off gassing requirements throughout this process, therefore the release of volatiles is not a limiting concern [126]. HIPing also has the potential for a wide operating window since it is independent of wasteform properties and canisters at a variety of scales can be processed. Since the HIP operating plant does not come into contact

with the waste stream throughout the process, multiple waste streams can be processed at the same plant. HIPing also has the potential advantage of volume reduction of wastes, allowing for a waste storage facility with a smaller footprint and therefore reducing associated costs [127].

Figure 3-4 – AIP 630H HIPing system used at The University of Sheffield.

Experimental Parameters

Chapter 5: The wasteforms in this chapter were HIPed using the University of Sheffield AIP 630H system (Figure 3-4). A glass frit was used with the addition of CeO_2 and Fe metal when packing into the 316 stainless steel can. The molybdenum furnace with an operating temperature of 1250 °C was utilised, with a ramp rate of 10 °C min^{-1} at 20 MPa with a 4 h dwell. 30 mL 316 stainless steel canisters were produced in house for these samples (Figure 3-3).

Chapter 6: The same HIPing system was used for these wasteforms as in Chapter 5 with the following HIPing conditions: 1320 °C at 100 MPa for 4 h.

Chapter 7: HIPed externally with the following conditions: 1350 °C at 185 MPa for 6 h.

3.2 Characterisation techniques

3.2.1 X-ray diffraction (XRD)

XRD can be used as a fingerprinting technique to determine the crystalline phases and whether any amorphisation is present within a material. An X-ray tube generates an X-ray beam by accelerating electrons across a potential (typically 30-50 keV). The electrons impinge on a metal anode, ionising the metal and creating an electron – hole pair. Relaxation of an electron at a higher energy level into the hole generates an X-ray with an energy that is characteristic of the metal anode. The X-ray beam also comprises a broad range bremsstrahlung wavelength generated when electrons are scattered by atoms in the anode.

The X-rays which target the material must be monochromatic therefore the beam must be filtered. For example, electrons hitting a Cu anode will cause 2 transitions: 2p → 1s (Kα) and 3p→1s (Kβ). A Ni filter is used to remove the Cu Kβ contribution. There are also two 2p spin states for the transitions contributing to the Kα emission, $K\alpha_1$ (λ = 1.54051 Å) and $K\alpha_2$ (λ = 1.54433 Å), which produce a weighted average wavelength of 1.5418 Å, and can be separated using a monochromator.

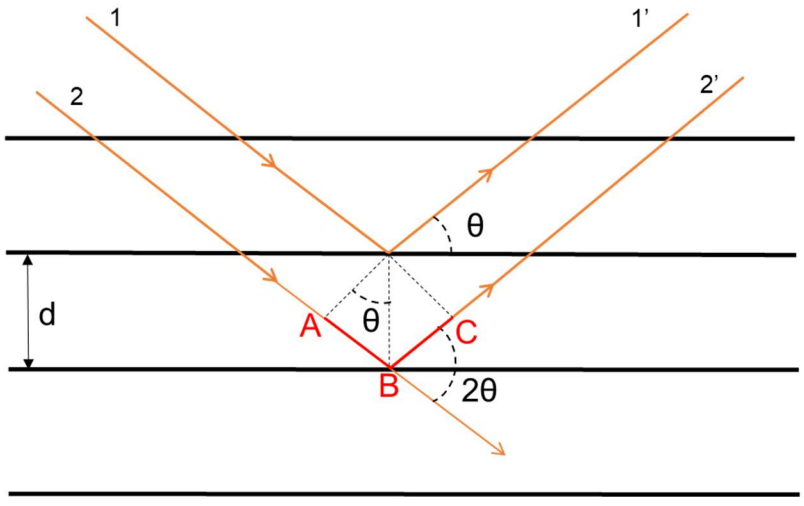

Figure 3-5 – Diagram of Bragg's law showing X-rays interacting with lattice planes.

For an X-ray to be detected with the arrangement discussed above, Bragg's law must be obeyed whereby diffraction can only occur with the constructive interference of X-rays. This happens when there is interaction between bound electrons in the material, as opposed to destructive interference caused by free electron interactions. With reference to Figure 3-5, for constructive interference to occur, the path difference between X-ray wavelets 1 and 2 must be equal to n number of wavelength [128].

$$ABC = n\lambda \tag{3.1}$$

$$AB = BC = dsin\theta \tag{3.2}$$

Combining Eq. 3.1 and 3.2 gives the equation for Bragg's law:

$$n\lambda = 2dsin\vartheta \tag{3.3}$$

Where n is the integer number of wavelengths, λ is the wavelength of X-ray (m), d is the interplanar spacing (m) and θ is the angle of incidence of the X-ray.

In summary, Bragg's law states that the angle which X-rays are diffracted is determined by the distance between the lattice planes, providing that the wavelength of X-rays used is fixed. Powdered materials are often analysed and crystallites must be randomly oriented to ensure that each lattice plane is represented equally at all orientations. Data is presented as X-ray intensity vs. the difference in angle between incident and diffracted rays (2θ). The position of peaks in the pattern allows the symmetry and size of the unit cell to be ascertained, as well as the atomic positions from which the structure of the material can be inferred [120], [129].

Diffuse scattering occurs when performing X-ray diffraction experiments on amorphous materials due to the lack of long range order present in the atomic

arrangement of these materials [128]. An example of this can be seen in Figure 3-6.

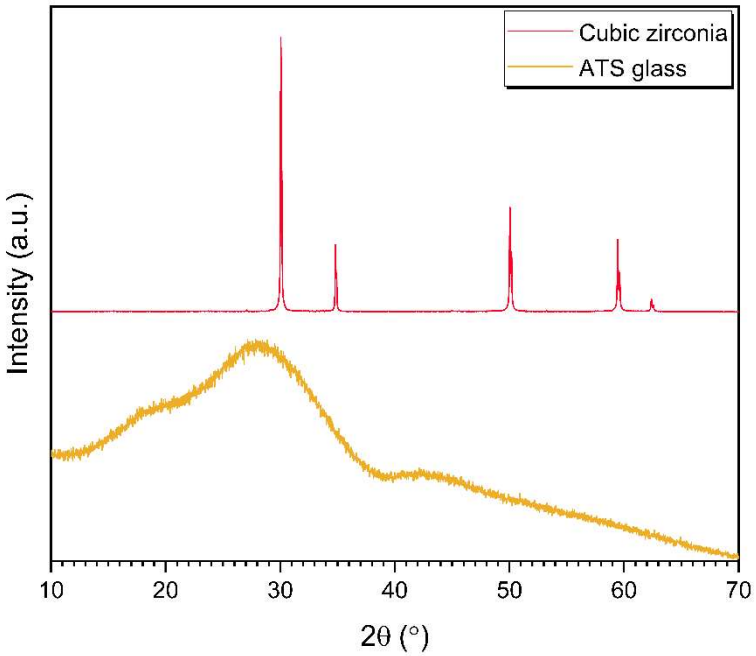

Figure 3-6 – XRD patterns of crystalline ceramics (*top*) and glass materials (*bottom*).

3.2.1.1 Rietveld refinement

Rietveld refinement is a computational method of fitting the XRD pattern to theoretical models of crystal structure [130]. This is an iterative process whereby input parameters can be modified to best fit the XRD data from a given material e.g. atomic coordinates and site occupancy. This data can be utilised to estimate the quantity of each phase present in the material and the unit cell parameters of each phase [131].

Experimental Parameters

A Bruker D2 Phaser diffractometer with LynxEye detector was used to analyse every wasteform synthesised in this project. It operates with Ni filtered Cu Kα radiation (λ = 1.5418 Å), a 10 mA current and 30 kV voltage. The ICDD PDF-4 library was used for phase analysis. The Bruker TOPAS software was used for Rietveld refinement in all chapters [131].

Chapters 4 and 5: Data was collected 10° < 2θ <70° with a step size of 0.02° 2θ and count time of 9.45 s per step. For Fe containing glasses, the detector was windowed to reject the Fe fluorescence due to the use of Cu radiation.
Chapters 6, 7 and 8: Data was collected 10° < 2θ <70° with a step size of 0.02° 2θ and count time of 1.18 s per step. For Fe containing ceramics, the detector was windowed to reject Fe fluorescence due to the use of Cu radiation

3.2.2 Scanning electron microscopy (SEM) and energy dispersive X-ray spectroscopy (EDX)

Scanning electron microscopy is an imaging technique used to analyse the surface of a material with a large range of magnifications, from micron to nanoscale, allowing the microstructure to be observed. This technique utilises an electron beam which is generated when primary electrons are accelerated to approximately 30 keV using an electron gun, and focused using electromagnetic lenses into a small beam on the surface of the material [120]. Elastic and inelastic scattering between the primary electrons and the material under observation lead to several types of emissions from the surface of the material, secondary electron, back scattered electrons, and X-rays, illustrated in Figure 3-7.

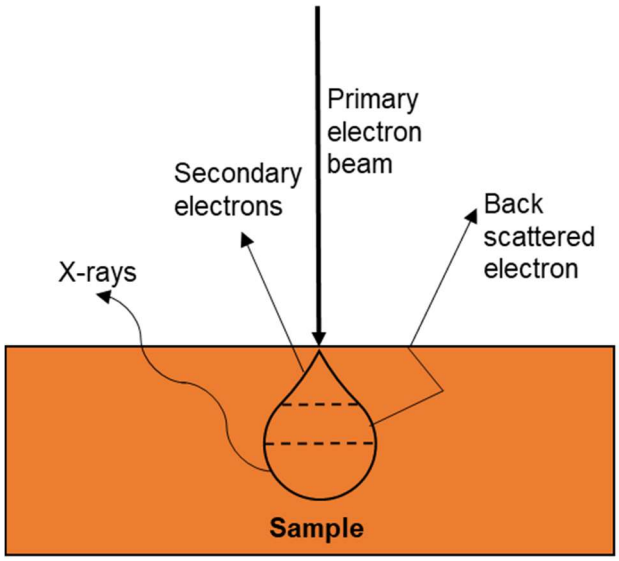

Figure 3-7 – Emissions from a sample using SEM with illustrative depths

3.2.2.1 Back scattered electrons (BSE)

Primary electrons are elastically scattered by the electrons in the material (depth < 1 μm) and consequently have high energy (maximum of 90% of the incident beam), compared to secondary electrons. The electrons are backscattered with intensity proportional to the Z of the scattering nuclei, since high Z nuclei are likely to scatter more electrons. As a consequence of this, images produced show contrast variation dependent upon the Z of the phase being imaged, with heavy elements, such as Ce and Pu, appearing brighter in the micrograph.

3.2.2.2 Secondary electrons

These electrons are emitted upon an inelastic collision between a primary electron and an electron in the conduction or valence band of the material. Only the electrons emitted close to the surface of the material (<10 nm) are detected due to their low energy (< 50 eV) and therefore can only provide information about the surface of the material e.g. topography. High resolution images can be produced due to their abundance and small sampling volume/scattering angle [132].

3.2.2.3 X-ray analysis (EDX)

The X-rays emitted can be used to provide compositional analysis of the material, when used in combination with BSE analysis. Electrons in the atoms of a material can be displaced by an incoming primary electron. When the energy of that electron is greater than the ionisation energy of the atom, a vacancy is created, which is then filled by a transitioning higher energy electron [133]. The transition of the electron to fill the vacancy causes the emission of an X-ray of discrete energy corresponding to the difference in energy levels between the electron and vacancy. This energy is characteristic of the element of the atom and can therefore be used to identify the elemental composition of the material. The intensity of the X-ray emission is proportional to the concentration of the element in the material and provides a semi-quantitative or quantitative compositional analysis.

Experimental Parameters

Chapters 4 - 7: Samples were prepared by first mounting in epoxy resin, cured overnight and then polished using P400, P800 and P1200 SiC grit papers followed by 6 µm, 3 µm and 1 µm polishing pads with corresponding diamond suspension. The samples were then carbon coated using the Agar Scientific Carbon Coater with sides coated with silver conductive paint to reduce charging on the surface of the sample. The SEM/EDX used at the MIDAS facility is the Hitachi TM3030 with Oxford Instruments Swift ED3000 Silicon drift detector. EDX mapping was processed using the Bruker Quantax 70 software with maps collected for a minimum of 10 min.

Chapter 8: Powder samples were mixed with isopropanol and sonicated. The mixture was pipetted onto a carbon tab and isopropanol left to evaporate leaving the powder evenly distributed on the carbon tab. The Philips XL30 FEG SEM was used to take images of the powders.

3.2.3 X-ray absorption spectroscopy (XAS)

XAS can be used to probe the oxidation state, coordination number and local atomic environment of a chosen element within the structure of a material. The photo electric effect is utilised, whereby a core electron absorbs the energy from an X-ray, is ejected, leaving behind a hole. The X-ray energy must be greater than the binding energy of the electron in this atom in order for the electron to be ejected and an absorption spectrum generated e.g. 5723 eV is the energy required to liberate the 2p electron in a Ce atom. There are two potential outcomes upon the generation of the photoelectron in this way: the hole is filled by an electron from a higher energy state transitioning and emitting a fluorescence X-ray which is characteristic of the material; or an Auger electron is emitted through an electron falling to a lower energy state to fill the hole.

The absorption coefficient, μ, of the X-rays by the material at a given energy, E, can be quantified by Equation 3.4, where t is the thickness, I_0 is the incident beam, and I_t is the transmitted beam [134]. The intensity of fluorescence X-

rays or measurement the Auger electrons emitted can also be used to investigate the absorption.

$$\mu(E)\, t = \ln\left(\frac{I_0}{I_t}\right) \tag{3.4}$$

The energy of the X-rays is increased and the absorption is measured to create a spectrum similar to that in Figure 3-8.

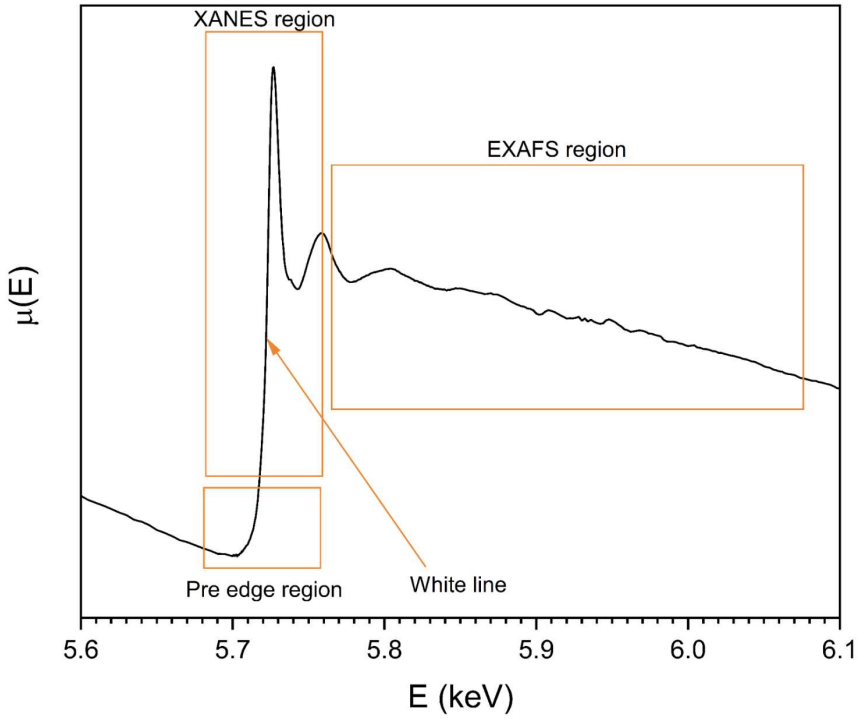

Figure 3-8 – A transmission XAS spectrum of $CePO_4$ at the Ce L_3-edge (5.723 keV) measured at ESRF BM26A.

An XAS spectrum can be split into two distinct regions (see Figure 3-8): X-ray Absorption Near Edge Structure (XANES) which is within 50 eV of the absorption edge and Extended X-ray Absorption Fine Structure (EXAFS) where high energy photoelectrons contribute to the spectrum (50 – 1000 eV from the edge). XANES is used to determine the oxidation state of the material and the EXAFS region can be fitted to generate a model of the local chemical structure around the element analysed [135]. The pre edge feature is related to electron transitions commonly seen in the transition metals e.g. Fe.

Linear combination fitting (LCF) is a technique that can be implemented to analyse XANES region data, where an estimate the average oxidation state of the selected element within a material is determined. XANES measurements of standards of a known oxidation state are measured and compared to the spectra of the sample spectra using the Athena software [136] to calculate the contribution of each standard to the spectra and give an average oxidation state. This is done by assigning weighting parameters to each standard spectrum, to total 100%, with the contribution of each standard spectra then varied to minimise the R-factor of the fit.

The EXAFS region can provide information about the local coordination environment by modelling the background subtracted spectrum using the EXAFS equation. This region of the spectrum is generated due to the scattering of the photoelectron with electrons of neighbouring atoms. The equation is given by Equation 3.5, where: N_j is the coordination number of atoms j at distance R_j, S_0 is the amplitude reduction factor, $e^{-2k^2\sigma^2 j}$ is the Debye-Waller factor and, e^{-2R_j/λ_j} is the mean free path.

$$\chi(k) = \sum_j \frac{S_0^2 N_j f_j(k)}{kR^2} e^{-2k^2\sigma^2 j} e^{-2R_j/\lambda_j} sin\left[2kR_j + 2\phi_j(k) + \delta_j(k)\right] \quad (3.5)$$

An EXAFS fit was performed using the Artemis software package, where a model of the neighbouring atoms of an element in a structure is generated based on fitted EXAFS spectra of a standard material with known structure. An example of this process implemented in this thesis can be found in Chapter 4.

Experimental Parameters

Samples were prepared by mixing the quantity of material required for 1 absorption length (calculated using the Hephaestus software [136]) with a minimal quantity of polyethylene glycol. The resulting powder was then uniaxially pressed into a 10 - 13 mm pellet to create a homogeneous pellet

without pin holes. Athena software was used to process the spectra and Artemis was used for EXAFS fitting, both of which are part of the Demeter software package.

Chapter 4: Ce L_3-edge XANES – BM28 at ESRF by myself, Fe K-edge XANES/EXAFS – BM26A at ESRF by myself
Chapter 5: Ce L_3-edge XANES at BM28 ESRF by myself, Dr. Jack Clarke and Dr. Martin Stennett.
Chapter 7: All data acquired at BM28 ESRF by myself, Dr. Martin Stennett and Prof. Neil Hyatt.
All other XAS data collected by Dr. Martin Stennett, Dr. Bruce Ravel, Dr. Dan Bailey and Ms. Lucy Mottram.

3.2.4 X-ray fluorescence (XRF)

X-ray fluorescence can be used to analyse the bulk composition of a material. An X-ray is absorbed by an atom in the material, emitting an electron and creating a hole. The hole is then filled by an electron from a higher shell replacing into the hole and a fluorescence X-ray is emitted. The energy is discrete since it corresponds to distinct transition from shell and is therefore characteristic of the elements present in the material. The signal received is proportional to the concentration of the element therefore gives a measurement of the elemental composition of the material.

Experimental Parameters

Chapters 4 and 5: Powder samples of four wasteform compositions used in dissolution testing were sent to AMG Analytical Services for XRF analysis.
Chapters 6 and 7: Powder samples of eight wasteform compositions used in dissolution testing were sent to AMG Analytical services for XRF analysis.

3.2.5 Mössbauer spectroscopy

In Mössbauer spectroscopy, gamma rays emitted by the radioactive decay of certain source materials (such as Fe-57 and Sn-119) can be used to probe the oxidation state and coordination environment of elements similar to that of the

radioactive source. The radiation generated is highly monochromatic since they are characteristic of the decay mechanism of the isotope. The Doppler effect is used to precisely tune this monochromatic energy by moving the source away from the material at constant velocity, thereby changing the incident energy [120].

The radiation emitted from the source is absorbed by the atom in the material. The gamma ray is then reemitted with a lower energy and analysed to understand the nuclear interactions which have occurred.

If the source and material have atoms in the same chemical environment, a resonant spectrum will be produced. For those atoms with different environment, nuclear interactions can occur with the following effects: isomer shift, quadrupolar splitting and hyperfine splitting [137].

1. Chemical/isomer shift – Caused by the difference in the s shell electron density between the standard, usually α-Fe, and the material. Can be used to measure the proportion of Fe^{2+} and Fe^{3+} in the material since Fe^{3+} has less shielding from d shell electrons so has a lower isomeric shift.
2. Quadrupolar splitting – In atoms with angular momentum > ½ (i.e. quadrupolar), the charge distribution is uneven. This changes the nuclear energy levels in the material creating a splitting of the nuclear energy levels to produce a doublet and can give information about the local environment of the atom.
3. Hyperfine splitting – When in the presence of a magnetic field from the nucleus, the change in doublet experienced due to quadrupolar splitting will then become a sextet.

Experimental Parameters

Chapters 4 & 5: Powdered samples were measured at room temperature using a Wissel MRG-500 spectrometer with a $^{57}Co/Rh$ source and a velocity range ± 10 mm s^{-1}. Samples were calibrated relative to an α-Fe reference standard. The Recoil software package was used to deconvolute the data by

assigning Lorentzian doublets to represent Fe oxidation states and co-ordination numbers using the Recoil analysis software [138].

3.2.6 Inductively coupled plasma spectrometry

Inductively coupled plasma (ICP) spectrometry can be used to determine the concentration of elements in a liquid. A nebuliser creates an aerosol from the solution which then passes over an Ar plasma torch. The plasma torch heats a spiral of Ar gas using an RF field to a maximum of 10000 °C. The aerosol passes through this hot plasma to produce ions due to collisions with the Ar^+ and e^- in the plasma.

For ICP-Optical Emission Spectroscopy (ICP-OES), ionisation causes the release of radiation which is characteristic of the elements in the solution and released with intensity proportional to the concentration of the element present. The photons released are separated using a diffraction grating. Photomultipliers are used to detect the photons.

The ions produced by the plasma torch can also be sent to a mass spectrometry system as in ICP-Mass Spectrometry (ICP-MS). This system works by using a quadrupole to separate the singly charged ions by mass and only allowing ions of a single mass to pass through to the detector at any one time. The ICP-MS counts are directly proportional to the concentration of the element in solution and can be compared to concentration in a known standard to analyse the concentration of the element in a liquid. This technique is more sensitive compared to ICP-OES has a sensitivity in the ppt (ng L^{-1}) range.

Experimental Parameters

Chapters 4 and 5: iCAP 6300 ICP-OES operated under the supervision of Dr. Claire Corkhill and Dr. Colleen Mann and using Fluka elemental standards. AMG Analytical Services analysed 4 samples for Li and B concentration using ICP-MS.

Chapters 6 and 7: iCAP RQ ICP-MS was operated under the supervision of Dr. Colleen Mann and using Fluka elemental standards.

3.2.7 Gas pycnometry

The density of solid materials can be measured using gas displacement in gas pycnometry. An inert gas such as helium is used due to its small particle size allowing it to completely penetrate the accessible internal porosity of particles. The pycnometer consists of two chambers of known volume, one a reference chamber and the other containing the sample. The gas fills the sample chamber to a predefined pressure. This same volume of gas then fills the reference chamber, with the difference in pressure allowing the software to calculate the sample volume. The volume of gas displaced by the sample is used to calculate the density for a sample of known mass [121].

Experimental Parameters

Chapters 4 - 7: A Micromeritics Accupyc 1340 II pycnometer was used to measure the density of samples and sample mass was measured to an accuracy of ±0.0001 g prior to measurement. Samples were placed in a 1 cm^3 chamber with a fill pressure of 19.5 psig for 25 purges and 25 cycles each.

3.3 Use of surrogates

Surrogate materials for active isotopes are important in the preliminary studies of a potential wasteform, when optimising the synthesis parameters. The criteria that must be taken into consideration when selecting a candidate are electron configuration, ionic radius and oxidation state. These must be compared to the active counterpart to assess their suitability.

Several candidate surrogate elements have been proposed when investigating the immobilisation of Pu, the most ubiquitous of which is Ce. This is because Ce^{4+} and Pu^{4+} have similar ionic radii (0.087 nm and 0.086 nm respectively) [139]. Also, Ce exhibits trivalent and tetravalent oxidation state, similarly to Pu. For example in borosilicate glass, the Ce oxidation state shows a high dependence on the melting temperature of silicate glasses [140] where Ce^{3+} is more soluble than Ce^{4+} at increased temperature. The same is true for Pu, where Pu^{3+} is more soluble than Pu^{4+} in borosilicate glass. The same result is shown in the presence of a reducing agent within the glass melt [54].

However, it should be noted that the redox potential of Ce^{4+} is significantly smaller than Pu^{4+}, therefore Pu^{4+} is more stable in reducing conditions.

Lopez *et al.* [140] also compared Ce to Nd and Hf in borosilicate glass melts. Nd exists in a trivalent state only and Hf exists in a tetravalent state only. For the same processing temperature (1300 °C), Nd showed a similar solubility to Pu^{3+} compared to Hf, which showed similar solubility to Pu^{4+}. This confirms the results observed on the temperature dependence of the solubility of Ce.

An extensive study of other potential waste surrogates was completed by Bingham *et al.* [141] and highlights the importance of exercising caution when using surrogate materials, since there are no perfect replacements for the active counterparts. In the case of Ce and Pu, they have different redox potentials and Ce is more easily reduced to its Ce^{3+} state, compared to Pu, which should be considered in the interpretation of results from surrogate experiments.

Experimental Parameters

Chapters 4 - 7: CeO_2 used as a PuO_2 surrogate in all samples.
Chapter 8: CeO_2 used as a MA surrogate for the entrained actinides in pyrochemical reprocessing wastes, as well as PuO_2.

3.4 Wasteform durability

A measure of the suitability of a wasteform for immobilisation of a waste stream can be ascertained by assessing the aqueous durability of the material relative to other wasteform materials. Since the material is required to immobilise the waste for over 100,000 years [7], several techniques are used to accelerate the test including increased the temperature of the test and using acidic solutions for dissolution.

There are two types of dissolution tests which have been developed with the most commonly used being the Product Consistency Test B (PCT-B) [101] and the Materials Characterisation Centre 1 (MCC-1) [102] methods, which have

ASTM standards describing each methodology. These standardised methods allow for comparison between tests on different wasteforms.

3.4.1 PCT-B

The Product Consistency Test B is a test of the durability of powdered wasteforms and allows for a variety of temperatures, particle size, durations and leachants. The test must be performed in either PTFE or stainless steel vessels. The ASTM also describes Test A which has very specific experimental parameters, constraining the temperature to 90 °C and with stainless steel vessels. Both tests are performed in static conditions.
Sample surface area can be calculated using pycnometry measurements [142] For both glass and ceramic materials, an approximation can be made that the particles are spherical, leading to pycnometry being the most accurate approximation of surface area in this instance [101].

The elemental concentration of the leachate is analysed using ICP-OES or ICP-MS. Normalised elemental mass loss (NL_i in g m^{-2}) and normalised elemental mass loss rate (NR_i in g m^{-2} d^{-1}) are calculated using the equations:

$$NL_i = \frac{(c_i - c_{i,b})}{f_i \quad {SA}/{V}} \tag{3.6}$$

$$NR_i = \frac{NL_i}{t} \tag{3.7}$$

Where: c_i (g L^{-1}) is the average element *i* concentration of the triplicate sample, $c_{i,b}$ (g L^{-1}) is the average element *i* concentration of the duplicate blank, f_i is the fraction of element *i* in the sample, SA/V (m^{-1}) is the surface area to volume ratio of the sample in the test, t (d) is the duration of the experiment.

3.4.2 MCC-1

Monolith durability testing is described by the MCC-1 ASTM standard and is used to provide more detail about the initial rates of dissolution by reducing

the SA/V compared to powder dissolution tests. Monoliths are sectioned to 10 mm x 10 mm x 5 mm, polished and cleaned by sonicating three times in isopropanol and dried at 90 ± 2 °C overnight. Each monolith is placed on a PTFE basket in a 60 mL PTFE vessel with 40 mL of UHQ water to give a SA/V of 10 m^{-1}. The vessels are prepared in triplicate with duplicate blanks, sealed and placed in an oven at 90 ± 2 °C until sacrificial sampling at selected time point. At each sampling time point, an aliquot of leachate is removed from each vessel, the pH measured, acidified with 20 µL of ultrapure HNO_3 and the solution analysed for elemental composition. The monoliths are dried, mounted in epoxy resin and analysed using SEM/EDX to provide information about any surface alteration effects. The mass of each element released is used to calculate the normalised elemental loss using Equations 3.8 and 3.9 respectively, where: m_{ij} is mass of element *i* released from sample *j* (g), C_{ij} is the concentration of element *i* measured in leachate from sample *j* (g L^{-1}), V_{fj} is the final volume of leachate in test vessel containing sample *j* (L), B_{ik} is the concentration of element *i* measured in blank test *k* (g L^{-1}), V_{Bk} is the final volume of solution in test vessel containing sample *j* (L), a is the total number of blank solutions, NL_{ij} is normalised mass loss of element *i* from sample *j* (g m^{-2}), f_i is the mass fraction of element *i* in sample *j* and, S_j is the surface area of sample *j* (m^2).

$$m_{ij} = \left(c_{ij} \times V_{ij}\right) - \sum_{k=1}^{a} V_{Bk} \times \frac{B_{ik}}{a} \tag{3.8}$$

$$NL_{ij} = \frac{m_{ij}}{f_i \times S_j} \tag{3.9}$$

The normalised dissolution rate (NR_i) in g m^{-2} d^{-1} is calculated using Equation 3.7, where *t* is the dissolution time in d. The SA/V should be adjusted at each time point to account for the evaporative losses. The surface area is calculated geometrically.

3.4.3 Geochemical modelling

The elemental concentrations measured using ICP-MS and ICP-OES can be used with the PHREEQC geochemical modelling software [143] to model the potential mineral phases which may precipitate out of the solution. Thermodynamic and kinetic data can be used to simulate chemical reactions in systems which are either in or out of equilibrium [144]. The SI (saturation index) of a phase was calculated in this software using Equation 3.10, where: IAP is the ion activity product for the phase and K_s^0 is the standard solubility constant of the phase.

$$SI = \log\left(\frac{IAP}{K_s^0}\right) \tag{3.10}$$

The IAP is calculated using the parameters of the experiment (e.g. temperature and solution pH) and K_s^0 of a mineral phase is provided by inputting an appropriate thermodynamic database into the software (whereby the Lawrence Livermore National Laboratory thermodynamic database was used throughout this thesis).

Experimental Parameters

Chapter 4: There were three durability tests performed on the selected wasteforms produced for this chapter:

1. PCT-B: 18 MΩ cm^{-1} UHQ water at 90 ± 2 °C with SA/V of 1200 m^{-1} in 15 mL PTFE vessels. Samples were in triplicate with duplicate blanks for 1, 3, 7, 14, 21 and 28 d sampling points. 10 mL of solution was removed from each pot, filtered with 0.22 µm cellulose acetate filters, placed into a centrifuge tube and acidified with 20 µL ultra-pure HNO_3. ICP-OES analysis was performed on each centrifuge tube.
2. PCT-B: As above with a SA/V = 10,000 m^{-1}.
3. MCC-1: 18 MΩ cm^{-1} UHQ water at 90 ± 2 °C with SA/V of 10 m^{-1} in 60 mL PTFE vessels with basket. Cuboidal monoliths were polished with P1200 SiC grit on each face, with their dimensions measured using calipers (± 0.005 mm). Samples were in triplicate with duplicate blanks

for 1, 3, 7, 14, 21, 28, 42, 56, 70 and 84 d sampling points. 10 mL of solution was removed from each pot, filtered with 0.22 µm cellulose acetate filters, placed into a centrifuge tube and acidified with 20 µL of ultra-pure HNO_3 solution. ICP-OES analysis was performed on each centrifuge tube.

Chapter 5: A PCT-B test identical to Chapter 4 Test 1 was used.

Chapter 6 and 7: A modified PCT-B type test was used using 0.01M HNO_3 as a leachant at 90 ± 2 °C. 60 mL PFA Teflon vessels were used with 40 mL of 0.01 M HNO_3 solution (pH = 2), to give a surface area to volume ratio (SA/V) equal to 100 m^{-1}. Triplicate sample and blank vessels were prepared. At each sampling time point (1, 2, 3, 4, 7 and 10 d), an aliquot of leachate (0.4 mL) was removed from each vessel, diluted using 10 mL of ultra high quality (UHQ, 18 MΩ cm^{-1}) water and passed through a PTFE syringe filter. Each vessel was then sealed and returned to the oven. Upon completion of the experiment, each solution was analysed for elemental concentration using an ICP-MS (Thermofisher iCAP RQ).

4 Alkali tin silicate glass as a wasteform for the immobilisation of the UK PuO_2 stockpile

Amber R. Mason, Martin C. Stennett, Claire L. Corkhill, Laura J. Gardner and Neil C. Hyatt*

Immobilisation Science Laboratory, Department of Materials Science and Engineering, University of Sheffield, Sir Robert Hadfield Building, Sheffield S1 3JD, UK

*To whom correspondence should be addressed. Email n.c.hyatt@sheffield.ac.uk, phone +44 (0) 114 222 5470.

Abstract

A suite of alkali tin silicate (ATS) glasses were produced for the immobilisation of the UK PuO_2 stockpile, with Ce used as a surrogate for Pu. Overall, ATS glasses were successfully fabricated at all waste loadings with a maximum waste loading of 5.6 mol.% CeO_2 achieved at 1100 °C, using metallic Fe^0 as a reducing agent for Ce by exploiting the increased solubility of trivalent actinides and lanthanides in borosilicate glasses. The oxidation state and local coordination environment of Ce and Fe were investigated with a combination of XANES, EXAFS and Mössbauer spectroscopy. The total reduction of Ce^{4+} to Ce^{3+} was achieved with the addition of Fe^0, where Fe was shown to be majority 3+ oxidation state and with an average 5-fold coordination, suggesting the role of Fe as a both network former and modifier in the glass. The normalised mass loss of B and Si were in agreement with durability values reported for other ATS glass formulations, revealing that the addition of Fe^0 improved the short term chemical durability. Despite this, the addition of Fe^0 is known to promote the formation of secondary Fe-rich clay phases, which are detrimental to the long term durability of borosilicate glasses.

Key words: ATS glass, cerium, plutonium stockpile, immobilisation, glass dissolution, wasteform durability

4.1 Introduction

On completion of civil nuclear fuel reprocessing in the UK in 2020, a total of 140 tHM of separated PuO_2 will be stored as a zero value asset at the Sellafield site [11]. The current UK government policy for this material is to fabricate mixed oxide ($(U,Pu)O_2$) (MOX) fuel, however, this option presents challenges due to the lack MOX fuel uptake for use in current and future light water reactors [145]. A small proportion of the stockpile (approximately 5 mT) is heavily contaminated (e.g. Am-241 ingrowth or chloride arising from radiation damage to PVC storage containment [14]) and is unsuitable for recycle as MOX fuel so must be immobilised for disposal. In the event that recycling the plutonium stockpile *via* MOX fuel cannot be delivered, immobilisation and disposal is the only alternative and credible disposition route. There is also increasing pressure for the UK government to ensure the proliferation resistance for this material and, therefore, progress towards a management end point, which should be based on evidenced maturity and value for money of both reuse and immobilisation technologies [14].

Borosilicate glass is currently used in the UK for high level waste (HLW) immobilisation, specifically using the MW composition defined in Table 4-1. Vitrification technology was selected for the immobilisation of UK HLW based on the technical maturity of the process, tolerance of the glass composition to changes in waste feed chemistry, chemical durability and the resistance to self-radiation damage of the vitrified products, which are key considerations for disposability [21], [40]. The concentration of actinides in HLW borosilicate glasses, such as those produced at Sellafield, is at trace level, since U and Pu are effectively removed from HLW raffinate by the PUREX process, leaving only the minor actinides behind (Np, Am, Cm) [146]. For the purpose of PuO_2 immobilisation by vitrification, several glass compositions have been considered, including silicate based (aluminosilicate, lanthanum borosilicate (LaBS), lanthanum aluminosilicate (LaAS) and calcium borosilicate [54], [147], [148]) and phosphate based glasses (including sodium aluminium phosphate, iron phosphate and lead iron phosphate) [45], [149]. The use of each glass type presents a compromise in the processing temperature, durability,

radiation tolerance and/or aqueous durability, which have been compared in more detail in previous research [68], [150], [151].

Table 4-1 – Comparison of UK HLW glass composition, MW, and reported ATS compositions with experimental ATS compositions used in this work. N.B. 5.6CeFe refers to the addition of Fe^0 in an equimolar quantity to the CeO_2.

Oxide	MW [13]	ATS [15] Bates *et al.*		ATS [16] Harrison *et al.*		ATS 2.9Ce		ATS 5.6Ce		ATS 5.6CeFe	
	wt.%	wt.%	mol.%	wt.%	mol.%	wt.%	mol.%	wt.%	mol.%	wt.%	mol.%
SiO_2	60.27	43.31	51.25	40.78	49.32	45.20	50.48	42.11	49.15	40.39	48.17
B_2O_3	24.11	12.59	12.86	11.74	12.25	12.98	12.51	12.10	12.18	11.60	11.94
Na_2O	10.88	9.57	10.97	9.13	10.70	10.31	11.17	9.61	10.87	9.21	10.66
Li_2O	4.75	4.18	9.96	4.09	9.94	4.73	10.62	4.40	10.34	4.22	10.13
Al_2O_3	-	2.41	1.68	2.35	1.67	2.60	1.71	2.42	1.67	2.33	1.63
CeO_2	-	-	-	-	-	7.32	2.86	13.65	5.56	13.09	5.45
Cs_2O	-	0.71	0.18	0.52	0.13	-	-	-	-	-	-
Fe	-	-	-	-	-	-	-	-	-	4.10	1.85
Gd_2O_3	-	3.34	0.65	3.30	0.66	-	-	-	-	-	-
HfO_2	-	-	-	15.0	5.18	-	-	-	-	-	-
K_2O	-	5.40	4.08	5.13	3.96	5.87	4.18	5.47	4.07	5.24	3.99
PuO_2	-	8.51	2.19	-	-	-		-	-	-	-
SnO	-	2.34	1.10	2.61	1.26	2.89	1.44	2.69	1.25	2.58	1.37
TiO_2	-	2.11	1.88	1.91	1.74	2.12	1.78	1.98	1.73	1.89	1.50
ZrO_2	-	5.53	3.19	5.39	3.18	5.97	3.25	5.57	3.17	5.34	3.11

One potential family of glass compositions developed for PuO_2 immobilisation are the alkali tin silicate (ATS) glasses, first developed by Bates *et al.* [66] for the immobilisation of US defence Pu. The composition includes an increased quantity of alkali elements (Li, Na, K), which bind to trivalent or tetravalent elements such as Pu, with the effect of increasing waste incorporation into the glass network [67]. These elements reduce the viscosity of the glass, which may be advantageous for processing, but also reduce the chemical durability, which is undesirable for PuO_2 immobilisation. To counter for these deleterious effects, Sn (in addition to other tetravalent elements, e.g. Zr and Ti) is included in the batch composition to improve durability and balance the effect of an increased alkali loading on glass performance. Bates *et al*. observed that PuO_2

was not fully incorporated in their ATS glass melt, with the Pu content of the glass phase estimated to be 7.2 ± 0.3 wt.% Pu [66], which is equivalent to 8.5 wt.% or 2.2 mol.% PuO_2 within the glass phase (the undissolved fraction was present as crystalline PuO_2). PCT-B [152] dissolution testing performed on a 1.39 mol.% PuO_2 waste loaded ATS glass by Chamberlain *et al.* [67], demonstrated the relatively low normalised mass loss of this composition (NL_B = 0.48 g m^{-2} and NL_{Si} = 0.26 g m^{-2} after 28 d), with the same order of magnitude observed for MW UK HLW glass modified to target Pu immobilisation (NL_B = 0.65 g m^{-2} and NL_{Si} = 0.30 g m^{-2} after 28 d [153]).

Following the seminal work of Bates *et al.* in 1996, further investigations in the UK made a preliminary assessment of the potential of ATS glass, alongside other glass compositions, for the immobilisation of the UK PuO_2 stockpile [68]–[70], [153]. The aim of the preliminary study by Harrison *et al.* was to provide an assessment for the optimum vitreous wasteforms for PuO_2 immobilisation which could then be compared to other ceramic and glass-ceramic options. Hf was used as a surrogate for Pu in this work, with the motivation that Pu is a stable tetravalent element in borosilicate glass, and hence Hf would best represent Pu redox behaviour, despite Hf having a smaller ionic radius [141]. A Hf solubility of 5.18 mol.% was achieved in ATS glass at a melt temperature of 1300 °C, whilst durability testing (PCT-B) revealed relatively low normalised mass loss (NL_B = 0.43 g m^{-2} and NL_{Si} = 0.25 g m^{-2} at 28 d) [153] in agreement with previous literature for ATS glasses [67].

The solubility of lanthanide and actinide elements in borosilicate glasses is known to be higher for the 3+ oxidation state compared to the 4+ oxidation state (primarily relevant to Ce/Pu) [147]. This is due to the competition of the element with network formers, such as Si, in bonding with oxygen in the glass network. At lower oxidation state, in an environment with lower oxygen activity, lanthanide and actinide cations can more readily bond with oxygen anions and incorporate into the glass network [7]. This effect can be attributed to the Dietzel field strength, F, of a cation, M, at a particular valence, Z, which is dependent on the ratio Z/d^2, where d is the cation oxygen bond distance (Å)

[154]. Network formers such as Si and B typically have higher field strength (F > 1.3) due to their high valence, but the opposite is true for network modifiers, such as Na where F < 0.4 [63]. Elements with the 3+ oxidation state have a lower field strength and therefore act like network modifiers whereas species with the 4+ oxidation state have a higher field strength causing them to behave closer to a network former [155]. Controlling the oxidation state of Pu and surrogates such as Ce, is an important consideration in optimising the incorporation rate of these elements. Cachia *et al.* [54] successfully demonstrated a doubling of the PuO_2 waste loading from 0.45 mol.% to 0.9 mol.% in alkali borosilicate glass. This was achieved by reduction of Pu^{4+} to Pu^{3+} with either the inclusion of a reducing agent (e.g. aluminium nitride) or increasing the melt temperature to effect auto-reduction [54], with the reducing agent being most effective mechanism for the reduction of Pu^{4+} to Pu^{3+}. This steered our research to modify the processing conditions (1100 - 1300 °C) and batch composition to effectively increase the waste loading of the glass whilst controlling the speciation of the waste cation.

In this study, CeO_2 is used as inactive surrogate for PuO_2, to avoid the hazard and cost of working with PuO_2, as is common practice in wasteform design, formulation and development research. Although Ce cannot fully emulate the behaviour of Pu, the similar ionic radius and availability of Ce^{3+}/Ce^{4+} oxidation states, albeit with different redox potential, enable useful and more comprehensive investigation of the relevant wasteform phase diagram and materials properties [140], [141]. In the original work of Bates *et al.*, Cs_2O and Gd_2O_3 were included in the batch composition to act, respectively, as a proliferation deterrent (if spiked as $^{137}Cs_2O$, resulting in a high gamma field) and as a neutron poison. In the context of the current UK immobilisation strategy, a proliferation deterrent gamma field is not a requirement (as in the US spent fuel standard [156]). It is possible that a disposability assessment could require addition of Gd_2O_3 as a neutron poison, preliminary calculations for plutonium wasteforms suggest a ratio of Pu/Gd = 0.03 would suffice, which would not be expected to significantly impact the glass forming ability or

PuO_2/CeO_2 solubility. Therefore, these components were not included in the formulation design for this study.

A suite of ATS glasses were developed in this study, with the aim of investigating their potential to immobilise the UK civil PuO_2 stockpile, with the formulations shown in Table 4-1 in comparison to those of Bates *et al.* and Harrison *et al.* [66], [69]. The initial ATS glass formulations targeted CeO_2 incorporation at 2.9 mol.% (7.3 wt.%) and 5.6 mol.% (13.7 wt.%), to enable direct comparison with the chemical durability of PuO_2 in ATS glasses reported by Bates *et al.* [66]. Additionally, metallic Fe^0 was included into the 5.6 mol.% CeO_2 glass composition, equivalent to one third of the Ce concentration i.e. 1.9 mol.%, to effect complete reduction of Ce^{4+} to Ce^{3+} according to the redox reaction: $3\ CeO_2 + Fe = 1.5\ Ce_2O_3 + 0.5\ Fe_2O_3$, which was postulated to improve Ce waste loading within ATS glasses. The structural environment of Ce and Fe within the glass network was investigated using X-ray absorption spectroscopy and Mössbauer spectroscopy, to provide a greater understanding of the relative roles of these elements in the glass network as the redox environment of the glass changes. The chemical durability of these formulations was also investigated, using PCT- B and MCC-1 methodologies, to offer a preliminary understanding of the dissolution behaviour of these ATS glasses, and therefore underpin the safety case for use of these materials in a geological disposal environment.

4.2 Experimental

4.2.1 Glass processing

The following high purity (> 99.9%) materials were selected for the batching of each glass melt: $Al(OH)_3$, H_3BO_3, CeO_2, Fe filings, K_2CO_3, Li_2CO_3, Na_2CO_3, SiO_2, SnO, TiO_2, ZrO_2. The materials were batched to 60 g with compositions shown in Table 4-1, all dry precursors were mixed well before placing into an alumina crucible. The filled crucible was placed into a muffle furnace (in air), heated at 3 °C min^{-1} until the desired melt temperature (1100 °C, 1200 °C or 1300 °C) was reached and held for 2 h. The melt was poured into preheated stainless steel block moulds, after which the glass monoliths were immediately placed into a muffle furnace to anneal in air at 510 °C for 1 h, and then cooled at 1 °C min^{-1} to room temperature.

4.2.2 Materials characterisation

4.2.2.1 X-ray Diffraction (XRD)

A small representative aliquot of each glass type was crushed into a fine powder and analysed using powder XRD. A Bruker D2 Phaser diffractometer with LynxEye detector was used with Ni filtered Cu Kα radiation (λ = 1.5418 Å), a 10 mA current and 30 kV voltage. Data was collected between 10° < 2θ < 70° with a step size of 0.02° 2θ and count time of 9.45 s $step^{-1}$. For Fe containing glasses, the detector was windowed to reject Fe fluorescence due to the use of Cu radiation. The ICDD PDF-4 library was used for phase identification.

4.2.2.2 Scanning electron microscopy with energy dispersive X-ray spectroscopy (SEM/EDX)

Specimens of each glass were mounted in epoxy resin and polished to 1 μm diamond finish. The mounted specimens were carbon coated and painted with conductive silver paint to reduce charge build up. SEM analysis was performed using the Hitachi TM3030 with Bruker Quantax EDX with an accelerating voltage of 15 kV, with backscattered electron (BSE) micrographs collected at

a working distance of 8.0 mm. EDX mapping was completed using the Bruker Quantax 70 software with maps collected for a minimum of 20 min.

4.2.2.3 X-ray absorption spectroscopy (XAS)

The oxidation state of Ce was determined using Ce L_3-edge (5723.0 eV) X-ray absorption near edge spectroscopy (XANES) at BM28, ESRF. The optical arrangement consisted of a Si(111) double crystal monochromator, a toroidal focussing mirror and a Si/Rh harmonic rejection mirror. Incident beam intensity was measured using an ionisation chamber, filled with mixtures of He and N_2 gas, operated in a stable region of the I/V curve. Ce L_3-edge fluorescence radiation was detected using a Vortex Si Drift Detector.

The oxidation state and coordination environment of Fe was investigated using Fe K-edge (7112.0 eV) XANES at BM26A, ESRF. The beamline was configured with a Si(111) channel cut monochromator and Si mirror for harmonic rejection [157]. Incident and transmitted beam intensities were measured using ionisation chambers, filled with mixtures of He and N_2 gases, operated in a stable region of their I/V curve. Fitting of the Fe K-edge XANES pre-edge region, from 7106 - 7120 eV, was completed using the method described by Wilke *et al.* [158], [159]. The normalised data was fitted using a maximum of three Gaussian functions to describe the pre-edge region, with an arctangent function used to describe the background of the pre-edge region. The weighted mean centroid and height of the Gaussian functions were used to calculate the integrated pre-edge intensity, which is diagnostic of the oxidation state and coordination environment when compared to fitted standard reference compounds of known Fe environment.

Extended X-ray Absorption Fine Structure (EXAFS) data at the Fe K-edge were collected on selected ATS glass compositions and appropriate reference compounds at the National Synchrotron Light Source II (NSLS-II) at Brookhaven National Laboratory (Upton, New York) on beamline 6-BM. NSLS-II operates at 3 GeV storage ring with a 400 mA current and 6-BM utilises a 3-

pole wiggler to deliver X-rays in the energy range between 4.5 and 23 keV. The optical arrangement consists of a parabolic collimating mirror, a Si(111) 2 monochromator, a toroidal focussing mirror, and a harmonic rejection mirror.

Specimens for XAS analysis were prepared by mixing the quantity of material required for 1 absorption length (calculated using the Hephaestus software [136]) with a minimal quantity of polyethylene glycol. The resulting powder was then uniaxially pressed into a 10-13 mm pellet to create a homogeneous pellet without pin holes. Calibration, dead time correction [160], integration, normalisation, background subtraction of XAS data was achieved using the Athena software package [136] and analysed for average oxidation state using linear combination fitting (LCF) where appropriate. The EXAFS data were analysed using the Artemis software package [136]. A structural model (FEFF7 [161]) of a reference compound was created, comprising of X-ray scattering paths taken from a CIF model (using the corresponding file to the reference compound data on ICSD).

Bond valence sum calculations provide validation for the structural models generated using EXAFS fitting, by comparing the expected oxidation state to the calculated oxidation state (V_i), which is generated using the bond length in the EXAFS model. They were calculated according to the Brown – Altermatt equations which is given by Equation 4.1:

$$V_i = \sum_j \exp\left(\frac{r_0 - r_j}{B}\right) \tag{4.1}$$

where r_0 and r_{ij} are the tabulated and observed bond distance between atoms *i* and *j* respectively (Å), and B is a constant. The tabulated values for B and r_0 are published by Brese and O'Keeffe [162].

4.2.2.4 Mössbauer spectroscopy

Powdered samples were measured at room temperature using a Wissel MRG-500 spectrometer in transmission mode with a ^{57}Co/Rh source and a velocity

range ± 10 mm s^{-1}. Samples were calibrated relative to an α-Fe reference standard. The Recoil software package was used to deconvolute the spectra by assigning Lorentzian doublets to represent Fe oxidation states and co-ordination numbers using the Recoil analysis software [138].

4.2.2.5 Compositional analysis

The composition of two glasses (1200 °C 5.6Ce and 5.6CeFe) was measured by X-ray fluorescence (XRF) spectroscopy and Inductively Coupled Plasma – Optical Emission Spectroscopy (ICP-OES) prior to conducting dissolution experiments on these glasses. AMG Analytical Services completed this analysis, where ICP-OES was utilised for compositional analysis of B and Li. For XRF analysis, powders were pressed into pellets and analysed under vacuum using the Panalytical PW 2404 with a Rh source. For Li and B compositional analysis, the Thermo Jarrell Ash IRIS Advantage ICP-OES was used, where the powdered glass was completely digested in acid prior to analysis.

4.2.3 Dissolution experiments

4.2.3.1 Powdered glass tests

Batch dissolution experiments were completed using a derivative of the ASTM PCT-B method [101]. Glass material was crushed using a percussion mortar and sieved to retain the 75 – 150 µm size fraction. The resulting powder was sonicated in isopropanol to remove adhered fines and dried overnight at 90 ± 2 °C. The clean glass powder was placed into a 15 mL PTFE vessel with 10 mL of ultra high quality (UHQ, 18 MΩ cm^{-1}) water with a surface area to volume ratio (SA/V) of 1200 m^{-1}. Each experiment was performed in triplicate with duplicate blanks, the sealed vessels were stored in an oven at 90 ± 2 °C until sacrificial sampling at the following time points: 1, 3, 7, 14, 21 and 28 d. At each sampling point, selected vessels were removed, allowed to cool to room temperature and an 8 mL aliquot removed. After the removal of aliquots, powders were dried at room temperature and analysed using XRD and SEM/EDX. The aliquot pH was measured, then acidified using 20 µL ultra pure

HNO_3 and analysed for elemental concentration (c_i) by ICP-OES (ThermoFisher iCAPDuo 6300). The normalised mass loss (NL_i) of elements from the glass was calculated using Equation 4.2, where: NL_i is the normalised mass loss (g m^{-2}), c_i is the concentration in leachate (mg L^{-1}), $c_{i,b}$ is the concentration in blank (mg L^{-1}), f_i is the fraction of element *i* in the glass, SA/V is the surface area to volume ratio (m^{-1}).

$$NL_i = \frac{(c_i - c_{i,b})}{f_i \quad SA/_V} \tag{4.2}$$

$$NR_i = \frac{NL_i}{t} \tag{4.3}$$

The normalised dissolution rate (NR_i) in g m^{-2} d^{-1} was calculated using Equation 4.3, where *t* is the dissolution time in d.

The SA/V was adjusted to account for evaporative losses (if any) at each time point. The surface area was calculated geometrically using the density of the glass, which was determined using a Micromeritics Accupyc 1340 II pycnometer.

This methodology was repeated at SA/V = 10,000 m^{-1} to enable the investigation of the performance of this wasteform in the residual rate regime.

4.2.3.2 Monolith glass test

Static dissolution experiments were completed using a derivative of the MCC-1 ASTM [102] method. Glass monoliths were sectioned to 10 mm x 10 mm x 5 mm using a Buehler Isomet 1000 low speed saw and polished to P1200 grit finish using SiC abrasive paper. The monoliths were cleaned by sonicating three times in isopropanol and dried at 90 ± 2 °C overnight. Each monolith was placed on a PTFE basket in a 60 mL PTFE vessel with 40 mL of UHQ water to give a SA/V of 10 m^{-1}. The vessels were prepared in triplicate with duplicate blanks, sealed and placed in an oven at 90 ± 2 °C until sacrificial sampling at the following time points: 1, 3, 7, 14, 21, 28, 42, 56, 70 and 84 d. At each

sampling time point, a 10 mL aliquot was removed from each vessel, the pH measured, acidified with 20 µL of ultrapure HNO_3 and the solution analysed for elemental composition as described above. The monoliths were dried at room temperature, mounted in epoxy resin and analysed using SEM/EDX. The mass of each element released was used to calculate the normalised elemental loss using Equations 4.4 and 4.5 respectively, where: m_{ij} is mass of element *i* released from sample *j* (g), C_{ij} is the concentration of element *i* measured in leachate from sample *j* (g L^{-1}), V_{fj} is the final volume of leachate in test vessel containing sample *j* (L), B_{ik} is the concentration of element *i* measured in blank test *k* (g L^{-1}), V_{Bk} is the final volume of solution in test vessel containing sample *j* (L), a is the total number of blank solutions, NL_{ij} is normalised mass loss of element *i* from sample *j* (g m^{-2}), f_i is the mass fraction of element *i* in sample *j* and, S_j is the surface area of sample *j* (m^2).

$$m_{ij} = \left(c_{ij} \times V_{ij}\right) - \sum_{k=1}^{a} V_{Bk} \times \frac{B_{ik}}{a} \tag{4.4}$$

$$NL_{ij} = \frac{m_{ij}}{f_i \times S_j} \tag{4.5}$$

The normalised dissolution rate (NR_i) in g m^{-2} d^{-1} was calculated using Equation 4.3, where *t* is the dissolution time in d. The SA/V was adjusted at each time point to account for the evaporative losses. The surface area was calculated geometrically. The thickness of the alteration layer was measured using 10 separate measurements using representative SEM micrographs for monoliths at each sampling time point.

4.2.3.3 Geochemical modelling

Geochemical modelling using the elemental composition and pH of the leachates was completed using PhreeqC v.3 software [163] with the LLNL database [144] to find the saturation indices of mineral phases from the database. The saturation index (SI) of a phase was calculated in this software using Equation 4.6, where: *IAP* is the ion activity product for the phase and K_s^0 is the standard solubility constant of the phase.

$$SI = \log\left(\frac{IAP}{K_s^0}\right) \tag{4.6}$$

4.3 Results and discussion

4.3.1 XRD

Figure 4-1 shows the powder XRD patterns of each ATS glass, where the melt temperature was varied from 1100 – 1300 °C for three different compositions: (i) 2.9 mol.% CeO_2 (ii) 5.6 mol.% CeO_2 and (iii) 5.6 mol.% CeO_2 with equimolar addition of Fe^0. At 1100 °C, diffuse scattering between 15° < 2θ < 35° revealed the presence of a largely amorphous material consistent with the formation of a glass, in addition to Bragg reflections, which were indexed to CeO_2. The addition of equimolar Fe^0 at 5.6 mol.% CeO_2 resulted in a reduction in the relative intensity of the CeO_2 reflections. This clearly demonstrates that the inclusion of Fe^0 successfully promoted a higher incorporation rate of CeO_2 into the glass phase when compared to the compositions without Fe^0. Diffuse scattering was present in all glasses melted at 1200 °C with weak CeO_2 reflections observed in both glasses at 5.6 mol.% waste loading, whilst in the 2.9 mol.% glass, no crystalline CeO_2 was evident, indicating full CeO_2 incorporation at this waste loading. At 1300 °C, CeO_2 was fully dissolved into the glass phase for the 2.9 mol.% and 5.6 mol.% compositions, as indicated by the presence of diffuse scattering with no observable reflections attributable to CeO_2. At 5.6 mol.% CeO_2 loading, the addition of Fe^0 at 1300 °C resulted in the detection of weak reflections for CeO_2.

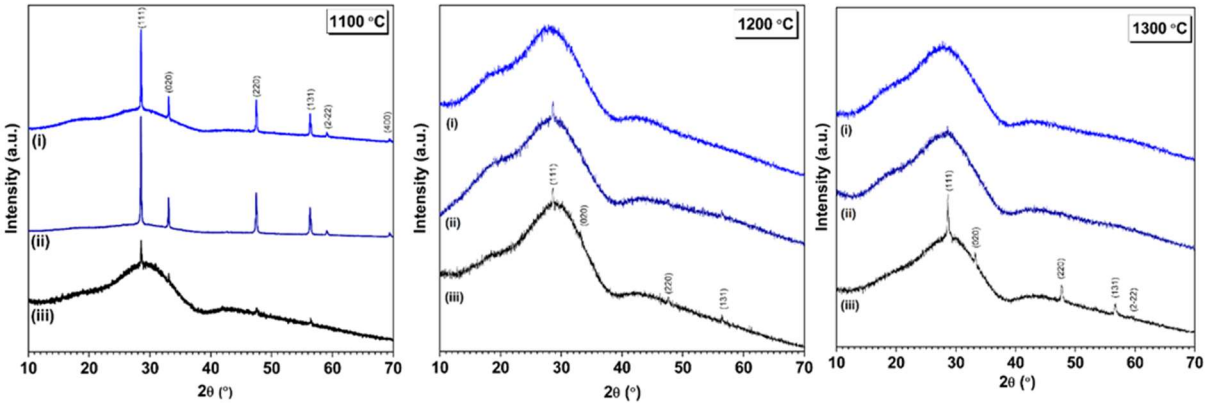

Figure 4-1 - XRD pattern of each glass produced at melt temperatures 1100 °C, 1200 °C and 1300 °C with miller indices indicating the primary reflections of CeO_2 (PDF - 01-081-0792) : (i) 2.9 mol.% CeO_2, (ii) 5.6 mol.% CeO_2 and (iii) 5.6 mol.% CeO_2 + Fe.

4.3.2 SEM/EDX

For ATS glasses melted at 1100 °C, the SEM micrographs in Figure 4-2 display a dark grey matrix with bright white crystallites, which correspond to ATS glass and CeO_2 respectively, confirmed by EDX analysis and as expected from XRD analyses (Figure 4-1). Micrographs in Figure 4-3A and B show a comparison between CeO_2 crystallites, with size < 1 µm in the 1100 °C 5.6 mol.% CeO_2 composition, and larger CeO_2 crystallites, at approximately 20 µm, observed in the 1100 °C 5.6 mol.% CeO_2 + Fe glass. The increase in crystallite size upon the addition of Fe^0 to the glass melt suggests that a small quantity of CeO_2 has precipitated from the melt and crystallised in the glass. These crystallites were associated with a darker phase in the glass (Figure 4-3C and D), which is richer in Al (Figure 4-4).

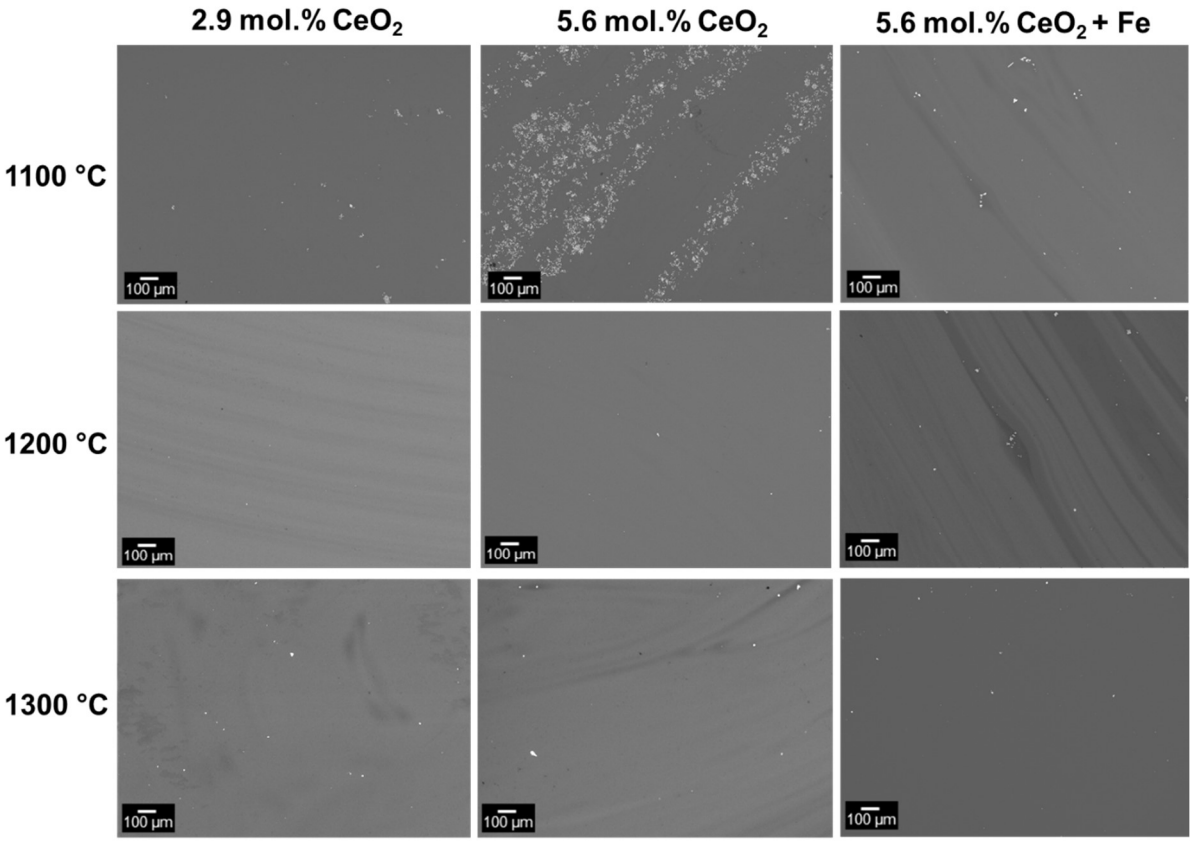

Figure 4-2 – Representative BSE micrographs of each ATS glass (2.9 mol.% CeO_2, 5.6 mol.% CeO_2 and 5.6 mol.% CeO_2 + Fe) at each melt temperature (1100 °C, 1200 °C and 1300 °C).

The SEM micrographs for glasses melted at 1200 °C are shown in Figure 4-2, with the features observed in these micrographs in agreement with corresponding XRD analysis (Figure 4-1). Small quantities of undissolved CeO_2 for the 2.9 mol.% CeO_2 and 5.6 mol.% CeO_2 compositions were observed, with precipitated CeO_2, which is larger in diameter, associated with a darker phase observed in the 5.6 mol.% CeO_2 + Fe composition. These observations are also in agreement with observations made of ATS glasses melted at 1100 °C and 1300 °C.

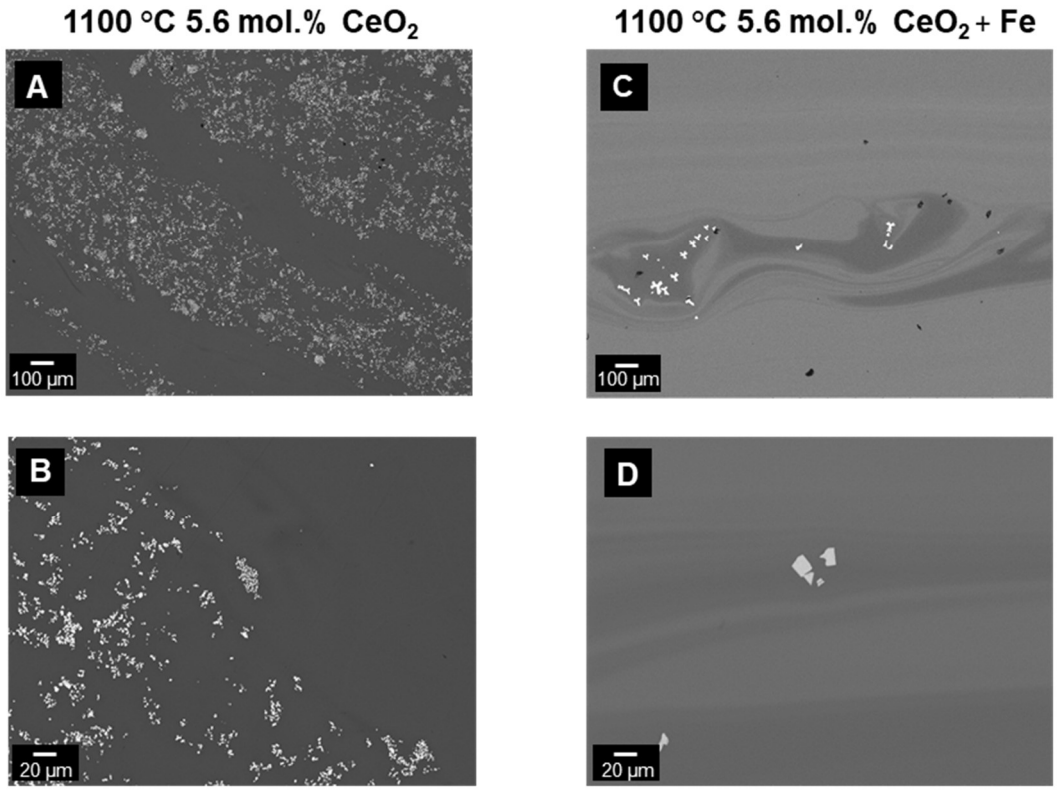

Figure 4-3 – BSE micrographs A, B: 1100 °C 5.6 mol.% CeO_2 showing unreacted CeO_2 crystallites of particle size < 1 µm, C, D: 1100 °C 5.6 mol.% CeO_2 + Fe showing reprecipitated CeO_2 crystallites of 20 µm.

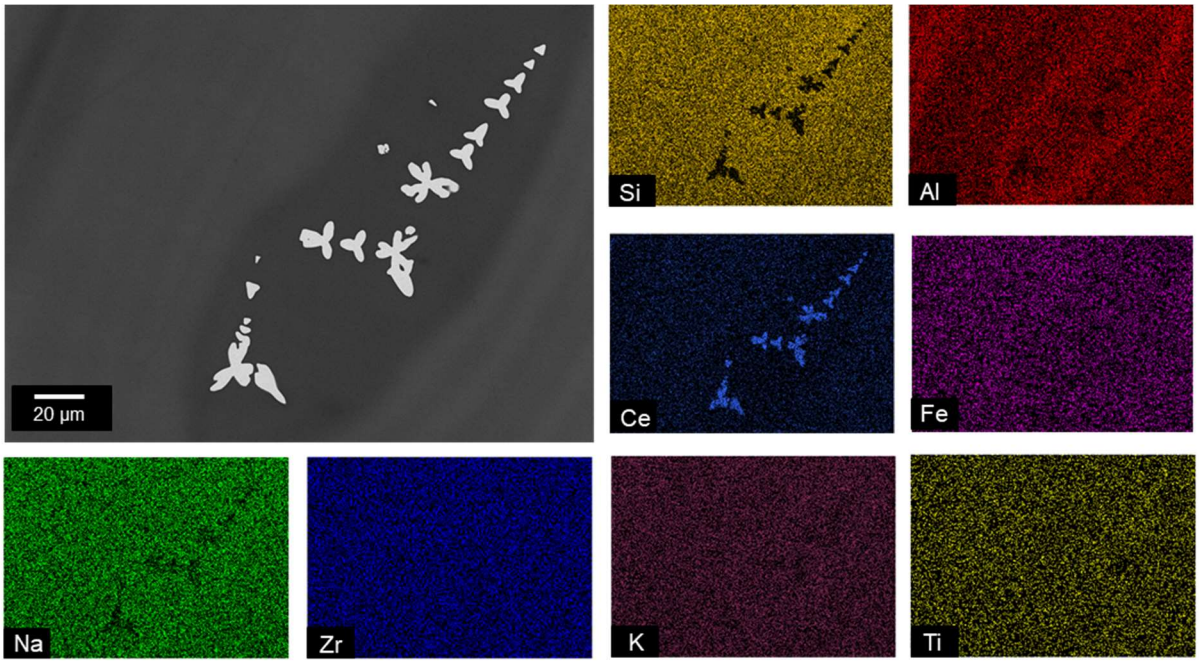

Figure 4-4 – BSE micrograph of ATS 1300 °C 5.6 mol.% CeO_2 + Fe glass with associated EDX analysis showing phase separation and CeO_2 crystallites.

The BSE micrographs for ATS glasses melted at 1300 °C are also shown in Figure 4-2, with the features observed in these micrographs in agreement with corresponding XRD analysis (Figure 4-1). The BSE micrograph for the 1300 °C 5.6 mol.% CeO_2 + Fe glass (Figure 4-4) shows phase separation with areas that are darker in contrast, which are enriched in Al according to the corresponding EDX maps. This phase separation was also apparent for 5.6 mol.% CeO_2 + Fe compositions synthesised at 1100 °C (Figure 4-3) and 1200 °C (Figure 4-2), with the crystalline CeO_2 associated with the darker contrast phase. The presence of crystalline CeO_2 in the glasses is in agreement with XRD analysis, however, the quantity of CeO_2 within this sample was low (as judged from relative intensity of reflections). This was demonstrated in Figure 4-2, where the bulk of all glasses produced in this study are amorphous (with the exception of 1100 °C 5.6 mol.% CeO_2 composition). The glasses were all melted in alumina crucibles and, since Ce is dense in comparison to the other glass forming elements, it was apparent that some stratification of CeO_2 occurred.

The BSE micrographs and EDX maps in Figure 4-2 - Figure 4-4 reveal CeO_2 crystallites in each of the glasses, with different crystallite sizes suggesting different formation mechanisms. Small crystallites observed in glasses without Fe^0 suggests that some CeO_2 remains unincorporated into the glass network. Upon the addition of Fe^0 to the composition at all melt temperatures, a growth in crystallite size suggests that the CeO_2 observed was a consequence of the solubility limit of CeO_2 being reached in the glass, causing CeO_2 to precipitate. The CeO_2 crystallites in the 5.6 mol.% CeO_2 + Fe compositions was observed to be associated with an Al-rich phase within the glass at all melt temperatures, suggesting that Ce solubility was lower in the Al-rich phase. This could be due to Al and Ce adopting similar structural roles within the glass network and, since Al has a higher field strength it therefore preferentially incorporated into the glass. This caused CeO_2 to precipitate and crystalise in the Al-rich phase. The presence of these crystallites in the glass is undesirable since Ce must be incorporated into the glass for immobilisation, proliferation resistance and criticality considerations [41].

4.3.3 Ce structural analysis

The local coordination environment and oxidation state of Ce in each glass was investigated using Ce L_3-edge X-ray absorption spectroscopy, to further understand how the change in melt temperature and addition of Fe^0 influence Ce within the glass structure. Ce L_3-edge XANES (Figure 4-5) were acquired for each glass to calculate the average Ce oxidation state. The following reference spectra were also acquired: CeO_2 (Ce^{4+} in 8-fold coordination) and $CePO_4$ (monazite; Ce^{3+} in 9-fold coordination). The Ce L_3-edge XANES of $CePO_4$ presents a single intense feature on the rising absorption edge, whereas CeO_2 presents three features, of lower relative intensity which have been described in previous studies [164], [165]. The ATS glass spectra were analysed using linear combination fitting (LCF) to estimate the proportion of Ce^{3+} and Ce^{4+} in each glass using the reference spectra (Table 4-2). Spectra were fitted over the range 5710 – 5760 eV, under the constraint that the fractional weights of the reference spectra sum to unity (100%).

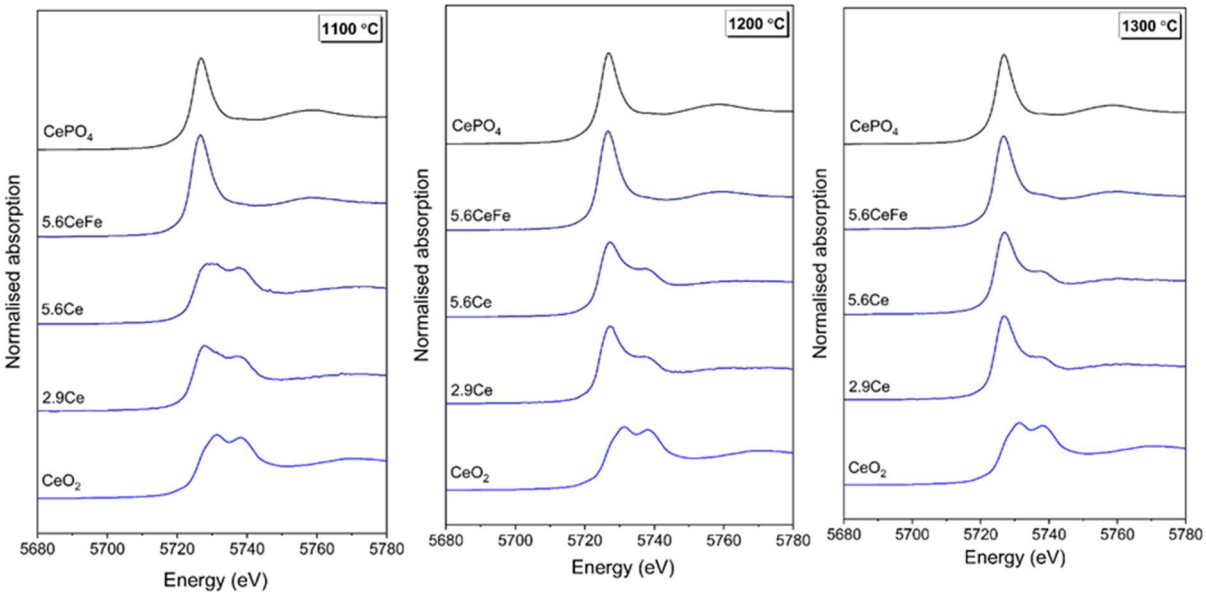

Figure 4-5 – Ce L_3-edge XANES spectra of 2.9 mol.% CeO_2 (2.9Ce), 5.6 mol.% CeO_2 (5.6Ce) and 5.6 mol.% CeO_2 + Fe (5.6CeFe) ATS glasses synthesised at 1100 °C, 1200 °C and 1300 °C compared with $CePO_4$ (Ce^{3+}) and CeO_2 (Ce^{4+}) reference compounds.

The Ce L_3-edge XANES spectra and LCF results, shown in Figure 4-5 and Table 4-2 respectively, illustrated that increasing the melt temperature of the glass increased the proportion of Ce^{3+} from 22 ± 1% at 1100 °C to 94 ± 1% at 1300 °C, for the 5.6 mol.% CeO_2 composition. This result was expected due to the auto-reduction of CeO_2 in borosilicate glasses with increasing melt temperature, which has been widely reported in the literature [54], [155]. The introduction of Fe^0 into the melt resulted in the complete reduction of Ce^{4+} to Ce^{3+} at all melt temperatures, hence creating a sufficiently reducing environment in the glass melt. These results, in combination with the results from XRD (Figure 4-1), demonstrate a greater incorporation of CeO_2 within the glass structure at 1100 °C, compared to the 5.6 mol.% CeO_2 composition at the same temperature, which can be attributed with Ce being 100 % present as Ce^{3+} (Table 4-2), caused by the introduction of Fe^0 to the glass melt. This total reduction of Ce in the Fe containing glasses is contradictory to the result of the XRD in Figure 4-1, since the presence of CeO_2 would suggest a quantity of Ce^{4+} present. However, the intensity of the reflections in the XRD patterns

for the Fe containing glasses is small, caused by small quantities of crystalline CeO_2 associated with the alumina rich phase in these glasses (see Figure 4-3 C-D and Figure 4-4). This contribution would be within the error of the Ce XANES linear combination fitting.

Table 4-2 – Linear combination fitting of Ce L_3-edge XANES spectra in Figure 4-5, showing the Ce speciation in each composition (2.9 mol.% CeO_2 (2.9Ce), 5.6 mol.% CeO_2 (5.6Ce) and 5.6 mol.% CeO_2 + Fe (5.6CeFe)), errors are reported in parentheses.

Composition		Ce speciation (%)		Average ox. state	R factor
		Ce^{3+}	Ce^{4+}		
1100 °C	2.9Ce	33(1)	67(1)	3.67	0.01
	5.6Ce	22(1)	78(1)	3.78	0.003
	5.6CeFe	100(2)	0(2)	3.00	0.03
1200 °C	2.9Ce	63(2)	37(2)	3.37	0.02
	5.6Ce	59(2)	41(2)	3.41	0.03
	5.6CeFe	100(2)	0(2)	3.00	0.03
1300 °C	2.9Ce	78(2)	22(2)	3.22	0.02
	5.6Ce	75(2)	25(2)	3.25	0.02
	5.6CeFe	100(2)	0(2)	3.00	0.02

A waste loading of 5.6 mol.% CeO_2 was achieved at 1100 °C, due to the addition of Fe^0 into the glass melt, with minimal crystalline CeO_2 observed. The increased incorporation of CeO_2 observed at this melt temperature was due to the total reduction of Ce to the Ce^{3+} oxidation state, which increased solubility as observed by Lopez *et al*. [140]. This processing temperature was also significantly lower than the temperatures required for melting other glass compositions considered for Pu immobilisation such as; LaBS at 1475 °C [166] and iron phosphate glass at 1400 °C [70]. This lower melt temperature would be advantageous for consideration of future industrial operational costs [21]. This finding is promising for the successful incorporation of Pu into the glass structure since Pu has shown a similar redox response to a reducing agent in borosilicate glass as Ce, with a reduction towards Pu^{3+} upon the addition of

Si_3N_4 to the melt facilitating a doubling of the reported PuO_2 solubility from 0.45 mol.% to 0.9 mol.% [155]. The structural role of Ce and Pu in borosilicate glass is also very similar since they are both classified as intermediate cations using the Dietzel field strength parameter [151], [167]. This means that they can behave as either network formers or modifiers dependent upon the glass composition and the oxidation state of the cation, with lower oxidation state cations behaving more like network modifiers, aiding their incorporation into the glass network.

4.3.4 Fe structural analysis

The oxidation state and coordination environment of Fe in the ATS glass network was investigated using three independent techniques:

1. Fe K-edge X-ray Absorption Near-Edge Spectroscopy (XANES) pre-edge region fitting – analysed the *average* oxidation state and coordination number of all Fe sites in the glass network.
2. Fe K-edge Extended X-ray Absorption Fine Structure (EXAFS) – analysed the *average* coordination number of Fe in the glass network, as well as the Fe-O bond distance.
3. ^{57}Fe Mössbauer spectroscopy – detailed information about the oxidation state and coordination number of the distinct Fe sites within the glass.

These techniques were used in tandem to provide a complete analysis of the structural role of Fe in the glass network, how this role changes with increasing melt temperature and to elucidate further information on how the addition of Fe influenced the role of Ce in the glass network.

The Fe K-edge XANES spectra of each Fe containing ATS glass are shown in Figure 4-6 alongside the spectra of four reference compounds: Fe_2SiO_4 (Fe^{2+} with 6-fold coordination), staurolite (Fe^{2+} with 4-fold coordination), $NaFeSi_2O_6$ (Fe^{3+} with 6-fold coordination) and $FePO_4$ (Fe^{3+} with 4-fold coordination). The area under the pre-edge peaks is dependent upon the site symmetry, showing a linear relationship between average co-ordination environment for a given oxidation state. The pre-edge region was fitted according the method

presented by Farges *et al*. [168] and Wilke *et al.* [158] with a maximum of three Gaussian peaks fitted to the spectral envelope. A weighted mean of the height and energy position of these Gaussian peaks was used to describe the total spectral envelope. This fitting process was repeated for the data collected on the reference compounds; an example is shown in Figure 4-7.

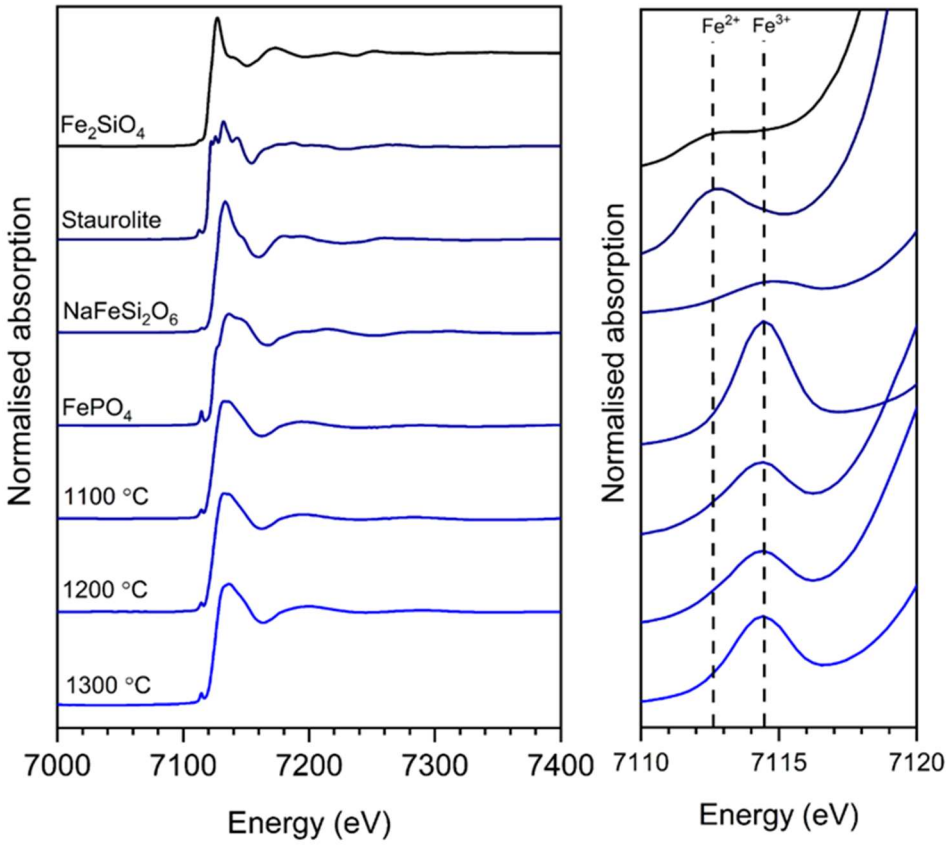

Figure 4-6 – Fe K-edge XANES spectra of reference compounds and three ATS 5.6 mol.% CeO_2 + Fe glasses produced at melt temperature 1100 °C, 1200 °C and 1300 °C *(left)* with detailed view of the pre-edge regions of the spectra *(right)*.

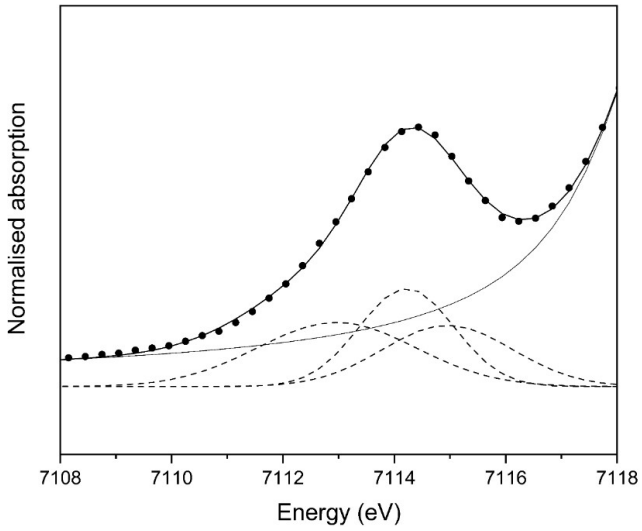

Figure 4-7 – Example of the fitting of Fe K-edge XANES pre-edge region (1100 °C 5.6 mol.% CeO_2 + Fe glass). The dotted line shows the data with the bold solid line showing the fit. Dashed lines represent the fitted gaussian peaks with the solid line showing the arctangent fitted to the background.

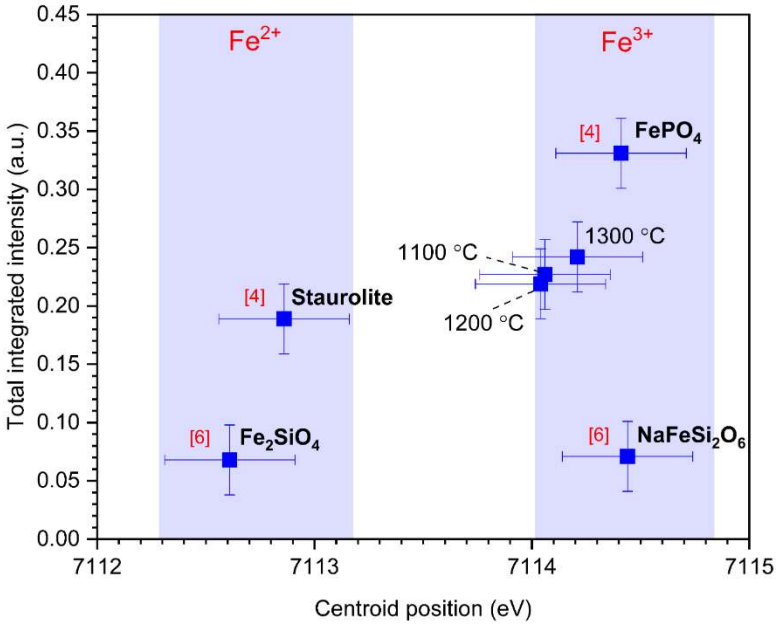

Figure 4-8 – Graphical representation of the centroid position and total integrated intensity of ATS 5.6 mol.% CeO_2 + Fe glasses and reference standard compounds determined by fits to the Fe K-edge pre-edge region. The oxidation state and coordination environment of Fe for each reference material is labelled in red, with the position of each ATS 5.6 mol.% CeO_2 + Fe glass also labelled.

Table 4-3 – Intensity weighted centroid position and total integrated intensity of the fitted pre-edge region of Fe K-edge XANES spectra for all 5.6 mol.% CeO_2 + Fe ATS glasses and reference compounds. Data presented in Figure 4-8.

Composition	Centroid position (eV) (± 0.3)	Total integrated intensity (± 0.03)	Average oxidation state (± 0.1)	Average coordination nº (± 0.2)
1100 °C	7114.1	0.23	2.8	4.7
1200 °C	7114.0	0.22	2.8	4.7
1300 °C	7114.2	0.24	2.9	4.8
$NaFeSi_2O_6$	7114.4	0.07	3	6
$FePO_4$	7114.4	0.33	3	4
Fe_2SiO_4	7112.6	0.07	2	6
Staurolite	7112.9	0.19	2	4

Figure 4-8 shows the centroid position and total integrated intensity/area of the pre-edge peaks of reference compounds and three 5.6 mol.% CeO_2 + Fe ATS glasses using data from Table 4-3. The centroid position of all glasses at ~7114 eV was consistent with dominant Fe^{3+}, as shown in comparison to reference standards in Figure 4-8. Linear interpolation of the glass centroid position using the average centroid position of the Fe^{2+} standards (7112.75 ± 0.3 eV) and Fe^{3+} standards (7114.4 ± 0.3 eV) from Table 4-3, yielded an average Fe oxidation state of 2.8 ± 0.1 at 1100 °C, rising to 2.9 ± 0.1 at 1300 °C. The area under the pre-edge curves of the ATS glasses was intermediate between 4-fold and 6-fold coordination when compared to the Fe^{3+} reference compounds. Linear interpolation of the average coordination number using the areas for the Fe^{3+} reference compounds gave an average coordination number of Fe of 4.7 – 4.8 ± 0.2 for all 5.6 mol.% CeO_2 + Fe ATS glasses.

The local coordination environment of Fe in the 5.6 mol.% CeO_2 + Fe ATS glass compositions was further investigated using Fe K-edge EXAFS analysis. For the coordination number of Fe to be accurately analysed, the amplitude reduction factor (S_0^2) was independently determined using an appropriate reference compound, $NaFeSi_2O_6$, since S_0^2 is directly correlated with the

coordination number. S_0^2 is generally assumed to be transferrable between different materials analysed at the same edge at the same beamline [169], enabling determination of the coordination number of Fe in ATS glass. Consequently, $NaFeSi_2O_6$ EXAFS data was fitted with seven paths from the FEFF calculation, with structural parameters shown in Table 4 and the fit shown in Figure 9. The degeneracy (N_{Fe-i}) for each path was held constant while S_0^2, the interatomic distance (R_{Fe-i}) and Debye-Waller factor (σ_i^2) were allowed to refine. The $NaFeSi_2O_6$ theoretical fit gave $S_0^2 = 0.67 \pm 0.08$, with the Fe-O distance 2.01 ± 0.01 Å, and the BVS is calculated as 3.0 ± 0.1, in agreement with Fe^{3+} oxidation state in $NaFeSi_2O_6$.

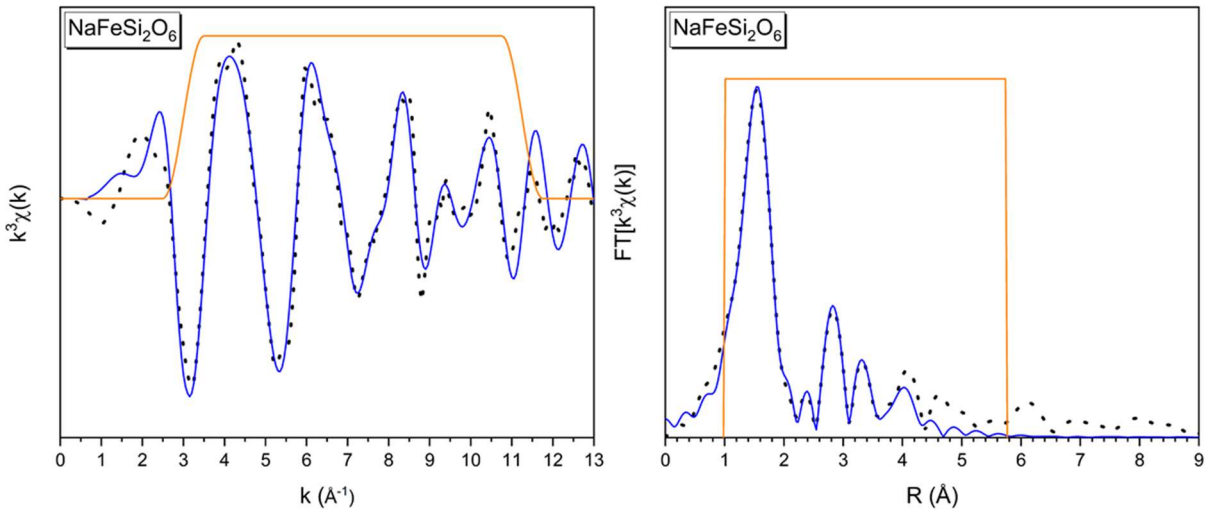

Figure 4-9 – Model fit to the Fe K-edge EXAFS spectra for $NaFeSi_2O_6$, where A – $k^3\chi(k)$, B – FT of $k^3\chi(k)$, with dashed black lines represent the data and solid blue lines present the theoretical fits. The fitting window is shown by a solid orange line.

Table 4-4 – Fitted structural parameters for the EXAFS model of $NaFeSi_2O_6$ in Figure 4-9. R_{Fe-i} is the average interatomic distance for a given Fe-i pair, σ^2_i is the Debye-Waller factor and N_{Fe-i} is the coordination number fixed in the model. The fit range in k was from 3 to 11 $Å^{-1}$ and in R from 1 to 5.5 Å. The R factor was 0.012 and the ΔE_0 = 1.83 ± 1.35. The number of independent variables (N_v) and data (N_{ip}, determined from the Nyquist theorem) was N_v = 24.7 and N_{ip} = 16, respectively.

$NaFeSi_2O_6$	R_{Fe-i} (Å)	±	σ^2_i	±	N_{Fe-i}
Fe-O1	2.01	0.01	0.011	0.002	6
Fe-Fe1	3.13	0.08	0.003	0.009	2
Fe-Si1	3.08	0.08	0.01	0.02	6
Fe-Na1	2.90	0.08	0.01	0.01	3
Fe-O2	3.78	0.08	0.01	0.02	8
Fe-O3	3.60	0.09	0.01	0.04	6
Fe-Si2	4.41	0.04	0.005	0.005	2

Table 4-5 – Structural parameter for the 5.6 mol.% CeO_2 + Fe ATS glass Fe K-edge EXAFS fits. R_{Fe-i} is the average interatomic distance between Fe and i, σ^2_i is the Debye-Waller factor and N_{Fe-i} is the refined number of scatterers in the first oxygen shell. The amplitude reduction factor, refined from the $NaFeSi_2O_6$ fit, was fixed at $S_0^2 = 0.67$. BVS is the bond valence sum for the first oxygen coordination shell.

Glass	1100 °C		1200 °C		1300 °C	
		±		±		±
E_0 (eV)	-2.3	0.9	-4.8	0.9	-5.6	1.2
R_{Fe-O1} (Å)	1.90	0.01	1.89	0.007	1.89	0.01
N_{Fe-O1}	5.5	0.4	5.5	0.4	5.1	0.4
σ^2_O (Å^2)	0.009	0.001	0.009	0.001	0.006	0.001
R_{Fe-Si1} (Å)	3.19	0.04	3.17	0.03	3.21	0.04
N_{Fe-Si1}	2	-	2	-	2	-
σ^2_{Si} (Å^2)	0.017	0.005	0.017	0.005	0.016	0.007
R-factor	0.006	-	0.005	-	0.005	-
BVS (v.u.)	3.2	0.2	3.2	0.2	3.2	0.2

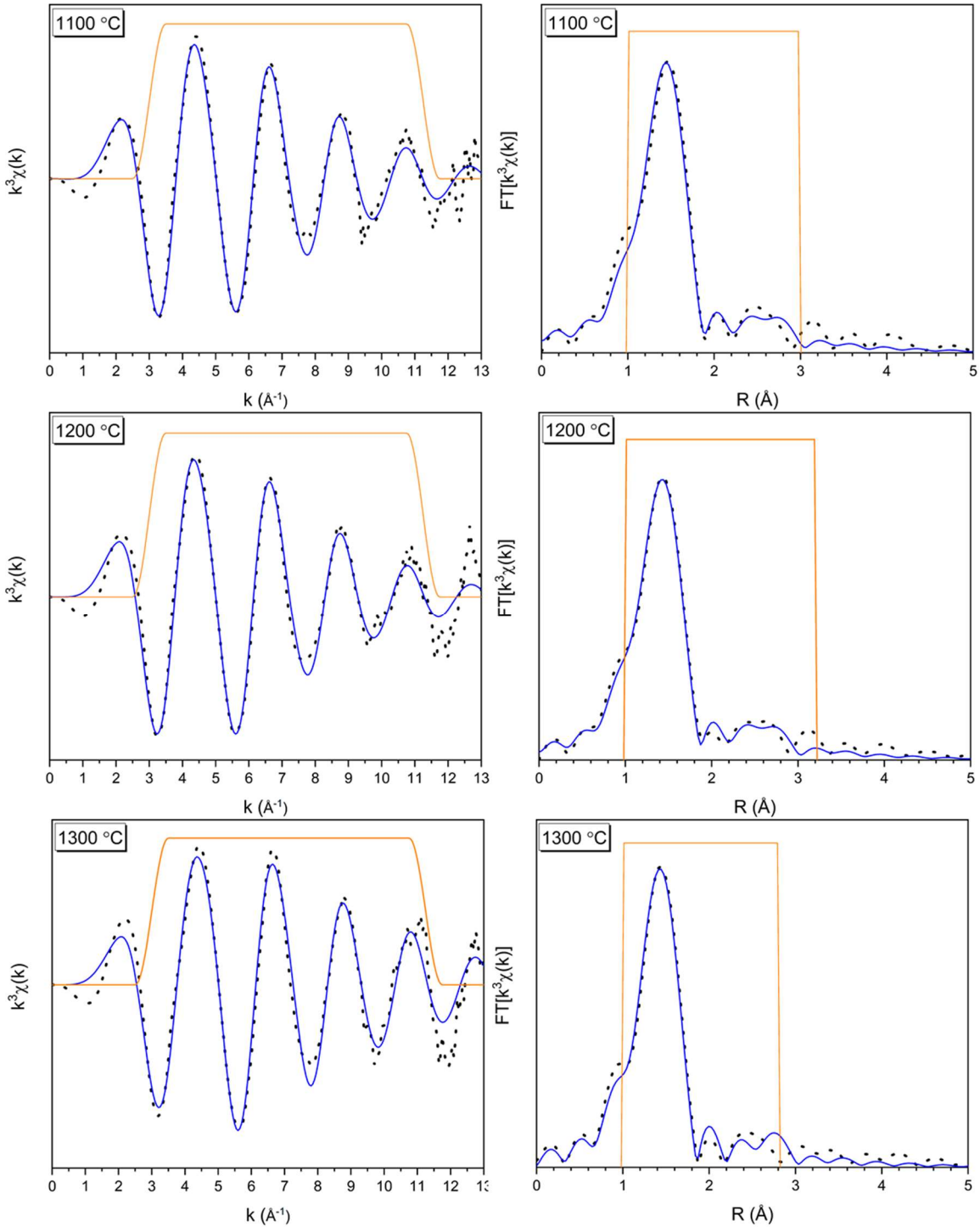

Figure 4-10 – $k^3\chi(k)$ and the FT of $k^3\chi(k)$ at the Fe K-edge EXAFS data of all 5.6 mol.% CeO_2 + Fe ATS glasses. Dashed black lines represent the data and solid blue lines present the theoretical fits. The fitting window is shown by a solid orange line.

The Fe K-edge EXAFS spectra in $k^3\chi(k)$ and respective FT waveforms of the ATS 5.6 mol.% CeO_2 + Fe glasses are shown in Figure 4-10, along with the fitted waveforms, with refined structural parameters for these fits in Table 4-5. The waveforms show a simple damped sine wave, with relatively few components, characteristic of amorphous materials. The spectra were fitted using $S_0^2 = 0.67$, calculated using the $NaFeSi_2O_6$ theoretical fit as reported above. The theoretical fits for ATS glass spectra used a scattering path based on the first oxygen shell with the degeneracy (N_{Fe-i}), the interatomic distance (R_{Fe-i}) and Debye-Waller factor (σ_i^2) allowed to refine. The addition of a second path, Fe-Si, optimised the fit, typically reducing the R factor by two thirds, giving a refined value of N_{Fe-Si} of 1.7 ± 1.5. The precision of this value was low, as expected for a disordered system, therefore for the final stage of refinement, we fixed $N_{Fe-Si} = 2$ which afforded a reasonable R_{Fe-Si} path length and significant reduction in the R-factor. The quality of the fit was validated for each model using a BVS, with results in Table 4-4, which were consistent with the oxidation state values calculated using Fe K-edge XANES pre-edge fitting in Table 4-3. Modelling the EXAFS data determined an Fe coordination number of 5.5 ± 0.4 for the ATS glasses produced at 1100 °C and 1200 °C 5.6 mol.% CeO_2 + Fe glasses, and 5.1 ± 0.4 for the glass produced at 1300 °C.

The ^{57}Fe Mössbauer spectra for 5.6 ATS 5.6 mol.% CeO_2 + Fe glasses produced at 1100 °C, 1200 °C and 1300 °C are shown in Figure 4-11 along with the fitted contribution to the spectral envelope. For each glass, two quadrupolar doublet sites were fitted with values for the isomer shift, quadrupolar shift and full width half maximum of each doublets reported in Table 4-6. Each doublet represents a separate crystallographic site for Fe present in the glass, which suggests there are two separate Fe environments within the glass structure, referred to as site A and site B. The values associated with the fitting of Mössbauer spectra are well defined, particularly the isomer shift, which is sensitive to the Fe coordination number and oxidation state. Quadrupolar shift is also indicative of the oxidation state with ferrous ions having a larger quadrupolar splitting than ferric ions, however, due to the

large range of possible environments in an amorphous environment, these results must be carefully interpreted.

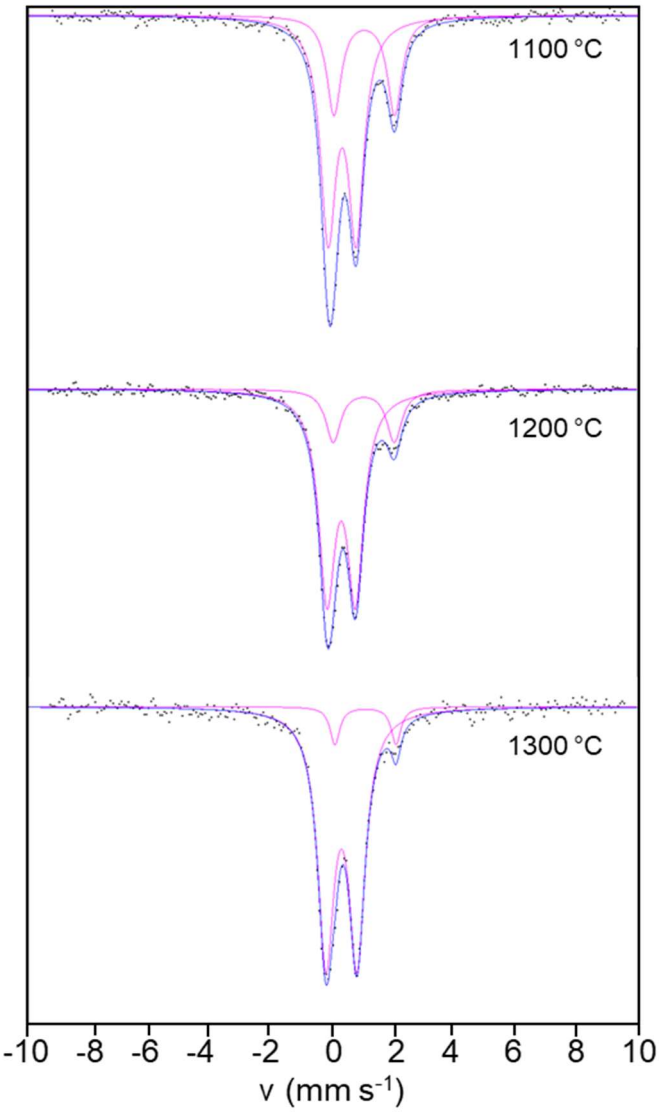

Figure 4-11 – Room temperature ^{57}Fe Mössbauer spectra of all ATS 5.6 mol.% CeO_2 + Fe glasses. Pink line - fitted doublet; blue line - data fit; black dots - data.

Table 4-6 – ^{57}Fe Mössbauer parameters for site A and B for ATS 5.6 mol.% CeO_2 + Fe glasses where: δ – isomer shift (mm s^{-1}), Δ – quadrupolar shift (mm s^{-1}) and Γ – full width half maximum (mm s^{-1}). The proportion of site A relative to the total is also shown.

Composition	A Site			B site			Fe(A)/ ΣFe
	δ (mm s^{-1})	Δ (mm s^{-1})	Γ (mm s^{-1})	δ (mm s^{-1})	Δ (mm s^{-1})	Γ (mm s^{-1})	
1100 °C	0.27(1)	0.91(2)	0.31(1)	1.00(2)	1.99(3)	0.29(2)	0.70(2)
1200 °C	0.27(1)	0.94(1)	0.33(1)	1.01(2)	2.01(5)	0.30(4)	0.81(2)
1300 °C	0.27(1)	1.02(1)	0.33(1)	1.06(3)	2.00(7)	0.19(5)	0.92(2)

Using the information about the fitted values for each site (Table 4-6) in combination with the data on ^{57}Fe Mössbauer spectroscopy collated by Dyar *et al*. [170], [171], site B was assigned as Fe^{2+} in 6-fold coordination, however it should be noted that the isomer shift values for Fe^{2+} were at the low end of the boundary for 6-fold coordination [172]. Site A, with Δ = 0.91(2) - 1.04(1) (mm s^{-1}), was assigned to Fe^{3+}, with 5-fold coordination, however, the boundary in quadrupolar splitting between 4- and 5-fold coordinated Fe^{3+} is poorly defined particularly for amorphous materials [173]. The recoil free fraction was assumed to be unity in these glasses since it has been shown in silicate glass melts that Mössbauer spectroscopy and wet chemical analysis produce the same average bulk Fe oxidation state [174]. Although the assignments of oxidation state can be given over a wide range of isomer shift and quadrupolar splitting values, the values in Table 4-6 and their respective assignments were supported by published data for crystalline materials with well-defined ^{57}Fe Mössbauer spectroscopy parameters [170], [171]. There was a higher proportion of site A in the glass as the melt temperature increased, which therefore confirmed that Fe^{3+} speciation increased with melt temperature, from 70 ± 2% at 1100 °C to 92 ± 2% at 1300 °C. The coordination number decreased from 5.3 ± 0.2 at 1100 °C to 5.1 ± 0.2 at 1300 °C. These values are in excellent agreement with Fe XANES pre-edge fit values reported in Table 4-3.

Fe XANES, EXAFS and Mössbauer spectroscopy results are in agreement and show that the quantity of Fe^{3+} in 5-fold coordination increased with increasing temperature, with the remainder being a small contribution of Fe^{2+} in 6-fold coordination. The dominant Fe^{3+} oxidation state was to be expected due to the redox environment of the glass i.e. the glass was melted in an oxidising environment with the presence of the Ce redox couple. The literature states that Fe in borosilicate glass typically favours the Fe^{3+} oxidation state and 4-fold coordination environment [65], [172], acting as a network former in the glass structure, especially with the redox coupling with Ce providing an oxidising environment. However the presence of 5-fold coordinate Fe^{3+} in silicate glass melts has been reported [158], [173], [175], [176] using both XANES and molecular dynamics, but it has been suggested that these findings could be attributed to distorted tetrahedral and octahedral Fe in the glass network [177]. There is also a contribution of Fe^{2+} in 6-fold coordination, decreasing with increasing temperature, suggesting that Fe is initially oxidised from Fe^{0} to Fe^{2+}, at which point it is incorporated into the glass and oxidised further to Fe^{3+}. This observation could be attributed to repolymerisation of the glass with increasing temperature associated with the reduction in quantity of Fe^{2+} in 6-fold coordination. The diffusion of alkali network modifying cations through the glass network controls the kinetics of this reaction [178].

4.3.5 Compositional analysis

The composition of two glasses, 1200 °C 5.6 mol.% CeO_2 and 5.6 mol.% CeO_2 + Fe, were determined using a combination of XRF and ICP-OES (for Li and B) and are presented in

Table 4-7. These compositions were chosen for chemical durability assessment because they showed minimal presence of crystalline Ce and to allow the effect of Fe incorporation on the overall durability to be determined at a fixed melt temperature. In the 5.6 mol.% CeO_2 composition, approximately half of the batched quantity of CeO_2 was incorporated into the glass, postulated due to low Ce^{4+} solubility in the glass, of which there was 41 ± 2 % in this composition (Table 4-2). Upon the addition of Fe, the batched CeO_2 was fully incorporated into the glass. Both compositions were enriched in Al_2O_3

(by 1 – 2.5 mol.%) due to corrosion of the alumina crucible, as observed from SEM/EDX (Figure 4-4).

Table 4-7 – Comparison of batched composition and XRF/ICP-OES results for two ATS glasses: 1200 °C 5.6 mol.% CeO_2 and 1200 °C 5.6 mol.% CeO_2 + Fe.

Oxide	1200 °C 5.6 mol.% CeO_2 (mol.%)		1200 °C 5.6 mol.% CeO_2 + Fe (mol.%)	
	Batch	ICP/XRF (± 0.05)	Batch	ICP/ XRF (± 0.05)
Al_2O_3	1.67	3.95	1.63	2.49
B_2O_3	12.18	11.81	11.94	11.93
CeO_2	5.56	2.68	5.45	5.11
Fe	0.00	0.07	1.63	1.93
K_2O	4.07	3.72	3.99	3.42
Li_2O	10.34	11.56	10.13	11.19
Na_2O	10.87	10.57	9.21	8.89
SiO_2	49.15	49.32	48.17	46.11
SnO_2	1.25	1.43	1.37	1.26
TiO_2	1.73	1.78	1.50	1.64
ZrO_2	3.17	3.02	3.11	2.57

4.3.6 Dissolution behaviour

PCT-B tests were performed on the materials prepared at 1200 °C, with and without Fe^0, to assess and compare their chemical durability. Two SA/V ratios were selected for the 5.6 mol.% CeO_2 + Fe composition, with the higher value giving insight to dissolution behaviour in the residual rate regime. The solution pH for both glass compositions rapidly reached a value of 10.2 ± 0.1 after 1 d of dissolution (Figure 4-12). For the duration of the experiment, the pH for the lower SA/V experiments remained between pH 10 and 10.5, while the higher SA/V experiment showed a slightly higher pH (~pH 11). This reflects the greater reaction progress imposed by the high SA/V.

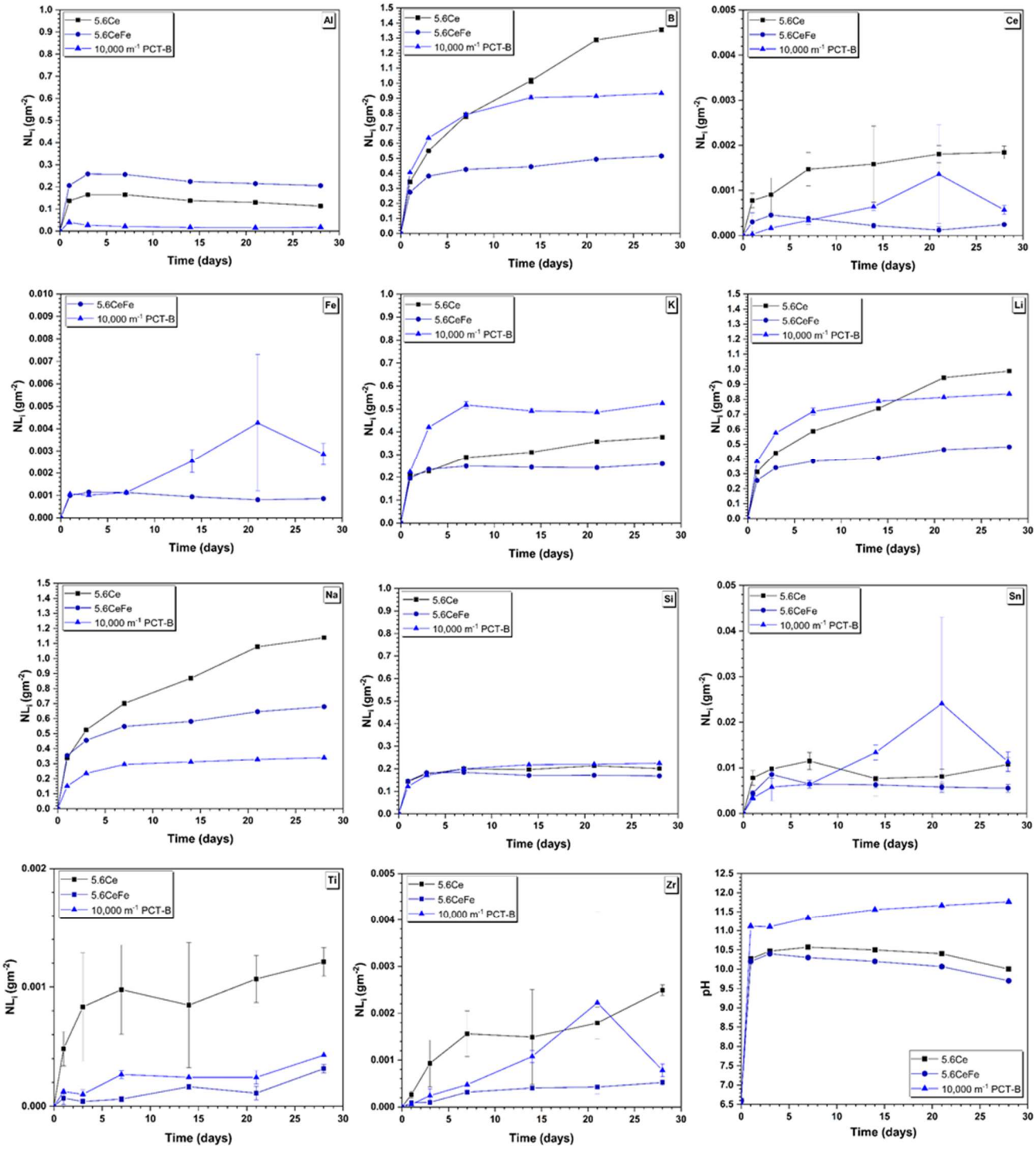

Figure 4-12 – Normalised elemental mass loss (NL_i) of Al, B, Ce, Fe, K, Li, Si, Na, Sn, Ti and Zr, and the pH for 5.6 mol.% CeO_2 (5.6Ce) and 5.6 mol.% CeO_2 + Fe (5.6CeFe) PCT-B tests.

The normalised mass loss of elements from the 5.6 mol.% CeO_2 glass showed incongruent dissolution: B, Li and Na leached at similar rates (Table 4-8), however, the normalised mass loss of Si and Al were much lower, indicating the attainment of steady state, or residual rate conditions, during which time a silica-rich gel layer and/or silicate secondary phases typically form [109]. This behaviour is reflected in the NL_i of other elements, for example, the NL_{Ce} initially increased but after 1 d of dissolution the rate of increase slowed to a plateau, with a dissolution rate of 3.30(3) x 10^{-5} g m^{-2} d^{-1}.

When Fe was added to the glass formulation, the NR_i of B, Li and Na was an order of magnitude lower than for the 5.6 mol.% CeO_2 composition (Table 4-8). The NL_{Si} was comparable with the Fe-free composition, however, suggesting that any gel layer formation processes occurred at a similar rate for both glasses. Since the NL_{Fe} showed similar behaviour to NL_{Si} (Figure 4-12), this indicates that the silica gel/silicate secondary phases formed likely also incorporate Fe [179], [180]. The NL_i of other elements, including Ti, Zr and Ce was also lower for this glass, with the resulting NR_{Ce} being two orders of magnitude lower.

For the PCT-B experiment at SA/V = 10,000 m^{-1}, similar behaviour was observed, however, owing to the greater SA/V value, the NL_i of B, Na and Li were greater than for the SA/V = 1200 m^{-1} counterparts.

Table 4-8 – Normalised elemental loss rate (NR_i calculated from 7 – 28 d) calculated using linear regression for each PCT-B experiment (where 5.6Ce = 5.6 mol.% CeO_2 compositions and 5.6CeFe = 5.6 mol.% CeO_2 + Fe). For MCC-1, the normalised elemental loss rate was calculated from 21 – 84 d. ND (not detected) signifies that the element was below the detection limit for ICP-OES measurement.

NR_i	Experiment (error = ± 1%)			
($g\ m^{-2}\ d^{-1}$)	5.6Ce	5.6CeFe	5.6CeFe SA/V = 10000 m^{-1}	5.6CeFe MCC-1
B	3.57×10^{-2}	4.98×10^{-3}	4.45×10^{-3}	0.35
Ce	3.30×10^{-5}	6.65×10^{-7}	1.35×10^{-5}	ND
Fe	ND	0	9.41×10^{-5}	ND
K	6.45×10^{-3}	3.57×10^{-5}	2.36×10^{-3}	0.15
Li	2.31×10^{-2}	4.49×10^{-3}	3.99×10^{-3}	0.22
Na	2.60×10^{-2}	6.79×10^{-3}	1.79×10^{-3}	0.11
Si	6.89×10^{-4}	7.91×10^{-4}	6.87×10^{-4}	0.14

To explore the dissolution behaviour of the glass further and to examine the nature of the silica gel and/or secondary phases formed, monolith experiments were performed using the MCC-1 methodology. Figure 4-13 shows the corresponding normalised mass loss (NL_i) of Al, B, Si, Na, Li and K from these experiments. Given the much lower SA/V ratio than the PCT-B experiments described above, the concentrations of Ce, Sn, Ti and Zr were below the detection limit of the ICP-OES and, as such, no data are shown. Within error, all elements reached saturation, and therefore the residual rate, by 28 d. It should be noted that the normalized mass loss values were significantly higher than those from the PCT-B experiments, despite the lower SA/V ratio as reported in several other studies [181]. This is postulated to be caused by an underestimation of the surface area attributed to the polishing of the monoliths.

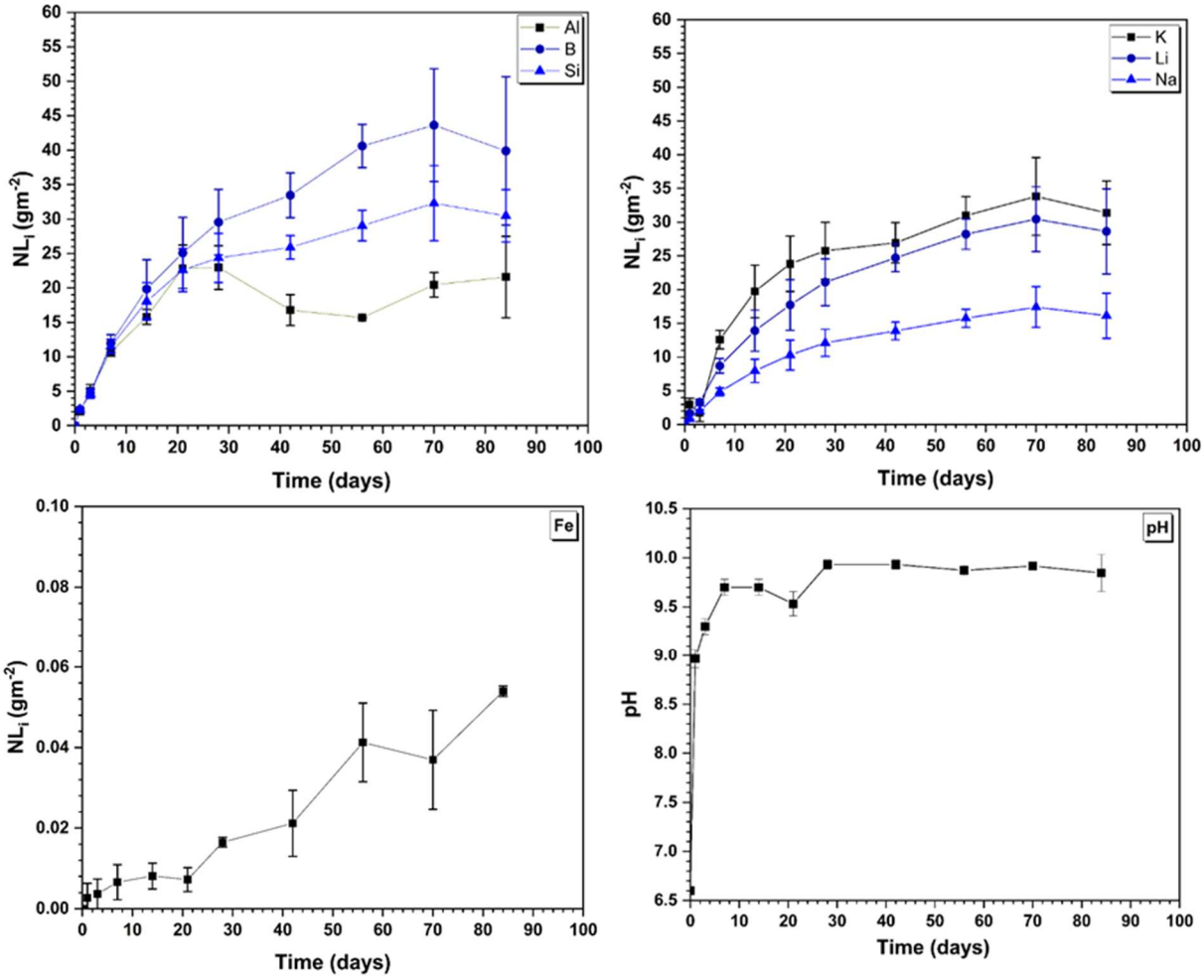

Figure 4-13 – Normalised elemental mass loss (NL_i) of Al, B, Si, K, Li, Na and Fe alongside the pH for the 5.6 mol.% CeO_2 + Fe MCC-1 test.

Figure 4-14 shows SEM micrographs of the cross section of monoliths from 7 - 84 d from the 5.6 mol.% CeO_2 + Fe MCC-1 test (monoliths for 1 and 3 d do not have an observable alteration layer when using SEM). A gel layer on the outer edge of the pristine glass was observed, with a thickness that increased as a function of time; at 7 d the average thickness was 8.4 ± 0.9 µm, compared to 24.0 ± 0.4 µm at 84 d. The thickness increased linearly up to 42 d, after which time it the rate of gel layer growth slowed. This is consistent with the normalised mass loss values, which showed that elements were released more slowly after 42 d (Figure 4-13), and suggests that the alteration layer is passivating in nature. EDX mapping of the cross section of the 70 d monolith shows that the gel layer contained Si, Ce, Fe, Ti and Zr, with smaller

concentrations of Na and K. The outer edge was particularly enriched in Ce and Zr, as shown in Figure 4-15, with a depletion in Al, Na, Si and K compared to the pristine glass.

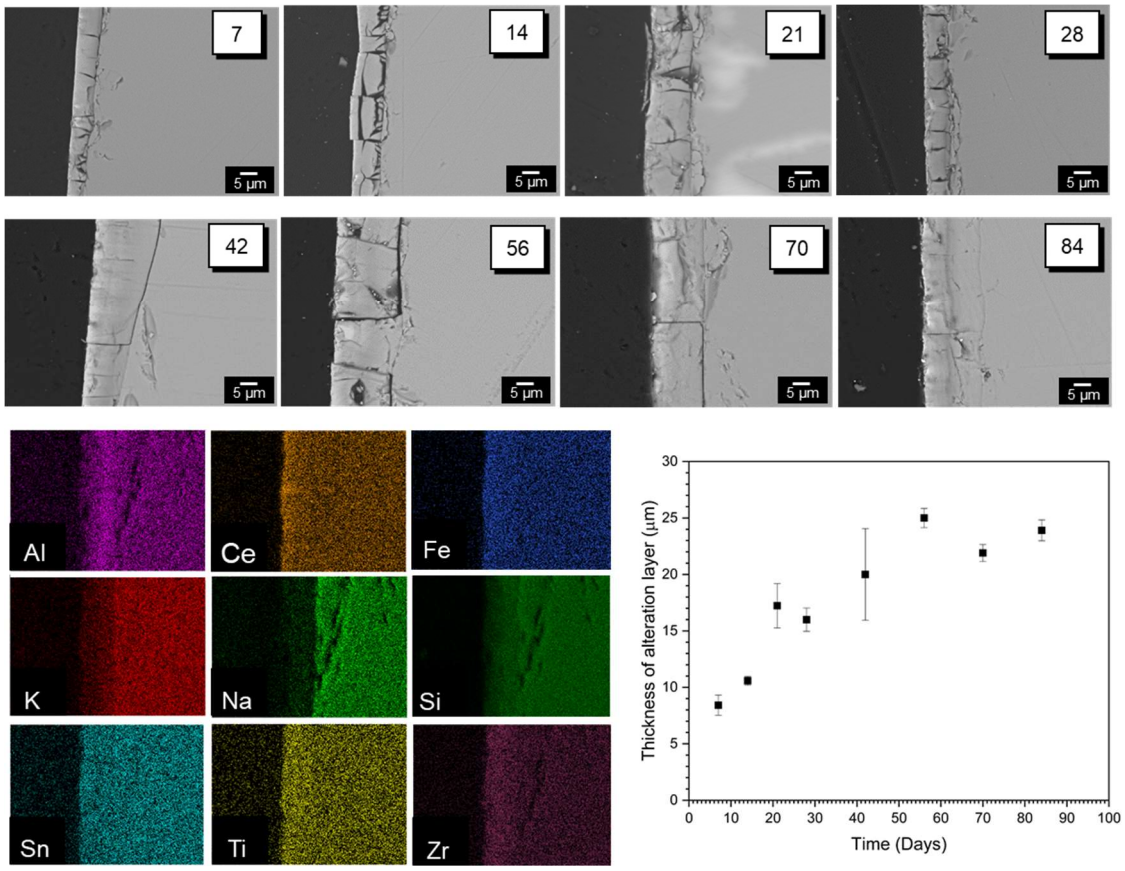

Figure 4-14 – BSE micrographs of the cross section of 5.6 mol.% CeO_2 + Fe MCC-1 samples from 7 – 84 d, along with EDX maps of the 70 d micrograph. A graphical representation of the change in thickness of the alteration layer with time is also included

Geochemical modelling (using PhreeqC) was used to determine which secondary crystalline phases were saturated with respect to the solution, based on elemental concentration analysis and pH values from PCT-B experiments. For the 5.6 mol.% CeO_2 + Fe composition, the Fe-containing clay mineral nontronite ($(H,Na,K)_{0.33}Fe_2Al_{0.33}Si_{3.67}H_2O_{12}$) was predicted to form, with similar results observed when analysing the MCC-1 dissolution data, however, no secondary phases were predicted for the dissolution of the 5.6 mol.% CeO_2 glass.

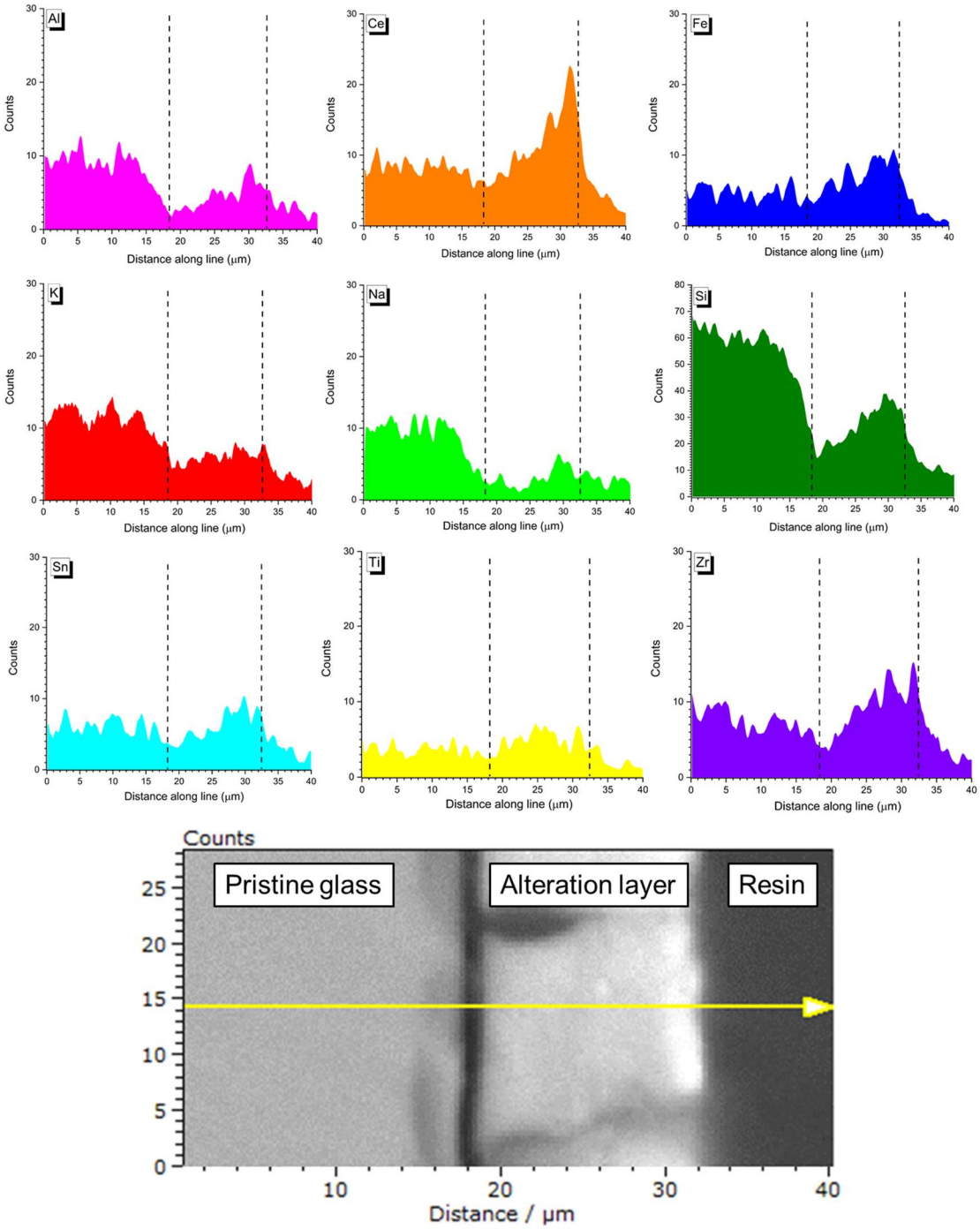

Figure 4-15 – EDX line scans showing the number of counts of each element along the cross section imaged, which shows the alteration layer of the 5.6 mol.% CeO_2 + Fe ATS glass after 84 d MCC-1 test. Dashed lines represent the alteration layer limits.

It is apparent from these results that 5.6 mol.% CeO_2 + Fe glass was more durable than the 5.6 mol.% CeO_2 glass. This may be because: (1) the presence of Fe caused a higher degree of polymerisation in the glass network [172], which is known to improve the chemical durability of glasses; (2) the Ce content of the Fe-containing glass was twice that of the Fe-free counterpart (Table 4-7), and this additional Ce, also known to enhance polymerisation of the glass network [65], may have promoted greater durability. Since Fe is generally understood to *decrease* glass durability, due to the precipitation of Fe-silicate phases that drive the thermodynamic equilibrium of the leaching media towards silica dissolution, the second option seems the most probable to dominate the dissolution, however it is postulated that both are contributing factors to the improved dissolution. The normalised mass loss at 28 d for B and Si for the 5.6 mol.% CeO_2 + Fe composition were of the same order of magnitude as reported for other ATS glass compositions, which do not contain Fe [67], further highlighting the positive role of Ce on durability.

The NL_{Ce} from the Fe-containing glass was on the order of 10^{-3} g m^{-2} at 28 d, which is comparable in magnitude to NL_{Pu} derived from Pu-containing ATS glass by Bates *et al.* [67] (NL_{Pu} = 2 x 10^{-3} g m^{-2}). The use of CeO_2 as a surrogate for PuO_2 in the leaching tests, therefore, seems to be well justified. In high temperature Vapour Phase Hydration testing (VHT method) of ATS glass (Bates *et al.*) the formation of an Fe and Al-containing clay phase was observed approximately 5 nm in size at 56 d, which is in good agreement with the geochemical modelling results performed here, despite the fact that such phases were not experimentally observed. It is likely that longer time durations may be required for these phases to form under the PCT-B and MCC-1 conditions employed in the present study. It should be noted that the gel layer was rich in the elements required to form such clays, which can nucleate within the gel layer itself [180], [182]. As noted above, the presence of iron-rich clay precipitates typically accelerates glass dissolution [183], [184] and can lead to “stage III” dissolution rate resumption [185]. Further investigation of dissolution over longer time scales is required to evaluate whether such behaviour may occur.

In the VHT experiment performed by Bates *et al*., it was found that the secondary phases contained no/negligible Pu, and that Pu was incorporated within the silica gel [66]. In the present study, Ce also accumulated within the gel layer, but was concentrated on the outer edge. However, it is possible that other Ce-oxide, or even silicate phases that are not included within geochemical modelling databases, could precipitate. The outer edge of the gel layer is formed at the beginning of the glass hydrolysis process; therefore, another explanation could be the initial solubilisation of Ce^{3+} from the glass, which was incorporated within the silica gel to charge compensate silicate anions, forming a dense outer layer. Future work should be directed at understanding the role of Ce/Pu in alteration products on ATS glasses, and in borosilicate glass compositions proposed for PuO_2 immobilisation.

4.4 Conclusion

Vitrification is suggested for the immobilisation of the UK civil PuO_2 stockpile due to the technological readiness advantages over other proposed waste form technologies for PuO_2. A series of CeO_2 doped ATS glasses were developed for this purpose, with a waste loading of 5.6 mol.% CeO_2 achieved at 1100 °C, showing minimal crystalline CeO_2 present due to recrystallisation upon reaching the solubility limit within an Al rich second glass phase. This waste loading was achieved at this temperature with the use of a reducing agent, metallic Fe^0, in the glass, allowing the complete reduction of Ce^{4+} to Ce^{3+} at lower melt temperatures than previously reported, since Ce^{3+} was more readily incorporated into the borosilicate glass structure. The introduction of Fe^0 into the glass showed a short-term improvement in the durability of the wasteform, demonstrated by all elements reaching saturation more rapidly than glass compositions without the presence of Fe^0. However, this increase in durability is postulated to primarily be caused by the introduction of a greater quantity of Ce into the glass matrix, which is known to cause repolymerisation in the glass network.

Acknowledgements

ARM is funded by the Engineering, Physical Sciences Research Council via the Next Generation Nuclear Centre for Doctoral Training (EP/L015390/1). NCH is grateful to the Royal Academy of Engineering and Nuclear Decommissioning Authority for funding. This research utilised the HADES/MIDAS facility at the University of Sheffield established with financial support from EPSRC and BEIS, under grant EP/T011424/1 [186]. With thanks to Dr C. Mann for ICP-OES analyses. This research used BM26A (DUBBLE) [157] and BM28 (XMaS) at the European Synchrotron Radiation Facility. XMaS is a UK national research facility supported by EPSRC. This research used beamline 6-BM of the National Synchrotron Light Source II, a U.S. Department of Energy (DOE) Office of Science User Facility Operated for the DOE office of Science by Brookhaven National Laboratory under Contract No. DE-SC0012704. We are grateful to all the beamline team staff for their support.

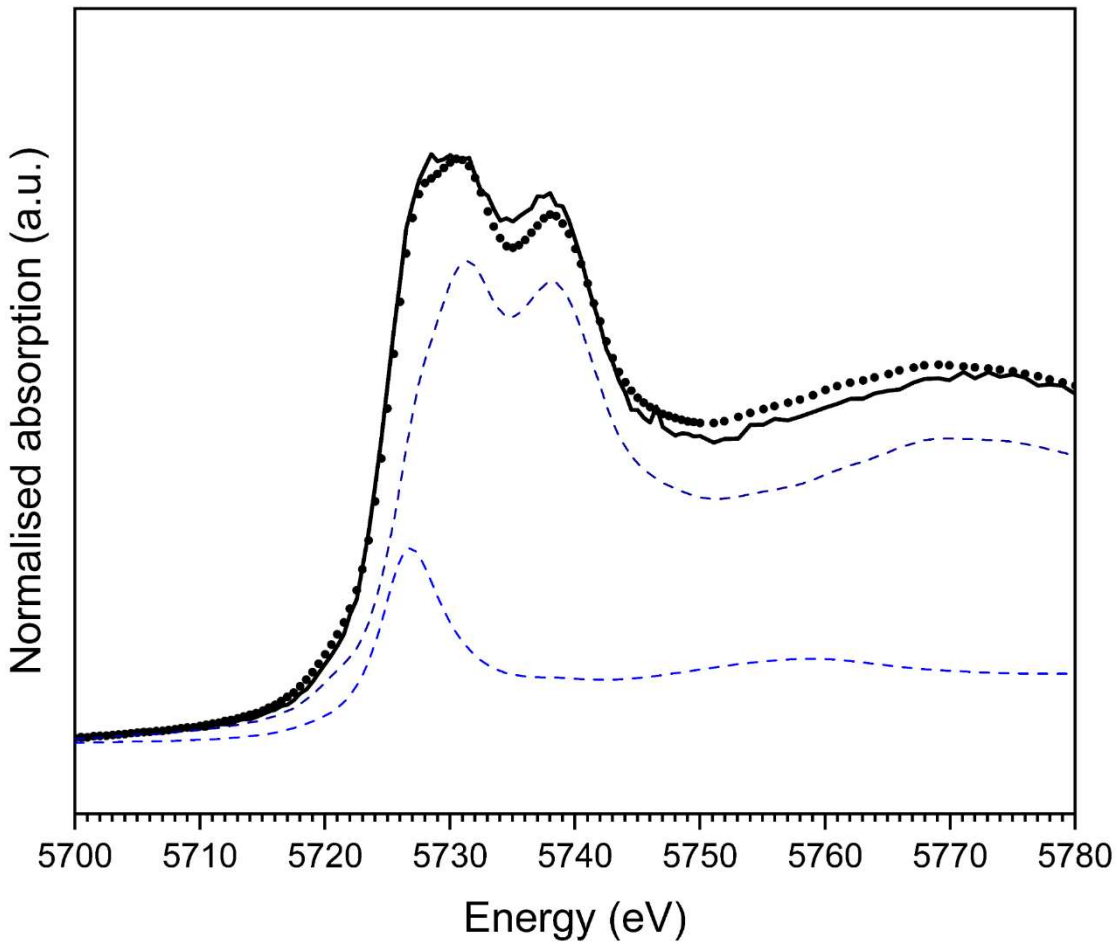

Supplementary Figure 4-1 - Example of fitting of Ce L_3-edge XANES pre-edge region of 1100 °C 5.6 mol.% CeO_2 glass measured in fluorescence mode. The dotted line shows the data with the bold solid line showing the fit. Dashed lines represent the Ce reference standards (light blue = $CePO_4$, dark blue = CeO_2).

5 Hot isostatic pressing of alkali tin silicate glass as a wasteform for the immobilisation of the UK plutonium stockpile

Amber R. Mason, Martin C. Stennett, Claire L. Corkhill, Neil C. Hyatt*

Immobilisation Science Laboratory, Department of Materials Science and Engineering, University of Sheffield, Sir Robert Hadfield Building, Sheffield S1 3JD, UK

To whom correspondence should be addressed. Email n.c.hyatt@sheffield.ac.uk, phone +44 (0) 114 222 5470

Abstract

The potential application of hot isostatic pressing (HIPing) to the immobilisation of the UK PuO_2 stockpile using vitrification was investigated in this work. ATS glasses were produced in stainless steel (SS) HIP canisters, targeting a 5.6 mol.% CeO_2 waste loading, where CeO_2 was used as a surrogate for PuO_2. The effect of HIPing, and addition of Fe^0, on CeO_2 solubility in the glass was investigated, along with the chemical durability of these glasses, compared to other ATS glass formulations. When HIPed at 1100 °C, CeO_2 was not fully incorporated into the glass, despite being fully reduced upon the addition of Fe^0. However, when HIPed at 1250 °C, Ce was fully incorporated into the glass and fully reduced to Ce^{3+} irrespective of the quantity of Fe^0 added. SEM/EDX and structural analysis of Fe in the glass using ^{57}Fe Mössbauer spectroscopy found that interaction between the glass wasteform and the SS canister walls induced the retention of Fe metal and the formation of Fe-Cr spinel phase in the glass at when HIPed at 1250 °C. These crystalline phases were found not to be detrimental to the short term chemical durability of the wasteform in static dissolution experiments (in deionised water, at 90 ± 2 °C, surface area/volume ratio = 1200 m^{-1}, up to 28 d).

Key words: Hot isostatic pressing, ATS glass, cerium, plutonium stockpile, immobilisation, glass dissolution, wasteform durability.

5.1 Introduction

Upon cessation of civil nuclear fuel reprocessing in the UK, there will be a total of 140 tHM of separated PuO_2 stored as a zero value asset at the Sellafield site [11]. The fabrication of mixed oxide ($(U,Pu)O_2$, MOX) fuel is the current chosen end state for this material by the UK government, however, the lack MOX fuel uptake in the UK nuclear fuel cycle at present suggests this approach may not be deliverable [145]. A small fraction of the stockpile (approximately 5 mT) is contaminated due to Am-241 ingrowth or Cl derived from radiation damage of PVC storage containment [14]. This material is therefore unsuitable for recycle as MOX fuel and so must be immobilised for disposal. Immobilisation and subsequent disposal is the only alternative and credible disposition route, in the event that recycling of this stockpile cannot be delivered. The proliferation resistance of this material is also of public concern, therefore there is increasing pressure for the UK government to progress towards a management end point, which should be based on evidenced technology maturity and value for money of both reuse and immobilisation technologies [14].

When considering the immobilisation of high activity nuclear wastes, vitrification is the current disposition route for high level waste (HLW) in the UK, using an optimised borosilicate glass composition, known as MW (Mixed Windscale) glass (Table 5-1). This technology has reached maturity for nuclear waste immobilisation and could therefore be a suitable choice for PuO_2 immobilisation. However, compositions appropriate for HLW, such as the MW glass, have low solubility limits for actinides such as Pu [187]. Investigations of promising glass compositions for PuO_2 immobilisation include: silicate based glasses (e.g. aluminosilicate, alkali tin silicate (ATS), lanthanum borosilicate (LaBS), lanthanum aluminosilicate (LaAS) and calcium borosilicate [54], [66], [70], [147], [148]) and phosphate based glass (including sodium aluminium phosphate, iron phosphate and lead iron phosphate [45], [149]). Each glass type presents different compromises in the processing temperature, durability, radiation tolerance and aqueous durability, which have been considered in previous research [68], [150], [151]

Table 5-1– Comparison of UK HLW glass composition MW and reported ATS compositions with experimental batched HIPed ATS compositions used in this work. (*N.B 5.6Ce1.00Fe corresponds to 5.6 mol.% CeO_2 with equimolar addition of Fe^0, therefore 5.6Ce0.50Fe corresponds to half of the required equimolar addition of Fe^0).*

Oxide	MW [188]	ATS Bates *et al.* [66]		ATS Harrison *et al.* [153]		ATS 5.6Ce0.00Fe		ATS 5.6Ce0.50Fe		ATS 5.6Ce0.75Fe		ATS 5.6Ce1.00Fe	
	wt.%	wt.%	mol.%	wt.%	mol.%	wt.%	mol.%	wt.%	mol.%	wt.%	mol.%	wt.%	mol.%
SiO_2	60.27	43.48	53.44	46.9	51.91	42.11	49.15	41.22	48.62	40.84	48.42	40.39	48.17
B_2O_3	24.11	5.06	5.37	13.5	12.89	12.10	12.18	11.84	12.05	11.73	12.00	11.60	11.94
Na_2O	10.88	9.60	11.49	10.5	11.32	9.61	10.87	9.40	10.75	9.32	10.71	9.21	10.66
Li_2O	4.75	4.20	10.39	4.7	10.46	4.40	10.34	4.31	10.23	4.27	10.18	4.22	10.13
Al_2O_3	-	6.04	4.37	2.7	1.76	2.42	1.67	2.37	1.65	2.35	1.64	2.33	1.63
CeO_2	-	-	-	-	-	13.65	5.56	13.36	5.5	13.24	5.48	13.09	5.45
Cs_2O	-	0.71	0.19	0.6	0.14	-	-	-	-	-	-	-	-
Fe	-	-	-	-	-	-	-	2.12	0.94	3.02	1.35	4.10	1.84
Gd_2O_3	-	3.35	0.68	3.8	0.70	-	-	-	-	-	-	-	-
K_2O	-	5.42	4.25	5.9	4.16	5.47	4.07	5.35	4.03	5.30	4.01	5.24	3.99
PuO_2	-	12.12	3.24	-	-	-	-	-	-	-	-	-	-
SnO	-	2.35	1.29	3	1.48	2.69	1.25	2.64	1.39	2.61	1.38	2.58	1.37
TiO_2	-	2.12	1.96	2.2	1.83	1.98	1.73	1.93	1.72	1.92	1.71	1.89	1.70
ZrO_2	-	5.56	3.33	6.2	3.35	5.57	3.17	5.45	3.13	5.40	3.12	5.34	3.11

Alkali tin silicate (ATS) glasses were initially developed by Bates *et al.* [66] for the immobilisation of US defence Pu. The composition was modified to increase the waste loading with an increased quantity of alkali elements (Li, Na, K), which charge compensate the non-bridging oxygens on tetravalent elements, such as Pu, in the structure of the glass [67]. Sn (in addition to other tetravalent elements, e.g. Zr and Ti) were added to the glass composition to counter for the reduced chemical durability resulting from increased alkali concentration [57]. When synthesising these glasses doped with Pu, Bates *et al*. observed that PuO_2 was not fully incorporated in the ATS glass melt, with the dissolved Pu content of the glass phase estimated to be 7.2 ± 0.3 wt.% Pu [66], which is equivalent to 2.2 mol.% PuO_2 within the glass phase (the undissolved fraction was present as crystalline PuO_2). PCT-B dissolution testing performed on a 1.39 mol.% Pu waste loaded ATS glass by Chamberlain *et al.* [67], demonstrated relatively low normalised mass loss values for this composition (NL_B = 0.48 g m^{-2} and NL_{Si} = 0.26 g m^{-2} after 28 d), which were in the same order of magnitude as a MW UK HLW glass modified to target PuO_2 immobilisation (NL_B = 0.65 g m^{-2} and NL_{Si} = 0.30 g m^{-2} after 28 d [153]).

Preliminary assessments of the potential of a variety of glass compositions deemed to suitable for PuO_2 immobilisation were completed, and included ATS glasses [68]–[70], [153]. In these studies, tetravalent HfO_2 was used as a surrogate for PuO_2, with the motivation that Pu is a stable tetravalent element in borosilicate glass, and hence Hf would best represent Pu redox behaviour, despite Hf having a smaller ionic radius [141]. For these experiments with ATS glass, a 5.2 mol.% HfO_2 incorporation was achieved at a melt temperature of 1300 °C, whilst PCT-B durability testing PCT-B revealed relatively low normalised mass loss (NL_B = 0.43 g m^{-2} and NL_{Si} = 0.25 g m^{-2} at 28 d) [153], in agreement with previous literature for ATS glasses [67]. Further work on ATS glasses was completed by the current authors, producing ATS glasses with a waste loading of 5.6 mol.% CeO_2 at 1100 °C; PCT-B durability tests showed a material of comparable durability to those mentioned above (NL_B = 0.38 ± 0.01 g m^{-2} and NL_{Si} = 0.17 ± 0.01 g m^{-2} at 28 d). CeO_2 was used as an

inactive surrogate for PuO_2 to avoid the hazard and cost of working with Pu, as is common practice in wasteform design, formulation and development research. Although Ce cannot fully emulate the behaviour of Pu, the similar ionic radius and availability of Ce^{3+}/Ce^{4+} oxidation states, albeit with different redox potential, enable useful and more comprehensive investigation of the relevant wasteform phase diagram and materials properties [140], [141].

The tetravalent oxidation state of actinides and lanthanides is known to be less soluble in borosilicate glass compositions, compared to the trivalent oxidation state [147]. This is due to competition with other tetravalent network forming elements to bond with oxygen in the glass network, where in the trivalent oxidation state, lanthanide and actinide cations can more readily bond with oxygen anions and incorporate into the glass network [7]. This effect can be explained with the Dietzel field strength, F, of a cation at a particular valence, Z, which is dependent on the ratio Z/d^2, where d is the cation oxygen bond distance (Å) [154]. Network forming elements, for example Si and B, generally have higher field strength values ($F > 1.3$) due to their typically high valence, but the opposite is true for network modifiers, such as the alkali elements (Li, Na and K) where $F < 0.4$ [63]. Using the Dietzel field strength, it is clear that trivalent actinide and lanthanide elements have a lower field strength than their tetravalent counterparts and therefore act as network modifiers in the glass structure, whereas the tetravalent species, have a higher field strength and therefore behave closer to a network forming element [155]. The oxidation state of Pu and surrogates such as Ce is an important consideration in optimising the incorporation and subsequent immobilisation of these elements. Cachia *et al.* [54] successfully demonstrated a doubling of the Pu waste loading from 0.45 mol.% to 0.9 mol.% in alkali borosilicate glass. This was achieved by reduction of Pu^{4+} to Pu^{3+} with either the inclusion of a reducing agent (e.g. aluminium nitride) or increasing the process temperature (from 1200 °C to 1400 °C) to effect auto-reduction [54]. This study revealed that the inclusion of a reducing agent was the most effective method for facilitating the reduction of Pu^{4+} to Pu^{3+}.

Thermal treatment using hot isostatic pressing (HIPing), which involves applying simultaneous heat and pressure to a hermetically sealed canister, offers several advantages over conventional vitrification methods. This is particularly true for the immobilisation of Pu, where the batch-to-batch processing allows for full accountancy of the waste material inventory and the process parameters can also be adjusted for changes in feedstock and criticality concerns. HIPing also minimises the production of secondary wastes and can help to reduce to overall volume of the waste packages *via* consolidation. HIPing is an immobilisation technology that is currently applied more widely to ceramic materials [53], [127], [189]–[191], however the advantages listed above also make it a suitable technology to investigate for the vitreous immobilisation of the PuO_2 stockpile.

In this study, a suite of ATS glasses were developed using hot isostatic pressing as the chosen thermal treatment method, with the formulations shown in Table 5-1, which also compared the formulations of Bates *et al.* and Harrison *et al.* [66], [69]. This work builds on previous investigation into the immobilisation of the PuO_2 stockpile using ATS glasses by the current authors using conventional glass melting techniques [192], with CeO_2 as inactive surrogate for PuO_2. The formulations in Table 5-1 targeted CeO_2 incorporation at 5.6 mol.% (13.7 wt.%), to enable direct comparison with the chemical durability of PuO_2 in ATS glasses reported by Bates *et al.,* as well as comparison to the formulations fabricated previously by the current authors by conventional melting [192]. Additionally, metallic Fe^0 was added to the glass composition, equivalent to one third of the Ce concentration (i.e. 1.9 mol.%), to effect complete reduction of Ce^{4+} to Ce^{3+} according to the redox reaction: $3\ CeO_2 + Fe = 1.5\ Ce_2O_3 + 0.5\ Fe_2O_3$, which has been proven to improve the CeO_2 incorporation rate within ATS glasses [192]. A range of Fe^0 concentrations was investigated to account for the potential effect of the SS canister on the redox environment within the canister; these were: equimolar addition (5.6Ce1.00Fe), 75% equimolar addition (5.6Ce0.75Fe) and 50% equimolar addition (5.6Ce0.5Fe). The effect of HIPing on the chemical durability of these formulations was also investigated to provide a preliminary

understanding of the dissolution behaviour of ATS glasses using a modified PCT-B methodology, in order to underpin the safety case required for the application of these materials in a geological disposal environment.

5.2 Experimental

5.2.1 Glass material processing

To produce an ATS glass frit, a 200 g batch was weighed using a 4 d.p. balance, with compositions shown in Table 5-1 (excluding Fe and CeO_2), using high purity (> 99.9 %) reagents: $Al(OH)_3$, H_3BO_3, K_2CO_3, Li_2CO_3, Na_2CO_3, SiO_2, SnO, TiO_2, ZrO_2. All precursors were mixed well before placing into an alumina crucible. The crucible was placed into a muffle furnace at 1200 °C in air and held for 2 h. The melt was poured onto a SS mesh in a bucket filled with cold water to produce a granular frit. The frit was dried overnight at 90 °C and then milled using a Fritch 23 planetary mill, then sieved using a SS mesh 150 µm. The frit was well mixed with the appropriate quantity of waste surrogate (CeO_2) and Fe fillings according to the ratio in Table 5-1. It should be noted that this process is simple two-step process of generating a frit and combining with the waste material, in comparison to the milling and calcining pre-treatment steps required for the processing of ceramics when HIPing.

5.2.2 Hot isostatic pressing (HIPing)

The glass frit and waste surrogate mixture were heated to 600 °C in a muffle furnace overnight. The dried batch was packed and sealed into a 30 mL SS canister, with a further in-canister bake out under vacuum at 600 °C to minimise volatile production in the HIP canister; this methodology was applied as described in Thornber *et al.* [52]. The cans were placed into an overpack and HIPed using the AIP-630H facility at The University of Sheffield. Ar gas was using as the pressurising medium and applied to a maximum of 20 MPa for all canisters. The temperature was increased at a rate of 10 °C min^{-1} to a maximum of either 1100 °C or 1250 °C, where it was held for 4 h. Post HIPing, canisters were sectioned using a Buehler Abrasimet 250 to remove the SS canister from the glass wasteform.

5.2.3 Materials characterisation

5.2.3.1 X-ray diffraction (XRD)

A sample representative of each glass type was crushed into a fine powder using a Fritsch Pulverisette 23 micro mill and analysed using powder XRD. Diffraction patterns were collected using a Bruker D2 Phaser diffractometer with LynxEye detector with the following parameters: Ni filtered Cu Kα radiation (λ = 1.5418 Å), 10 mA current, 30 kV voltage. Data was collected between 10° < 2θ < 70° with a step size of 0.02° 2θ and count time of 9.45 s per step. Due to the presence of Fe in each of the glasses, the detector was windowed to reject Fe fluorescence due to the use of Cu radiation. The ICDD PDF-4+ library was used for phase analysis.

5.2.3.2 Scanning electron microscopy with energy dispersive X-ray spectroscopy (SEM/EDX)

Specimens of each glass and a section of SS canister wall from each canister were mounted in epoxy resin, cured overnight and polished to 1 µm diamond finish. All mounted specimens were carbon coated and painted with conductive silver paint to reduce charge build up. Back scattered electron (BSE) micrographs were collected using the Hitachi TM3030 with Bruker Quantax EDX with an accelerating voltage of 15 kV and a working distance of 7.7 mm. EDX mapping was processed using the Bruker Quantax 70 software with maps collected for a minimum of 20 min.

5.2.3.3 X-ray absorption spectroscopy (XAS)

The Ce oxidation state in each glass was determined from analysis of X-ray absorption spectroscopy (XAS) data at the Ce L_3-edge (5723.0 eV). Measurements were conducted at the National Synchrotron Light Source II (NSLS-II) at Brookhaven National Laboratory (Upton, New York) on beamline 6-BM. NSLS-II operates at 3 GeV storage ring with a 400 mA current and 6-BM utilises a 3-pole wiggler to deliver X-rays in the energy range between 4.5 and 23 keV. The optical arrangement consists of a parabolic collimating mirror, a Si(111) monochromator, a toroidal focusing mirror, and a harmonic rejection mirror. For this study, an unfocussed beam was used, with the beam size

limited to 0.5 mm in the vertical and 6 mm in the horizontal using slits. An ionisation chamber was used to measure the incident X-ray energy and the fluorescence signal was collected using a SII Vortex ME4 (4-element) Si drift detector. To optimise collection efficiency, the samples were mounted at 45° to both the incident X-ray beam and the vortex detector. The fluorescence signal was dead-time corrected as previously described in Woicik *et al.* [160]. Spectra were recorded between 5533 and 5965 eV with energy steps of 10 eV (5533 – 5693), 2 eV (5693 – 5713), 0.3 eV (5713 – 5783) and 0.05k (5783 – 5965). An accumulation time of 0.5 s $step^{-1}$ was used for the first three regions and 0.25k $step^{-1}$ for the final region. Multiple scans were collected for each sample and averaged to improve the signal to noise ratio. To ensure energy reproducibility (± 0.1 eV) a CeO_2 standard was measured simultaneously with each sample; the CeO_2 standard was placed downstream of the sample and the transmitted intensity was measured using an ionisation chamber. Absolute energy calibration was performed by measuring a Cr foil and setting the position of the first inflection point in the derivative spectrum to 5989 eV [193]. The spectra of three reference materials with known oxidation state and coordination number were measured to use as standards; $CePO_4$ (Ce^{3+}, 9-fold), $Ce_2Si_2O_7$ (Ce^{3+}, 7 and 8-fold) and CeO_2 (Ce^{4+}, 8-fold).

Specimens for XAS analysis were prepared by mixing the quantity of material required for 1 absorption length (calculated using the Hephaestus software [136]) with a minimal quantity of polyethylene glycol. The resulting powder was then uniaxially pressed into a 10-13 mm pellet to create a homogeneous pellet without pin holes. Calibration, dead time correction, integration, normalisation, back-ground subtraction of XAS data was achieved using the Athena software package [136] and analysed for average oxidation state using linear combination fitting (LCF).

5.2.3.4 ^{57}Fe Mössbauer spectroscopy

A Wissel MRG-500 spectrometer in transmission mode was used to measure powdered samples with a ^{57}Co/Rh source and a velocity range ± 10 mm s^{-1}.

Samples were calibrated relative to an α-Fe reference standard at room temperature. The Recoil software package was used to deconvolute the data by assigning Lorentzian doublets to represent Fe oxidation states and co-ordination numbers using the Recoil analysis software [138].

5.2.3.5 Compositional analysis

The composition of two glasses was measured by X-ray fluorescence (XRF) spectroscopy prior to dissolution experiments. AMG Analytical Services completed this analysis with powdered specimens, including ICP-OES for measurement of boron and lithium. Powders were pressed into pellets and analysed under vacuum using the Panalytical PW 2404 with a Rh X-ray source. For Li and B compositional analysis, the Thermo Jarrell Ash IRIS Advantage ICP-OES was used, where the powdered glass was completely digested in acid prior to analysis.

5.2.4 Dissolution experiments

Dissolution experiments were performed using a derivative of the ASTM PCT-B methodology [101]. Glass material was crushed using a percussion mortar and sieved to retain the 75 – 150 μm size fraction. The resulting powder was sonicated in isopropanol to remove any fines and dried overnight at 90 ± 2 °C. The clean powder was placed into a 15 mL PFA Teflon vessel with 10 mL of ultra high quality (UHQ, 18 MΩ cm^{-1}) water with a surface area to volume ratio (SA/V) of 1200 m^{-1}. Each experiment was performed in triplicate with duplicate blanks and the sealed vessels were stored in an oven at 90 ± 2 °C until testing at the following time points: 1, 3, 7, 14, 21 and 28 d. At each time point, selected vessels were removed, allowed to cool to room temperature and an 8 mL aliquot removed. After the removal of aliquots, powders were dried at room temperature and analysed using SEM and XRD. The aliquot pH was measured, acidified with 20 μL of ultra pure nitric acid and then analysed for elemental concentration (c_i) using an ICP-OES (ThermoFisher iCAPDuo 6300). The normalised mass loss (NL_i) of elements from the glass was calculated using Equation 5.1, where: NL_i is the normalised mass loss (g m^{-2}),

c_i is the concentration in leachate (mg L^{-1}), $c_{i,b}$ is the concentration in blank (mg L^{-1}), f_i is the fraction of element i in the glass and, SA/V is the surface area to volume ratio (m^{-1}).

$$NL_i = \frac{(c_i - c_{i,b})}{f_i \quad {}^{SA}/_{V}} \tag{5.1}$$

$$NR_i = \frac{NL_i}{t} \tag{5.2}$$

The normalised mass loss rate (NR_i) in g m^{-2} d^{-1} was calculated using Equation 5.2, where *t* is the dissolution time in d. The SA/V was adjusted at each time point to account for the evaporative losses. The surface area was calculated geometrically using the density of the glass, where sample density was determined using a Micromeritics Accupyc 1340 II pycnometer and sample mass was measured to an accuracy of ± 0.0001 g prior to measurement.

5.2.4.1 Geochemical modelling

Geochemical modelling using the elemental composition and pH of leachates was completed using PhreeqC v.3 software [163] with the LLNL database [144] to find the saturation indices of mineral phases from the database. The saturation index (SI) of a phase was calculated in this software using Equation 5.3, where: IAP is the ion activity product for the phase and K_s^0 is the standard solubility constant of the phase.

$$SI = \log\left(\frac{IAP}{K_s^0}\right) \tag{5.3}$$

5.3 Results and discussion

5.3.1 XRD

The powder XRD patterns for each HIPed glass are shown in Figure 5-1, where Fe denotes the addition of Fe^0 to the glass frit in a mole ratio with CeO_2. For all materials, diffuse scattering was observed between 15° < 2θ < 35° which revealed the presence of a largely amorphous material consistent with the formation of a glass.

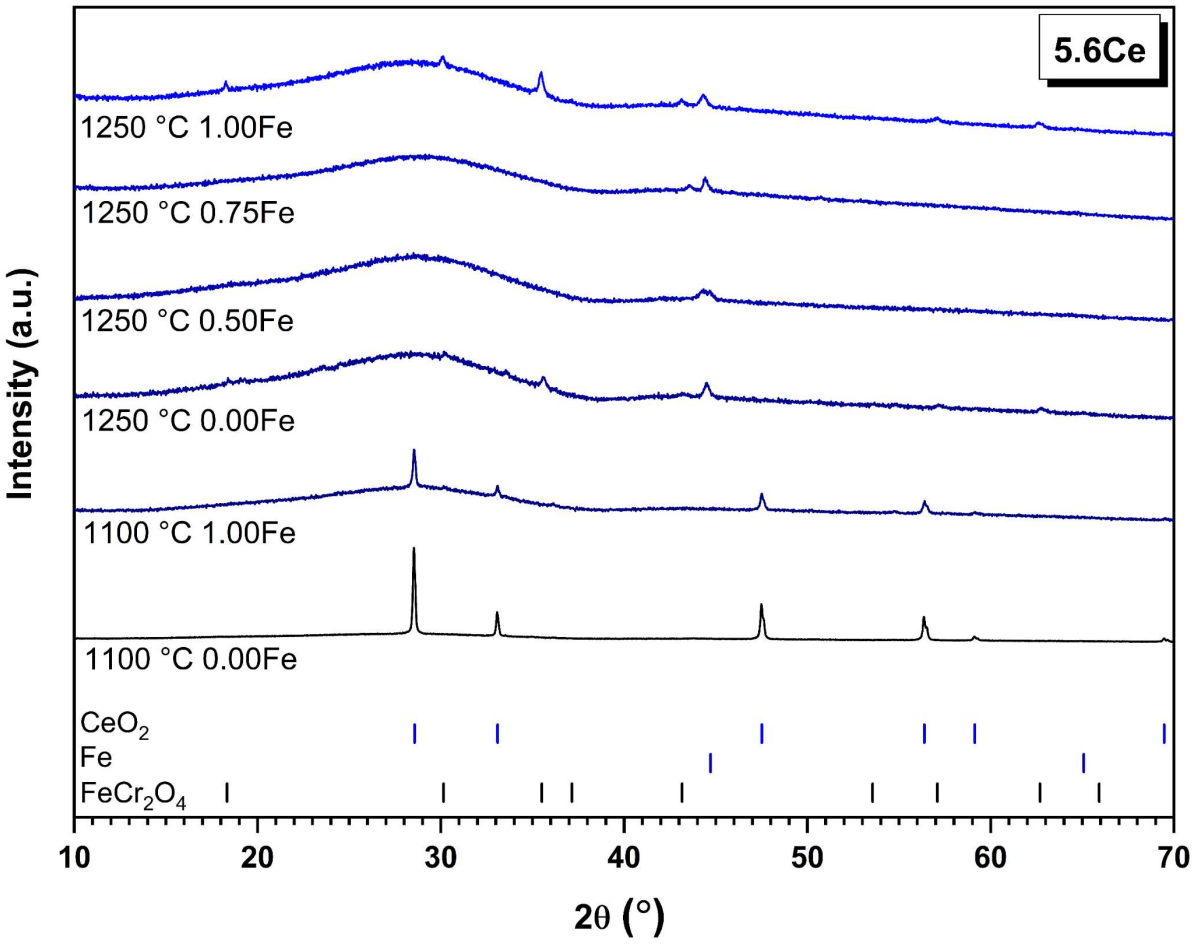

Figure 5-1- XRD patterns of each HIPed (20 MPa, 4 h) glass produced at 1100 or 1250 °C, where 5.6Ce is 5.6 mol.% CeO_2 and (0.00, 0.5, 0.75 and 1.00)Fe is the proportion of equimolar Fe^0 added. Tick marks indicate the Bragg reflections for the corresponding phases: CeO_2 (PDF: 01-081-0792), Fe (PDF: 01-071-3763) and $FeCr_2O_4$ (PDF: 00-060-0690).

Bragg reflections indexed to CeO_2 were apparent in the XRD data of the material HIPed at 1100 °C. These reflections appear reduced in relative intensity, upon the addition of Fe to the glass, suggesting a higher waste incorporation was achieved. In glasses HIPed at 1250 °C, Bragg reflections indexed to Fe metal were observed, including the glass where Fe^0 was not added prior to HIPing. The glasses with additional Fe^0 also exhibit reflections indexed as $FeCr_2O_4$ spinel. These observations confirm that when HIPed at 1250 °C, there was an interaction between the HIP SS canister walls and the glass resulting in Fe and Cr incorporation, generating a crystalline spinel phase within the glass. However, in the glasses HIPed at 1250 °C, CeO_2 was fully incorporated into the glass structure for all formulations studied (0.00Fe, 0.50Fe, 0.75Fe and 1.00Fe).

5.3.2 SEM/EDX

For glasses HIPed 1100 °C, the SEM micrographs in Figure 5-2A and B show the microstructure, displaying a dark grey matrix which corresponds to ATS glass, with bright crystalline regions corresponding to CeO_2. These bright crystalline regions composed of small (< 1 μm) crystals agglomerating into larger 10 - 50 μm regions, as also observed by Cachia *et al.* [54]. This illustrates that CeO_2 has failed to fully incorporate into the glass structure, in agreement with the corresponding XRD patterns (Figure 5-1).

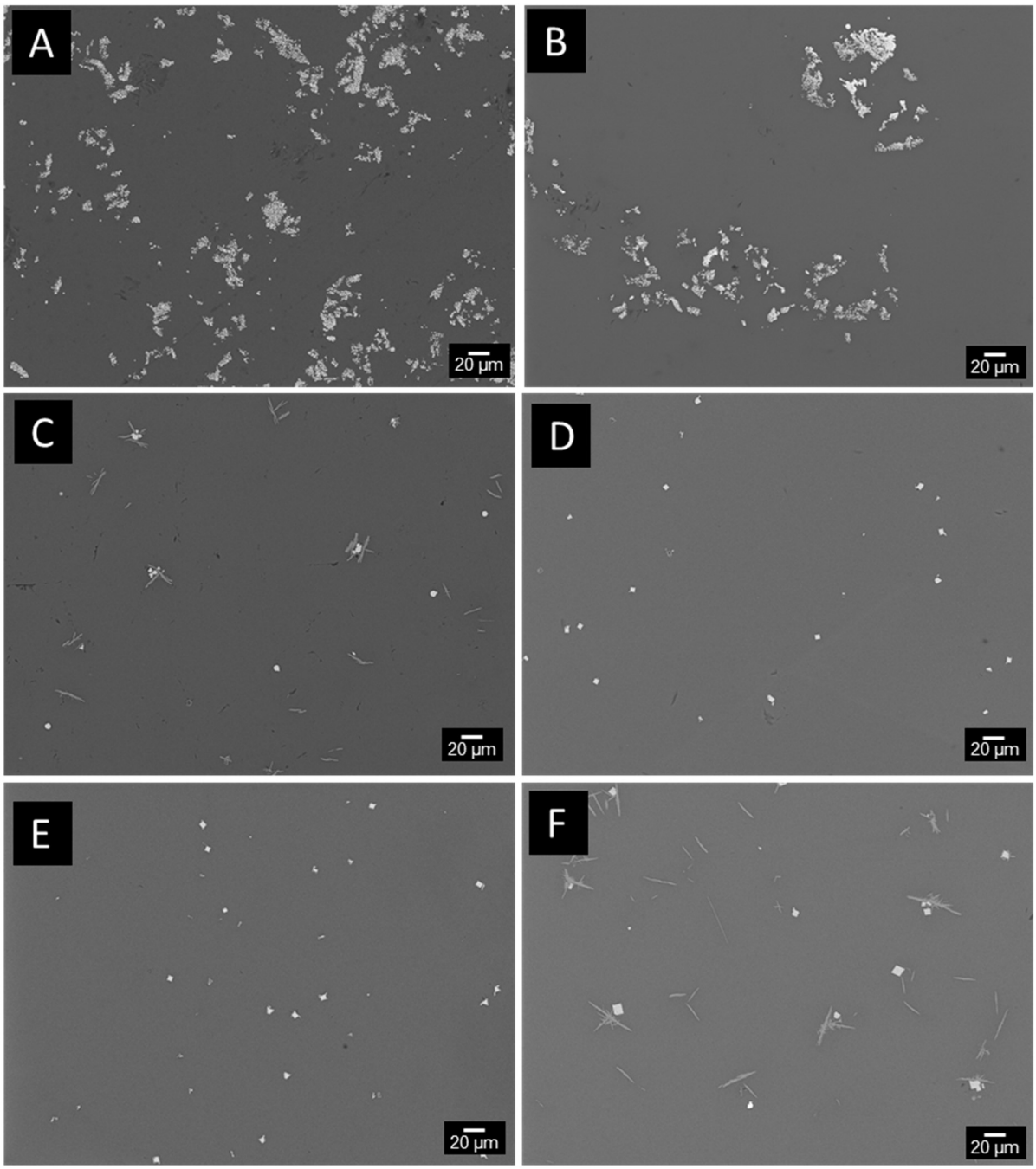

Figure 5-2 – BSE micrographs of each HIPed ATS glass where: A – 1100 °C 5.6Ce, B – 1100 °C 5.6Ce1.00Fe, C - 1250 °C 5.6Ce, D – 1250 °C 5.6Ce0.50Fe, E – 1250 °C 5.6Ce0.75Fe, F – 1250 °C 5.6Ce1.00Fe (5.6Ce is 5.6 mol.% CeO_2 and (0.00, 0.5, 0.75 and 1.00)Fe is the proportion of equimolar Fe^0 added).

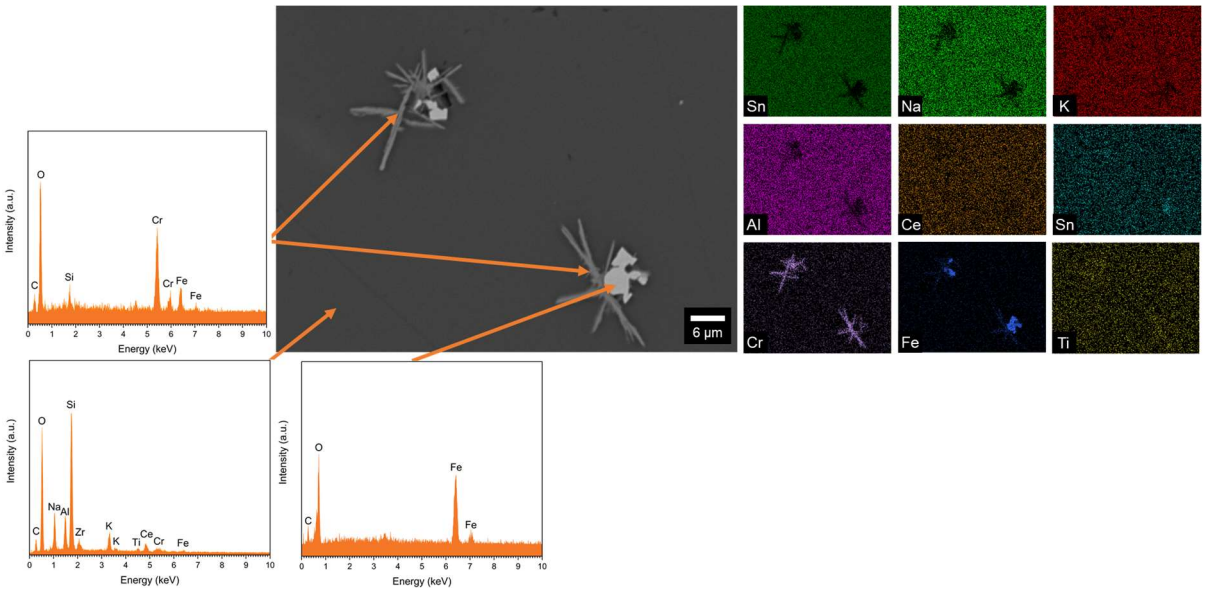

Figure 5-3 – BSE micrograph and EDX maps of the 1250 °C 5.6Ce1.00Fe HIPed ATS glass, showing Fe cubic crystallites and Fe/Cr rich dendritic crystallites, with corresponding EDX spectra for each phase.

For glasses HIPed at 1250 °C, a dark grey bulk of ATS glass was observed with bright cubic Fe metal inclusions of approximately 6 µm diameter in Figure 5-2(C-F) and Figure 5-3. The unincorporated Fe metal was also associated with dendritic Fe/Cr rich crystallites in the 5.6Ce0.00Fe and 5.6Ce1.00Fe compositions. These findings are in agreement with the XRD analysis in Figure 5-1, which identified the formation of $FeCr_2O_4$. These glasses also show no presence of undigested CeO_2, suggesting that Ce has fully incorporated into the glass structure, unlike materials produced at 1100 °C.

The interface between the SS HIP canister and the 5.6Ce1.00Fe composition produced at 1250 °C, is shown in the BSE micrograph with associated EDX maps in Figure 5-4. There is evidence in Figure 5-4 that interaction occurred between the SS and the glass, resulting in the canister wall to become enriched in Sn, K and Ni, and depleted in Fe. This interaction between the canister wall and the glass showed two correlated interaction regions, labelled as primary and secondary in Figure 5-4, with the primary interaction region being brighter in contrast than the SS canister. The primary interaction region showed almost complete depletion in Fe, with enrichment of Sn and a small

increase in concentration of K relative to the unreacted SS can. The secondary interaction region was concentric to the primary interaction region, with bright spots on a dark grey SS matrix. EDX maps of this region displayed less enrichment of Sn and no depletion of Fe and was observed to a maximum depth of 60 µm.

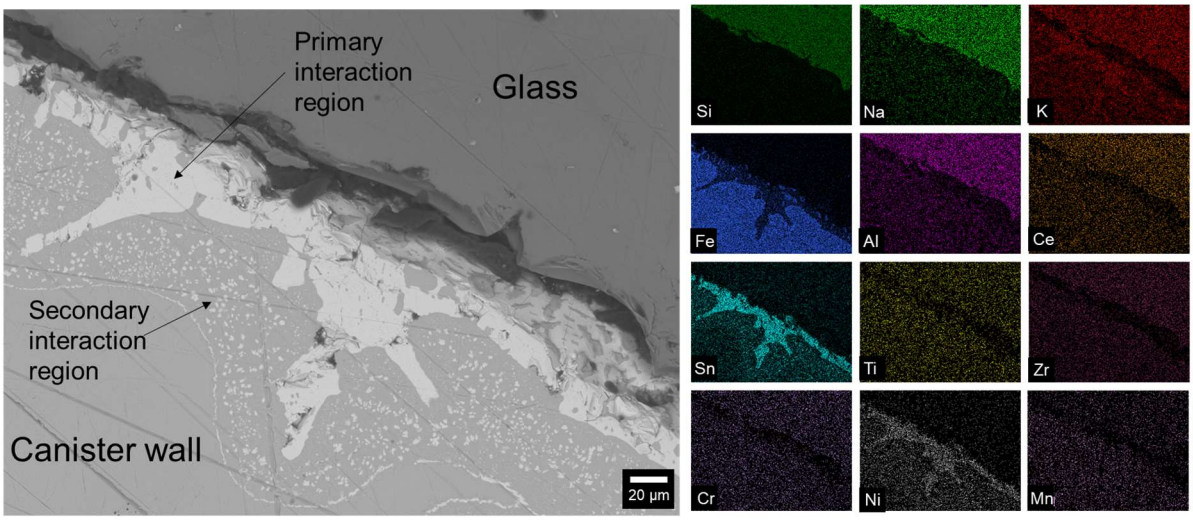

Figure 5-4– BSE micrograph and EDX maps of ATS HIP 1250 °C 5.6Ce1.00Fe glass at the boundary between the SS HIP canister and the glass melt.

Overall, the SEM observations in Figure 5-2 - Figure 5-4 were consistent with the XRD patterns indexed in Figure 5-1. The presence of Fe metal in all samples HIPed at 1250 °C was observed, with the increase in Fe metal causing an increase in spinel phase formed, due to saturation of Fe in the glass; however, this is challenging to fully quantify due to the diffuse scattering from the amorphous phase in XRD data. Supplementary Figure 2 presents an SEM micrograph of the 5.6Ce0.50Fe composition HIPed at 1250 °C, showing a cubic Fe metal inclusion alongside a region where Fe metal was removed during sampling polishing. The associated EDX maps provide evidence of the presence of Cr surrounding the Fe metal crystallite, despite the lack of observed formation of $FeCr_2O_4$ in this glass from Figure 5-2.

5.3.3 Ce L_3 XANES analysis

XANES spectra collected at the Ce L_3-edge on all HIPed ATS glasses are shown in Figure 5-5, along with three reference spectra: CeO_2 (Ce^{4+}, 8-fold), $Ce_2Si_2O_7$ (Ce^{3+}, 7- and 8-fold) and $CePO_4$ (Ce^{3+}, 9-fold). The Ce L_3-edge XANES of $CePO_4$ and $Ce_2Si_2O_7$ both present a single intense feature on the rising absorption edge, whereas CeO_2 presents three features of lower relative intensity, which have been described in previous work [164], [165]. The sample spectra were analysed using linear combination fitting (LCF) to estimate the ratio of Ce^{3+}/Ce^{4+} in each glass using the reference spectra (Table 5-2). Spectra were fitted over the range 5710 – 5760 eV, under the constraint that the fractional weights of the reference spectra sum to unity (100%).

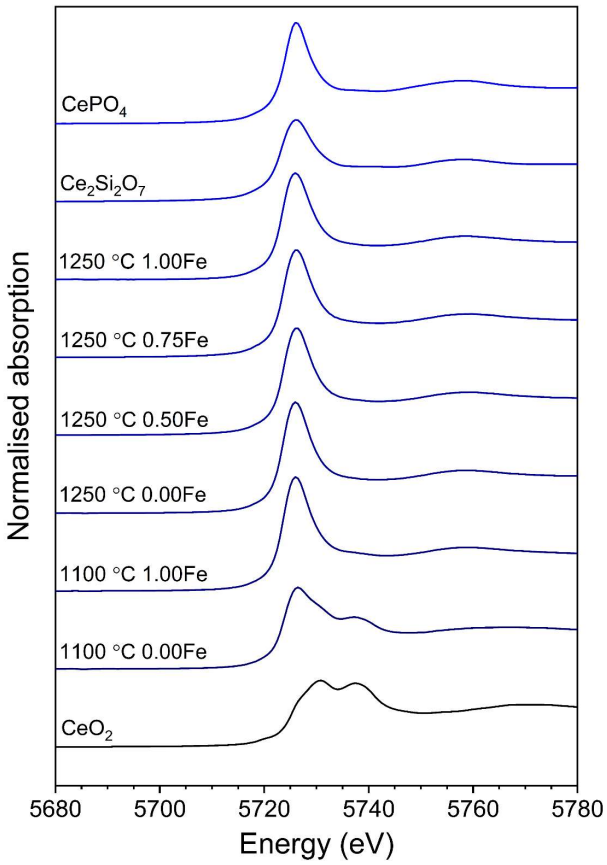

Figure 5-5 – Ce L_3-edge XANES spectra of all HIPed ATS glasses synthesised at 1100 °C and 1250 °C and doped with 5.6 mol% CeO_2, compared with $CePO_4$ (Ce^{3+}), $Ce_2Si_2O_7$ (Ce^{3+}) and CeO_2 (Ce^{4+}) standards (where 5.6Ce is 5.6 mol.% CeO_2 and (0.00, 0.5, 0.75 and 1.00)Fe is the proportion of equimolar Fe^0 added).

Table 5-2– Results of linear combination fitting of Ce L_3-edge XANES spectra of all HIPed ATS glasses in Figure 5, errors are reported in parentheses (where 5.6Ce is 5.6 mol.% CeO_2 and (0.00, 0.5, 0.75 and 1.00)Fe is the proportion of equimolar Fe^0 added).

Composition	Ce speciation			ΣCe^{3+}	R
	$Ce^{(3+)}PO_4$	$Ce_2^{(3+)}Si_2O_7$	$Ce^{(4+)}O_2$	(%)	factor
1100 °C 5.6Ce0.00Fe	55(3)	0(3)	44(1)	55(3)	0.006
1100 °C 5.6Ce1.00Fe	89(1)	11(1)	0	100	0.010
1250 °C 5.6Ce0.00Fe	93(1)	7(1)	0	100	0.010
1250 °C 5.6Ce0.50Fe	91(1)	9(1)	0	100	0.010
1250 °C 5.6Ce0.75Fe	89(3)	11(3)	0	100	0.005
1250 °C 5.6Ce1.00Fe	78(3)	21(3)	0	100	0.005

The XANES spectra and LCF fits demonstrate that Ce was completely reduced to Ce^{3+} in all glasses, with the exception of the 5.6Ce0.00Fe composition HIPed at 1100 °C, where 44 ± 1 % remained as Ce^{4+}. This contribution of Ce^{4+} is expected to originate from the undigested CeO_2 observed in this glass. For the 5.6Ce1.00Fe composition HIPed at 1100 °C, Ce^{4+} was successfully reduced to Ce^{3+} caused by the addition of Fe^0, however upon inspection of Figure 5-1 (XRD) and Figure 5-2B (SEM), there was evidence of unincorporated CeO_2 within the glass matrix. This suggests that the reduction of Ce^{4+} to Ce^{3+} was not sufficient to support full incorporation of Ce into the glass at 1100 °C, and that it is likely that the Ce solubility limit for ATS glass was exceeded at this temperature.

In glasses HIPed at 1250 °C, all Ce was reduced to Ce^{3+}, irrespective of an addition of Fe^0 to the glass. There are several factors that could be contributing to the reduction of Ce and effecting the overall redox environment in the can, including: the inert atmosphere inside the HIP can, interactions with the SS can wall, the temperature of the melt and the addition of Fe^0 to the melt.

5.3.4 ^{57}Fe Mössbauer analysis

The oxidation state and coordination environment of Fe in the HIPed ATS glass network was investigated using ^{57}Fe Mössbauer spectroscopy to verify the Fe contributions from XRD/SEM analysis. ^{57}Fe Mössbauer spectroscopy provides detailed information about the oxidation state and coordination number of the separate Fe sites within the glass. The ^{57}Fe Mössbauer spectra for all HIPed Fe-containing ATS glasses are shown in Figure 5-6 along with the fitted contribution to the spectral envelope. For each glass, two quadrupolar doublet sites were fitted with values for the isomer shift, quadrupolar shift and full width half maximum of each doublets reported in Table 5-3. Each doublet represents a distinctive chemical environment for Fe present in the glass, which suggests there are two such Fe environments within the glass structure, referred to as site A and site B. For the 1250 °C glasses, a third distinctive environment (site C), in the form of a sextet, was also fitted to the spectral envelope, indicating the presence of Fe within an additional magnetic phase. The values for the parameters of each site are shown in Table 5-3, along with the ratio of each site in each material. The values associated with the fitting of Mössbauer spectra are well defined, particularly the isomer shift, which is sensitive to the Fe coordination number and oxidation state. Quadrupolar shift is also indicative of the oxidation state with ferrous ions having a larger quadrupolar splitting than ferric ions, however due to the large range of possible environments in an amorphous environment, these results must be carefully interpreted

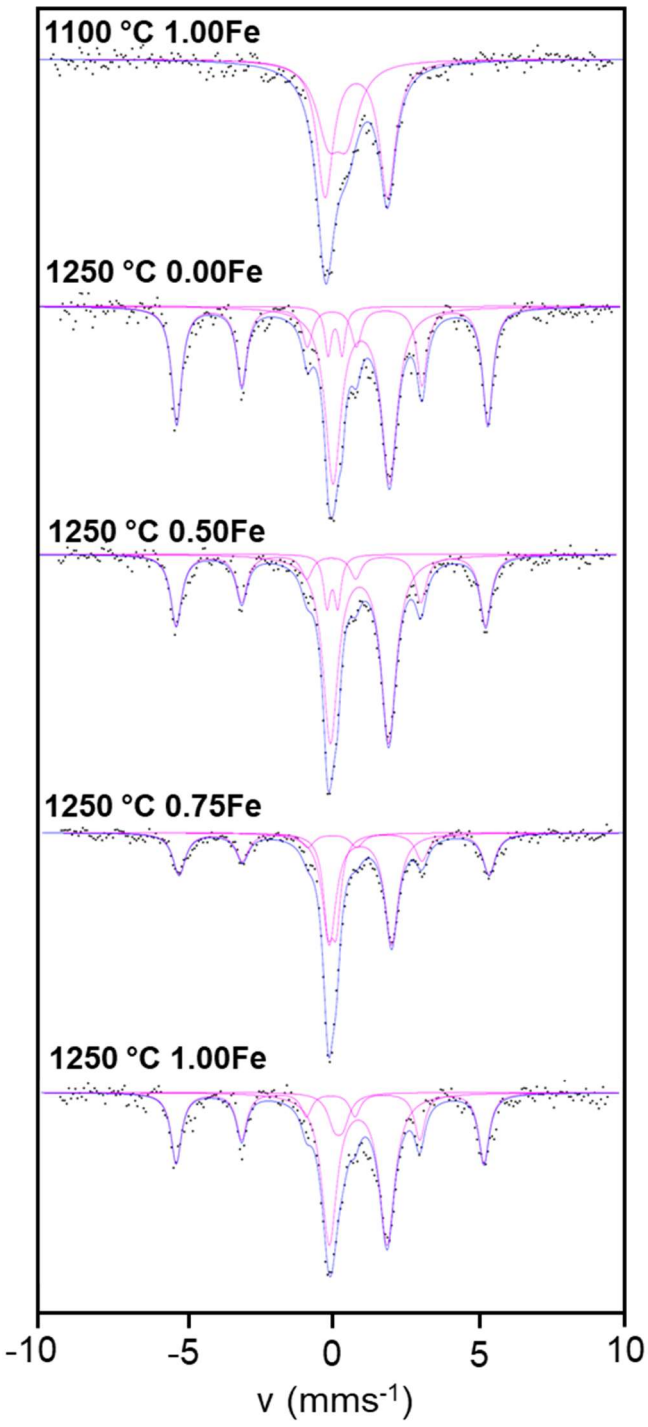

Figure 5-6– Room temperature ^{57}Fe Mössbauer spectra of all Fe-containing HIPed ATS glasses. Pink line - fitted doublet; blue line - data fit; black dots – data (where 5.6Ce is 5.6 mol.% CeO_2 and (0.00, 0.5, 0.75 and 1.00)Fe is the proportion of equimolar Fe^0 added).

.

Table 5-3 – ^{57}Fe Mössbauer parameters from the spectra in Figure 5-6 for site A, B and C for all Fe-containing HIPed ATS glasses where: δ – isomer shift (mm s^{-1}), Δ – quadrupolar shift (mm s^{-1}) and Γ – full width half maximum (mm s^{-1}). Errors in parentheses, 5.6Ce is 5.6 mol.% CeO_2 and (0.00, 0.5, 0.75 and 1.00)Fe is the proportion of equimolar Fe^0 added.

Composition	A Site			B site			C site			Relative site speciation (%)
	δ	Δ	Γ	Δ	Δ	Γ	Δ	Δ	Γ	
	(mm s^{-1})									Fe(A):Fe(B):Fe(C)
1100 °C 1.00Fe	0.35(7)	0.64(2)	0.47(1)	0.98(3)	2.09(6)	0.33(4)	-	-	-	41(6): 59(6): 0
1250 °C 0.00Fe	0.11(3)	0.14(4)	0.13(4)	1.01(1)	1.92(2)	0.32(2)	0.01(1)	0.01(1)	0.21(2)	6(1): 50(2): 44(3)
1250 °C 0.50Fe	0.08(3)	0.37(6)	0.14(4)	1.01(1)	2.00(2)	0.31(2)	0.04(2)	0.01(2)	0.23(3)	7(1): 59(3): 34(4)
1250 °C 0.75Fe	0.01(3)	0.28(5)	0.19(3)	0.97(3)	2.14(5)	0.28(2)	0.03(2)	0.03(2)	0.26(4)	23(2): 45(3): 32(4)
1250 °C 1.00Fe	0.31(1)	0.29(3)	0.28(2)	0.98(3)	1.99(4)	0.32(3)	0.03(2)	0.01(1)	0.22(3)	8(2): 55(3): 36(4)

Using the refined Mössbauer parameters for each site, Table 5-3, in combination with the reference data collated by Dyar *et al*. [170], [171], it was determined that site A may be interpreted as Fe^{3+} in 4-fold coordination and site B interpreted as Fe^{2+} in 6-fold coordination within the glass phase. However, it should be noted that the isomer shift values for Fe^{2+} were at the low end of the boundary for 6-fold coordination [172]. Site C corresponds to a sextet which indicates the presence of magnetic ordering within the glass. When compared to parameters for isomer shift and quadrupolar splitting in the literature [170], this contribution to the Mössbauer spectra was identified to derive from metallic Fe in the glass, in agreement with the SEM/EDX findings. For all glasses, the majority of the Fe was represented by site B, suggesting the majority of the Fe in the glass network was in the Fe^{2+} oxidation state and 6-fold coordinated. The values in Table 5-3 were supported by published data for crystalline materials with well-defined ^{57}Fe Mössbauer spectroscopy parameters [170], [171]. The recoil free fraction was assumed to be unity in these glasses since it has been shown that for silicate glass melts, Mössbauer spectroscopy and wet chemical analysis establish the same Fe oxidation state [174]. The contribution from the chromite spinel phase, Fe^{2+} in 4-fold coordination, was not detected in these spectra, postulated to be due to the low volume fraction of this phase within the glass.

The ^{57}Fe Mössbauer data is in agreement with the XRD and SEM/EDX data acquired, showing the presence of Fe metal within all glasses HIPed at 1250 °C. There are three factors contributing to overall redox environment in the glass with respect to Fe: the inert environment caused by the hermetically sealed HIP canister, the reducing effects of the SS canister wall and the oxidative effect of the Ce redox couple. These have combined to oxidise Fe^{0} to Fe^{2+} with some minor further oxidation to Fe^{3+}, demonstrating that the redox couple with Ce is still the dominant factor, as observed by previous work of the authors [192]. Fe^{0} was added to the glass composition with the sole aim of reducing Ce^{4+} to Ce^{3+} and therefore increasing the waste loading/incorporation of Ce into the glass, however the reducing effect of the stainless steel canister

interaction as well as autoreduction known to occur at these temperatures, Ce reduced without additional Fe^0, as seen in Figure 5-5.

5.3.5 Compositional analysis

The compositions of 5.6Ce0.00Fe and 5.6Ce1.00Fe glasses HIPed at 1250 °C, were measured using a combination of XRF and ICP-OES (for Li and B) in preparation for chemical durability analysis. These compositions were chosen for chemical durability assessment in order to directly compare their durability to those ATS glasses previously determined by the authors [192]. Compositional analysis revealed that both glasses have approximately identical compositions (Table 5-4). The interaction with the can wall, as shown in Figure 5-4, appears to have enriched both glasses with 1 – 1.2 mol.% Cr_2O_3 and approximately 0.1 mol.% Mn_3O_4. This interaction with the can wall has also caused both compositions to become depleted in SnO by approximately 1.2 mol.%. Both compositions were slightly enriched in Al_2O_3 (by 3.2 – 3.5 mol.%), which was due to corrosion of the alumina crucible when producing the glass frit, as previously observed from SEM/EDX and compositional analysis in Mason *et al.* [192].

Table 5-4 – Comparison of batched composition and XRF/ICP-OES results for two HIPed ATS glasses: 1250 °C 5.6Ce0.00Fe and 1250 °C 5.6Ce1.00Fe (where 5.6Ce is 5.6 mol.% CeO_2 and (0.00, 1.00)Fe is the proportion of equimolar Fe^0 added).

Oxide	HIP 1250 °C 5.6Ce0.00Fe		HIP 1250 °C 5.6Ce1.00Fe	
	Batch (mol.%)	ICP/XRF (mol.%) (± 0.1)	Batch (mol.%)	ICP/ XRF (mol.%) (± 0.1)
Al_2O_3	1.67	4.86	1.63	5.12
B_2O_3	12.18	11.75	11.94	11.43
CeO_2	5.56	5.71	5.45	5.46
Fe	0.00	1.68	1.63	2.05
K_2O	4.07	3.26	3.99	3.22
Li_2O	10.34	11.47	10.13	11.22
Na_2O	9.61	9.26	9.21	9.35
SiO_2	49.15	46.26	48.17	46.63
SnO	1.25	0.04	1.37	0.05
TiO_2	1.73	1.62	1.50	1.64
ZrO_2	3.17	2.74	3.11	2.72
Cr_2O_3	0.00	1.22	0.00	1.01
Mn_3O_4	0.00	0.08	0.00	0.07

5.3.6 Dissolution behaviour

PCT-B tests were performed on the 5.6Ce0.00Fe and 5.6Ce1.00Fe compositions HIPed at 1250 °C, using a modified PCT-B methodology in order to make direct comparisons of the durability of counterpart glasses produced by conventional melting. Each test was performed with a SA/V = 1200 m^{-1}, using UHQ water as a leachant at 90 ± 2 °C. The pH and normalised mass loss (NL_i) values for each experiment are reported and compared in Figure 14. The pH for both compositions was similar to other borosilicate glasses under similar dissolution conditions [194], reaching a value of (10.3 - 10.5) ± 0.1 at 1 d, increasing to (10.6 - 11.0) ± 0.1 by 28 d (Figure 5-7).

The normalised elemental mass loss (NL_i) of both compositions showed typical alkali borosilicate glass element dissolution behaviour, with an initial rapid release of elements, after which point the residual rate (steady state

dissolution) was attained [195], [196],[105], [197]. The NL_B, NL_{Li} and NL_{Na} reached a peak at 3 d, after which time the normalized mass loss did not increase significantly, giving values of between 0.15 - 0.75 ± 0.01 g m^{-2} at 28 d. For elements Ce, Fe, Ti and Zr, the normalised mass loss upon reaching the residual rate at 3 d was three orders of magnitude lower than that of B, Li and Na. All elements exhibited a similar trend in normalised mass loss across both compositions, indicative of similar dissolution behaviour, the one exception was Sn, which had a NL_{Sn} that was a factor of 4 greater in the 5.6Ce0.00Fe composition, compared to the 5.6Ce1.00Fe composition.

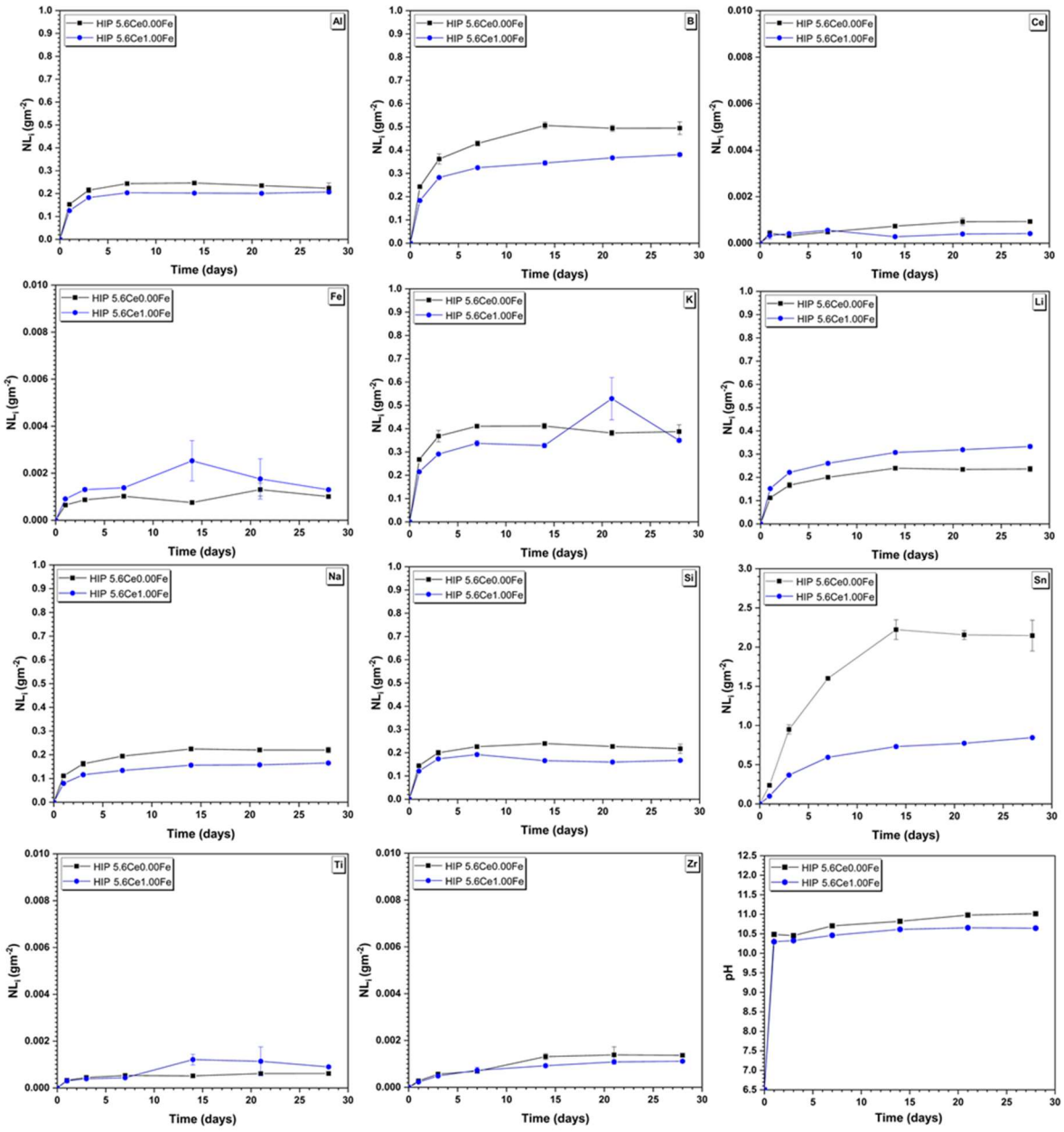

Figure 5-7– Normalised elemental mass loss (NL_i) of Al, B, Ce, Fe, K, Li, Si, Na, Sn, Ti and Zr, alongside the pH for HIPed ATS 1250 °C 5.6Ce0.00Fe and 5.6Ce1.00Fe PCT-B tests (where 5.6Ce is 5.6 mol.% CeO_2 and (0.00 and 1.00)Fe is the proportion of equimolar Fe^0 added). Error bars correspond to the SD of triplicate measurements.

In accordance with the lower elemental release of Ce, Fe, Ti and Zr, the normalised residual dissolution rates (NR_i), quantified by linear regression, for

both compositions revealed that incongruent dissolution occurred (Table 5-5). This was apparent by comparing the B, Li and Na elemental release, which achieved similar NR_i (0.001 - 0.004 g m^{-2} d^{-1}), whereas the rate of dissolution for Al, K and Si were negative (whilst being of the same order of magnitude). In the literature, negative leach rates are typically associated with the formation of secondary phases (such as (alumina)silicate gel and/or precipitates) on the surface of the glass [183]–[185].

Geochemical modelling of the solution chemistry of both glass compositions revealed that at 28 d of the dissolution experiment, magnetite (Fe_3O_4), hematite (Fe_2O_3), goethite (FeO(OH)), as well as nontronite ($(H,K,Na)_{0.33}Fe_2Al_{0.33}Si_{3.67}H_2O_{12}$) were likely to precipitate as a secondary phases. As with the previous work performed on ATS glass by the authors [192], it is suggested that the presence of Fe in a borosilicate glass network can result in the precipitation of these Fe-silicate secondary phases, which have been shown to be detrimental to the long term durability of the glass [183]–[185]. Despite this, it was not possible to detect the formation of such a phase, nor other phases, which is not unsurprising given the short duration of the experiment; extended time scales, of more than 50 d, are typically required for the formation of secondary phases in quantities that are detectable by techniques such as XRD, or observable by SEM.

Table 5-5 – Normalised residual dissolution rate (NR_i calculated from 7 – 28 d) for each PCT-B experiment (where 5.6Ce is 5.6 mol.% CeO_2 and (0.00 and 1.00)Fe is the proportion of equimolar Fe^0 added).

Element	Rate (g m^{-2} d^{-1})	
	5.6Ce0.00Fe	5.6Ce1.00Fe
Al	0	0
B	0.004(2)	0.003(1)
K	0	0
Li	0.0024(8)	0.0012(4)
Na	0.0013(7)	0.0002(7)
Si	0	0

When comparing the two glass compositions, the NL_i and NR_i values were very similar for all elements, with NL_B = 0.49 ± 0.01 g m^{-2} and NL_{Si} = 0.22 ± 0.01 g m^{-2} for the 5.6Ce0.00Fe composition, and NL_B = 0.38 ± 0.01 g m^{-2} and NL_{Si} = 0.17 ± 0.01 g m^{-2} for the 5.6Ce1.00Fe composition after 28 d. This could be due to both glasses having similar final compositions, despite the different batched compositions (Table 5-1), due to the effect of the SS canister interacting with the glass melt during HIPing (Table 5-4). These NL_i values are also comparable to the results obtained from PCT-B tests on the counterpart 5.6Ce1.00Fe composition produced by conventional melting (NL_B = 0.38 g m^{-2} and NL_{Si} = 0.17 g m^{-2} after 28 d) [192], and results from similar durability tests completed on other ATS glasses (NL_B = 0.48 g m^{-2} and NL_{Si} = 0.26 g m^{-2} after 28 d) [67]. The results are also within the same order of magnitude as an MW UK HLW glass modified to target Pu immobilisation (NL_B = 0.65 g m^{-2} and NL_{Si} = 0.30 g m^{-2} after 28 d [153]).The values presented here indicate that ATS glasses, and those processed using HIPing, should perform equally as well as UK HLW glasses for which there is significant technological maturity, hence adding to the safety case for the use of ATS glasses as an immobilisation matrix for the UK PuO_2 stockpile.

5.4 Conclusion

Hot isostatic pressing has been successfully demonstrated as a promising thermal treatment technology for the vitrification of the UK PuO_2 stockpile, with a series of HIPed, 5.6 mol.% CeO_2-doped ATS glasses. CeO_2 was not fully incorporated into the glass at 1100 °C, therefore the melt temperature and the addition of Fe^0 reductant were varied to understand the required conditions for full Ce incorporation. CeO_2 was fully incorporated into glasses HIPed at 1250 °C and fully reduced to Ce^{3+} at all levels of Fe addition, including without the addition of Fe^0. Fe-Cr crystallites formed within the glass at all Fe^0 dopant levels at 1250 °C, caused by glass interactions with the can wall at this increased temperature. SEM confirms that glass-SS interactions had taken place, where Sn and Fe exchanged into and out of the can walls respectively. HIPing has shown to have no detrimental effect on the chemical durability of the glasses produced despite the introduction of crystalline phases from glass

interaction with the can wall. However, a compromise in processing temperature could affect the total incorporation of Ce into the glass network without activating the HIP canister – glass interaction observed in this work. Overall, this work shows considerable promise in development of a simple processing route for plutonium immobilisation, which may find particular application to contaminated residues which pose a challenge to ceramic wasteforms (the glass component providing a flexible immobilisation matrix).

Acknowledgements

ARM is funded by the Engineering, Physical Sciences Research Council via the Next Generation Nuclear Centre for Doctoral Training (EP/L015390/1). NCH is grateful to the Royal Academy of Engineering and Nuclear Decommissioning Authority for funding. This research utilised the HADES/MIDAS facility at the University of Sheffield established with financial support from EPSRC and BEIS, under grant EP/T011424/1 [186]. With thanks to Dr C. Mann for ICP-OES analyses. This research used beamline 6-BM of the National Synchrotron Light Source II, a U.S. Department of Energy (DOE) Office of Science User Facility Operated for the DOE office of Science by Brookhaven National Laboratory under Contract No. DE-SC0012704; the authors are grateful to Dr B. Ravel for experimental assistance.

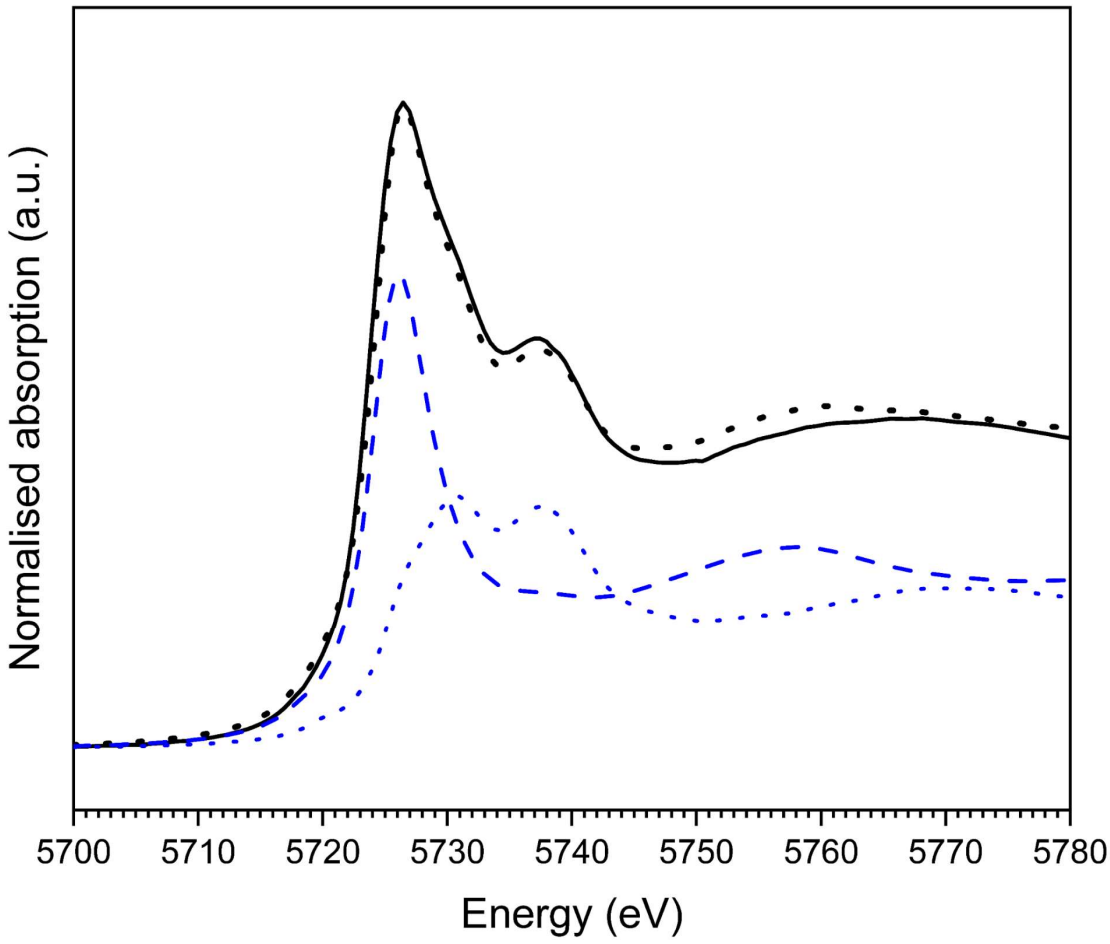

Supplementary Figure 1 - Example of fitting of Ce L_3-edge XANES spectra of HIPed 1100 °C 5.6Ce0.00Fe glass measured in transmission mode (where 5.6Ce is 5.6 mol.% CeO_2 and 0.00Fe is the proportion of equimolar Fe^0 added). The dotted black line shows the data with the bold solid black line showing the fit. Dashed lines represent the Ce reference standards (light blue corresponds to $CePO_4$, dark blue corresponds to CeO_2).

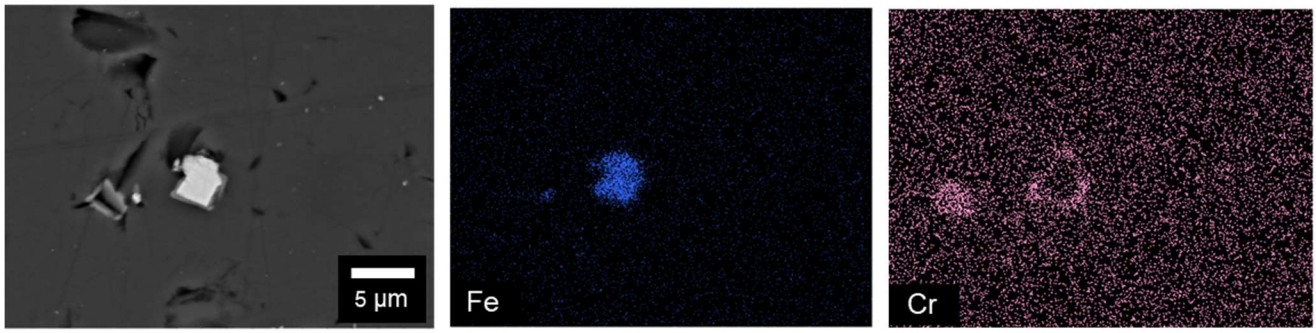

Supplementary Figure 2 – BSE micrograph and corresponding EDX maps of 5.6Ce0.50Fe showing the presence of Cr surrounding a Fe metal crystallite in the glass (where 5.6Ce is 5.6 mol.% CeO_2 and 0.00Fe is the proportion of equimolar Fe^0 added).

6 The effect of charge compensating ions on the phase assemblage and dissolution behaviour of HIPed Ce-doped zirconolite

Amber R. Mason, Colleen Mann, Laura J. Gardner, Lewis R. Blackburn, Martin C. Stennett, Claire L. Corkhill, Neil C. Hyatt*

Immobilisation Science Laboratory, Department of Materials Science and Engineering, University of Sheffield, Sir Robert Hadfield Building, Sheffield S1 3JD

**To whom correspondence should be addressed. Email n.c.hyatt@sheffield.ac.uk, phone +44 (0) 114 222 5470*

Abstract

A matrix of zirconolite wasteforms was developed using hot isostatic pressing as a thermal treatment method, to investigate their potential for the immobilisation of the UK PuO_2 stockpile. CeO_2 was used as a surrogate for PuO_2, targeting 0.2 formula units (f.u.) onto the Ca site and 0.1 f.u. onto both the Ca and Zr site. Appropriate Ti^{4+} site charge compensating ions, Al^{3+}, Mg^{2+} and Fe^{3+}, were selected which balance excess charge when targeting Ce^{4+} on the Ca^{2+} site. The resulting wasteforms were characterised using XRD, SEM/EDX, Ce L_3-edge and Fe K-edge XANES. Favourable phase assemblages resulted from the single site substitution of Ce^{4+} onto the Ca^{2+} site. The reduction of Ce^{4+} to Ce^{3+} resulted in the stabilisation of Ce-bearing perovskite phases in all formulations. Dissolution experiments using the PCT-B protocol, applying aggressive conditions (90 ± 2 °C with 0.01M HNO_3 (pH = 2) leachant at 100 m^{-1}), showed a direct correlation between the quantity of unincorporated CeO_2/perovskite present and the resulting leach rates, with the most homogeneous formulation generating the lowest leach rate ($Ca_{0.8}ZrCe_{0.2}Ti_{1.6}Fe_{0.4}O_7$ with NR_{Ce} = 0.0(11) x 10^{-5} g m^{-2} d^{-1}). This demonstrates that optimisation of the formulation with complete incorporation of the waste into the zirconolite structure, is key to optimising the performance of the wasteform.

Key Words: zirconolite, PuO_2 stockpile, HIPing, chemical durability

6.1 Introduction

In the UK, there is a stockpile of separated PuO_2 derived from nuclear fuel reprocessing, that is set to exceed 140 tHM in 2021, by which time both UK reprocessing plants (Magnox and ThORP) will have ceased operation [11], [13]. The stockpile is classified as a zero value asset and currently situated in an interim storage facility at the Sellafield site. Prior to the cancellation of the Fast Reactor Program in 1994, this material was designated for use in mixed oxide ($(U,Pu)O_2$) (MOX) fuel, however since this time, the fabrication of MOX fuel has become an increasingly unattractive proposition given the current design of UK nuclear reactor fleet. Despite this, the current strategy favoured by UK government is to utilise this material to fabricate MOX fuel for use in a new fleet of light water reactors. A dual track strategy of immobilisation and MOX fabrication has been promoted since a small fraction (~ 5 t) of the stockpile is already unsuitable for recycle as MOX fuel (due to contamination by Cl from PVC packaging degradation or Am-241 ingrowth) [16], [18]. Immobilisation will also provide a passively safe and proliferation resistant alternative solution if recycle in MOX fuel cannot be delivered.

Ceramic matrices, such as zirconolite, are well documented as successful candidates for the immobilisation of actinides, due to their radiation tolerance, chemical durability, high waste loading and proliferation resistance [40], [92]. The existence of natural analogues containing radioactive elements provides vital context for a geological disposal environment, due to retention of actinide elements for millions of years [198]. SYNROC, or synthetic rock, is a multi.phase crystalline material designed at ANSTO (Australian Nuclear Science and Technology Organisation) for the immobilisation of high level waste (HLW), where zirconolite is assigned as the main actinide bearing host phase [199], [200]. Zirconolite, with the general formula ABC_2O_7 and prototypically $CaZr_xTi_{3-x}O_7$ where $0.8 < x < 1.35$, exhibits several polytypes (2M, 3O, 3T, 4M and 6T), with 2M being the most commonly observed [80], [82], [94], [201]. The crystal structure of zirconolite 2M consists of a hexagonal tungsten bronze layer composed of corner sharing TiO_6 and TiO_5 polyhedra

(with the Ti (5-fold) site being 50% occupied), alternating with a layer of CaO_8 and ZrO_7 polyhedra. The zirconolite polytype which crystallises is determined by the stacking sequence of these layers and results primarily from changes in the cation site occupancy and vacancy distribution [85], however, oxygen fugacity and processing temperature are also contributing factors [86]. Zirconolite 4M is described by layers of zirconolite 2M alternating with pyrochlore structural units, which accommodates greater incorporation of actinide/lanthanide cations into the structure [87], and typically occurs as a result of the substitution of cations with large ionic radius onto the B site (e.g. substitution of Pu^{4+} (r = 0.91 Å) onto Zr^{4+} site (r = 0.78 Å) [88]) [89]. Due to the chemical flexibility of the zirconolite structure, Pu^{4+} immobilisation can be achieved by targeting substitution onto both the A (Ca^{2+}) site and the B (Zr^{4+}) site. Pu^{4+} is able to reside directly on the B (Zr^{4+}) site due to having equivalent oxidation state, however, to substitute onto the A site (Ca^{2+}), charge balancing species are required on the C site (Ti^{4+}). This is typically achieved with the incorporation of divalent or trivalent cations such as; Mg^{2+}, Al^{3+} and Fe^{3+} onto the Ti site which is demonstrated in both synthetic (e.g. $Ca^{2+}_{0.8}Nd^{3+}_{0.2}Zr^{4+}Ti^{4+}_{1.8}Al^{3+}_{0.2}O_7$ [202]) [90], [203], [204] and natural zirconolites [81], [205].

The chemical durability of zirconolite for nuclear waste immobilisation have been assessed in several works, particularly those focussed on the durability of zirconolite in SYNROC [206]–[208]. Monolith durability tests, such as the MCC-1 test [102], are the favoured methodology in the literature, however leach rates are very low for durable ceramics in these conditions, particularly when using water as a leachant (e.g. NR_{Ce} = 1.2 x 10^{-6} $g \cdot m^{-2} \cdot d^{-1}$ at 42 d for zirconolite [209]). PCT-B tests have also been performed on zirconolite ($Ca_{1-x}Zr_{1-x}Ce_{2x}Ti_2O_7$) by Meng *et al.* [210], where NR_{Ce} = 10^{-6} – 10^{-7} $g \cdot m^{-2} \cdot d^{-1}$ using UHQ as a leachant at 90 °C for 7 d. An approach considered for making comparisons between the relative durability of ceramic materials, is to accelerate the leaching process by modifying the pH of the leachant. This can be performed using a modified PCT-B test [101], as completed by Stennett *et al.* [211] and Corkhill *et al.* [212] whereby 0.01M HNO_3 was used as a leachant

at SA/V = 500 m^{-1} to assess the relative durability of spent nuclear fuel simulants, such as CeO_2, synthesised under several different conditions. Leach rates (NL_{Ce}) in the range of 10^{-3} - 10^{-5} g m^{-2} d^{-1} were measured at 28 d, ensuring that the comparison of dissolution rates between the samples synthesised under different conditions were measurable in a short duration. Based on the above leach rates, it should be noted that analysis of the resultant phase assemblage is of importance to identify the location of the PuO_2 surrogate, CeO_2, in the chemical structure. This will determine the eventual durability of the material, since the NR_{Ce} of unincorporated CeO_2 and secondary phases such perovskite, are reported to be several orders of magnitude than zirconolite under similar conditions [95], [213].

Hot isostatic pressing (HIPing) has been effectively utilised as a thermal treatment method for ceramic materials [127], [189]–[191], [214], whereby simultaneous heat and isostatic pressure are applied using an inert gas (e.g. Ar), in order to sinter inside a hermetically sealed stainless steel canister, to provide wasteform consolidation and densification to near theoretical density. The UK Nuclear Decommissioning Authority (NDA) have reported that HIPing is the preferred thermal treatment technology for PuO_2 disposition [14] due to the advantages of minimising secondary wastes as well as batch-to-batch processing allowing for criticality concerns to be addressed and full accountancy throughout waste processing [126]. Inactive surrogates are important in avoiding the hazards, and inevitable costs, of working with radioactive materials and have been implemented when investigating the feasibility of HIPing for the immobilisation of PuO_2 [189], [215].

In this work, a matrix of eight zirconolite materials were synthesised using HIPing as the thermal treatment technology, with Ce used as an inactive surrogate for Pu due to their similar ionic radii [141]. The objective was to investigate and compare the efficacy of different zirconolite ceramic formulations as an immobilisation matrix for Pu, considering two different Ce incorporation mechanisms and charge compensation species. Two ceramic formulations were devised (Table 6-1), which targeted Ce incorporation at 0.2

formula units (f.u.), equivalent to a ~15 wt.% PuO_2 waste loading, within the range of interest for the application. A-site formulations targeted 0.2 f.u. of Ce^{4+} incorporation on the Ca^{2+} (A) site, with charge compensation with an appropriate amount of Al^{3+}, Fe^{3+} or Mg^{2+} on the Ti^{4+} site. AB-site formulations targeted 0.1 f.u. Ce^{4+} incorporation on both the Ca^{2+}(A) and Zr^{4+} (B) site (i.e. total of 0.2 f.u. Ce), again with charge compensation with an appropriate amount of the same charge compensating ion on the Ti^{4+} site. For comparison, A-site and AB-site formulations were also fabricated, with the omission of charge compensating species (Table 6-1). Note, however, that the $Ca_{0.9}Zr_{0.9}Ce_{0.2}Ti_2O_7$ formulation is effectively charge compensated assuming Ce^{3+} incorporation. The resulting phase assemblage was analysed using X-ray diffraction and scanning electron microscopy, in addition to X-ray absorption spectroscopy which was applied to analyse the Ce and Fe oxidation states. The relative chemical durability was assessed using a modified PCT-B test on select compositions in order to determine the effect of the charge compensating ions on the chemical durability of the wasteforms.

Table 6-1 – Summary of zirconolite compositions synthesised in this work.

Formulation target compositions	
A-site	**AB-site**
$Ca_{0.8}Ce_{0.2}ZrTi_2O_7$	$Ca_{0.9}Zr_{0.9}Ce_{0.2}Ti_2O_7$
$Ca_{0.8}Ce_{0.2}ZrTi_{1.6}Al_{0.4}O_7$	$Ca_{0.9}Zr_{0.9}Ce_{0.2}Ti_{1.8}Al_{0.2}O_7$
$Ca_{0.8}Ce_{0.2}ZrTi_{1.8}Mg_{0.2}O_7$	$Ca_{0.9}Zr_{0.9}Ce_{0.2}Ti_{1.9}Mg_{0.1}O_7$
$Ca_{0.8}Ce_{0.2}ZrTi_{1.6}Fe_{0.4}O_7$	$Ca_{0.9}Zr_{0.9}Ce_{0.2}Ti_{1.8}Fe_{0.2}O_7$

6.2 Experimental

6.2.1 Materials synthesis

Zirconolite compositions summarised in Table 6-1 were batched stoichiometrically using the following reagents, which were dried overnight at 180 °C: $CaTiO_3$ (Alfa Aesar, purity 98%), TiO_2 (anatase) (Sigma Aldrich, 99% purity), ZrO_2 (Sigma Aldrich, purity 99%), Fe_2O_3 (Alfa Aesar, purity 98%), MgO (Fisher Scientific, purity >99%), Al_2O_3 (Fisher Scientific, purity >99%) and CeO_2 (Acros Organics, 99.9% trace metals basis). Batches were milled using a Fritsch Planetary Mill 23 operating at 400 rpm for 20 min, using isopropanol as a milling fluid. The milled slurry was dried overnight at 90 ± 2 °C, with a 212 µm stainless steel sieve used to separate the dried material from the zirconia milling media. The dried material was calcined in air at 600 °C overnight prior to packing the HIP canister. The calcined material was pressed into a 316 stainless steel HIP canister using 1 t of uniaxial pressure and evacuated under vacuum at 300 °C before being hermetically sealed. The sealed HIP canisters were placed into an AIP 630-H HIP unit and HIPed at 1320 °C (ramp rate 10 °C min^{-1}) for 4 h, using Ar gas to generate 100 MPa of pressure. After HIPing, the canister was separated from the wasteform material using a Buehler Abrasimet 250.

6.2.2 Characterisation techniques

6.2.2.1 X-ray Diffraction (XRD)

A representative fraction of each HIPed zirconolite formulation was finely ground and analysed using powder XRD. A Bruker D2 Phaser diffractometer with LynxEye detector was used to collect diffraction patterns with the following parameters selected: Ni filtered Cu Kα radiation (λ = 1.5418 Å), 10 mA current, 30 kV voltage, with data collected between 10° < 2θ < 70° with a step size of 0.02° 2θ and count time of 1.18 s per step. Due to the presence of Fe in two of the zirconolite compositions, the detector was windowed to reject Fe fluorescence resulting from Cu radiation. The ICDD PDF-4+ library was used for phase analysis and each diffraction pattern was refined using the Rietveld

method for quantitative phase analysis, using the Bruker TOPAS software [216]. Appropriate CIF files were selected based on the phase analysis, and the scale factor, lattice parameters and thermal parameters were refined, with errors reported as calculated by the refinement process. The PDF numbers used for pattern identification were: $CaZrTi_2O_7$ 2M (01-084-0163), $CaZrTi_2O_7$ 3T (01-072-7510), $CaZrTi_2O_7$ 4M (01-088-0414), ZrO_2 (01-072-1669), TiO_2 (16-934), CeO_2 (01-081-0792), Al_2O_3 (01-071-1123) and $CaTiO_3$ (01-082-0228).

6.2.2.2 Scanning electron microscopy with energy dispersive X-ray spectroscopy (SEM/EDX)

Small (~ 2.5 mm diameter) monoliths of each HIPed zirconolite were mounted in epoxy resin, cured overnight before polishing to a 1 µm diamond finish and sputter carbon coating. A Hitachi TM3030 SEM with Oxford Instruments Swift ED3000 silicon drift detector, using an accelerating voltage of 15 kV and working distance of 7.8 mm, was used to observe the microstructure and phase assemblage of the monolith. The Bruker Quantax 70 software was used to process energy dispersive X-ray spectroscopy (EDX) data, with maps collected for a minimum of 10 min.

6.2.2.3 X-ray absorption spectroscopy (XAS)

The average Ce oxidation state of each formulation was determined from analysis of XAS spectra acquired at the Ce L_3-edge (5723.0 eV) using beamline 6-BM at the National Synchrotron Light Source II (NSLS-II) at Brookhaven National Laboratory (Upton, New York). This facility operates at 3 GeV storage ring with a 400 mA current and 6-BM utilises a 3-pole wiggler to deliver X-rays in the energy range between 4.5 and 23 keV. The optical arrangement of the beamline consists of a parabolic collimating mirror, a Si(111) monochromator, a toroidal focusing mirror, and a harmonic rejection mirror. In this study an unfocussed beam was used, and the beam size was limited to 0.5 mm in the vertical and 6 mm in the horizontal using slits. An ionisation chamber was used to measure the incident X-ray energy and the fluorescence signal was collected using a SII Vortex ME4 (4-element) Si drift

detector. To optimise collection efficiency, the samples were mounted at 45° to both the incident X-ray beam and the vortex detector. The fluorescence signal was dead-time corrected as previously described in Woicik et al. [160]. Spectra were recorded between 5533 and 5965 eV with energy steps of 10 eV (5533 – 5693), 2 eV (5693 – 5713), 0.3 eV (5713 – 5783) and 0.05k (5783 – 5965). An accumulation time of 0.5 s $step^{-1}$ was used for the first three regions and 0.25k $step^{-1}$ for the final region. Multiple scans were collected for each sample and averaged to improve the signal to noise ratio. To ensure energy reproducibility (± 0.1 eV) a CeO_2 standard was measured simultaneously with each sample; the CeO_2 standard was placed downstream of the sample and the transmitted intensity was measured using an ionisation chamber. Absolute energy calibration was performed by measuring a Cr foil and setting the position of the first inflection point in the derivative spectrum to 5989 eV [193]. Measurements were completed on all zirconolite formulations produced as well as compounds of known Ce oxidation state and coordination environment: $CePO_4$ (monazite; Ce^{3+}) and CeO_2 (Ce^{4+}).

The oxidation state and coordination environment of Fe was investigated using Fe K-edge (7112 eV) XAS at the same beamline described above. Reference compounds of known Fe oxidation state and coordination environment were also measured: staurolite ($Fe_{1.5}Al_{9.1}Mg_{0.5}Si_{3.9}(OH)_2$, Fe^{2+}, 4-fold), $FePO_4$ (synthetic, Fe^{3+}, 4-fold), $FeCO_3$ (synthetic, Fe^{2+}, 6-fold), aegirine ($NaFeSi_2O_6$, Fe^{3+}, 6-fold). Fitting of the Fe pre edge region, from 7106 - 7120 eV, was completed for Fe XANES spectra using the method described by Wilke *et al.* [158], [159]. The normalised data were fitted using a maximum of three Gaussian functions to describe the pre-edge region, with an arctangent function used to describe the background of the pre-edge region. The weighted mean centroid and height of the Gaussian functions were used to calculate the integrated pre-edge intensity, which is diagnostic of the oxidation state and coordination environment when compared to fitted standard reference compounds of known Fe environment.

Preparation of samples, and reference compounds, was completed by homogenising finely powdered material with polyethylene glycol and uniaxial pressing to form a 13 mm pellet with a thickness equivalent to one absorption length. Data reduction and linear combination fitting (LCF) were performed using the Athena software package [136] allowing the proportion of Ce^{3+}:Ce^{4+} in each sample to be calculated. Standard reference compounds of CeO_2 (Ce^{4+}) and $CePO_4$ (monazite; Ce^{3+}) were used and spectra were fitted over the range 5700 – 5760 eV, under the constraint that the fractional weights of the reference spectra sum to unity.

6.2.2.4 Compositional analysis

The composition of HIPed zirconolite materials was measured by X-ray fluorescence (XRF) spectroscopy prior to dissolution experiments. Powder samples were analysed by AMG Analytical Services using a Panalytical PW 2404 XRF system with a Rh X-ray source under vacuum on pressed pellets.

6.2.3 Dissolution testing

Static dissolution experiments were completed using a derivative of the PCT-B methodology [101], using an aggressive leachant to accelerate dissolution. HIPed zirconolite materials were crushed using a percussion mortar and sieved to retain the 75 – 150 μm size fraction. The resulting powder was sonicated in isopropanol to remove adhered fines and dried overnight at 90 ± 2 °C. A Micromeritics Accupyc 1340 II He pycnometer was used to measure the density of each sample composition, which was then used to estimate the total surface area (SA) of each powder geometrically. The cleaned powder was placed into a 60 mL PFA Teflon vessel with 40 mL of 0.01 M HNO_3 solution (pH = 2), to give a surface area to volume ratio (SA/V) equal to 100 m^{-1}. Triplicate sample and blank vessels were prepared and placed into an oven at 90 ± 2 °C. At each sampling time point (1, 2, 3, 4, 7 and 10 d), the vessels were removed from the oven and allowed to cool to room temperature. An aliquot of leachate (0.4 mL) was removed from each vessel, diluted using 10 mL of ultra high quality (UHQ, 18 MΩ cm^{-1}) water and passed through a PTFE syringe filter. Each vessel was then sealed and returned to the oven

until sampling at the subsequent time point. The total volume sampled correlated to <10% of the solution volume, therefore the SA/V was not significantly altered during the experiment.

Upon completion of the experiment, each solution was analysed to determine the concentration of dissolved elements using an ICP-MS (Thermofisher iCAP RQ). The normalised mass loss (NL_i) of elements from the zirconolite ceramics were calculated using Equation 6.1, where: NL_i is the normalised mass loss (g m^{-2}) of element *i*, c_i is the concentration of *i* in the leachate (mg L^{-1}), $c_{i,b}$ is the concentration of *i* in the blank (mg L^{-1}), f_i is the fraction of *i* in the ceramic and, SA/V is the surface area to volume ratio (m^{-1}).

$$NL_i = \frac{(c_i - c_{i,b})}{f_i \ {}^{SA}/_{V}} \tag{6.1}$$

$$NR_i = \frac{NL_i}{t} \tag{6.2}$$

The normalised dissolution rate (NR_i) in g m^{-2} d^{-1} was calculated using Equation 6.2, where *t* is the dissolution time (d). The SA/V was adjusted at each sampling time point to account for the evaporative losses and leachant removal at each time point.

Geochemical modelling using the elemental concentration and pH of the leachates was performed using PhreeqC v.3 software [163] with the LLNL database [144] to find the saturation indices (SI) of mineral phases. The SI of a phase was calculated in this software using Equation 6.3, where IAP is the ion activity product for the phase and K_s^0 is the standard solubility constant of the phase.

$$SI = \log\left(\frac{IAP}{K_s^0}\right) \tag{6.3}$$

6.3 Results and discussion

In this study, eight ceramic formulations were synthesised (as listed in Table 6-1) targeting 0.2 f.u. of CeO_2 onto the A site (A-site target formulation series) and 0.1 f.u, CeO_2 onto both the A and B site (AB-site target formulation series). Each formulation was repeated with charge compensating ions, Al^{3+}, Mg^{2+} and Fe^{3+}, onto the Ti^{4+} site, to observe the effect of these on the resultant microstructure and phase assemblage. Characterisation of the microstructure, phase assemblage and Ce/Fe oxidation state for each formulation in each series is presented below.

6.3.1 A-site target formulation characterisation

6.3.1.1 XRD

The powder XRD patterns for each A-site target formulation HIPed at 1320 °C, 100 MPa for 4 h, are shown in Figure 6-1. Diffraction data were analysed using the Rietveld method, examples shown in Supplementary Figure S6-1a, to provide quantitative phase analysis for each formulation (see Table 6-2 and Figure 6-2). The primary phase was identified as zirconolite 2M for each formulation, with small quantities of zirconolite 3T in each formulation (ranging from 6.6 ± 0.2 wt.% to 16.0 ± 0.2 wt.%), and zirconolite 4M present in the $Ca_{0.8}Ce_{0.2}ZrTi_2O_7$ and $Ca_{0.8}Ce_{0.2}ZrTi_{1.8}Mg_{0.2}O_7$ formulations (13 ± 0.3 wt.% and 5.1 ± 0.3 wt.% respectively). The total quantity of zirconolite formed in each formulation, i.e. the total of the 2M, 3T and 4M polytypes, increased with the introduction of charge compensating ions from 87 ± 2 wt.% for the $Ca_{0.8}Ce_{0.2}ZrTi_2O_7$ formulation, to 94 ± 2 wt.% for the $Ca_{0.8}Ce_{0.2}ZrTi_{1.6}Fe_{0.4}O_7$ formulation. The addition of charge compensating ions also produced a minor increase in the quantity of perovskite formed, from 1.6 ± 0.3 wt.% for the $Ca_{0.8}Ce_{0.2}ZrTi_2O_7$ formulation, to 3.7 ± 0.3 wt.% for the $Ca_{0.8}Ce_{0.2}ZrTi_{1.6}Fe_{0.4}O_7$ formulation. However, the addition of charge compensating ions also minimised the residual unreacted batch materials, with the total ($\Sigma(ZrO_2, TiO_2\ CeO_2, Al_2O_3)$) decreasing from 10.5 ± 0.4 wt.% for the $Ca_{0.8}Ce_{0.2}ZrTi_2O_7$ formulation to 1.2 ± 0.4 wt.% for the $Ca_{0.8}Ce_{0.2}ZrTi_{1.6}Fe_{0.4}O_7$ formulation. In the case of the $Ca_{0.8}Ce_{0.2}ZrTi_{1.6}Al_{0.4}O_7$

formulation, Al_2O_3 was detected by XRD (1.5 ± 0.2 wt.%), evidencing incomplete incorporation of the charge balancing species.

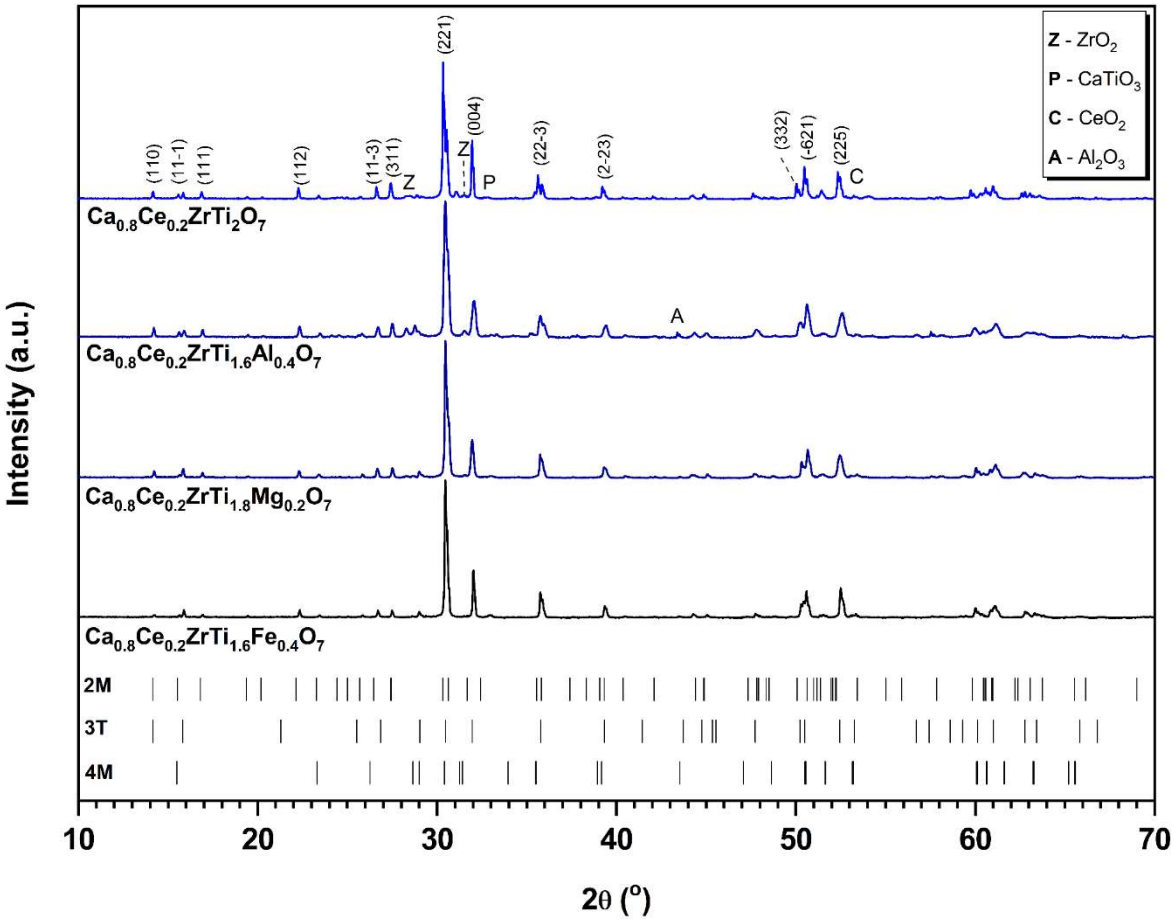

Figure 6-1 - Powder XRD patterns of each A-site target formulation. Miller indices highlight major reflections of the zirconolite 2M phase.

Table 6-2 – Quantitative analysis using Rietveld refinement on XRD patterns of A-site target formulations displayed in Figure 6-1. Errors in parentheses.

Composition	Phase fraction (wt.%)								
	Zirconolite								
	2M (± 2)	3T (± 0.2)	4M (± 0.3)	Total (± 2)	Perovskite (± 0.3)	CeO_2 (± 0.1)	TiO_2 (± 0.2)	ZrO_2 (± 0.4)	Al_2O_3 (± 0.2)
$Ca_{0.8}Ce_{0.2}ZrTi_2O_7$	67	6.6	13	86.6	1.6	0.3	2.9	7.3	-
$Ca_{0.8}Ce_{0.2}ZrTi_{1.6}Al_{0.4}O_7$	81	6.9	-	87.9	2.0	1.4	0.6	4.4	3.7
$Ca_{0.8}Ce_{0.2}ZrTi_{1.8}Mg_{0.2}O_7$	78	9.1	5.1	92.2	2.4	0.3	-	4.4	-
$Ca_{0.8}Ce_{0.2}ZrTi_{1.6}Fe_{0.4}O_7$	78	16	-	94.0	3.7	-	-	1.2	-

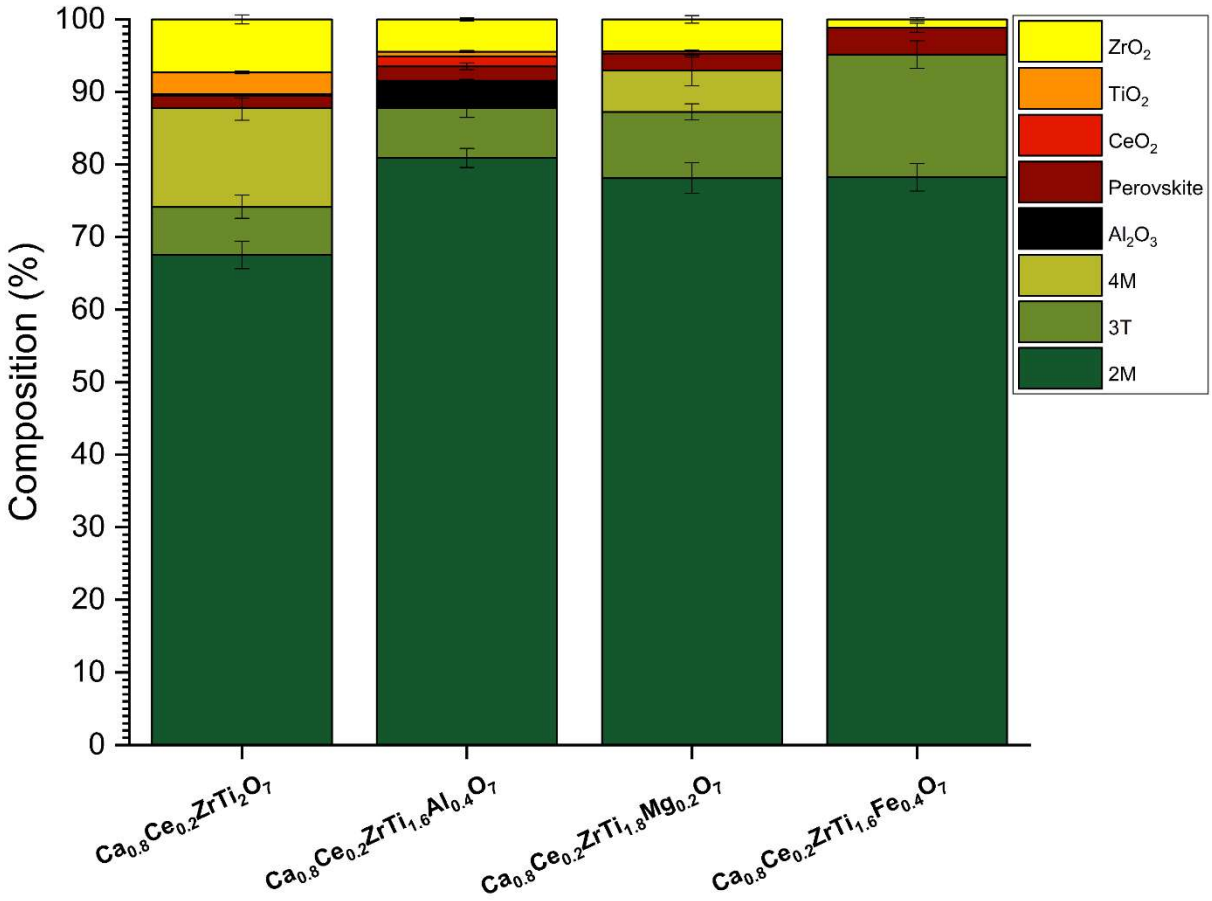

Figure 6-2 – Quantitative phase analysis of powder XRD data of A-site target formulations presented in Figure 6-1 and Table 6-2.

6.3.1.2 SEM/EDX

Scanning electron micrographs were acquired for each formulation to provide a greater understanding of the microstructure produced, verify the results obtained by XRD, and conduct semi-quantitative EDX analysis (based on a minimum of 5 spot analyses). BSE micrographs for each A-site target formulation are shown in Figure 6-3 where each labelled phase was identified by EDX analysis.

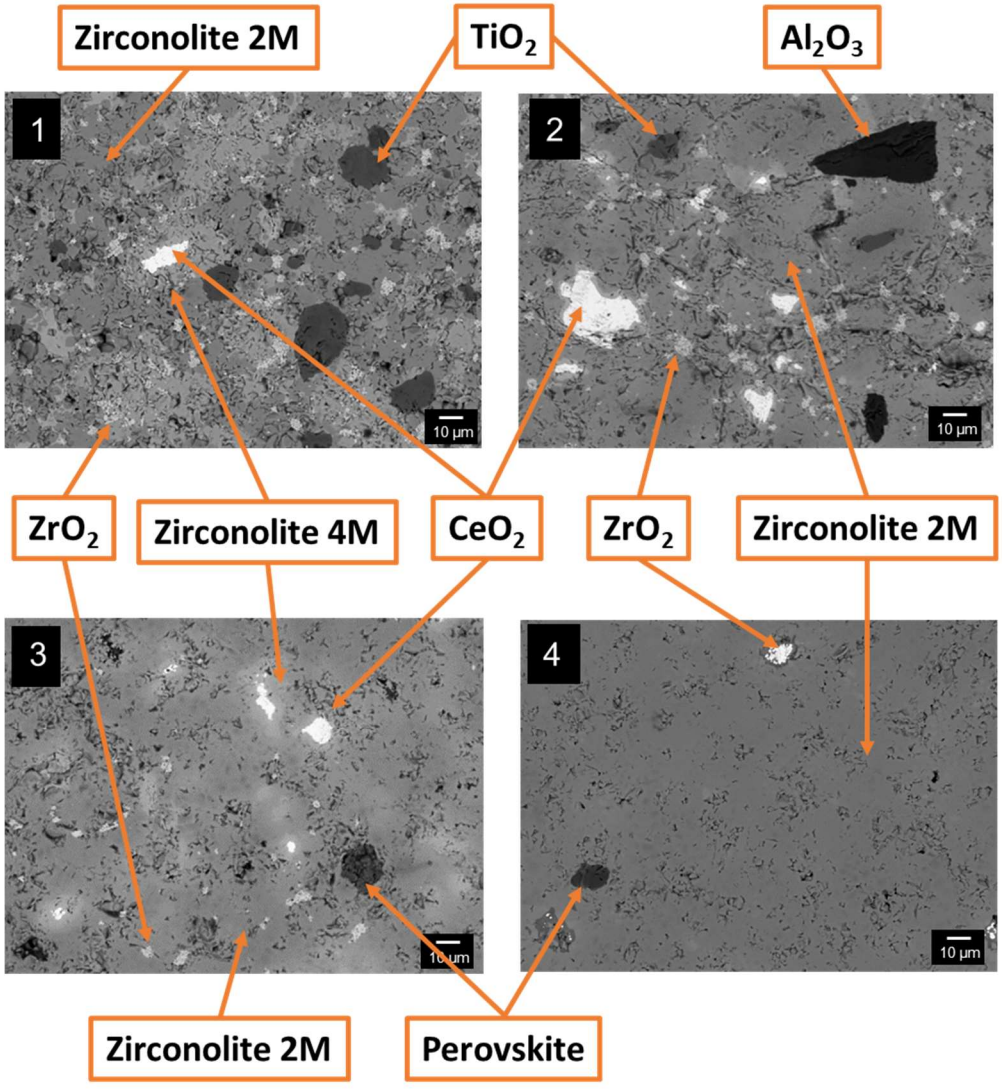

Figure 6-3– BSE images of a representative region of each A-site target forumulation where: 1 – $Ca_{0.8}ZrCe_{0.2}Ti_2O_7$, 2 - $Ca_{0.8}Ce_{0.2}ZrTi_{1.6}Al_{0.4}O_7$, 3 - $Ca_{0.8}Ce_{0.2}ZrTi_{1.8}Mg_{0.2}O_7$ and 4 - $Ca_{0.8}ZrCe_{0.2}Ti_{1.6}Fe_{0.4}O_7$. Each phase is labelled, and each micrograph is labelled with the average EDX composition of the zirconolite 2M/3T phase.

Table 6-3 – Avearge EDX determined composition of zirconolite 2M/3T for each A-site formulation, with associated deduced average Ce oxidation.

A-site EDX determined composition	Average Ce oxidation state
$Ca_{0.97(3)}Ce_{0.10(2)}Zr_{0.92(3)}Ti_{2.02(3)}O_7$	$Ce^{3.0+}$
$Ca_{0.89(5)}Ce_{0.11(2)}Zr_{1.03(6)}Ti_{1.77(6)}Al_{0.20(3)}O_7$	$Ce^{3.8+}$
$Ca_{0.75(6)}Ce_{0.16(2)}Zr_{1.04(6)}Ti_{1.85(2)}Mg_{0.20(3)}O_7$	$Ce^{3.4+}$
$Ca_{0.75(3)}Ce_{0.14(2)}Zr_{1.10(4)}Ti_{1.63(4)}Fe_{0.37(3)}O_7$	$Ce^{3.4+}$

In Figure 6-3, each micrograph shows a mid-grey matrix, identified as zirconolite 2M and zirconolite 3T, phases which are assumed to be indistinguishable due to similar contrast and therefore almost identical composition. Zirconolite 4M is clearly distinguished by brighter regions of higher contrast, with greater concentrations of Ce as evidenced with EDX. The phase assemblage of all specimens is heterogeneous, with the inclusion of unreacted materials such as TiO_2 (dark grey contrast) and ZrO_2 (light grey contrast), in agreement with XRD data in Figure 6-1. SEM and EDX analysis of the $Ca_{0.8}Ce_{0.2}ZrTi_{1.6}Al_{0.4}O_7$ formulation confirmed the presence of Al_2O_3 as a second phase, with the appearance of dark angular grains, consistent with XRD data.

The average EDX determined compositions for the zirconolite 2M/3T phase are reported in Table 6-3, alongside the average Ce oxidation state deduced from these compositions. These compositions assume the oxygen stoichiometry, given the low sensitivity of EDX to this element, and are consistent with the average Ce oxidation states determined by Ce L_3-edge XANES (see Figure 6-4), within uncertainties. The EDX determined compositions confirm the targeted A site substitution of Ce for Ca, with charge compensation by co-substitution of Al^{3+}, Mg^{2+} or Fe^{3+} on the Ti^{4+} site and/or partial reduction of Ce^{4+} to Ce^{3+} (see below). However, in the case of the formulation without charge compensation, at least some incorporation on the

Zr^{4+} (B) site was evident. Ce was determined to be lower than expected in all compositions and it is evident that the full inventory of CeO_2 was not incorporated.

Considering the SEM-EDX and XRD analysis, the $Ca_{0.8}Ce_{0.2}ZrTi_{1.6}Fe_{0.4}O_7$ and $Ca_{0.80}Ce_{0.20}ZrTi_{1.6}Mg_{0.2}O_7$ formulations were relatively successful, with an overall yield of 92 - 94 ± 2% zirconolite which has a composition close to the target stoichiometry, with the presence of only trace unincorporated CeO_2. The $Ca_{0.80}Ce_{0.20}ZrTi_{1.6}Al_{0.2}O_7$ formulation was comparably less successful; the EDX determined composition, and observation of free Al_2O_3 by XRD and SEM-EDX, imply that the solubility of Al^{3+} on the Ti^{4+} site in the zirconolite structure was exceeded. Consequently, the achieved Ce incorporation was much lower than the targeted formulation, with significant residual CeO_2 observed by XRD and SEM-EDX. The formulation without charge compensation afforded the lowest yield of zirconolite, as was expected due to the net positive charge associated with the substitution of Ce^{4+} into this formulation, however some Ce incorporation was achieved via preferential substitution onto the Zr^{4+} site. This comparison highlights the efficacy of Fe and Mg as charge compensating species, to maximise the yield and incorporation of Ce, according to the formulation design.

A trace amount of perovskite in all compositions was identified by XRD, which was determined to partially incorporate Ce by EDX (see Figure S6-3); however, the small size of these Ce-bearing perovskite grains, as well the similar BSE contrast of these grains to zirconolite 4M, prohibited semi-quantitative analysis of the composition. The observation of trace perovskite and residual ZrO_2 and/or TiO_2 observed in all formulations suggests that equilibrium may not have been fully achieved in the HIP cycle. This could be addressed by more aggressive milling conditions and a longer dwell period at 1320 °C.

6.3.1.3 Ce L_3-edge XANES

Ce L_3-edge XANES data were acquired to investigate the potential change in Ce oxidation state with the addition of each charge compensating ions. The

results for A-site target formulations are summarised in Table 6-4 with an example fit shown in Figure S6-2. Note that the Ce L_3-edge XANES of $CePO_4$ presents a single intense feature on the rising absorption edge, whereas CeO_2 presents three features, of lower relative intensity, for which the corresponding final state electron configurations were previously assigned [164], [217]–[219].

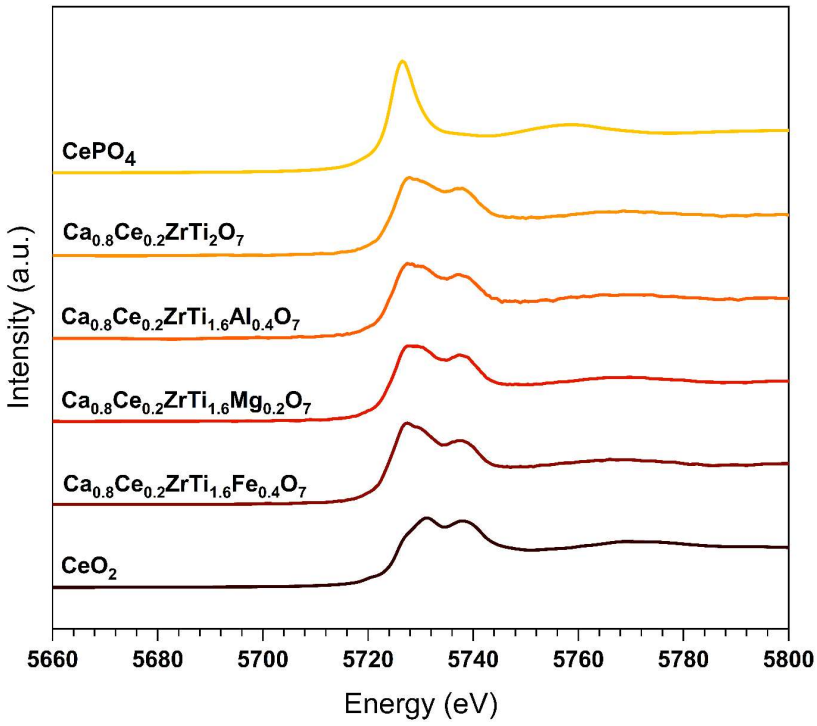

Figure 6-4 - Ce L_3-edge XANES spectra of A-site target specimens. Reference compounds for Ce^{3+} and Ce^{4+} are included ($CePO_4$ and CeO_2 respectively).

Table 6-4 - Average Ce oxidation state of each composition resulting from the linear combination fitting of spectra in Figure 6-4, with errors shown in parentheses.

Formulation	Average Ce speciation		R factor	Average Ce ox. state
	$CePO_4$ (3+)	CeO_2 (4+)		
$Ca_{0.8}Ce_{0.2}ZrTi_2O_7$	0.30(1)	0.70(1)	0.01	3.70(1)
$Ca_{0.8}Ce_{0.2}ZrTi_{1.6}Al_{0.4}O_7$	0.34(1)	0.66(1)	0.01	3.66(1)
$Ca_{0.8}Ce_{0.2}ZrTi_{1.8}Mg_{0.2}O_7$	0.29(2)	0.71(2)	0.03	3.71(2)
$Ca_{0.8}Ce_{0.2}ZrTi_{1.6}Fe_{0.4}O_7$	0.40(1)	0.60(1)	0.02	3.60(1)

The Ce L_3-edge XANES data and resultant LCF analysis (Figure 6-4 and Table 6-4, respectively) for A-site target formulations revealed the presence of Ce in mixed oxidation state, in a relatively narrow range of $Ce^{3.60(1)+}$ to $Ce^{3.71(1)+}$. The partial reduction of Ce^{4+} to Ce^{3+} is likely induced by the stainless steel HIP can under processing conditions, with consequent oxidation of Fe^0 to $Fe^{2/3+}$. The Ce L_3 XANES determined Ce oxidation state is representative of the bulk sample and averages over all Ce-bearing phases i.e. zirconolite polytypes, perovskite and CeO_2. Nevertheless, it can be considered approximately representative of the average Ce oxidation state within the zirconolite phase, given the trace abundance of the other Ce bearing phases. Thus, these data therefore evidence the presence of Ce^{3+} within the zirconolite formulations. The semi quantitative EDX determined zirconolite compositions are broadly in agreement with this conclusion, within uncertainties (note Fe K-edge XANES data below, which confirm presence of Fe^{3+} as a charge compensation species). It is difficult to be certain of the mechanism for charge compensation of Ce^{3+} within the zirconolite structure given the precision of the EDX determined compositions and presence of Ce-bearing accessory phases. It is conceivable that oxygen vacancies may stabilise Ce^{3+}; alternately, the EDX compositions of the charge compensated zirconolite compositions hint at higher Zr content than formulated, which could stabilise Ce^{3+}.

6.3.1.4 Fe K-edge XANES

The Fe K-edge spectra of $Ca_{0.8}Ce_{0.2}ZrTi_{1.6}Fe_{0.4}O_7$ and $Ca_{0.9}Zr_{0.9}Ce_{0.2}Ti_{1.8}Fe_{0.2}O_7$ formulation are shown in Figure 6-5 alongside the spectra of four reference compounds: staurolite (Fe^{2+} with 4-fold), $FePO_4$ (Fe^{3+} with 4-fold), $FeCO_3$ (Fe^{2+} with 6-fold) and $NaFeSi_2O_6$ (Fe^{3+} with 6-fold). The oxidation state of the element determines the position of the pre-edge peak in energy scale, whereas the site symmetry determines the area under the pre-edge peak, showing a linear relationship between average co-ordination environment for a given oxidation state. The pre-edge region was fitted with a maximum of three Gaussian peaks fitted to the spectral envelope, according the method presented by Farges *et al*. [168] and Wilke *et al.* [158]. The total

spectral envelope was described by the weighted mean average of the height and position of these Gaussian peaks. This fitting process was repeated for the data collected on the reference compounds; an example is shown in Figure 6-7.

The total integrated intensity and weighted mean centroid position of the Fe K-edge XANES pre-edge peak for $Ca_{0.8}Ce_{0.2}ZrTi_{1.6}Fe_{0.4}O_7$ and $Ca_{0.9}Zr_{0.9}Ce_{0.2}Ti_{1.8}Fe_{0.2}O_7$ formulations and reference compounds are shown in Table 6-5 and compared in Figure 6-6. The average oxidation state of Fe from each spectra was calculated using linear interpolation of the centroid position of the reference compounds (Fe^{2+} = 7114.55 eV and Fe^{3+} = 7112.95 eV). The average Fe oxidation states determined for $Ca_{0.8}Ce_{0.2}ZrTi_{1.6}Fe_{0.4}O_7$ and $Ca_{0.9}Zr_{0.9}Ce_{0.2}Ti_{1.8}Fe_{0.2}O_7$ were 2.9 ± 0.1 and 2.8 ± 0.1, consistent with the expected oxidation state of Fe^{3+} within error. The coordination number of Fe was estimated from the total integrated intensity using linear interpolation of the average of the 4-fold and 6-fold coordination standards, which were 0.115 and 0.41 for 4-fold and 6-fold coordination, respectively. The average coordination number for Fe was 5.6 ± 0.2 in both formulations. The zirconolite structure is characterised by three distinct Ti sites: two Ti sites are 6-fold coordinated and the remaining Ti site is 5-fold coordinated, and statistically 50% occupied [79], [220]. Our Fe K-edge XANES data are consistent with Fe incorporation in both 5- and 6-fold coordinate sites, with a clear preference for the former [221].

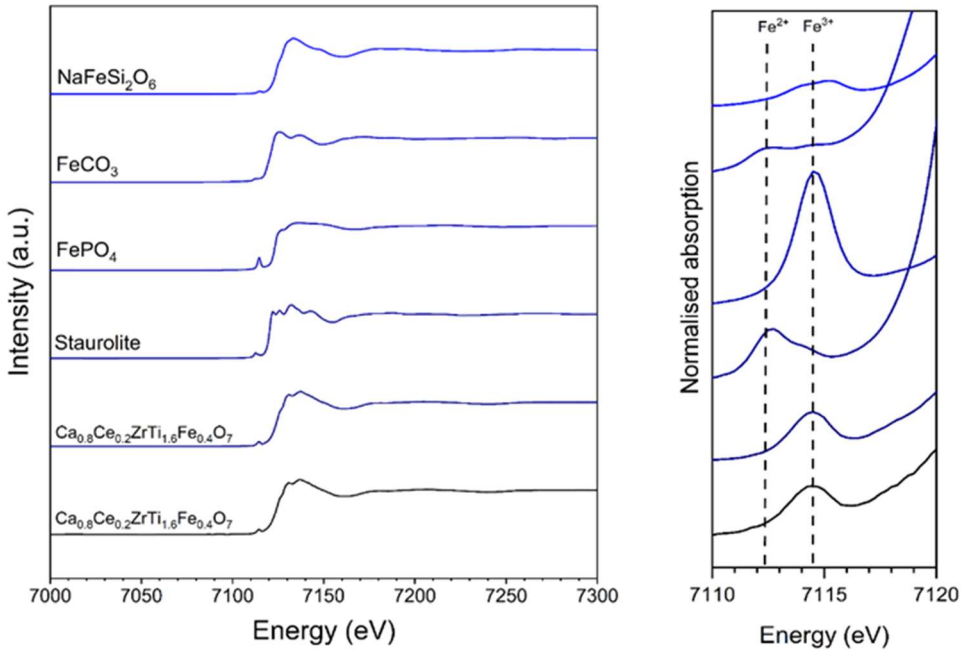

Figure 6-5 – Fe K-edge XANES spectra of reference compounds and all Fe-containing zirconolites (*left*), with a detailed view of the pre-edge region of the spectra (*right*).

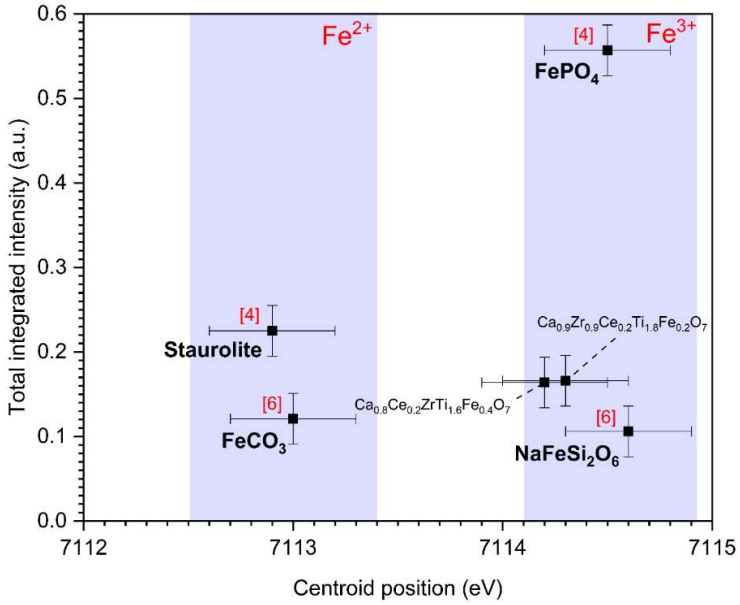

Figure 6-6 - Oxidation state and coordination environment of Fe in each formulation, characterised by the fitted Fe K-edge XANES pre-edge region and compared to the fitted parameters of the standard reference compounds.

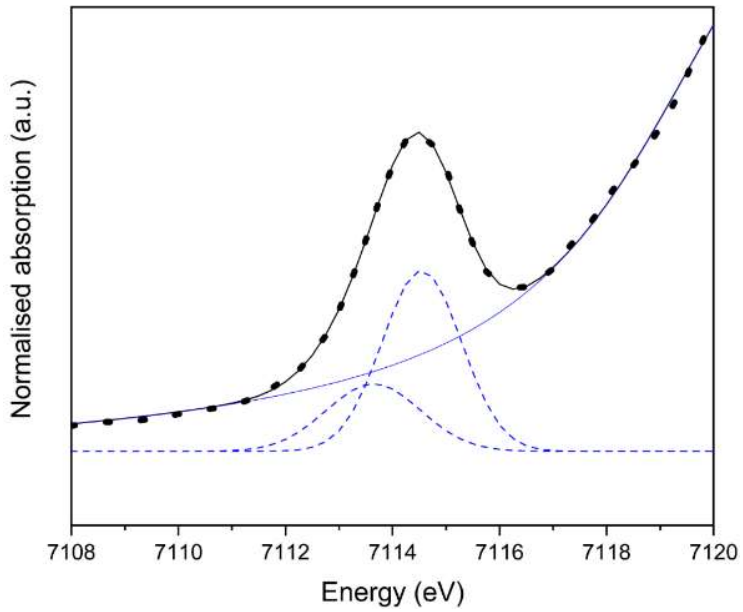

Figure 6-7 – Example of fitting of Fe K-edge XANES pre-edge region of $Ca_{0.8}Ce_{0.2}ZrTi_{1.6}Fe_{0.4}O_7$ measured in transmission mode. The dotted line shows the data with the bold solid line showing the fit. Dashed blue lines represent the fitted Gaussian peaks with the solid line showing the arctangent fitted to the background.

Table 6-5 - Intensity weighted centroid position and total integrated intensity of fitted pre-edge Fe XANES spectra of Fe reference compounds alongside $Ca_{0.8}Ce_{0.2}ZrTi_{1.6}Fe_{0.4}O_7$ and $Ca_{0.9}Zr_{0.9}Ce_{0.2}Ti_{1.8}Fe_{0.2}O_7$ formulations. Data presented in Figure 6-6.

Composition	Centroid position (eV) (± 0.3)	Total integrated intensity (± 0.03)	Average oxidation state (± 0.1)	Average coordination number (± 0.2)
$Ca_{0.8}Ce_{0.2}ZrTi_{1.6}Fe_{0.4}O_7$	7114.2	0.16	2.8	5.6
$Ca_{0.9}Zr_{0.9}Ce_{0.2}Ti_{1.8}Fe_{0.2}O_7$	7114.3	0.17	2.9	5.6
$NaFeSi_2O_6$	7114.6	0.11	3	6
$FePO_4$	7114.5	0.56	3	4
$FeCO_3$	7113.0	0.12	2	6
Staurolite	7112.9	0.26	2	4

6.3.2 AB-site target formulation characterisation

6.3.2.1 XRD

The powder XRD patterns for AB-site target HIPed zirconolite formulations are presented in Figure 6-8, with the corresponding phase analysis summarised in Table 6-6 and Figure 6-9, and Rietveld fits presented in Supplementary Figure S6-1b. The primary phase in these formulations was also identified as zirconolite 2M, with a small of zirconolite 3T (ranging from 3.9 ± 0.2 wt.% in the $Ca_{0.9}Zr_{0.9}Ce_{0.2}Ti_2O_7$ formulation to 7.4 ± 0.2 wt.% in the $Ca_{0.9}Zr_{0.9}Ce_{0.2}Ti_{1.8}Al_{0.2}O_7$ formulation) and zirconolite 4M (from 14 ± 0.3 wt.% in the $Ca_{0.9}Zr_{0.9}Ce_{0.2}Ti_2O_7$ formulation to 1.4 ± 0.3 wt.% in the $Ca_{0.9}Zr_{0.9}Ce_{0.2}Ti_{1.8}Fe_{0.2}O_7$ formulation). The total yield of zirconolite was maximised at 90 ± 2 wt.% for the $Ca_{0.9}Zr_{0.9}Ce_{0.2}Ti_2O_7$ formulation, and 84 ± 2 wt.% for the $Ca_{0.9}Zr_{0.9}Ce_{0.2}Ti_{1.8}Fe_{0.2}O_7$ formulation, which was concomitant with yield of perovskite (1.1 ± 0.3 wt.% to 10.0 ± 0.3 wt.% respectively). In the case of the $Ca_{0.9}Zr_{0.9}Ce_{0.2}Ti_{1.8}Al_{0.2}O_7$ formulation, Al_2O_3 was detected by XRD (1.5 ± 0.2 wt.%), evidencing incomplete incorporation of the charge balancing species.

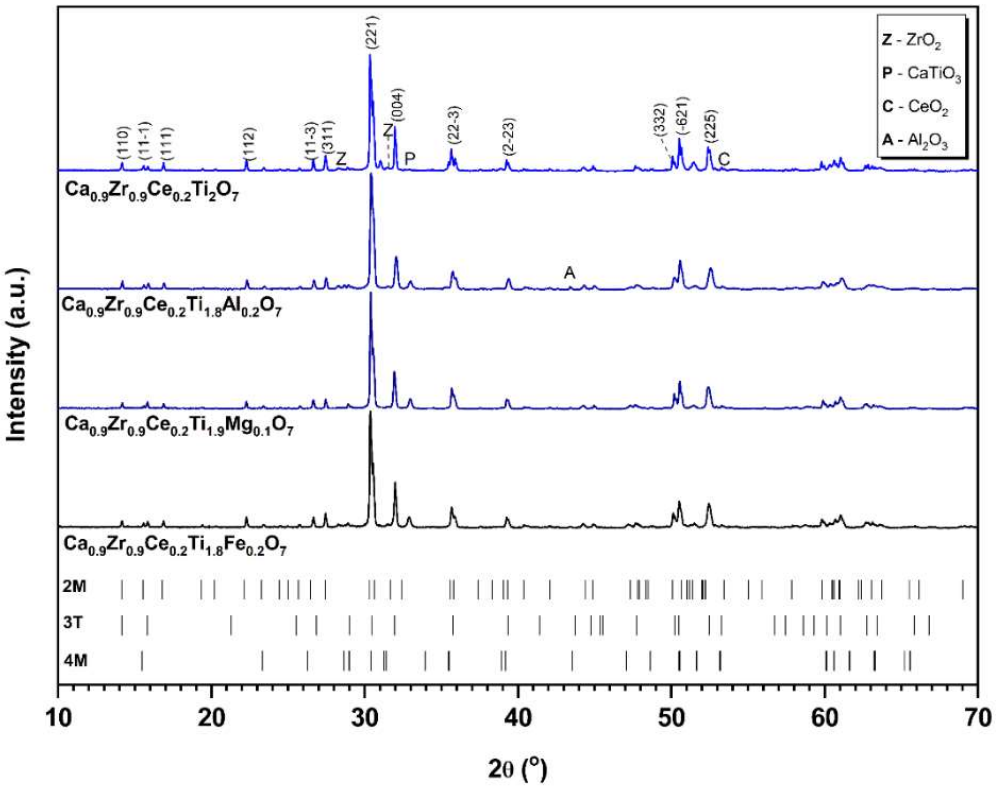

Figure 6-8 - Powder XRD patterns of each AB-site target Ce-doped zirconolite with Ti site charge compensating ions labelled. Miller indices highlight major reflections of the zirconolite 2M phase.

Table 6-6 – Quantitative analysis using Rietveld refinement of XRD patterns in Figure 6-8. Errors in parentheses.

Composition	Phase fraction (wt.%)								
	Zirconolite								
	2M (± 2)	3T (± 0.2)	4M (± 0.3)	Total (± 2)	Perovskite (± 0.3)	CeO_2 (± 0.1)	TiO_2 (± 0.2)	ZrO_2 (± 0.4)	Al_2O_3 (± 0.2)
$Ca_{0.9}Zr_{0.9}Ce_{0.2}Ti_2O_7$	72	3.9	14	89.9	1.1	4.7	2.5	1.5	-
$Ca_{0.9}Zr_{0.9}Ce_{0.2}Ti_{1.8}Al_{0.2}O_7$	79	7.4	1.8	88.2	6.8	0.7	0.9	2.0	1.5
$Ca_{0.9}Zr_{0.9}Ce_{0.2}Ti_{1.9}Mg_{0.1}O_7$	77	6.5	2.6	86.1	9.6	-	-	4.5	-
$Ca_{0.9}Zr_{0.9}Ce_{0.2}Ti_{1.8}Fe_{0.2}O_7$	77	5.2	1.5	83.7	10	0.6	1.1	5.0	-

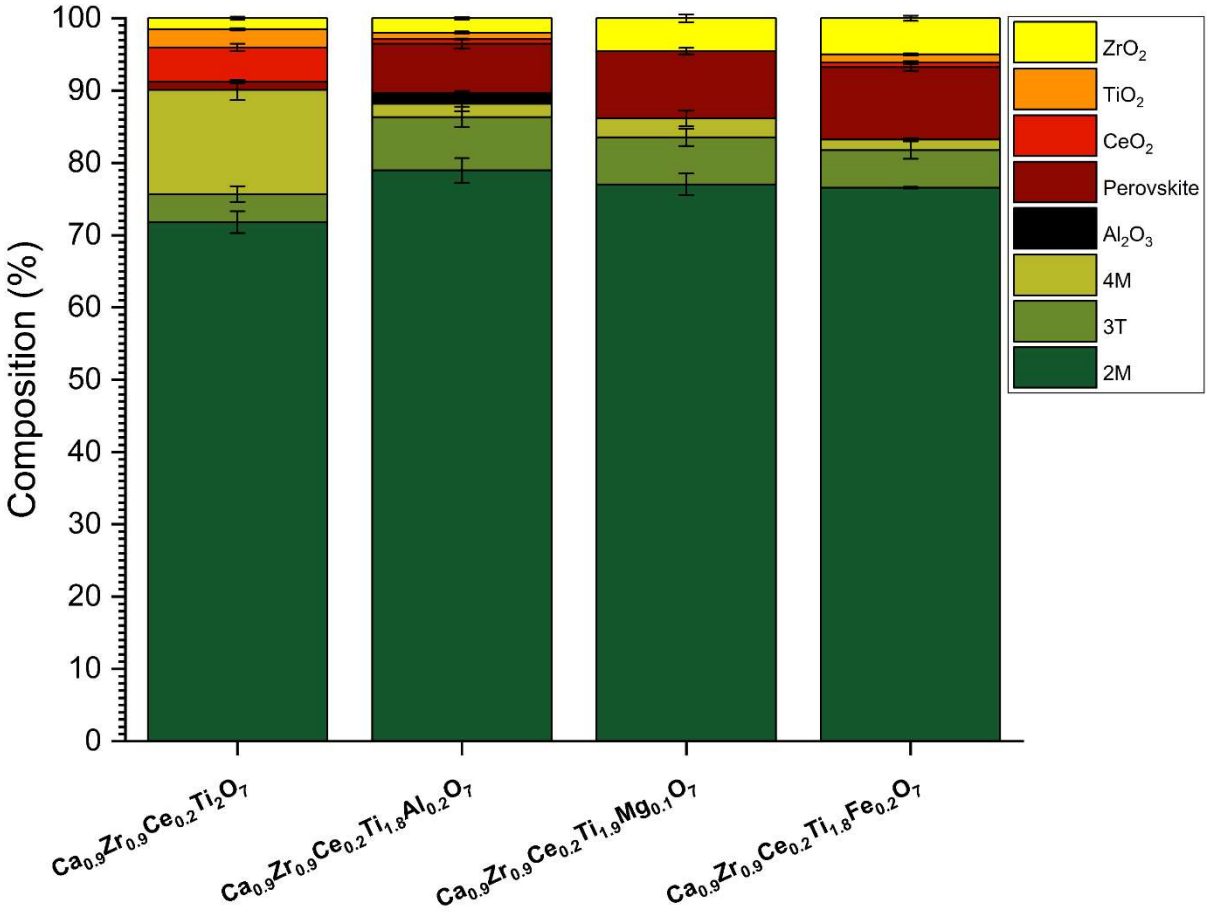

Figure 6-9 – Quantitative phase analysis of powder XRD data of HIPed AB-site target zirconolites presented in Figure 6-8, and Table 6-6.

6.3.2.2 SEM/EDX

Figure 6-10 shows the BSE micrographs of each AB-site target formulation, with the average EDX composition of the zirconolite 2M/3T phase in each formulation presented in Table 6-7. Each micrograph shows the representative microstructure of each formulation, which evidence greater heterogeneity compared to their counterpart A-site formulations. This is consistent with the quantitative phase assemblage, derived from XRD, Table 6-6, in which the overall yield of zirconolite is lower.

In Figure 6-10, the mid-grey matrix is again identified as zirconolite 2M and zirconolite 3T (indistinguishable due to similar composition and back scattered

contrast). Zirconolite 4M is clearly distinguished by regions of brighter contrast, again attributed to increased concentrations of Ce relative to zirconolite 2M. Regions of unreacted reagents were evident, in agreement with XRD data; in order of bright white to dark grey contrast, these regions were identified as CeO_2, ZrO_2, TiO_2, and Al_2O_3, confirmed by EDX analysis (see Figure S6-3). These data show that full incorporation of CeO_2 as the PuO_2 surrogate, and Al_2O_3, were not achieved. In Figure 6-3, Figure 6-10 and Figure 6-11, there is a reaction rim of light grey contrast observed around several of the CeO_2 particles. Following semi-quantitative EDX phase analysis the composition was identified to be a Ce-rich and Zr-deficient zirconolite, which is broadly consistent with available literature data on zirconolite 4M compositions [87].

The average EDX determined compositions for the zirconolite phase are reported in Table 6-7, along with the resulting average Ce oxidation state (again assuming oxygen stoichiometry). These compositions are consistent with the average Ce oxidation states determined by Ce L_3-edge XANES (see Figure 6-12), within uncertainties. The EDX determined compositions confirm the targeted AB-site substitution of Ce^{4+} for Ca^{2+} and Zr^{4+}, with charge compensation achieved by co-substitution of Mg^{2+}, Al^{3+} or Fe^{3+} the Ti^{4+} site and/or partial reduction of Ce^{4+} to Ce^{3+} (see below). Ce incorporation into the zirconolite phase was determined to be lower than expected in all compositions, along with Mg, Al, and Fe, and it is evident that the full inventory of CeO_2 was not incorporated.

The AB-site formulations were evidently less successful that the counterpart A-site formulations, in terms of the overall yield of target zirconolite phases, which was below 90 wt.%. Arguably, the $Ca_{0.9}Zr_{0.9}Ce_{0.2}Ti_2O_7$ formulation was the least successful, achieving the lowest incorporation of Ce, according to EDX and XRD data. The Mg^{2+}, Al^{3+}, and Fe^{3+} charge compensated formulations all afforded a comparable overall yield of zirconolite, with similar Ce incorporation, together with trace residual CeO_2. The comparably higher yield of perovskite in these AB-site formulations implies incorporation of Ce within this phase, identified with EDX spectra (see Figure S6-3). The observation of perovskite and residual ZrO_2 and/or TiO_2 observed in all

compositions formulations suggests that equilibrium may not have been fully achieved in the HIP cycle, as noted for the A-site formulations.

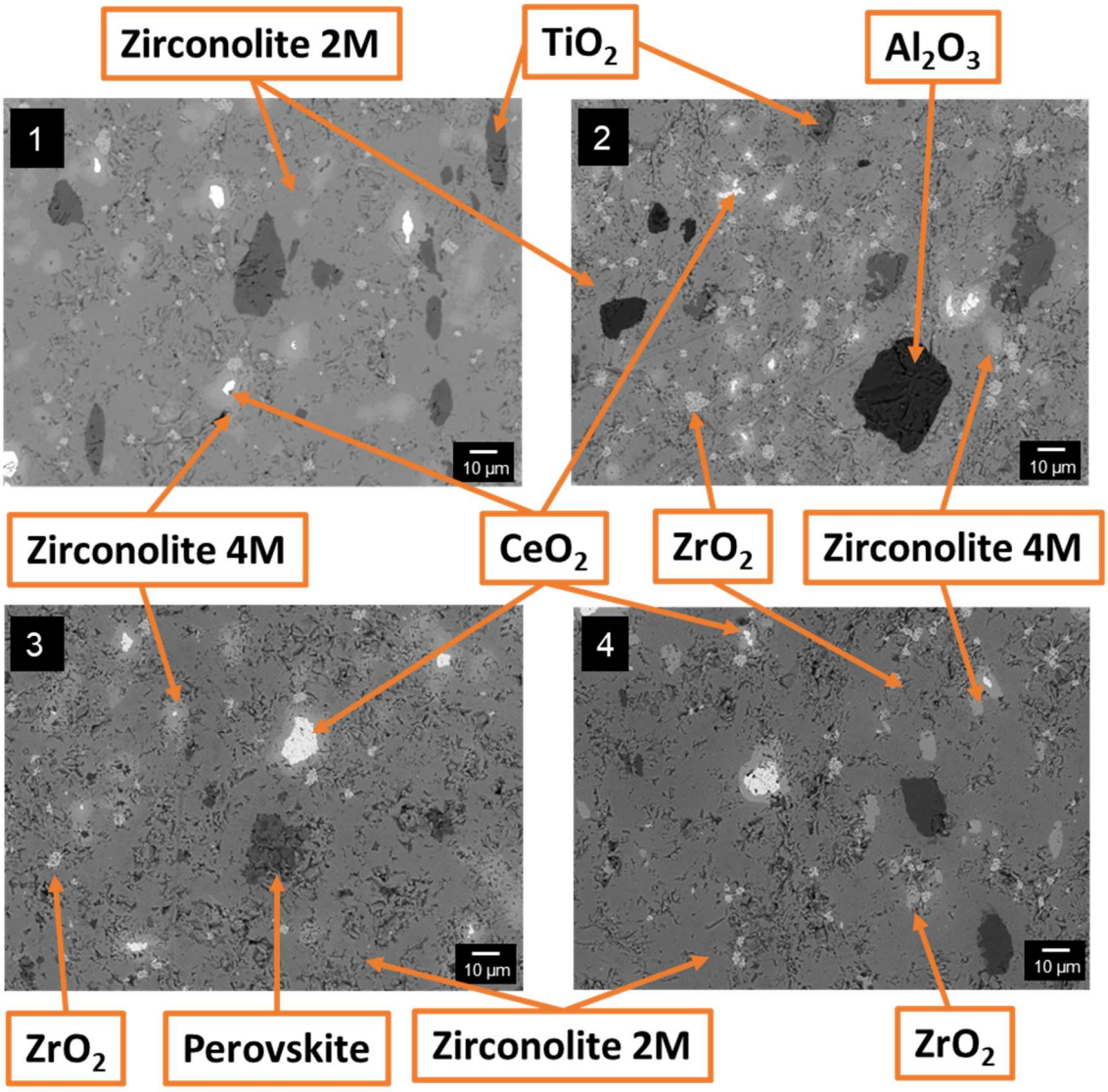

Figure 6-10– BSE images of each AB-site target formulation where: 1 - $Ca_{0.9}Zr_{0.9}Ce_{0.2}Ti_2O_7$, 2 - $Ca_{0.9}Zr_{0.9}Ce_{0.2}Ti_{1.8}Al_{0.2}O_7$, 3 - $Ca_{0.9}Zr_{0.9}Ce_{0.2}Ti_{1.9}Mg_{0.1}O_7$ and 4 - $Ca_{0.9}Zr_{0.9}Ce_{0.2}Ti_{1.8}Fe_{0.2}O_7$. Each phase is labelled, and each image is labelled with the average EDX composition of the zirconolite 2M/3T phase.

Table 6-7 – Avearge EDX composition of zirconolite 2M/3T for each AB-site formulation with associated deduced average Ce oxidation.

AB-site EDX determined composition	Average Ce oxidation state
$Ca_{0.99(3)}Ce_{0.08(6)}Zr_{0.92(2)}Ti_{2.02(7)}O_7$	$Ce^{3.1+}$
$Ca_{0.86(5)}Ce_{0.13(5)}Zr_{0.94(3)}Ti_{1.87(6)}Al_{0.20(5)}O_7$	$Ce^{3.4+}$
$Ca_{0.86(6)}Ce_{0.10(6)}Zr_{0.93(2)}Ti_{2.03(5)}Mg_{0.07(3)}O_7$	$Ce^{3.0+}$
$Ca_{0.94(7)}Ce_{0.12(7)}Zr_{0.98(2)}Ti_{1.85(6)}Fe_{0.12(3)}O_7$	$Ce^{3.7+}$

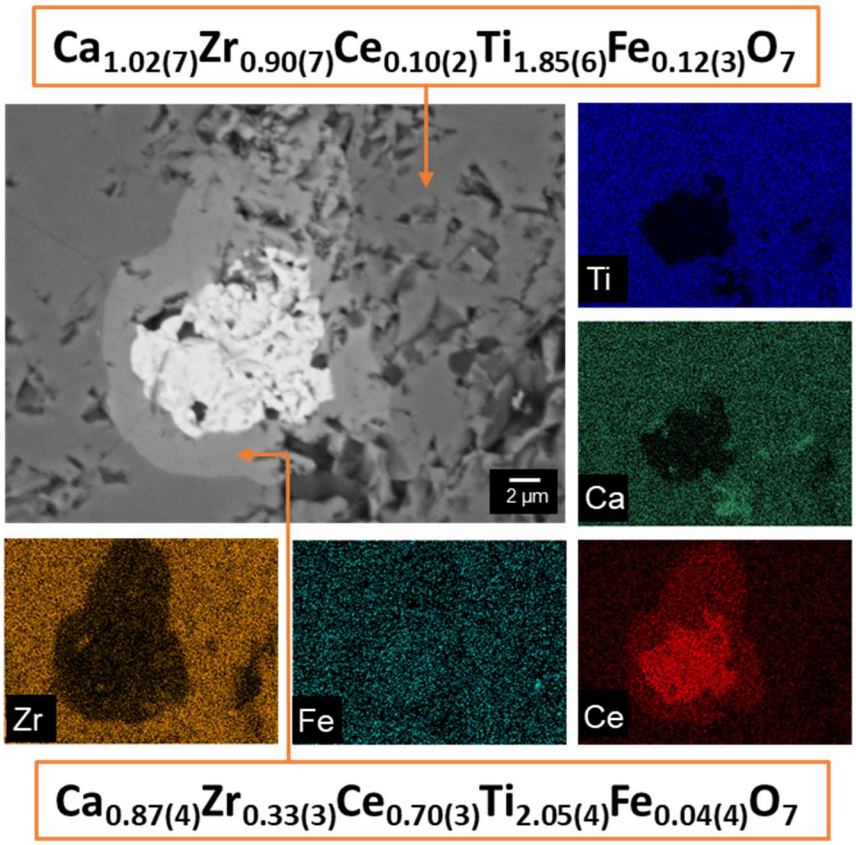

Figure 6-11 – BSE micrograph and EDX maps of HIPed zirconolite $Ca_{0.9}Zr_{0.9}Ce_{0.2}Ti_{1.8}Fe_{0.2}O_7$ composition, showing an area of reaction around a CeO_2 particle, forming a Ce-enriched zirconolite phase.

6.3.2.3 Ce L_3-edge XANES

Ce L_3-edge XANES data were acquired for AB-site formulations, with spectra shown in Figure 6-12 and LCF results presented in Table 6-8. An example of an LCF fit is shown in Figure S6-2. This analysis revealed the presence of Ce in mixed oxidation state, in a relatively narrow range of $Ce^{3.35(1)+}$ to $Ce^{3.64(1)+}$. Compared to the A-site formulations, the Ce^{3+}/Σ Ce ratio is greater for the AB-site formulations, in particular for those designed with Fe and Mg charge compensation (note Fe K-edge XANES data in Figure 6-6 and Table 6-5, which confirm presence of Fe^{3+} as a charge compensation species). The presence of 6.8 – 10 wt.% perovskite in the AB-site formulations is consistent with the higher Ce^{3+}/Σ Ce ratio, since this phase is known to preferentially incorporate Ce^{3+} [86], [87]. The significant fraction of perovskite means it is more difficult to have confidence that the Ce L_3-edge XANES determined Ce^{3+}/Σ Ce ratio is representative of the zirconolite phase. However, the semi-quantitative EDX compositions are consistent with the incorporation of significant Ce^{3+} concentration, within uncertainties, as implied by Ce L_3-edge XANES.

Figure 6-12 - Ce L_3-edge XANES spectra of AB-site specimens.

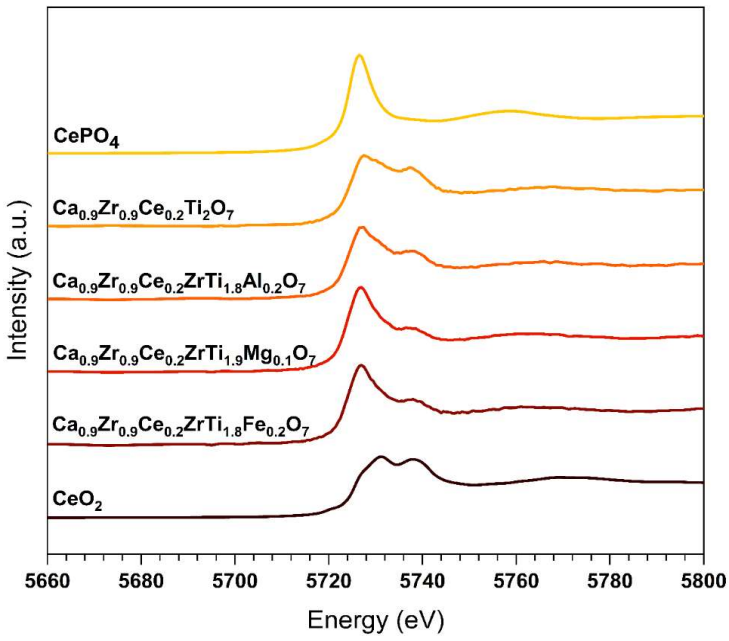

Reference compounds for Ce^{3+} and Ce^{4+} are included ($CePO_4$ and CeO_2 respectively).

Table 6-8 - Average Ce oxidation state of each AB-site target formulation resulting from the linear combination fitting of spectra in Table 6-8, with errors shown in parentheses.

Formulation	Average Ce speciation		R factor	Average Ce ox. state
	$CePO_4$ $^{(3+)}$	CeO_2 $^{(4+)}$		
$Ca_{0.9}Zr_{0.9}Ce_{0.2}Ti_2O_7$	0.36(1)	0.64(1)	0.02	3.64
$Ca_{0.9}Zr_{0.9}Ce_{0.2}Ti_{1.8}Al_{0.2}O_7$	0.55(2)	0.45(2)	0.03	3.55
$Ca_{0.9}Zr_{0.9}Ce_{0.2}Ti_{1.9}Mg_{0.1}O_7$	0.75(2)	0.25(2)	0.02	3.75
$Ca_{0.9}Zr_{0.9}Ce_{0.2}Ti_{1.8}Fe_{0.2}O_7$	0.65(1)	0.35(1)	0.02	3.65

6.3.3 Compositional analysis

The bulk composition of each A-site target formulation was determined using XRF in preparation for chemical durability experiments. These formulations were selected for these experiments due to their superior phase assemblage compared to AB-site formulations, with only trace perovskite and unincorporated CeO_2. Compositional analysis shown in Table 6-9 revealed that each formulation contained approximately 0.05 - 0.09 wt.% Fe, considered to derive from interaction/contamination from the SS HIP canister. With the exception of this finding, the batched composition and XRF analyses were in agreement.

Table 6-9 - Comparison of the batched composition and XRF results for each A-site target formulation.

Element	$Ca_{0.8}Ce_{0.2}ZrTi_2O_7$		$Ca_{0.8}Ce_{0.2}ZrTi_{1.6}Al_{0.4}O_7$		$Ca_{0.8}Ce_{0.2}ZrTi_{1.8}Mg_{0.2}O_7$		$Ca_{0.8}Ce_{0.2}ZrTi_{1.6}Fe_{0.4}O_7$	
	Batch	XRF (± 0.1)	Batch	XRF (± 0.1)	Batch	XRF (± 0.1)	Batch	XRF (± 0.1)
	(wt.%)							
Ca	8.93	8.50	9.14	8.88	9.05	8.79	8.85	8.53
Zr	25.41	23.44	26.02	24.44	25.75	24.44	25.19	23.71
Ti	26.66	28.73	21.84	23.85	24.32	26.76	21.14	22.99
Ce	7.80	5.90	7.99	6.26	7.91	6.13	6.17	6.00
Al	0.00	0.00	3.08	3.14	0.00	0.00	0.00	0.03
Mg	0.00	0.00	0.00	0.00	1.37	1.12	0.00	0.00
Fe	0.00	0.06	0.00	0.09	0.00	0.05	6.17	5.22
O	31.20	33.22	31.93	33.22	31.60	32.61	32.48	33.43
Total	100.00	100.00	100.00	100.00	100.00	100.00	100.00	100.00

6.3.4 Durability assessment

The A-site target formulations were selected for dissolution experiments, due to their more desirable phase assemblage (trace perovskite and unincorporated CeO_2), to quantify the influence of charge compensating ions, and the resultant phase assemblage, on the dissolution kinetics. As noted previously, highly accelerated dissolution conditions (0.01M HNO_3 at 90 °C) were necessary to obtain kinetic dissolution data on these highly refractory materials on the short time scale of this study (< 28 d).

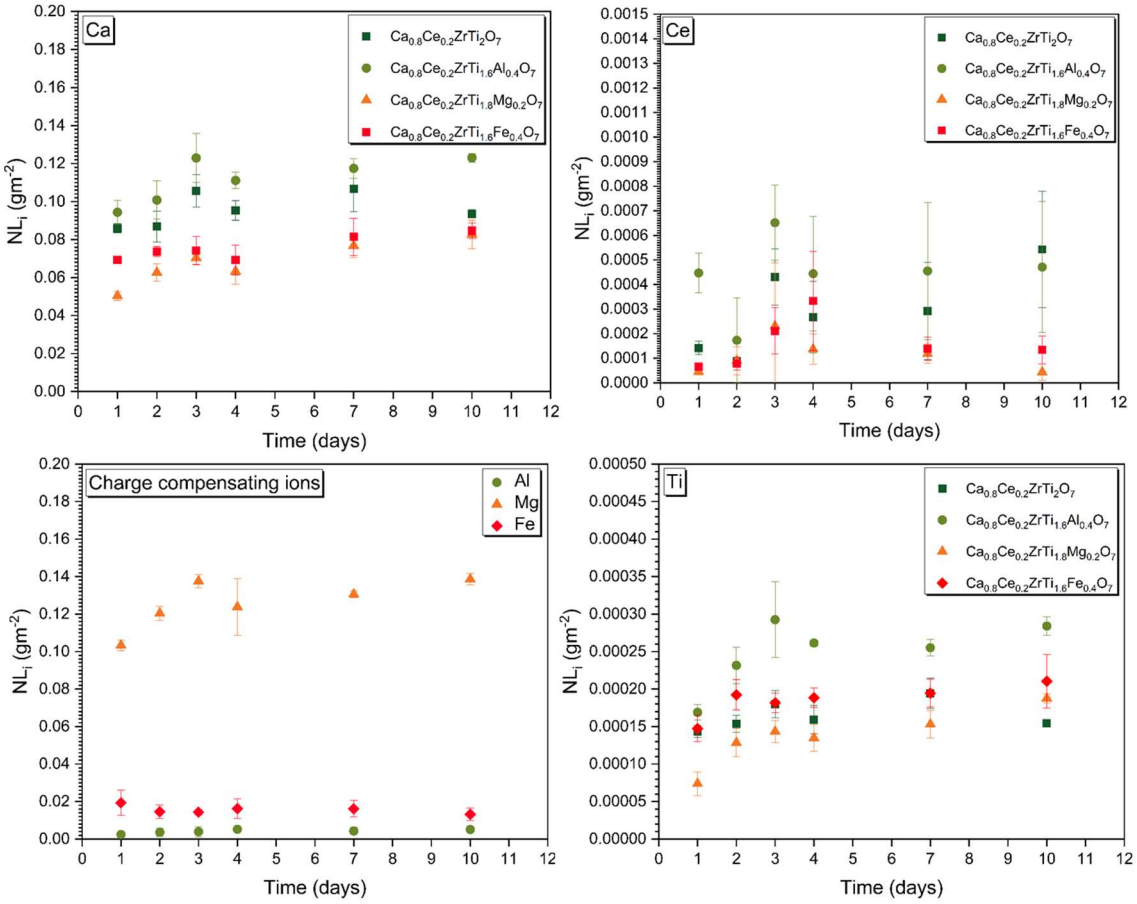

Figure 6-13 – Normalised mass loss of NL_i for Ca, Ce, Ti and the charge compensating ions (Al, Mg and Fe) for each A-site target material.

The normalised mass loss (NL_i) for each of the target formulations are shown in Figure 6-13. Of the elements released to solution, Zr could not be detected

as results were below the limit of detection for the ICP-MS, therefore results are not displayed here. Solution saturation was rapidly achieved, with an initial (1 – 3 d) increase in NL_i for all elements, except for the Al and Fe charge compensating ions, which then slowed to a steady rate (within error). The dissolution is incongruent, with Ca leaching at a rate at least two orders of magnitude greater than Ce, Ti, Al and Fe. Such behaviour is attributed to the multiphase nature of all of the formulations; both CeO_2 and Ce-bearing perovskite are known to leach more rapidly than zirconolite [213].

The greatest $NL_{Ca,\ Ti,\ Ce}$ values were observed for the $Ca_{0.8}ZrCe_{0.2}Ti_{1.6}Al_{0.4}O_7$ formulation at 10 d, indicating that this was the least durable of the materials investigated. This result is expected since this formulation has the greatest quantity of unincorporated CeO_2, as well as high quantities of other unreacted reagents which also contribute to the dissolution of this formulation. The lowest $NL_{Ca,\ Ti,\ Ce}$ values were observed for the $Ca_{0.8}ZrCe_{0.2}Ti_{1.6}Fe_{0.4}O_7$ formulation, which exhibited NR_{Ce} = 0.0(11) x 10^{-5} g m^{-2} d^{-1} (Table 6-10), suggesting that equilibrium was reached. This implies that this formulation was the most durable, consistent with the fact that this material was the most homogenous of the A-site targeted phases, containing only trace perovskite and no free CeO_2 (Table 6-2).

Table 6-10 – NR_i for each composition calculated from d 4 - 10. Errors in parentheses.

Formulation	NR_i (g m^{-2} d^{-1})			
	Ca	Ti	Ce	Charge compensator
$Ca_{0.8}ZrCe_{0.2}Ti_2O_7$	0.0(46) x 10^{-4}	0.0(30) x 10^{-6}	4.0(2) x 10^{-5}	-
$Ca_{0.8}ZrCe_{0.2}Ti_{1.6}Al_{0.4}O_7$	1.9(4) x 10^{-3}	2.5(3) x 10^{-6}	4.4(4) x 10^{-6}	0.0(19) x 10^{-5}
$Ca_{0.8}ZrCe_{0.2}Ti_{1.8}Mg_{0.2}O_7$	3.3(1) x 10^{-3}	1.1(1) x 10^{-5}	0.0(18) x 10^{-5}	2.7(1) x 10^{-3}
$Ca_{0.8}ZrCe_{0.2}Ti_{1.6}Fe_{0.4}O_7$	2.4(1) x 10^{-3}	3.0(1) x 10^{-6}	0.0(11) x 10^{-5}	0.0(56) x 10^{-4}

Geochemical modelling (using PhreeqC) was used to determine which secondary crystalline phases were saturated with respect to the solution, based on elemental concentration analysis and pH values from PCT-B

experiments. All experiments were predicted to be in equilibrium with the Ti-O phases, anatase and rutile, with SI values ranging between 1 and 2, which is in agreement with the small dissolution rates observed. The precipitation of Ti-O phases is known to occur during the dissolution of perovskite-containing zirconolite/SYNROC [207] with the effect of creating a passivating layer and slowing dissolution. No such evidence was found in the present study, however, this is unsurprising given the proximity of the solution to equilibrium.

When compared with literature data for the dissolution of zirconolite materials, the NR_{Ce} in the present study is approximately one order of magnitude greater than that reported by Meng *et al.* (NR_{Ce} = 10^{-6} – 10^{-7} $g \cdot m^{-2} \cdot d^{-1}$ with UHQ water as a leachant) [210]. This is to be expected given the aggressive leaching conditions (0.01M HNO_3 leachant) implemented in this experiment and the phase assemblage produced, particularly the presence of unincorporated CeO_2. Under identical leaching conditions to those applied here, the NR_{Ce} of single phase CeO_2 was reported as (0.26 ± 0.002) × 10^{-4} g m^{-2} d^{-1} at 28 d [211]; therefore, it can be concluded that the wasteforms produced in this investigation are capable of reducing the dissolution rate of Ce by at least one order of magnitude. This suggests that, despite the presence of unincorporated CeO_2 and Ce-bearing perovskite in these formulations, they remain a credible wasteform, although further optimisation of the processing conditions would inevitably improve the dissolution behaviour of these materials. This provides confidence in the performance of these materials as a durable wasteform for the immobilisation of PuO_2.

6.4 Conclusion

Zirconolite is recommended as wasteform for the immobilisation of the UK PuO_2 stockpile, with HIPing suggested as a viable thermal treatment method. An investigation into the role of charge compensating ions on the phase assemblage and relative dissolution rate HIPed Ce-doped zirconolite is presented. CeO_2 was used as a surrogate for PuO_2, which was targeted onto both the Ca^{2+} and Ca^{2+}/Zr^{4+} site, with Al^{3+}, Mg^{2+} and Fe^{3+} used as charge compensating species. Each material was characterised using XRD, SEM/EDX and Ce/Fe XANES to investigate the resulting phase assemblage. Zirconolite 2M was the dominant phase produced with small quantities of zirconolite 3T/4M, with trace unreacted reagents and secondary perovskite present. Targeting the Ca^{2+} site with Ce^{4+}, and utilising the charge compensation mechanism, proved to generate the most desirable phase assemblage, with 94 ± 2 wt.% zirconolite produced using Fe^{3+} as a charge compensating species. The oxidation state of Ce was found to influence the phase assemblage formed, with the formulations containing the highest $Ce^{3+}/\Sigma Ce$ ratio found to contain the greatest quantity of perovskite. The relative chemical durability of these wasteforms was assessed using a modified PCT-B test with aggressive leaching media (0.01M HNO_3). These durability assessments showed that the NL_i and NR_i for all elements was dependent upon the phase assemblage of each material, with the most homogeneous material, $Ca_{0.8}ZrCe_{0.2}Ti_{1.6}Fe_{0.4}O_7$, containing minimal free CeO_2 and perovskite, attaining the lowest dissolution rates (NR_{Ce} = 0.0(11) x 10^{-5} g m^{-2} d^{-1}), which was comparable to leach rates for dissolution experiments completed on Ce-doped zirconolite in similar conditions. In summary, further work must be completed to optimise the phase assemblage formed, taking into consideration the autoreduction of Ce^{4+} at the temperatures required to synthesise zirconolite, and the subsequent preferential formation of Ce-bearing perovskite.

Acknowledgements

ARM is funded by the Engineering, Physical Sciences Research Council via the Next Generation Nuclear Centre for Doctoral Training (EP/L015390/1). NCH is grateful to the Royal Academy of Engineering and Nuclear Decommissioning Authority for funding. This research utilised the HADES/MIDAS facility at the University of Sheffield established with financial support from EPSRC and BEIS, under grant EP/T011424/1 [186]. This research used beamline 6-BM of the National Synchrotron Light Source II, a U.S. Department of Energy (DOE) Office of Science User Facility Operated for the DOE office of Science by Brookhaven National Laboratory under Contract No. DE-SC0012704; the authors are grateful to Dr B. Ravel for experimental assistance.

Supplementary Figures

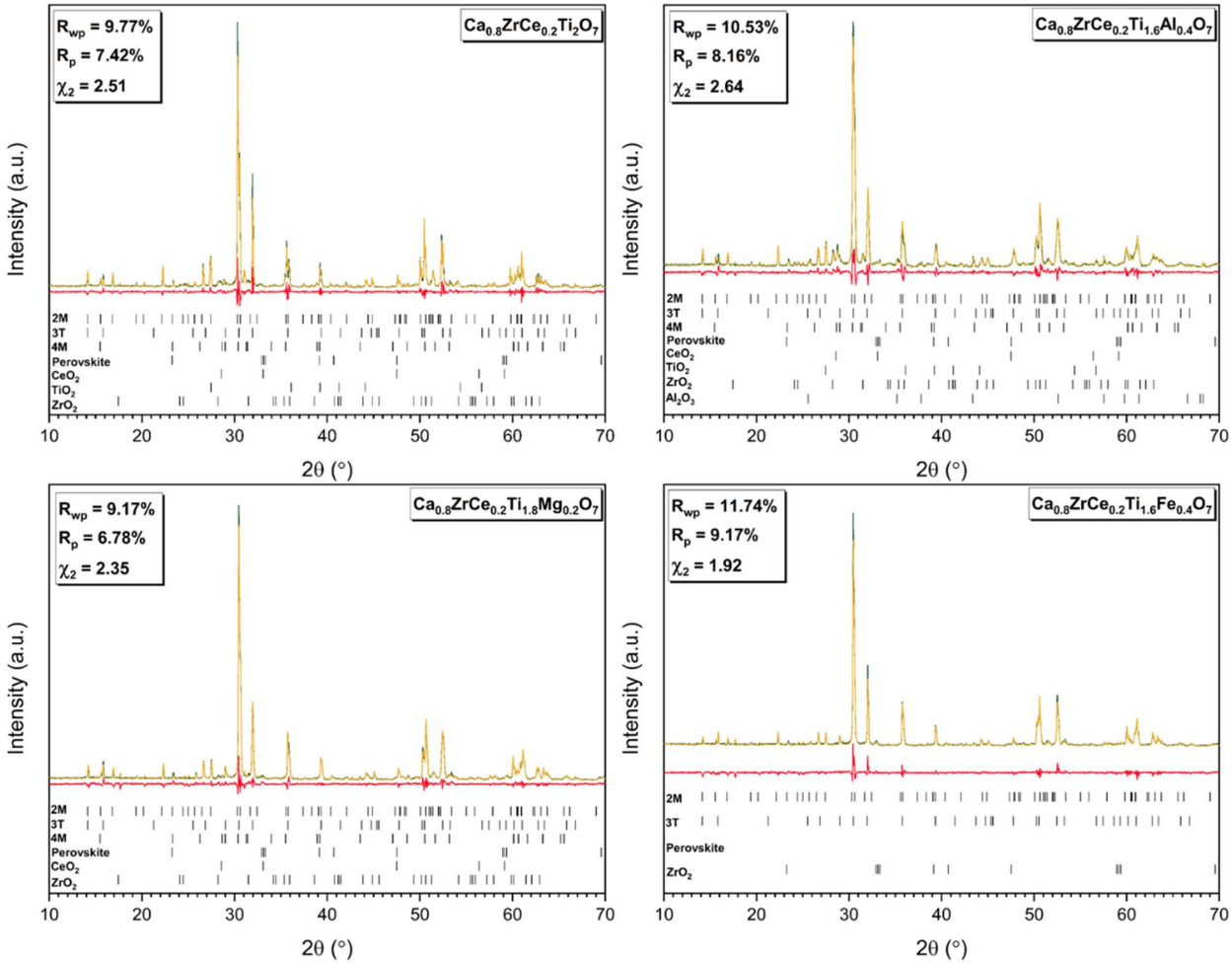

Supplementary Figure 6-1a - Rietveld fits of XRD data (green line) for QPA of each A-site targetted formulation. Fitted data is shown with amber line and red is the difference profile.

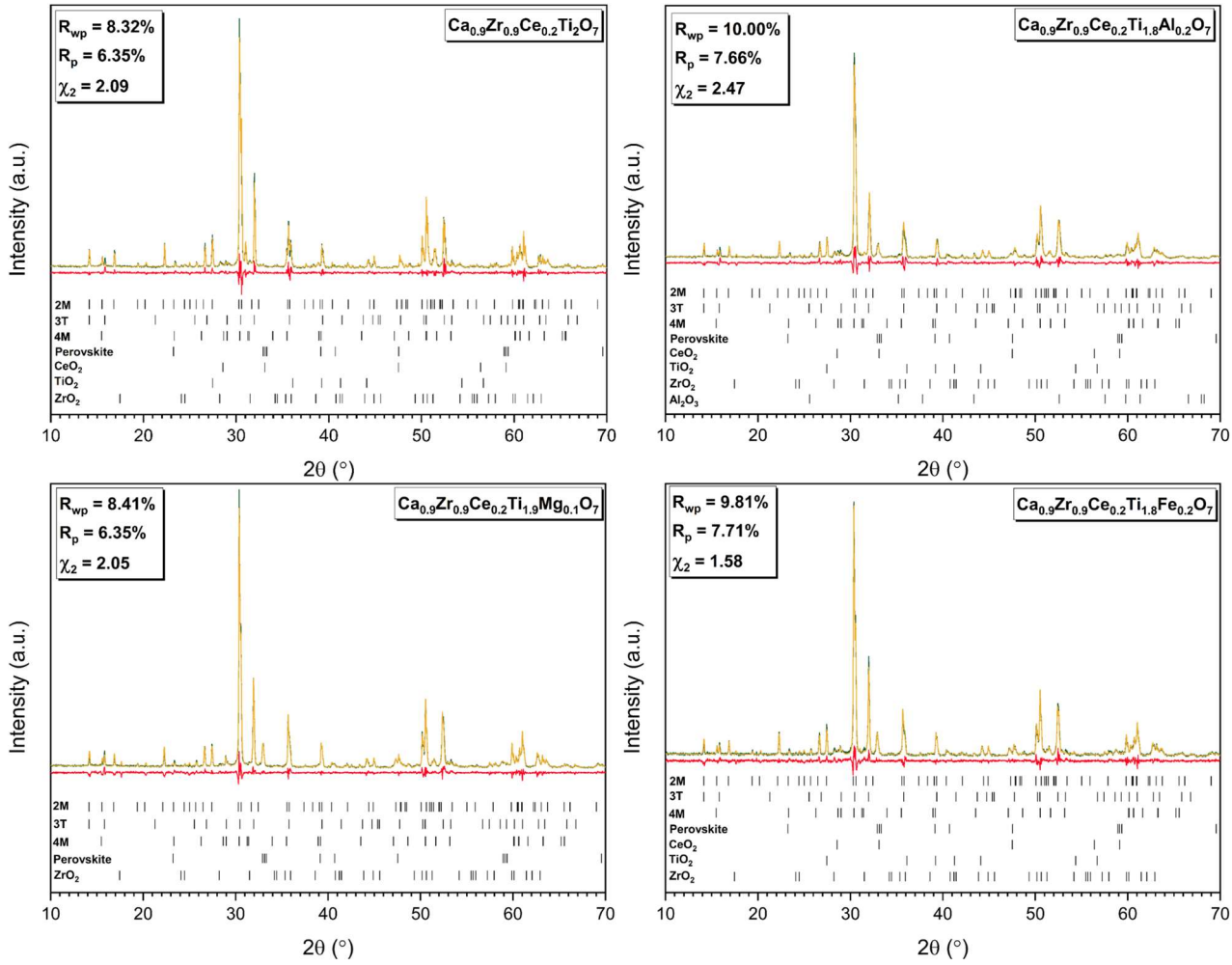

Supplementary Figure 6-1b - Rietveld fits of XRD data (green line) for QPA of each AB-site targetted formulation. Fitted data is shown with amber line and red is the difference profile.

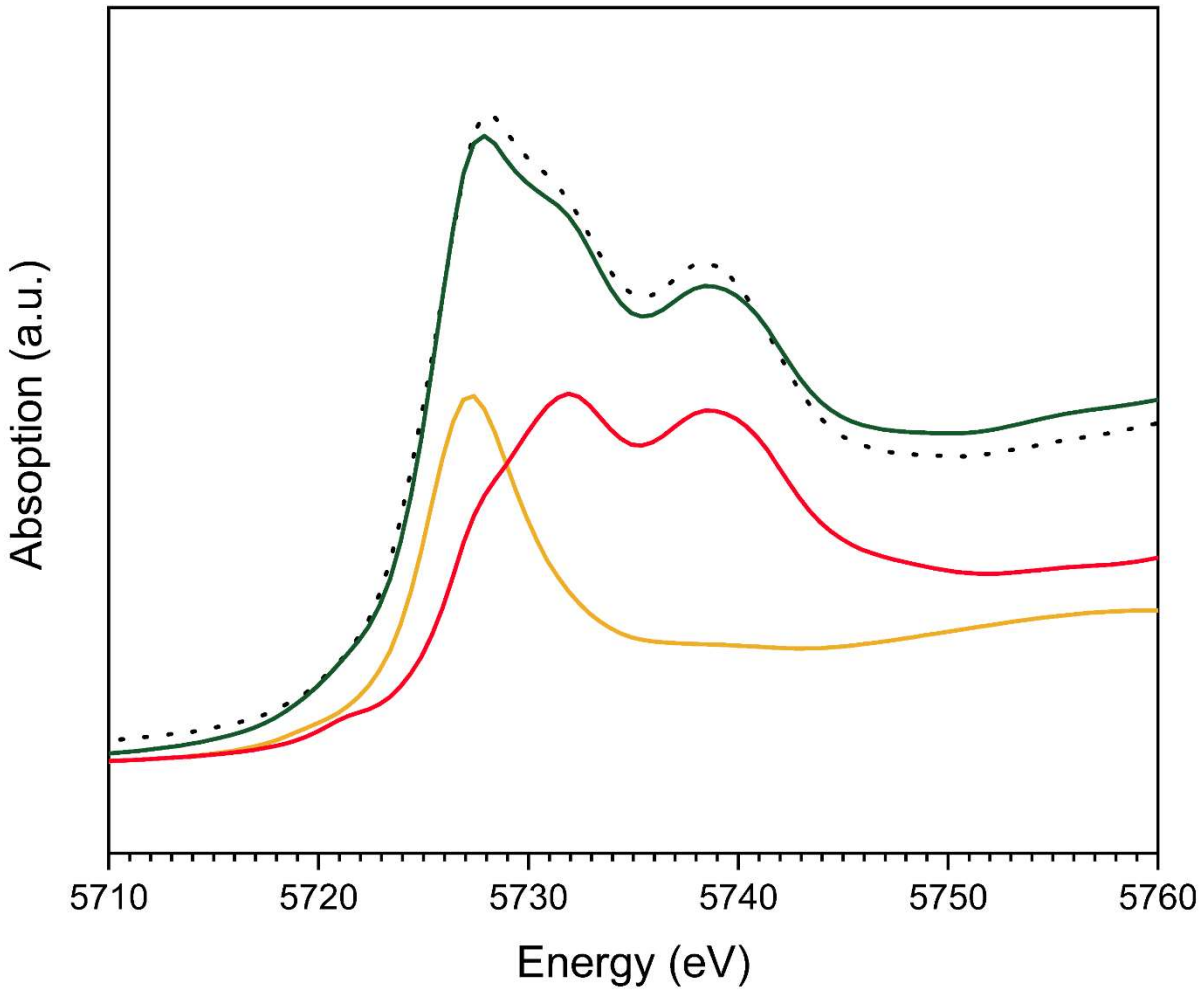

Supplementary Figure 6-2 - Example of linear combination fitting of Ce L_3-edge XANES of the $Ca_{0.8}Ce_{0.2}ZrTi_{1.6}Al_{0.4}O_7$ specimen measured in transmission mode. The dotted line shows the data with the green solid line showing the fit. Yellow and red lines represent the Ce reference standards $CePO_4$ and CeO_2 respectively.

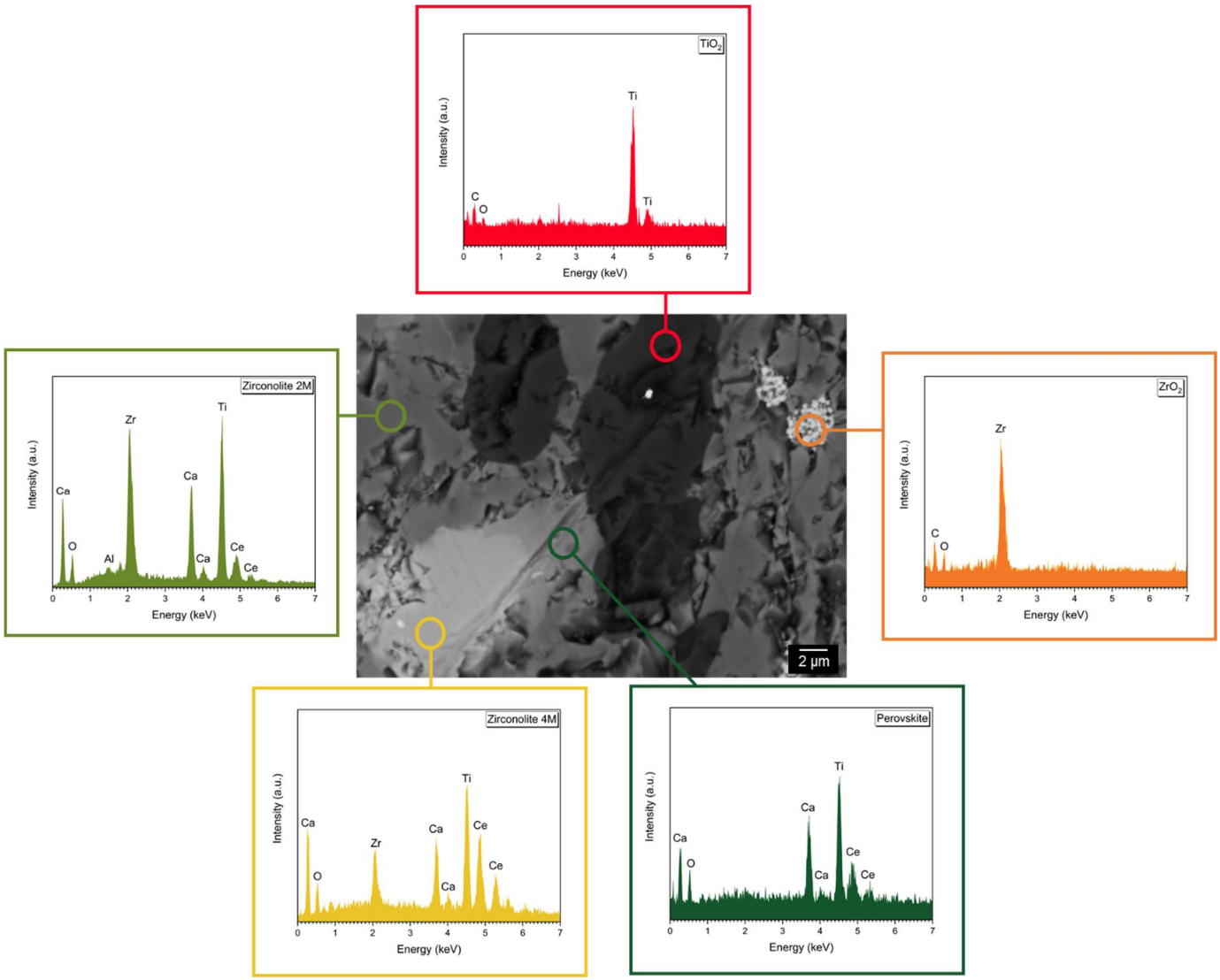

Supplementary Figure 6-3 – BSE micrograph of $Ce_{0.9}Zr_{0.9}Ce_{0.2}Ti_{1.8}Al_{0.2}O_7$ formulation with EDX spectra illustrating the composition of each phase (*clockwise from top*): TiO_2, ZrO_2, perovskite, zirconolite 4M and zirconolite 2M.

7 Hot isostatic pressing and durability assessment of fluorite related ceramic wasteforms containing neutron absorbers for PuO_2 disposition

Amber R. Mason, Colleen Mann, Martin C. Stennett, Claire L. Corkhill, Laura J. Gardner, Lewis R. Blackburn, Neil C. Hyatt*

Immobilisation Science Laboratory, Department of Materials Science and Engineering, University of Sheffield, Sir Robert Hadfield Building, Sheffield S1 3JD, UK

To whom correspondence should be addressed. Email n.c.hyatt@sheffield.ac.uk, phone +44 (0) 114 222 5470

Abstract

A selection of fluorite related ceramic wasteforms, with zirconolite, zirconate pyrochlore and cubic zirconia formulations, were fabricated using hot isostatic pressing as a thermal treatment method, to investigate their potential for PuO_2 disposition. Ce was utilised as an inactive surrogate for Pu whilst neutron absorbers, Gd and Hf, were added to understand their effect on the phase assemblage and dissolution rates. The resulting wasteforms were characterised by XRD, SEM and Ce L_3-edge XANES, which revealed Ce, Gd and Hf were fully incorporated into the zirconolite and cubic zirconia compositions, with some heterogeneity observed for the pyrochlore composition. This was reflected in the dissolution of these materials, whereby the dissolution rates for zirconolite and cubic zirconia ($NR_{Ce,\ Gd}$ = 10^{-5} – 10^{-6} g m^{-2} d^{-1}) were similar to those reported in the literature, however the pyrochlore composition produced the highest $NL_{Ce,Gd}$, which were two orders of magnitude greater than those reported in the literature due to phase heterogeneity, with a $(Ce,Gd)O_{2-x}$ solid solution observed. The $NL_{Ce,Gd}$ for zirconolite and cubic zirconia were approximately of the same order of magnitude, providing confidence that neutron absorbers could maintain an effective safeguard against criticality over the disposal timeframe.

Key Words: HIPing, durability, PuO_2 stockpile, XANES, neutron absorber

7.1 Introduction

The UK holds the largest stockpile of separated civil PuO_2, totalling 140 tHM [13], which was generated from the reprocessing of spent nuclear fuel (SNF), and is stored at the Sellafield site as a zero value asset [18]. Current UK government policy recommends that this material be recycled to generate mixed oxide fuel (MOX) ($(U,Pu)O_2$) [14], however there is limited uptake by reactors which could utilise MOX fuel within the current UK reactor fleet. Therefore, a dual track strategy of MOX fuel fabrication and immobilisation in a passively safe matrix has been proposed. This is especially pertinent as there is a small portion of the PuO_2 stockpile that unsuitable for recycling in MOX fuel [16], due to contamination from ingrowth of Am-241 (arising from Pu-241 β-decay), as well as Cl arising from the degradation of PVC packaging. A suitable end state for this stockpile should also be determined to ensure proliferation resistance is maintained in the future.

The feasibility of the immobilisation of PuO_2 in a ceramic matrix has been demonstrated extensively in the literature [45], [64], [92]. There have been several different types of ceramic investigated for this purpose including simple oxides such as zirconia [92], as well as complex oxides such as pyrochlore [22], [217], [222], [223] and zirconolite [91], [204], [223], [224]. The use of these matrices is often validated by the presence of natural analogues which have retained actinide elements for millions of years, therefore demonstrating their chemical flexibility, chemical durability and radiation tolerance [1], [40], [225]. These compositions, with the exception of zirconia, are also included as target actinide host phases in the multiphase ceramic wasteform, SYNROC (synthetic rock), developed by Australia's Nuclear Science and Technology Organisation (ANSTO) [97], [200].

Cubic zirconia (ZrO_{2-x}) has a fluorite structure which can accommodate a wide range of elements substituted onto the Zr site, particularly tetravalent cations such as Pu^{4+}, Ce^{4+} and Hf^{4+}. Trivalent elements such as Gd^{3+} can also be accommodated by the introduction of vacancies into the structure, without

changing the overall crystal structure. These compositions are arguably as chemically flexible as more complex oxides such as pyrochlore and zirconolite, despite only having a single site within the chemical structure onto which actinides, neutron poisons and charge balancing species can be substituted [226]. The fluorite structure has proven to be particularly radiation tolerant [73], [227], and chemically durable with average dissolution rates comparable to other ceramic phases (NR_{Zr} = 10^{-6} – 10^{-7} g m^{-2} d^{-1} in ultra high quality (UHQ) water at 7 d), as such, zirconia is an excellent candidate for the immobilisation of actinides [117], [226].

Pyrochlore is a derivative of the cubic fluorite structure with general formula $A_2B_2O_7$ [228], where actinides and other cations with large radii (e.g. r(Gd^{3+}) = 1.05 Å for 8-fold coordination) occupy the 8-fold coordinated A site, with smaller cations (r(Zr^{4+}) = 0.72 Å for 6-fold coordination) occupying the 6-fold coordinated B site. Zirconate pyrochlores ($A_2Zr_2O_7$), particularly $Gd_2Zr_2O_7$, are radiation tolerant ceramic materials, remaining crystalline at accumulated dose which cause amorphisation in equivalent titanate pyrochlore compositions [217], [229]. However, sintering temperatures for ceramics of near theoretical density are reported to be very high for these compositions, compared to equivalent titanate compositions (> 1500 °C for zirconate, with ca. 1350 °C for titanates) [22], [76], [150]. The chemical durability of Gd, Sm and Ce doped gadolinium zirconate pyrochlore materials was investigated by Wang *et al.*; these authors reported low release rates of 10^{-6} – 10^{-7} g m^{-2} d^{-1} for all elements leached from $GdSmZrCeO_7$ formulation during a 7 d standard PCT-B test (90 °C with deionised water (DIW) used as a the leachant) [230].

Zirconolite, prototypically $CaZr_xTi_{3-x}O_7$ with 0.8 < x < 1.35 with an anion deficient fluorite superstructure, is considered the main actinide host phase in SYNROC [231], and is one of the preferred wasteforms suggested by the Nuclear Decommissioning Authority for PuO_2 immobilisation, alongside pyrochlore [14]. There are several different zirconolite polytypes, e.g. 2M, 3T and 4M [79], [80], [82], where zirconolite 2M is the most commonly observed polytype. The crystal structure of zirconolite 2M is comprised of CaO_8 and ZrO_7

polyhedra between layers of TiO_6/TiO_5 polyhedra arranged to form a hexagonal tungsten bronze motif. The polytype formed is characterised by the stacking sequence of the CaO_8/ZrO_7 and TiO_6/TiO_5 layers and depends upon cation occupancy, vacancy distribution, oxygen fugacity, and processing temperature [86], [94]. The substitution of a range of cation charges onto the Ca and Zr sites can be achieved via charge compensation whereby divalent and trivalent charge balancing species (e.g. Cr^{3+}) are substituted onto the Ti site (for example, $Ca^{2+}_{1-x}Ce^{4+}_{x}Zr^{4+}Ti^{4+}_{2-2x}Cr^{3+}_{2x}O_7$ [204]), as observed with many natural zirconolite specimens [232], as well as synthetic zirconolites. A standard 7-d PCT-B test was performed on Gd-doped zirconolite ($Gd_{0.5}Sm_{1.5}Zr_{1.5}Ce_{0.5}O_7$), which demonstrated low release rates in the range of 10^{-6} - 10^{-8} $g \cdot m^{-2} \cdot d^{-1}$ for all elements (DIW leachant at 90 °C) [233], hence confirming the high chemical durability of zirconolite ceramics.

Fabrication of ceramic wasteforms by hot isostatic pressing has been investigated for the immobilisation of PuO_2 [189], [190], [221], [222]. The application of simultaneous heat and pressure to a wasteform within a hermetically sealed canister has several advantages compared to standard thermal treatment methods such as cold pressing and sintering (CPS), hence why the Nuclear Decommissioning Authority (NDA) have recommended this as a preferred thermal treatment method for PuO_2 disposition [14]. Hot isostatic pressing is a process whereby minimal secondary wastes are produced alongside the potential for waste volume reduction, which will in turn reduce the footprint required for a geological disposal facility (GDF). Batch-to-batch processing when HIPing also allows for criticality concerns to be addressed and full accountancy throughout waste processing [127], [234], [235].

The use Ce as an inactive surrogate for Pu is justified due to the inherent costs and hazards associated with the use of high activity isotopes. Whilst it is recognised that a surrogate cannot fully emulate the behaviour of its radioactive counterpart, Ce is selected in this case due to similar ionic radii and accessible oxidation states [141]. Neutron poisons, such as Gd or Hf, may

also be required in the wasteform composition to ensure that the system remains subcritical over the disposal period. However, the differential release rates of Pu, surrogates and neutron poisons are not well understood. The leaching of the neutron absorber and Pu must be congruent to maintain a subcritical wasteform and prevent a criticality event in storage or at a GDF facility, ideally minimising the dissolution rate of these elements.

In this study four ceramic formulations were prepared, which were previously investigated by Stennett *et al.* [236], [237] and Hyatt *et al.* [238], and are shown in Table 7-1. These specific compositions were selected based on the Ce solubility limits of the Gd zirconate pyrochlore ($Gd_2Zr_2O_7$), zirconolite ($CaZrTi_2O_7$) and cubic zirconia (ZrO_{2-x}) end members. These compositions were previously synthesised by Stennett *et al.* and Hyatt *et al.* using the traditional cold uniaxial pressing and sintering (CPS) technique, however, the density of these wasteforms was found to be < 95 % theoretical density when sintered at 1500 °C. HIPing was therefore used as the thermal treatment method in this work in order to improve the ceramic density, which will be pertinent for future large scale processing parameters. Ce was used as a surrogate for Pu, with Gd and Hf used as neutron poisons to achieve a ratio of (Hf + Gd)/Ce ≥ 2; in the case of the zirconate pyrochlore, the parent $Gd_2Zr_2O_7$ stoichiometry ensures an excess of Gd relative to Ce. The principle of the formulation design is that Gd^{3+} and Hf^{4+} should enable partitioning of neutron poisons with $Ce/Pu^{3/4+}$ within the wasteform over different crystallographic sites (if required), according to ionic radii. Thus, release of $Ce/Pu^{3/4+}$ from the ceramic could therefore be mitigated by co-release of Gd^{3+}/Hf^{4+}, however, it should be noted that the Gd/Hf concentration utilised are significantly excess of that required to achieve effective mitigation of wasteform criticality in storage and disposal concepts. Each ceramic wasteform was characterised using XRD, SEM/EDX and Ce L_3-edge XANES, and the resultant phase assemblage and Ce incorporation was compared. The relative chemical durability of each material was also compared using a modified PCT-B test where an aggressive leachant was used for rapid comparison of the durability of each material. The

relative dissolution rate of the Pu surrogate and neutron absorbers was also investigated.

Table 7-1 – Composition of each wasteform investigated in this work where Ce is the Pu surrogate and Hf/Gd are neutron absorbers.

Label	Composition
Zirconolite A	$(Ca_{0.9}Gd_{0.1})(Zr_{0.5}Ce_{0.2}Hf_{0.2}Gd_{0.1})Ti_2O_7$
Zirconolite B	$(Ca_{0.7}Gd_{0.1}Ce_{0.2})(Zr_{0.7}Hf_{0.2}Gd_{0.1})Mg_{0.2}Ti_{1.8}O_7$
Pyrochlore (zirconate)	$Gd_2(Zr_{1.6}Ce_{0.2}Hf_{0.2})O_7$
Cubic zirconia	$(Ca_{0.1}Zr_{0.75}Ce_{0.05}Hf_{0.05}Gd_{0.05})O_{2-d}$

7.2 Materials and methods

7.2.1 Wasteform synthesis

The matrix forming materials and neutron absorbers were prepared by weighing out each precursor to 4 d.p, according to the target stoichiometry (Table 7-1). The precursors were homogenised in a tumbling ball mill for 16 h, with yttria stabilised zirconia milling media and isopropanol as the milling fluid. The slurries were separated from the media using a sieve and dried overnight at 90 ± 2 °C. Once dry, the powder batches were passed through a 250 µm mesh sieve and a stoichiometric quantity of the plutonium surrogate (CeO_2) was added. Homogenisation of the surrogate and the batched reagents was completed using a rotary tumbling mixer for 16 h. Each batch was HIPed in a Ni HIP canister for 6 h, at 1350 ˚C with a pressure of 185 MPa. The temperature at which the material can be HIPed is limited by the melting temperature of the HIP canister material.

7.2.2 Characterisation techniques

7.2.2.1 2.2.1. X-ray Diffraction (XRD)

A representative sample of each HIPed ceramic material was finely ground and analysed using powder XRD. A Bruker D2 Phaser diffractometer with

LynxEye detector was used to collect diffraction patterns with the following parameters selected: Ni filtered Cu Kα radiation (λ = 1.5418 Å), 10 mA current, 30 kV voltage. Data was collected between 10° < 2θ < 70° with a step size of 0.02° 2θ and count time of 1.18 s per step. The ICDD PDF-4+ library was used for phase analysis and each diffraction pattern was refined using the Rietveld method in order to extract unit cell parameters and provide quantitative phase analysis, using the Bruker TOPAS software [216]. The PDF numbers used for the pattern identification are: $CaZrTi_2O_7$ 2M (01-084-0163), $CaZrTi_2O_7$ 3T (01-072-7510), $CaZrTi_2O_7$ 4M (01-088-0414), $CaTiO_3$ (01-082-0228), CeO_2 (01-089-8436), $Gd_2Zr_2O_7$ (01-079-1146) and, cubic ZrO_2 (01-081-1550).

7.2.2.2 Scanning electron microscopy with energy dispersive X-ray spectroscopy (SEM/EDX)

Small (~ 2.5 mm diameter) monoliths of each HIPed ceramic were mounted in epoxy resin, cured overnight before polishing to a 1 μm diamond finish and carbon coating. The microstructure was observed using a Hitachi TM3030 SEM with Oxford Instruments Swift ED3000 silicon drift detector, using an accelerating voltage of 15 kV and a working distance of 7.8 mm. Energy dispersive X-ray spectroscopy (EDX) mapping was processed using the Bruker Quantax 70 software with maps collected for a minimum of 10 min. The average composition of each phase was calculated using a minimum of 5 EDX spot analyses, assuming stoichiometric oxygen for each phase.

7.2.2.3 Ce L_3-edge X-ray absorption near edge spectroscopy (XANES)

The average oxidation state of Ce in each ceramic material was determined using Ce L_3-edge (5723.0 eV) XANES at BM28, ESRF. The optical arrangement consisted of a Si(111) double crystal monochromator, a toroidal focussing mirror and a Si/Rh harmonic rejection mirror. Incident beam intensity was measured using an ionisation chamber, filled with mixtures of He and N_2, operated in a stable region of the I/V curve. Ce L_3-edge fluorescence was detected using a Vortex Si Drift Detector.

Specimens for XAS analysis were prepared by mixing the quantity of material required for 1 absorption length (calculated using the Hephaestus software [136]) with a minimal quantity of polyethylene glycol. The resulting powder was then uniaxially pressed into a 10-13 mm pellet to create a homogeneous pellet without pin holes. Calibration, dead time correction [160], integration, normalisation, background subtraction of XAS data was achieved using the Athena software package [136]. The spectra were analysed using linear combination fitting (LCF) to estimate the ratio of Ce^{3+}:Ce^{4+} in each product, using standard reference compounds of CeO_2 (Ce^{4+}) and $CePO_4$ (monazite; Ce^{3+}). Spectra were fitted over the range 5700 – 5760 eV, under the constraint that the fractional weights of the reference spectra sum to unity. Note that the Ce L_3-edge XANES of $CePO_4$ presents a single intense feature on the rising absorption edge, whereas CeO_2 presents three features, of lower relative intensity, for which the corresponding final state electron configurations were previously assigned [164], [217]–[219].

7.2.2.4 Compositional analysis

The composition of HIPed zirconolites were measured by X-ray fluorescence (XRF) spectroscopy prior to dissolution experiments. Powder samples were analysed by AMG Analytical Services using a Panalytical PW 2404 system with a Rh X-ray source under vacuum on pressed pellets.

7.2.3 Dissolution experiments

A derivative of the PCT-B methodology was used to complete these experiments [101], In order to accelerate the release of elements in concentrations that could be conveniently measured using ICP-MS, an aggressive leachant was used (0.01 M HNO_3). A percussion mortar was used to crush HIPed ceramic wasteform materials and sieved to retain the 75 – 150 µm size fraction. The resulting powder was sonicated in isopropanol to remove adhered fines and dried overnight at 90 ± 2 °C. Pycnometry, using a Micromeritics Accupyc 1340 II gas pycnometer, was used to measure the density of each powder. The geometric geometric surface area (SA) of each material was calculated using these density measurements. The cleaned

powder was placed into a 60 mL PFA Teflon vessel with 40 mL of 0.01 M HNO_3 solution (pH = 2), to give a surface area to volume ratio (SA/V) equal to 100 m^{-1}. Triplicate sample and blank vessels were prepared and placed into an oven at 90 °C. The vessels were removed from the oven and allowed to cool to room temperature at each sampling time point (1, 2, 3, 4, 7 and 10 d). An aliquot of leachate (0.4 mL) was removed from each vessel, diluted using 10 mL of ultra high quality (UHQ, 18 MΩ cm^{-1}) water and passed through a PTFE syringe filter. Each vessel was then sealed, weighed and returned to the oven, and removed again at the next sampling time point. Upon completion of the experiment, each solution was analysed to measure the elemental concentration using an ICP-MS (Thermofisher iCAP RQ). The normalised mass loss (NL_i) of elements from the zirconolite ceramics were calculated using Equation 7.1, where: NL_i – normalised mass loss (g m^{-2}) of element *i*, c_i – concentration of element *i* in leachate (mg L^{-1}), $c_{i,b}$ – concentration element *i* in blank (mg L^{-1}), f_i – fraction of element *i* in the ceramic and, SA/V – surface area to volume ratio (m^{-1}).

$$NL_i = \frac{(c_i - c_{i,b})}{f_i \quad SA/_V} \tag{7.1}$$

$$NR_i = \frac{NL_i}{t} \tag{7.2}$$

The normalised dissolution rate (NR_i) in g m^{-2} d^{-1} was calculated using Equation 7.2, where *t* is the dissolution time in d. The SA/V was adjusted at each sampling time point to account for the evaporative losses and leachant removal at each time point. The total volume sampled from each vessel was < 10% of the initial solution volume, ensure that the SA/V was not adjusted significantly throughout the experiment.

The elemental composition and pH of the leachates was used to perform geochemical modelling using PhreeqC v.3 software [163]. The LLNL database [144] was selected, in order to find the saturation indices (SI) of mineral phases from the database. The SI of a phase was calculated in this software using Equation 7.3, where: IAP – ion activity product for the phase and K_s^0 is the standard solubility constant of the phase.

$$SI = \log\left(\frac{IAP}{K_s^0}\right) \tag{7.3}$$

7.3 Results and discussion

7.3.1 Characterisation of wasteforms

In this study, four fluorite related ceramic formulations previously developed for the immobilisation of PuO_2 were fabricated using HIPing as the thermal treatment method. This synthesis method was used to improve the resulting microstructure of the wasteform at reduced temperatures. Each formulation is characterised separately below, with a comparison of the impact of the deduced phase assemblage on the relative chemical durability of each ceramic. This will enable a discussion on the suitability of HIPing of these wasteforms.

7.3.1.1 $(Ca_{0.9}Gd_{0.1})(Zr_{0.5}Ce_{0.2}Hf_{0.2}Gd_{0.1})Ti_2O_7$ (zirconolite A)

Zirconolite A has a formulation which targeted substitution of Ce (0.2 formula units (f.u.)), Hf (0.2 f.u.) and Gd (0.1 f.u.) onto the Ca site and Gd (0.1 f.u.) on the Zr site. In Figure 7-1, the powder XRD pattern for *zirconolite A*, revealed Bragg reflections that were indexed to zirconolite 2M and zirconolite 4M, with weak reflections assigned to perovskite. Quantitative phase analysis (QPA), using the Rietveld method demonstrated that the wasteform contained two zirconolite polytypes, 2M and 4M, which totalled 97.5 wt.% of the wasteform. The full composition consisted of zirconolite 2M = 49.2(4) wt.%, zirconolite 4M = 48.3(4) wt.% and perovskite = 2.6(3) wt.%. Analysis of the fitted unit cell

parameters for zirconolite 2M, *a* = 12.4938(5) Å, *b* = 7.2875(3) Å, *c* = 11.3865(5) Å exhibited unit cell expansion compared to the reported literature values (*a* = 12.4430 Å, *b* = 7.2729 Å, *c* = 11.3809 Å [79]). This was expected following the substitution of cations with larger radii onto the Ca and Zr sites (e.g. Ce and Gd, see Table 7-2).

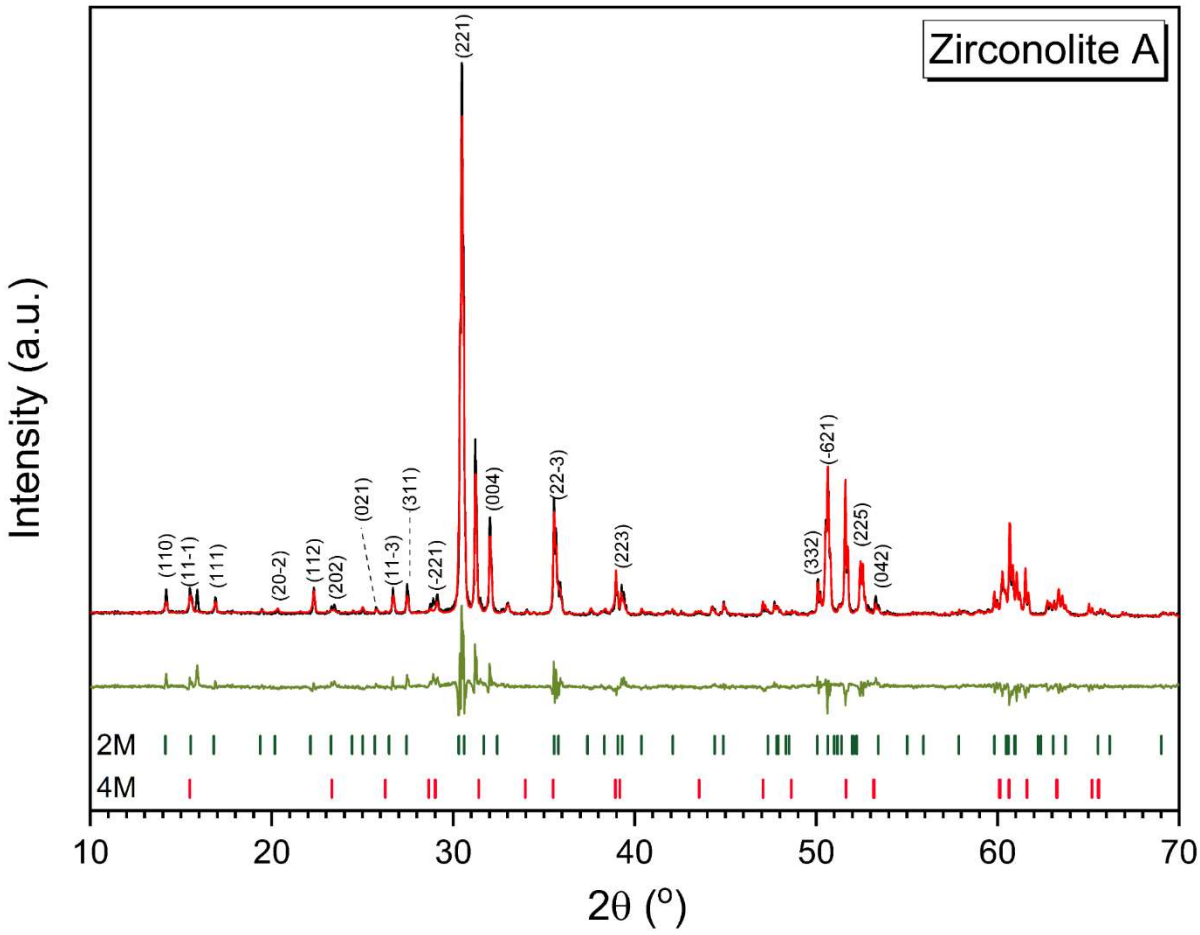

Figure 7-1 – Powder XRD pattern of $(Ca_{0.9}Gd_{0.1})(Zr_{0.5}Ce_{0.2}Hf_{0.2}Gd_{0.1})Ti_2O_7$ (black line), showing the Rietveld refinement fit (red line) and difference (green). Bragg reflections labelled for zirconolite 2M and 4M, with (hkl) values labelled for zirconolite 2M. R_p = 5.86 and R_{wp} = 8.17 %.

Table 7-2 – Coordination number of each ion targeting the Ca and Zr sites of zirconolite [88].

Ion	Target site ionic radius (Å)	
	Ca^{2+} (8-fold) – 1.12 Å	Zr^{4+} (7-fold) – 0.78 Å
Ce^{3+}	1.14	1.07
Ce^{4+}	0.97	0.92
Pu^{4+}	0.96	0.91
Gd^{3+}	1.05	1.00
Hf^{4+}	0.83	0.76

Representative BSE micrographs of *zirconolite A* are shown in Figure 7-2, which shows a fully densified material with two phases; a phase of light grey contrast and another of dark grey contrast. EDX maps in Figure 7-2 presented a Zr/Hf enrichment and depletion of Ce/Gd in the dark phase, with the trend reversed for the light phase (Ce/Gd rich, Zr/Hf deficient). This was confirmed by the EDX determined compositions for each phase (assuming oxygen stoichiometry, given the low sensitivity of EDX to oxygen determination): dark grey phase, $Ca_{0.91(7)}Zr_{0.51(9)}Ce_{0.15(1)}Gd_{0.17(2)}Hf_{0.24(5)}Ti_{2.02(1)}O_7$ (implying, $Ce^{3.9+}$); and light grey phase, $Ca_{0.89(7)}Zr_{0.55(9)}Ce_{0.23(6)}Gd_{0.17(2)}Hf_{0.12(4)}Ti_{2.04(1)}O_7$ (implying $Ce^{3.7+}$). When considering this result alongside the XRD analysis (Figure 7-1), the dark phase was assigned as zirconolite 2M and the light phase assigned as zirconolite 4M. The perovskite phase identified by XRD was not observed, which could be due to having a similar contrast to the dark phase, and/or being present in a small quantity.

Figure 7-3 shows the Ce L_3-edge XANES of *zirconolite A* alongside Ce^{3+} and Ce^{4+} reference spectra. Linear combination fitting of the spectra show Ce has an average oxidation state of $Ce^{3.63(3)+}$. The partial reduction of Ce^{4+} to Ce^{3+} is likely induced by the nickel HIP can under processing conditions, with consequent oxidation of Ni^0 to Ni^{2+}. This was reported in other work, where an oxidation state of Ce^{4+} could not be achieved in zirconolites when processed under similar conditions by HIP [189], [215]. The Ce L_3 XANES determined Ce oxidation state is representative of the bulk sample and averages over all Ce

bearing phases. Nevertheless, it can be considered representative of the average Ce oxidation state within the zirconolite phase, given the trace abundance of the (potentially Ce-bearing) perovskite phase. The average Ce oxidation state is in reasonable agreement with that implied from semi quantitative EDX analysis, within uncertainties.

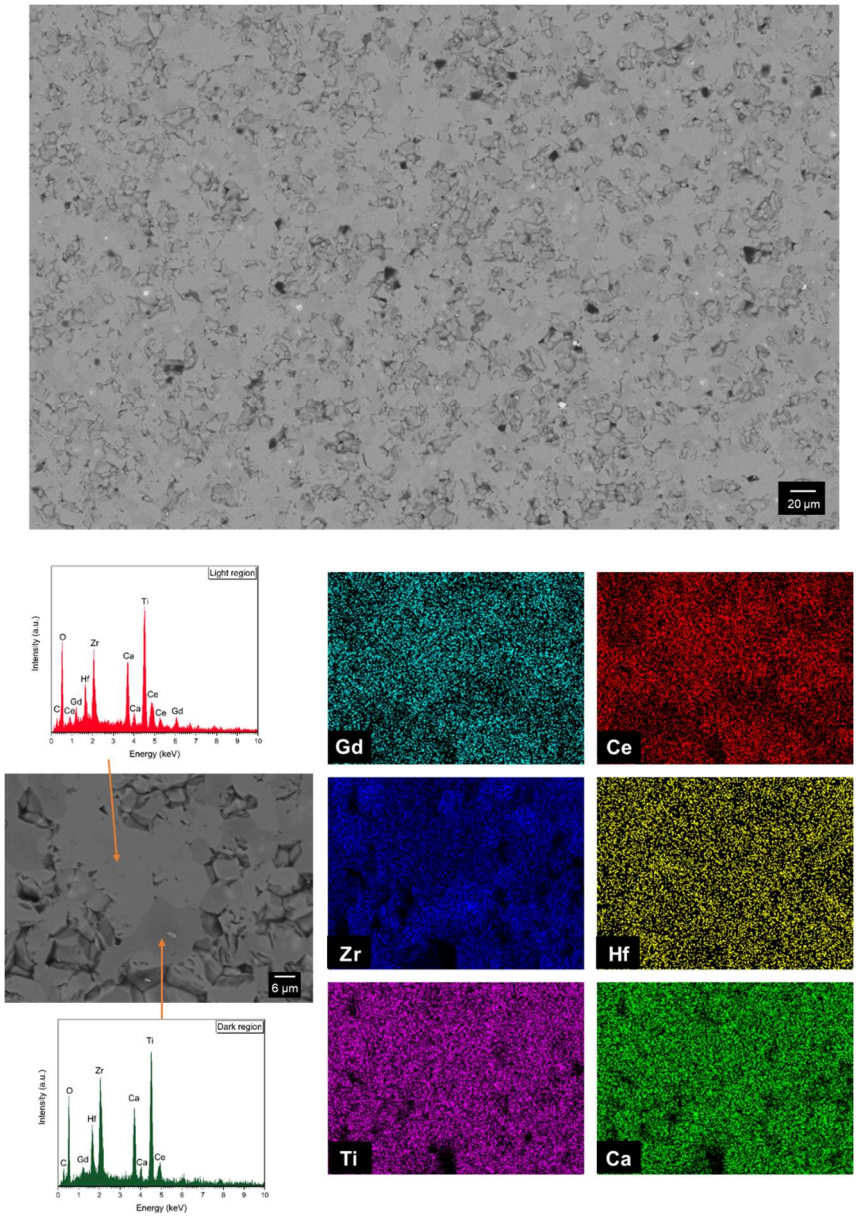

Figure 7-2 – BSE micrographs of the bulk of $(Ca_{0.9}Gd_{0.1})(Zr_{0.5}Ce_{0.2}Hf_{0.2}Gd_{0.1})Ti_2O_7$, with low magnification image (*top*) and high magnification image (*bottom*) with EDX maps and EDX spectra of the light grey and dark grey regions observed.

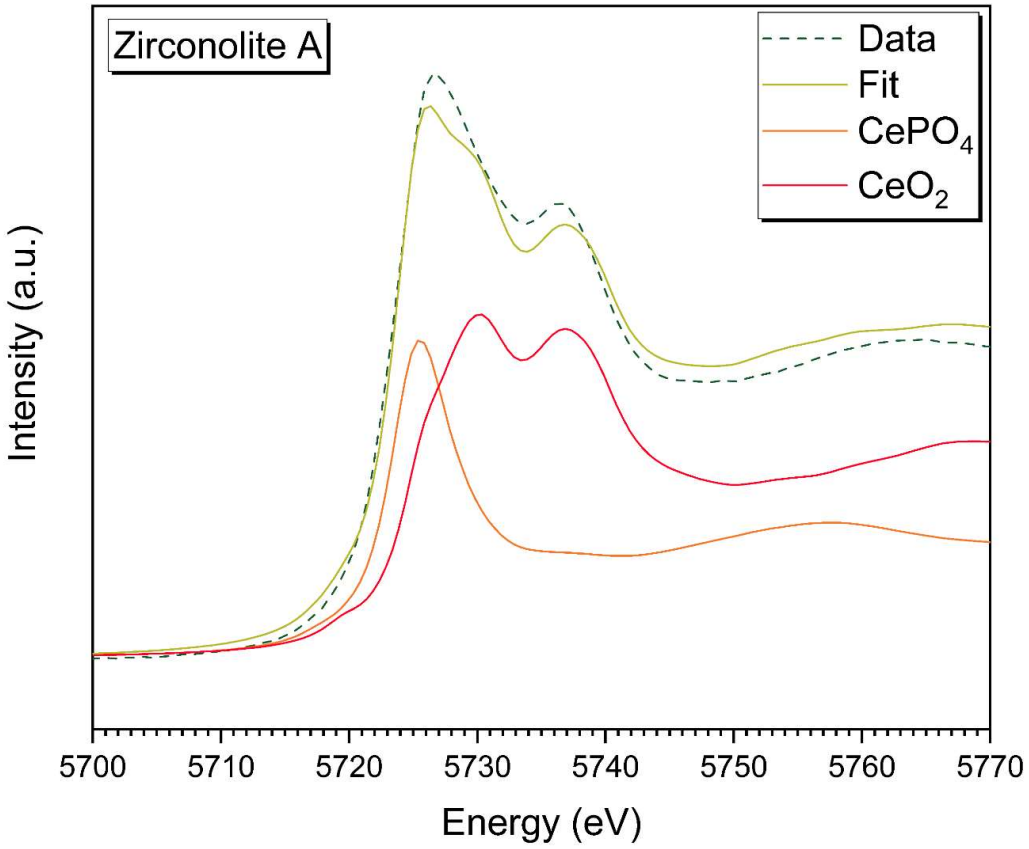

Figure 7-3 – Ce L_3-edge XANES spectra of $(Ca_{0.9}Gd_{0.1})(Zr_{0.5}Ce_{0.2}Hf_{0.2}Gd_{0.1})Ti_2O_7$ (*zirconolite A*), showing the LCF fit with $CePO_4$ and CeO_2 reference spectra.

Overall, for *zirconolite A*, the Pu surrogate and neutron absorbers were fully incorporated into the wasteform. The presence of a small quantity of perovskite measured by QPA alongside a contribution of Ce^{3+} to the average oxidation state, indicates that the perovskite phase is likely to have been Ce-bearing within this wasteform since Vance *et al.* demonstrated that 0.1 f.u. Ce^{3+} could be accommodated onto the perovskite structure without the requirement for charge balancing species [86]. Despite being a target host phase for actinides in SYNROC [231], perovskite has displayed significantly reduced chemical durability compared to zirconolite [95], therefore the presence of this secondary phase should be avoided. When considering that the reduction potential of Pu is much lower than that of Ce, it is to be expected

that Pu would remain as Pu^{4+} under these processing conditions, reducing the probability of stabilising deleterious secondary phases such as perovskite, even in trace quantities [89], [223], [239], [240].There were also two different zirconolite polytypes produced in this material, zirconolite 2M and zirconolite 4M, the latter of which has higher Ce wasteloading due to greater cation incorporation into the structure [91]. The formation of the zirconolite 4M polytype was expected since the target site for the waste loading is the Zr site [90]. This is due to the difference in ionic radii between the target site and the Ce/Gd causing restructuring of the unit cell to accommodate the larger ions [89]. The transition from the 2M to 4M polytype is reported for substitution of 0.1 – 0.2 f.u. of Ce onto the Zr site, therefore this observation is in agreement with the literature [87], [139], [241]. However, it is currently unknown whether the polytype formed has any effect on the dissolution performance of the materials.

7.3.1.2 $(Ca_{0.7}Gd_{0.1}Ce_{0.2})(Zr_{0.7}Hf_{0.2}Gd_{0.1})Mg_{0.2}Ti_{1.8}O_7$ (zirconolite B)

The *zirconolite B* formulation targeted 0.2 f.u. Ce and 0.1 f.u. Gd on the Ca site, plus 0.2 f.u Hf and 0.1 f.u. Gd on the Zr site, with 0.2 f.u. Mg on the Ti site for charge compensation. Figure 7-4 shows the powder XRD pattern for *zirconolite B*, with Bragg reflections indexed to zirconolite 2M and zirconolite 3T. Quantitative phase analysis (QPA), using the Rietveld method revealed that only zirconolite polytypes were formed (no secondary phases), comprising 95.8(4) wt.% zirconolite 2M and 4.2(4) wt.% zirconolite 3T. Analysis of the unit cell parameters for zirconolite 2M, a = 12.4950(9) Å, b = 7.2826(6) Å, c = 11.4182(9) Å, showed expansion of the unit cell compared to reported literature as expected with the substitution of cations with larger radii (Ce and Gd, see Table 7-2) onto the Ca and Zr sites. There was also an expansion of the unit cell compared to zirconolite 2M phase of the *zirconolite A* formulation. This is consistent with greater incorporation of Ce/Gd/Hf, since the majority of Ce/Gd/Hf will reside in the dominant zirconolite 2M phase in *zirconolite B* compared to across two polytypes for *zirconolite A*, as demonstrated in Figure 7-2.

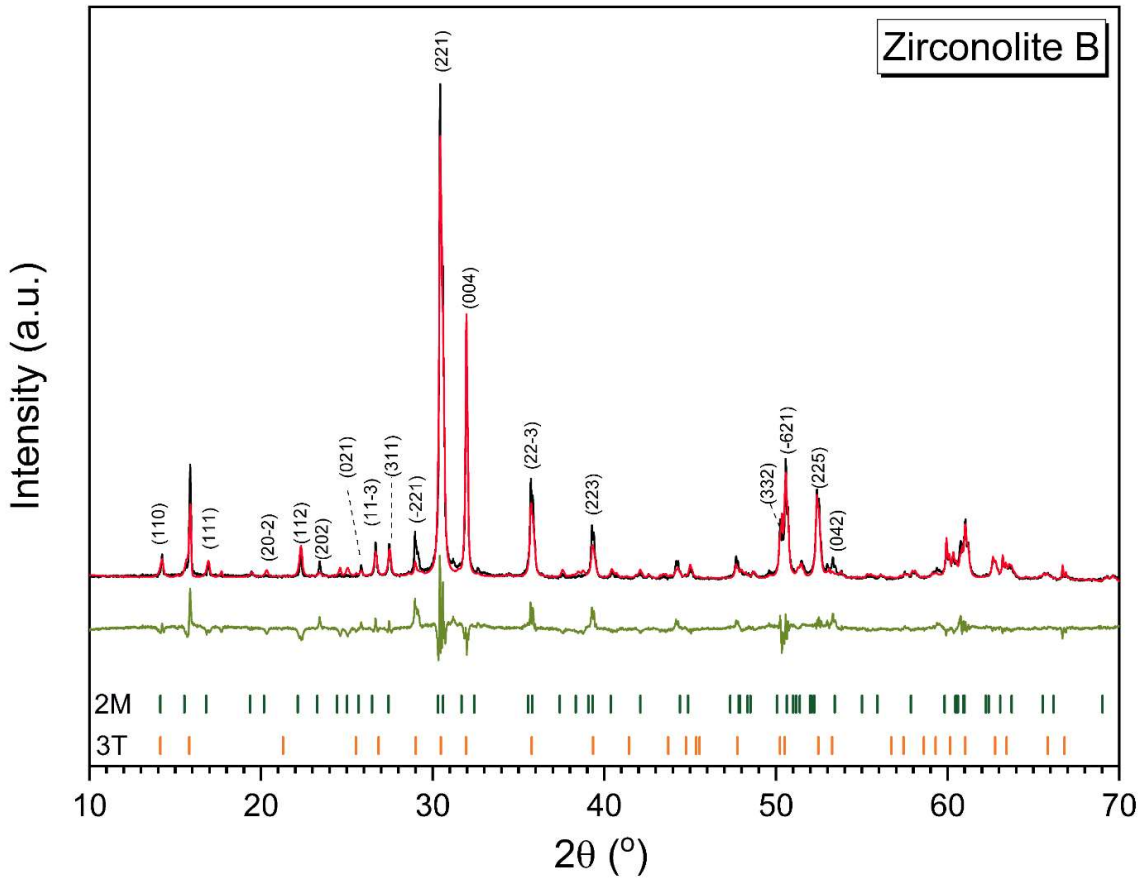

Figure 7-4 - Powder XRD pattern of *zirconolite B* ($(Ca_{0.7}Gd_{0.1}Ce_{0.2})(Zr_{0.7}Hf_{0.2}Gd_{0.1})Mg_{0.2}Ti_{1.8}O_7$) (black line), showing the Rietveld fit (red line) and difference (green). Bragg reflections labelled for zirconolite 2M and 3T, with (hkl) values labelled for zirconolite 2M. R_p = 6.81 % and R_{wp} = 9.56 %.

A representative BSE micrograph of the *zirconolite B* formulation is shown in Figure 7-5, which presents a fully densified bulk zirconolite of mid grey contrast. The EDX maps show very little difference in the composition across the bulk, with individual EDX spectra in close agreement. The average EDX derived composition was, assuming oxygen stoichiometry $Ca_{0.68(4)}Zr_{0.81(6)}Ce_{0.13(4)}Gd_{0.11(2)}Hf_{0.11(1)}Ti_{1.92(8)}Mg_{0.23(3)}O_7$ (implying, $Ce^{3.7+}$). The trace zirconolite 3T phase was not distinctively observed in the SEM micrographs, presumably due to a composition, and hence contrast, similar to the major zirconolite 2M polytype.

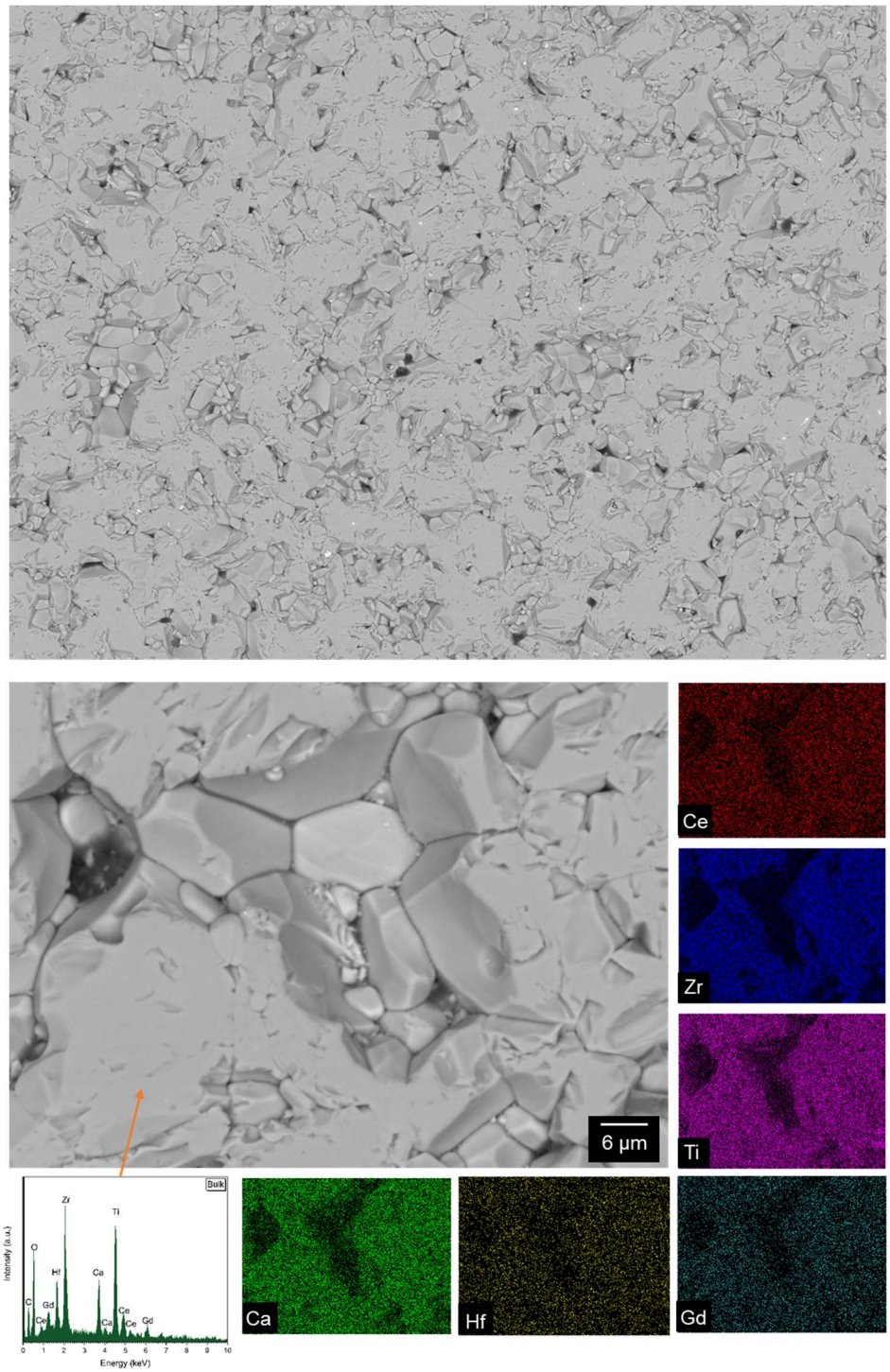

Figure 7-5 - BSE micrographs of the bulk of *zirconolite B* ($(Ca_{0.7}Gd_{0.1}Ce_{0.2})(Zr_{0.7}Hf_{0.2}Gd_{0.1})Mg_{0.2}Ti_{1.8}O_7$), with EDX maps and EDX spectra.

Figure 7-6 shows the Ce L_3-edge XANES of *zirconolite B* alongside Ce^{3+} and Ce^{4+} reference spectra. Linear combination fitting of the spectra showed that Ce has an average oxidation state of $Ce^{3.67(3)+}$, induced by redox interaction with the HIP can. This determination is in good agreement with that implied from semi quantitative EDX analysis, within uncertainties.

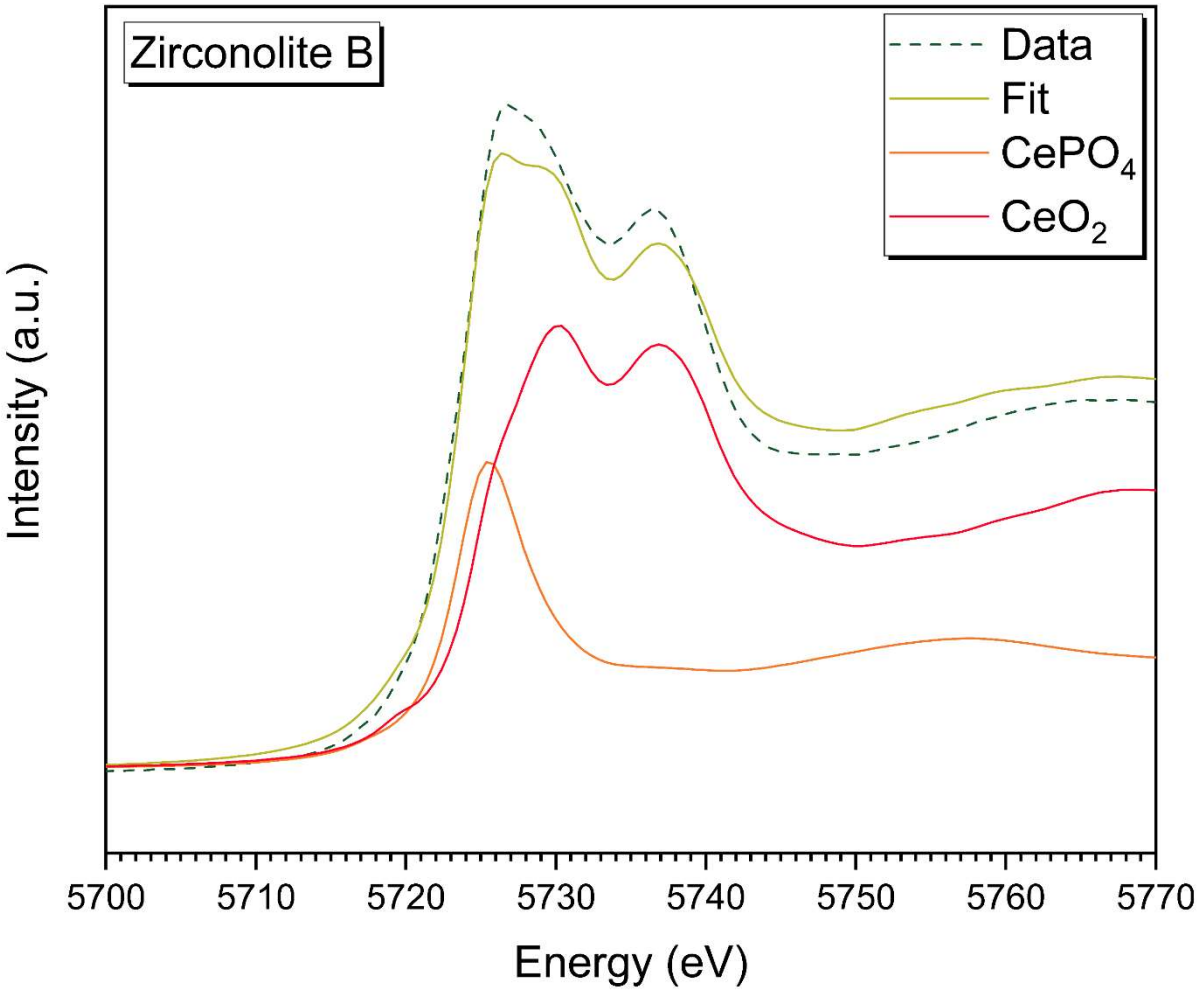

Figure 7-6 - Ce L_3-edge XANES spectra of $(Ca_{0.7}Gd_{0.1}Ce_{0.2})(Zr_{0.7}Hf_{0.2}Gd_{0.1})Mg_{0.2}Ti_{1.8}O_7$ (*zirconolite B*), showing the LCF fit with $CePO_4$ and CeO_2 reference spectra.

The *zirconolite B* formulation crystallised primarily as the zirconolite 2M polytype, with a trace of the 3T polytype, whereas the *zirconolite A* formulation afforded both zirconolite 2M and 4M polytypes in equal proportion (a trace quantity of perovskite was also formed in *zirconolite A*). Both formulations

effectively immobilised the Ce inventory, with no evidence for significant unincorporated CeO_2.

7.3.1.3 $Gd_2(Zr_{1.6}Ce_{0.2}Hf_{0.2})O_7$ (Pyrochlore)

The *pyrochlore* formulation targeted 0.2 f.u. of Ce and Hf onto the Zr^{4+} site. Figure 7-7 shows the powder XRD pattern for $Gd_2(Zr_{1.6}Ce_{0.2}Hf_{0.2})O_7$, with Bragg reflections that were indexed to pyrochlore, CeO_2 and zirconia. Quantitative phase analysis (QPA), using the Rietveld method afforded the following phase assemblage: 70(3) wt.% pyrochlore, 1.5(2) wt.% CeO_2, and 28(2) wt.% zirconia. Analysis of the fitted unit cell parameters for $Gd_2(Zr_{1.6}Ce_{0.2}Hf_{0.2})O_7$, a = 10.5970(9) Å showed expansion of the unit cell compared to reported literature for $Gd_2Zr_2O_7$ (a = 10.5327(4) Å [242]) which was expected due to the substitution of cations with larger radii onto the Zr site.

Figure 7-8 depicts a representative BSE micrograph of the $Gd_2(Zr_{1.6}Ce_{0.2}Hf_{0.2})O_7$, formulation which revealed a heterogeneous material with minimal porosity. Four distinct phases were identified with the bulk material observed as mid grey in contrast and each secondary phase characterised by an enrichment in: Hf (bright contrast), Zr (dark grey contrast), or Ce (mid grey contrast, indistinguishable from the bulk). Note that Ce L_3 XANES determined an average Ce oxidation state of $Ce^{3.95(1)+}$, for this formulation, as discussed below. EDX spectra for each phase are shown in Figure 7-8, with the average composition for each phase calculated as: bulk, pyrochlore $Gd_{2.05(10)}(Zr_{1.66(10)}Ce_{0.16(3)}Hf_{0.14(9)})O_7$ (implying $Ce^{4.0+}$, on assumption of oxygen stoichiometry); zirconia solid solutions, Hf-rich, $Gd_{0.35(5)}Hf_{0.43(5)}Zr_{0.21(3)}O_{2-x}$ (implying $x \approx 0.19$), and Zr-rich, $Zr_{0.74(7)}Gd_{0.25(7)}O_{2-x}$ (implying $x \approx 0.19$); and ceria solid solution, $Ce_{0.53(9)}Gd_{0.23(6)}Zr_{0.23(6)}O_{2-x}$ (implying $x \approx 0.19$, for $Ce^{4.0+}$). The estimated oxygen non-stoichiometry is within the range of $0.00 < x < 0.23$ reported for fluorite structured $CeO_2 – Gd_2O_3 – ZrO_2$ solid solutions [243] The EDX compositions were calculated in conjunction with XRD data to assist in making the assumptions regarding the oxygen stoichiometry for each composition. Notwithstanding, the trace ceria

solid solution, the CeO_2 inventory is otherwise immobilised in the target pyrochlore phase, which is formed with two zirconia solid solution phases rich in either Zr or Hf. This is also represented in the XRD pattern in Figure 7-7, as a broadening and shift of the peaks.

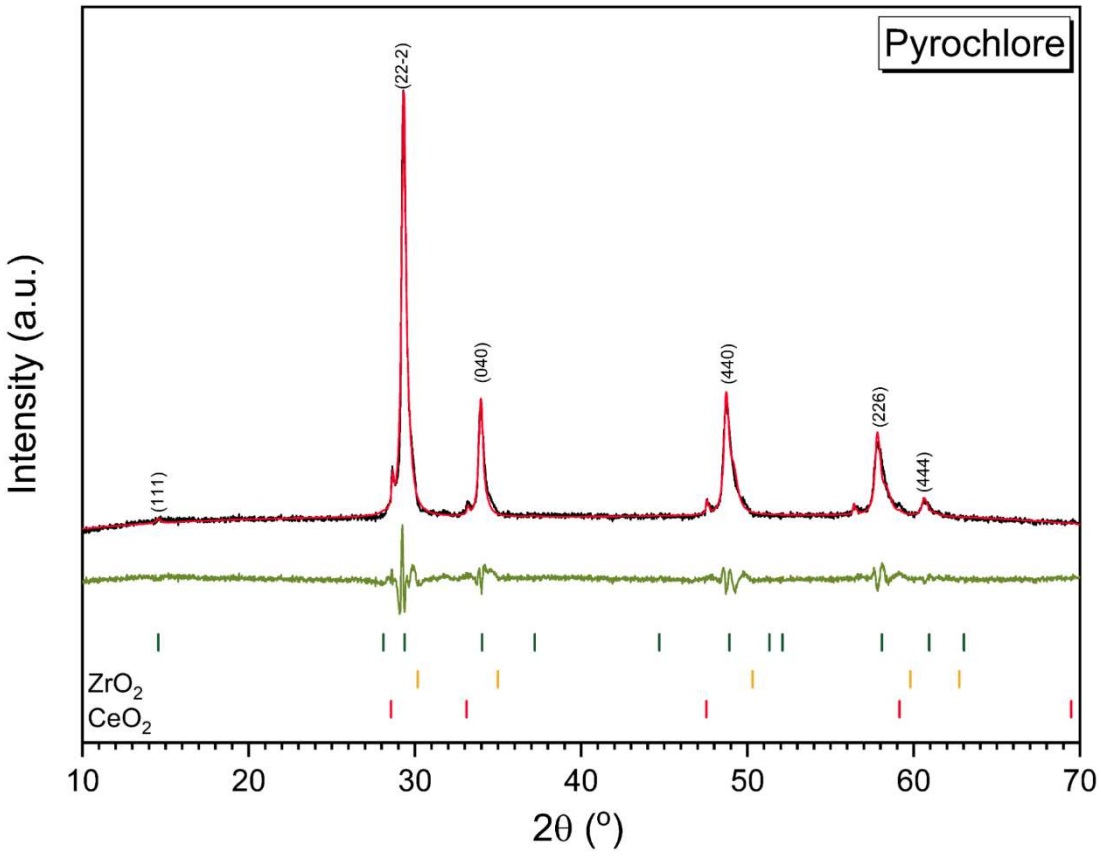

Figure 7-7 - Powder XRD pattern of the $Gd_2(Zr_{1.6}Ce_{0.2}Hf_{0.2})O_7$ specimen (black line), showing the Rietveld refinement fit (red line) and difference profile (green). Bragg reflections labelled for $Gd_2Zr_2O_7$, cubic ZrO_2 and CeO_2, with (hkl) values labelled for $Gd_2Zr_2O_7$.R_{wp} = 4.39 % and R_p = 3.19 %.

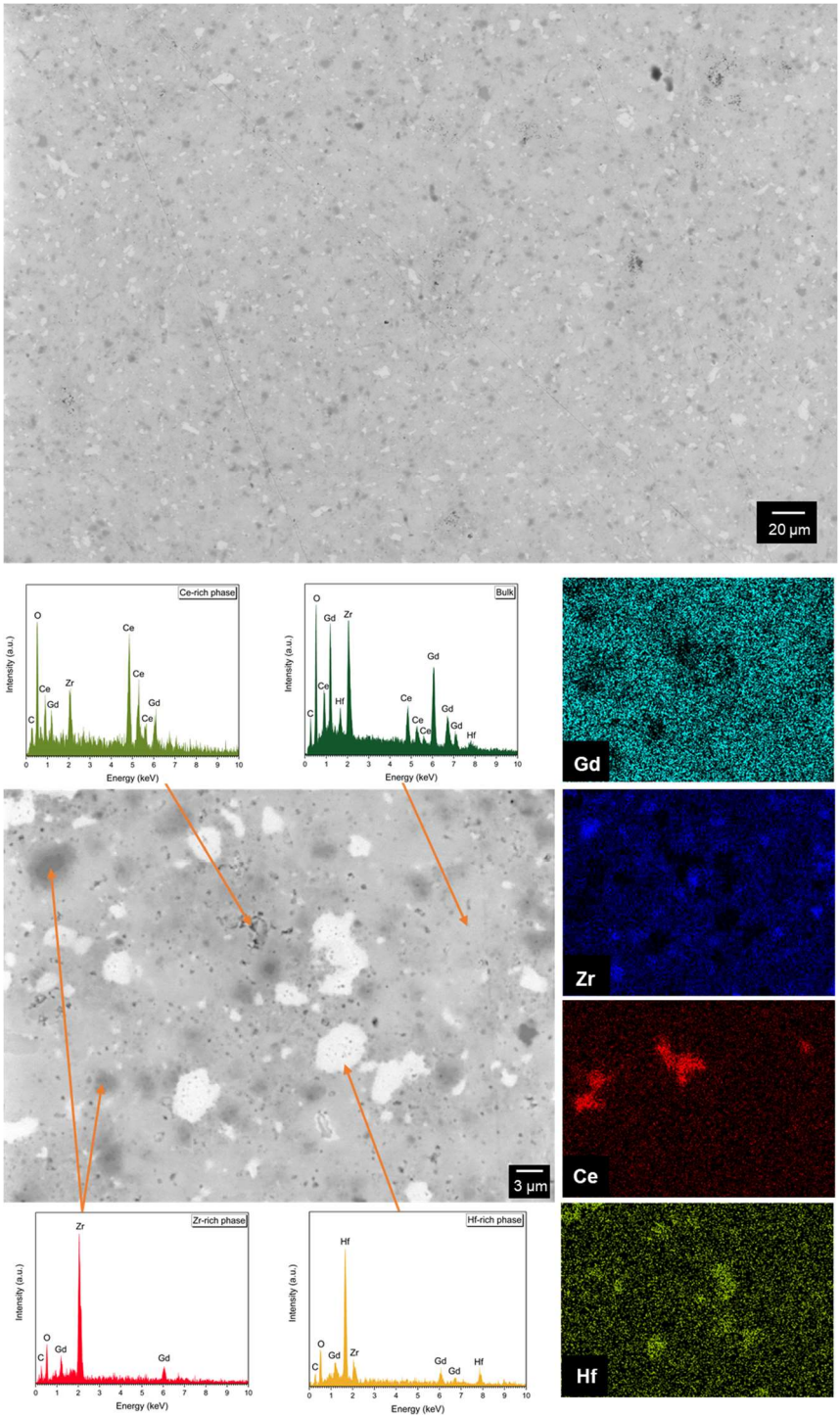

Figure 7-8 - BSE micrographs of the bulk of $Gd_2(Zr_{1.6}Ce_{0.2}Hf_{0.2})O_7$, with low magnification (*top*) and low magnification (*bottom*). EDX maps and EDX spectra for each of the four phases identified: bulk pyrochlore, Hf-rich phase, Ce-rich phase and Zr-rich phase.

Figure 7-9 shows the Ce L_3-edge XANES data of $Gd_2(Zr_{1.6}Ce_{0.2}Hf_{0.2})O_7$ alongside Ce^{3+} and Ce^{4+} reference spectra. Linear combination fitting of the spectra show Ce has an average oxidation state of $Ce^{3.95(1)+}$. The target oxidation state for Ce in the *pyrochlore* formulation is Ce^{4+} which shows that minimal reduction of Ce had occurred for this composition despite being synthesised using the same processing conditions as *zirconolite A* and *zirconolite B*. This is likely due, in part, to the absence of perovskite phase in the pyrochlore formulation, which is known to incorporate Ce^{3+}. However, even synthesis of simple single phase zirconolite 2M compositions in air, show some autoreduction of Ce^{4+} to Ce^{3+}, irrespective of whether the formulation targets Ce substitution at the Ca or Zr site [204], [241]. This suggests that zirconolite structure may be effectively stabilised by incorporation of Ce^{3+}, which is facilitated by interaction of the HIP canister in these formulations.

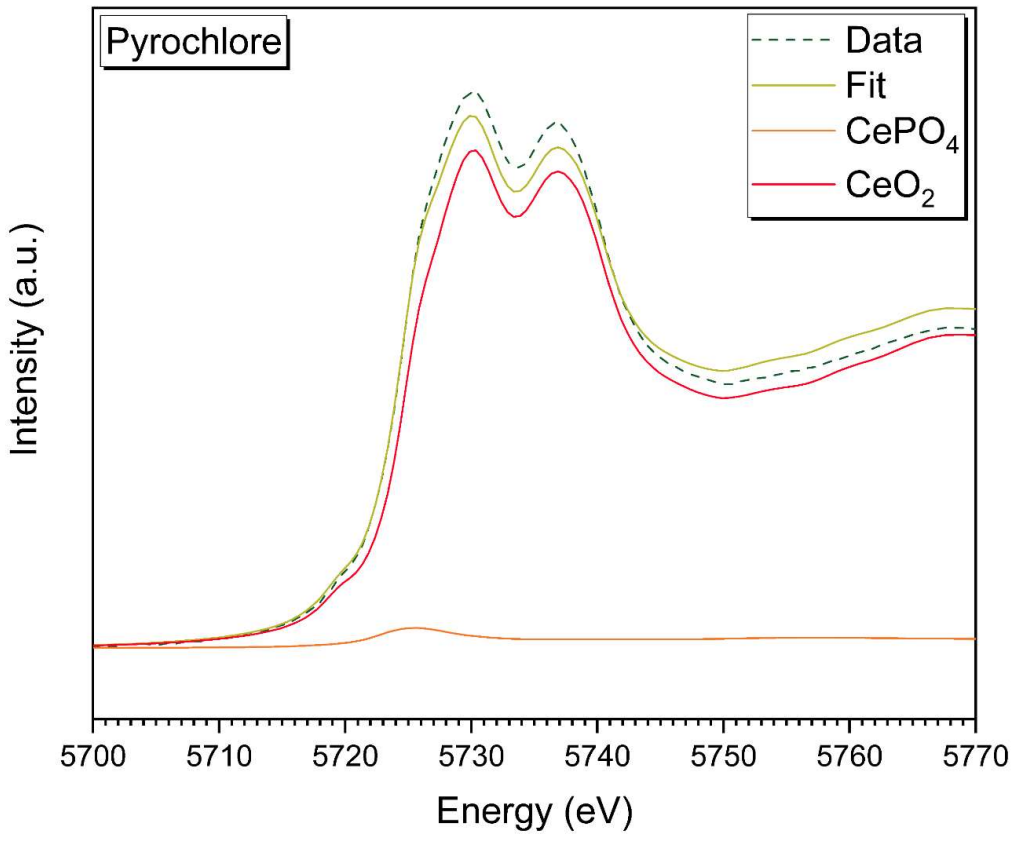

Figure 7-9 - Ce L_3-edge XANES spectra of $Gd_2(Zr_{1.6}Ce_{0.2}Hf_{0.2})O_7$ (*pyrochlore*), with $CePO_4$ and CeO_2 reference spectra.

The synthesis of this *pyrochlore* formulation resulted in a heterogeneous material which demonstrated that Ce, Gd and Hf were not fully incorporated into the pyrochlore structure. This is postulated to be due to the refractory nature of the pyrochlore structure, which provides additional challenges when synthesising these materials, but a characteristic which ensures pyrochlores are an excellent candidate for nuclear waste immobilisation [74], [244]. Figure 7-8 demonstrated that Ce was associated with a share of the neutron absorbing cations (Hf, Gd) in each phase (the bulk, Ce-rich and Hf-rich phases), ensuring that subcriticality could be maintained. Since this material was milled under the same conditions as *zirconolite A* and *zirconolite B,* this suggests that diffusion of the reagents was slower in this material, therefore more aggressive milling conditions could produce a single phase pyrochlore with an identical heat treatment. Increasing the synthesis temperature from 1350 °C to > 1500 °C could also improve the phase assemblage formed, as reported by Hyatt *et al.* [238] and Stennett *et al*. [236] when synthesising this composition using CPS, however this is not possible with the limitations on the upper processing temperature of HIPing using Ni canisters.

7.3.1.4 $(Ca_{0.1}Zr_{0.75}Ce_{0.05}Hf_{0.05}Gd_{0.05})O_{2-x}$ (cubic zirconia)

The powder XRD pattern for the $(Ca_{0.1}Zr_{0.75}Ce_{0.05}Hf_{0.05}Gd_{0.05})O_{2-x}$ *cubic zirconia* formulation is shown in Figure 7-10, with Bragg reflections that could only be indexed to cubic zirconia. Quantitative phase analysis (QPA), using the Rietveld refinement method confirmed that the zirconia wasteform was 100 wt.% cubic zirconia. Analysis of the fitted unit cell parameters for cubic zirconia, a = 5.1603(1) Å, once again showed considerable expansion of the unit cell compared to reported literature of cubic ZrO_2 (a = 5.1291(4) Å [245]).

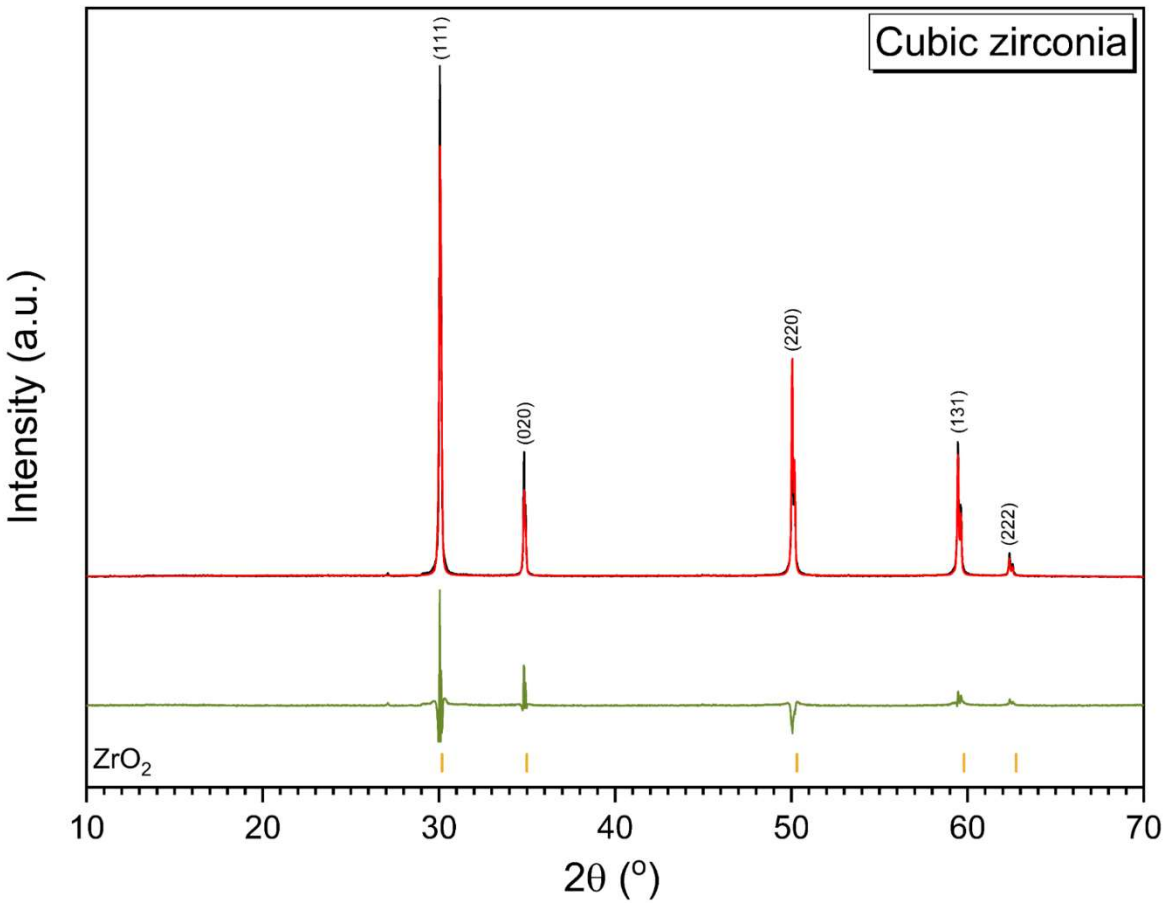

Figure 7-10 - Powder XRD pattern of $(Ca_{0.1}Zr_{0.75}Ce_{0.05}Hf_{0.05}Gd_{0.05})O_{2-d}$ (black line), showing the Rietveld refinement fit (red line) and difference (green). Bragg reflections labelled for cubic ZrO_2, with (hkl) values labelled for cubic ZrO_2. R_{wp} = 10.86 % and R_p = 7.83 %.

Figure 7-11 shows representative BSE micrograph of nominal composition $(Ca_{0.1}Zr_{0.75}Ce_{0.05}Hf_{0.05}Gd_{0.05})O_{2-x}$, which displays a fully densified material with two distinct phases present. The bulk material was mid grey in contrast with smaller regions of bright contrast, EDX spectra showed that the latter was enriched in Hf, compared to the former. Note that Ce L_3 XANES determined an average Ce oxidation state of $Ce^{3.73(1)+}$, for this formulation, as discussed below. The average composition for each phase was calculated using semi-quantitative EDX analysis with results as follows: bulk, $Ca_{0.10(1)}Zr_{0.80(2)}Ce_{0.03(1)}Hf_{0.03(1)}Gd_{0.04(1)}O_{2-x}$ (implying x = 0.12, for $Ce^{3.7+}$); and

for the bright phase, $Ca_{0.12(2)}Zr_{0.66(4)}Ce_{0.04(1)}Hf_{0.16(4)}Gd_{0.03(1)}O_{2-x}$ (implying x = 0.13, for $Ce^{3.7+}$). Again, the estimated oxygen non-stoichiometry is within the range of 0.00 < x <0.23 reported for fluorite structured CeO_2 – Gd_2O_3 – ZrO_2 solid solutions [243]. These results confirm that in the bright phase, Hf enrichment occurred as a substitute for Zr in the structure. This suggests that there are two solid solutions present in the material, a Hf-rich solution and a Zr-rich solution, however, Ce was fully incorporated into these solutions as there is no free CeO_2 identified in the XRD/SEM analysis. The bright and dark phases are postulated to both form the cubic zirconia structure, since there are no other peaks identified in the XRD pattern (Figure 7-10).

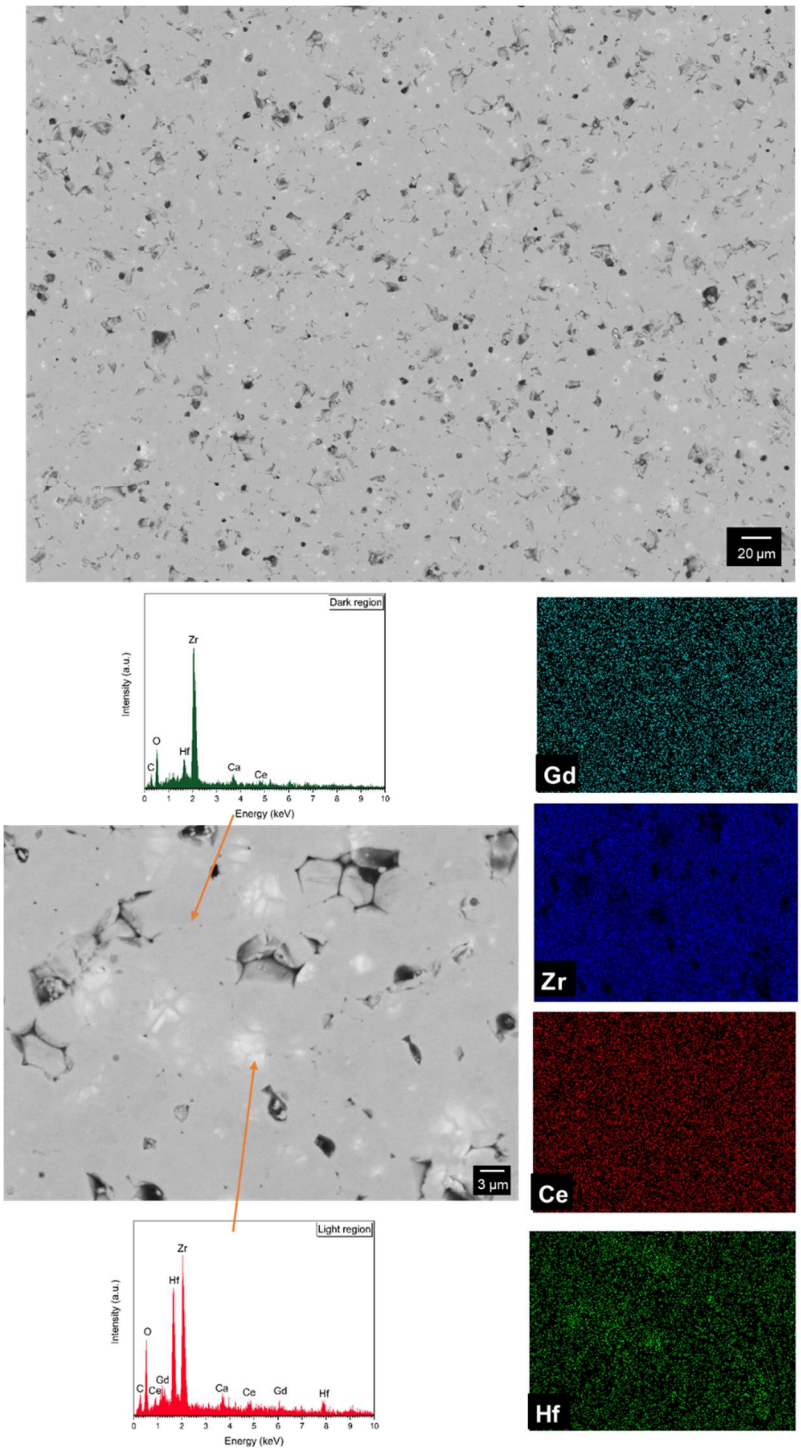

Figure 7-11 - BSE micrograph of the bulk of $(Ca_{0.1}Zr_{0.75}Ce_{0.05}Hf_{0.05}Gd_{0.05})O_{2-x}$ formulation with EDX maps and EDX spectra for each of the two phases identified with light contrast Hf-rich phase and dark contrast Zr-rich phase.

Figure 7-12 shows the Ce L_3-edge XANES of $(Ca_{0.1}Zr_{0.75}Ce_{0.05}Hf_{0.05}Gd_{0.05})O_{2-x}$ alongside Ce^{3+} and Ce^{4+} reference spectra. Linear combination fitting of the spectra show Ce has an average oxidation state of $Ce^{3.72(2)+}$. The target oxidation state for Ce in this composition is Ce^{4+} to maintain charge balance in the system, however oxygen vacancies can allow for charge balance in this material, which evidently facilitate redox interaction with the HIP can, to form Ce^{3+}.

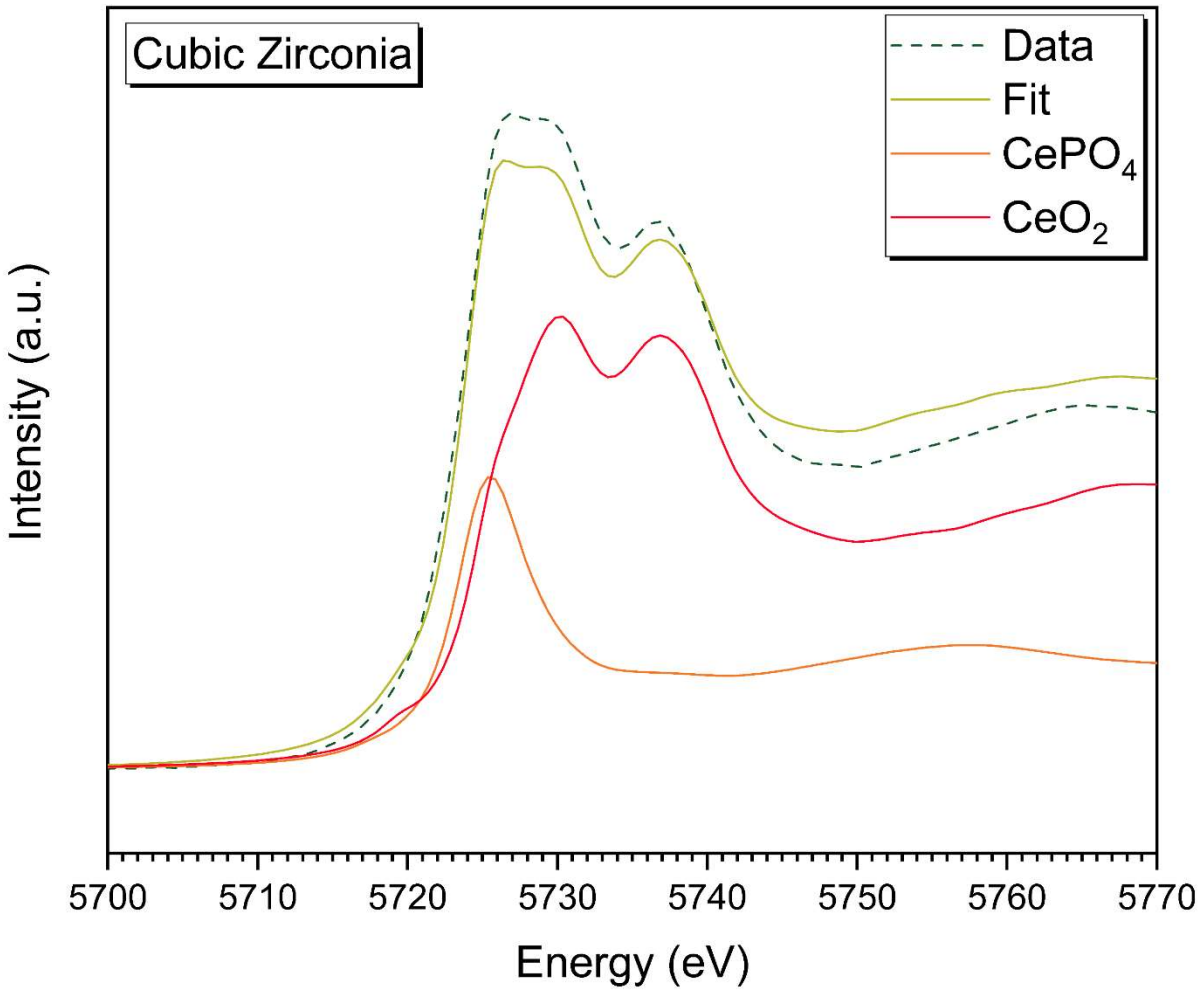

Figure 7-12 - Ce L_3-edge XANES spectra of $(Ca_{0.1}Zr_{0.75}Ce_{0.05}Hf_{0.05}Gd_{0.05})O_{2-x}$ (*cubic zirconia* formulation), showing the LCF result with $CePO_4$ and CeO_2 reference spectra.

Cubic zirconia doped with 0.05 f.u. of Ce, Hf and Gd was successfully formed with a fully densified microstructure with minimal porosity, showing some heterogeneity with respect to the relative concentration of Hf and Zr across the specimen. This was postulated to occur due to insufficient mixing of the reagents used. Increasing the synthesis temperature to > 1500 °C could improve the overall homogeneity of the sample as observed in the literature [237], however there are limitations caused by the melt temperature of containment materials, such as stainless steel and nickel, when HIPing. As with the *pyrochlore* formulation, increasing the duration of milling could improve the phase assemblage of the wasteform produced, or perhaps using a planetary mill for more aggressive size reduction of the reagents prior to HIPing. A wet synthesis route, to produce a $(Zr,Hf,Gd,Ca)O_2$ precursor, would also be advantageous as the material would have increased homogeneity due to reaction prior thermal treatment using HIPing [246].

7.3.2 Compositional analysis

A comparison between the composition of batched materials and the composition determined using XRF is shown in Table 7-3. The batched composition and XRF composition were in agreement within the expected errors. However, the phase assemblage observed in upon characterisation did not produce single phase materials as targeted. The synthesis of *zirconolite A* resulted in the formation of two different zirconolite polytypes, 2M and 4M, along with a small quantity of perovskite. Two zirconolite polytypes were also formed in *zirconolite B*, zirconolite 2M and zirconolite 3T. A heterogeneous phase assemblage was observed when characterizing *pyrochlore*, dependent upon the enrichment of Ce, Hf and Gd observed. Two fluorite solid solutions, one Zr-rich and another Hf-rich, were observed for the *cubic zirconia* produced. From this perspective, the *zirconolite* and *cubic zirconia* formulations could be considered as the most successful, effectively achieving full immobilisation of the CeO_2 surrogate inventory, in contrast to the pyrochlore formulation. In making the safety case for geological disposal of ceramic wasteforms for plutonium immobilisation, it would be preferable for the Pu inventory to be incorporated in a single phase, to avoid the complication

of modelling Pu and neutron poison release from multiple phases. Against this consideration, the *zirconolite B f*ormulation is arguably superior, affording a yield of 95.8(4) wt.% zirconolite 2M, with trace zirconolite 3T.

Table 7-3 - Comparison of the batched composition and XRF results for each HIPed ceramic formulation.

Element	Zirconolite A		Zirconolite B		Pyrochlore		Cubic Zirconia	
	Batched	XRF (± 0.1)	Batched	XRF (± 0.1)	Batched	XRF (± 0.1)	Batched	XRF (± 0.1)
	wt.%							
Ca	9.38	7.97	7.19	6.08	0.00	0.00	3.13	2.96
Zr	11.86	11.92	16.37	15.62	22.95	22.56	53.37	50.62
Ti	24.89	24.21	22.09	21.78	0.00	0.09	0.00	0.12
Mg	0.00	0.00	1.25	1.03	0.00	0.00	0.00	0.00
Gd	8.18	8.08	8.06	7.77	49.43	49.64	6.13	7.29
Ce	7.29	7.08	7.18	6.95	4.40	5.24	5.46	6.16
Hf	9.28	9.26	9.15	9.16	5.61	5.62	6.96	6.96
O	29.12	31.49	28.71	31.60	17.61	16.66	24.95	25.88
Total	100.00	100.00	100.00	100.00	100.00	100.00	100.00	100.00

7.3.3 Durability assessment

Modified PCT-B tests were performed on each HIPed ceramic material to assess the effect of the phase assemblage on their relative chemical durability, as well as the relative dissolution rate of the PuO_2 surrogate and neutron absorbers. Aggressive leaching conditions were implemented (0.01M HNO_3 at 90 °C) to ensure that kinetic dissolution data could be obtained on short time scales (< 28 d), enabling rapid evaluation of comparative dissolution behaviour.

The normalised mass loss (NL_i) for each element is shown in Figure 7-13 (*zirconolite A* and *zirconolite B*) and Figure 7-14 (*pyrochlore* and *cubic zirconia*), and the normalised dissolution rates are shown in Table 7-4. The concentration of Zr and Hf for all wasteforms were below the limits of detection for the ICP-MS.

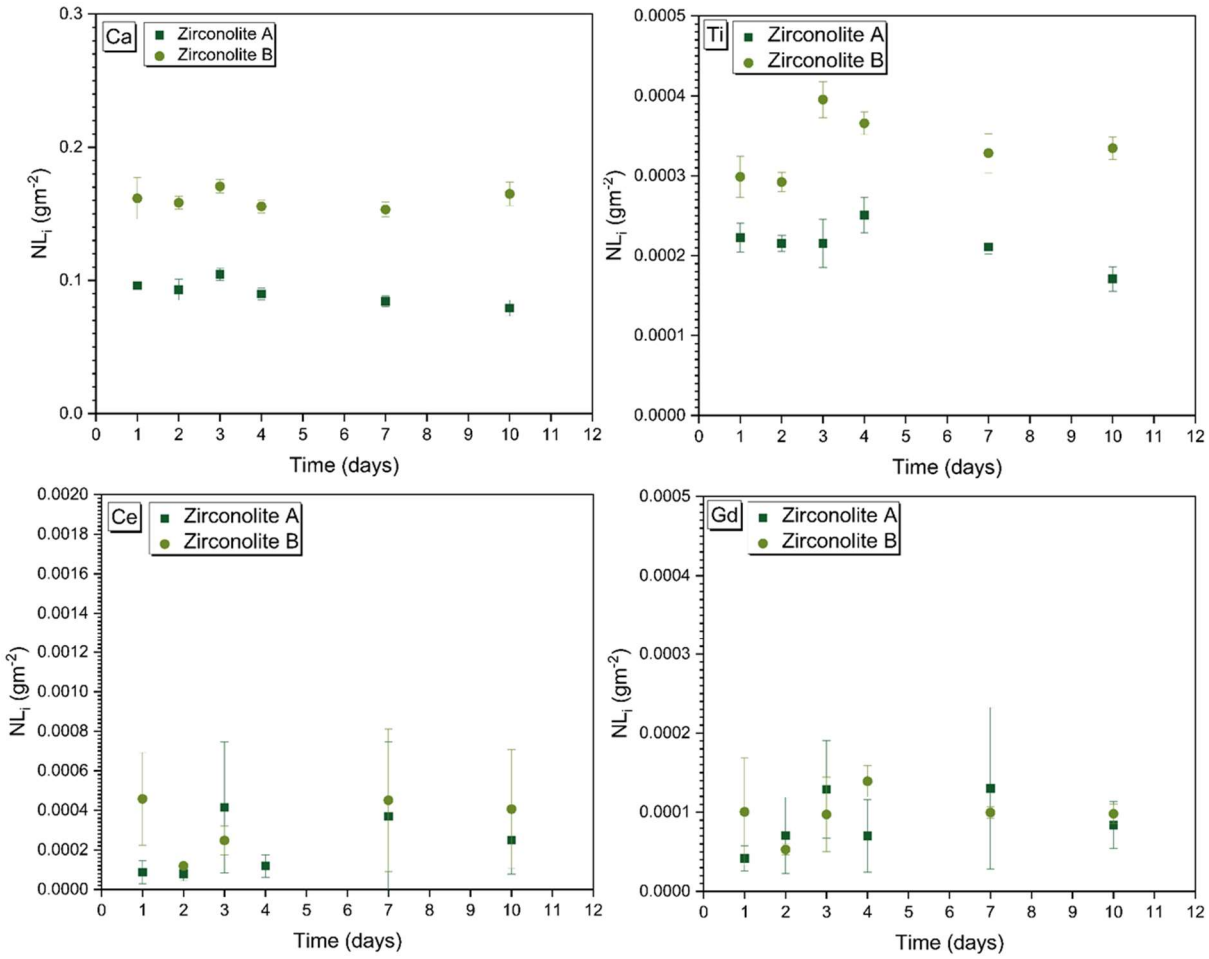

Figure 7-13 - Normalised elemental mass loss (NL_i) of Ca, Ti, Gd and Ce for PCT-B tests on *zirconolite A* (dark green) and *zirconolite B* (light green).

The NL_i for all elements in *zirconolite A* and *zirconolite B* compositions were constant within error for the duration of the experiment, which indicates that solution equilibrium was rapidly attained. The dissolution of *zirconolite A* and *zirconolite B* was incongruent, where elements such as Ca leached more rapidly than Ti, Ce and Gd, with the highest NL_i observed for Ca (0.1 - 0.2 g

m^{-2} at 10 d). The normalised mass loss for Ce, Gd and Ti was approximately three orders of magnitude lower than for Ca (0.5 – 5 x 10^{-4} g m^{-2} at 10 d). The general trend of NR_{Ce} for the materials investigated in this study is: *pyrochlore* < *cubic zirconia* < *zirconolite A* < *zirconolite B*. A similar trend was displayed for NR_{Gd}, however the release rate of Gd was at least one order of magnitude lower. This is with the exception of the pyrochlore formulation, where the release of Gd into solution is greater than for Ce, attributed to the multiphase nature of this wasteform, with the presence of 1.5 wt.% (Ce, Gd)O_{2-x} identified in Figure 7-7.

Table 7-4 – NR_i for each composition calculated from d 4 – 10. Errors in parentheses.

Composition	NR_i (g m^{-2} d^{-1})			
	Ca	Ti	Ce	Gd
Zirconolite A	0	0	2.4(1) x 10^{-5}	1.8(4) x 10^{-6}
Zirconolite B	1.0(1) x 10^{-3}	0	0	0
Pyrochlore	-	-	3.3(2) x 10^{-3}	1.5(1) x 10^{-2}
Cubic zirconia	-	-	3.7(4) x 10^{-4}	5.9(5) x 10^{-5}

Geochemical modelling (using PhreeqC) was used to determine which secondary crystalline phases were saturated with respect to the solution, based on elemental concentration analysis and pH values from PCT-B experiments. For the *zirconolite A* and *zirconolite B* formulation experiments, anatase and rutile were the only phases predicted to be saturated in solution, giving a SI of between 1 and 2. Such behaviour has previously been reported for zirconolite materials [112], [247] and of SYNROC materials [96], and it is possible that the lower NR_{Ce} observed for these materials, when compared with pyrochlore and cubic zirconia, occurs because the Ti-containing precipitates form a passivating layer.

Zirconolite A and *zirconolite B* proved to be the most durable of all of the materials, which could be attributed to their single phase nature. The small quantity of perovskite in *zirconolite A* may have contributed to the higher NR_{Ce}

of this material when compared to zirconolite B. It is also possible that the different polytypes of zirconolite dissolve at different rates, i.e. the combination of 2M and 4M in *zirconolite A* result in greater dissolution than 2M and 3T in *zirconolite B*, however the data presented here are insufficient for such a conclusion to be drawn.

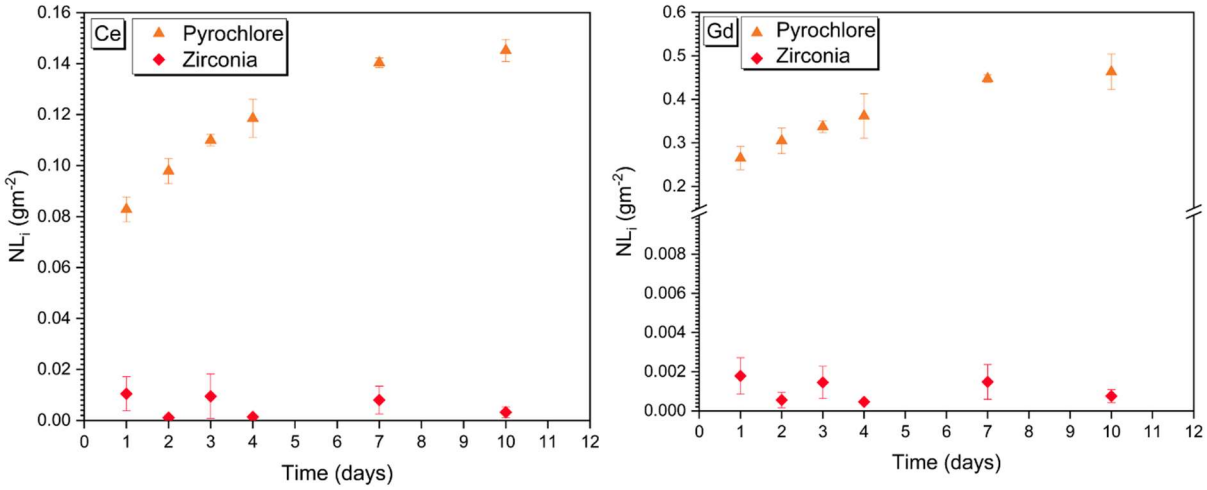

Figure 7-14 - Normalised elemental mass loss (NL_i) of Gd and Ce for PCT-B tests on *pyrochlore* (orange) and *cubic zirconia* (red).

The normalised mass loss of Ce was approximately twice that of Gd for both zirconolite formulations, even when errors and scatter are taken into consideration. However, Gd is present in a concentration at least an order of magnitude greater than required to maintain post-closure sub-criticality under the most pessimistic and conservative assumptions. No release of Zr or Hf was detected from either zirconolite formulation, which indicates that retention of Hf as a neutron poison will ensure the residual material is also maintained sub-criticality. This behaviour, when combined with the extremely low release rates of Ce and Gd provides confidence in the performance of both *zirconolite* formulations as ceramic wasteforms for Pu disposition. The performance of the *cubic zirconia* and *pyrochlore* phases may also be acceptable, if further optimised, in particular to achieve Ce and neutron poison partitioning into a single phase. However, these zirconate formulations are much more refractory

in comparison with the titanate zirconolite formulations [22], [248], and the relatively slow reaction kinetics afforded a multi-phase assemblage and microstructure in the current work. The HIP process temperature cannot be realistically increased and, therefore, one or a combination of increased dwell time, compositional modification, more reactive reagents, and aggressive milling.

When compared with the literature dissolution experiments performed in UHQ, each wasteform, with the exception of *pyrochlore*, had an NR_{Ce} value of approximately one order of magnitude greater. This result was to be expected due to the aggressive leachant implemented here, where the U release rate from zirconolite at pH = 2 was report to be approximately one order of magnitude greater than at pH = 6, at 75 °C by Roberts *et al.* [249]. The higher Ce/Gd dissolution rates presented for *pyrochlore* when compared with the literature values in UHQ, which are three orders of magnitude lower [210], [230], are due to the multiphase nature of the pyrochlore synthesised in the present investigation. In agreement with other published data on titanate ceramic dissolution [113], this serves to highlight the role of secondary phases in dissolution and the importance of developing single phase wasteforms, where the Pu/Ce inventory is fully incorporated into the target phase. Performing durability analysis on optimised homogeneous materials is required to develop understanding of the behaviour of the materials relative to the other wasteforms. As such, durability experiments should be repeated with an optimised pyrochlore to fully assess the chemical durability in fair comparison.

7.4 Conclusion

Four ceramic materials based upon the fluorite structure, including *zirconolite*, *zirconate pyrochlore* and *cubic zirconia* were synthesised for the immobilisation of PuO_2 using hot isostatic pressing as a thermal treatment method. CeO_2 was used as a PuO_2 surrogate, with the addition of neutron absorbers (Gd/Hf) to provide a preliminary understanding of their role in the

phase assemblage, and their effect on the durability of these materials. *Zirconolite* and *cubic zirconia* successfully incorporated Ce, Hf and Gd into the ceramic structure, however some heterogeneity was observed for the *zirconate pyrochlore* composition (likely due to processing conditions). Dissolution experiments using the PCT-B methodology in aggressive conditions (0.01M HNO_3 at 90 °C) showed equilibrium was reached rapidly for Ca, Ce, Gd and Ti for the *zirconolite* and *cubic zirconia* compositions, with dissolution rates comparable to those reported in the literature (when the aggressive conditions were considered). The NR_{Ce} and NR_{Gd} were within the one order of magnitude for these compositions which provides confidence that subcriticality will be maintained in a post-closure scenario. The heterogeneity in the *pyrochlore* composition, including a $(Ce,Gd)O_{2-x}$ solid solution, is postulated to have increased the dissolution rate for Ce and Gd to three orders of magnitude above those reported in the literature, however, caution is urged as the processing conditions for this formulation were not optimised. Zirconate pyrochlore ceramics typically achieve $NR_{Ce,\ Gd} = 10^{-5} – 10^{-6}$ g m^{-2} d^{-1}, similar to dissolution rates measured for zirconolite and cubic zirconia in this work. In summary, further optimisation of the synthesis technique is required for the pyrochlore formulation is ensure full waste incorporation, however the zirconolite and cubic zirconia formulation show some promise for the application, where the use PuO_2 could be used to further demonstrate this.

Acknowledgements

ARM is funded by the Engineering, Physical Sciences Research Council via the Next Generation Nuclear Centre for Doctoral Training (EP/L015390/1). NCH is grateful to the Royal Academy of Engineering and Nuclear Decommissioning Authority for funding. This research utilised the HADES/MIDAS facility at the University of Sheffield established with financial support from EPSRC and BEIS, under grant EP/T011424/1 [186]. This research used BM28 (XMaS) at the European Synchrotron Radiation Facility. XMaS is a UK national research facility supported by EPSRC. We are grateful to all the beamline team staff for their support.

8 Molten salt synthesis of Ce doped zirconolite for the immobilisation of pyroprocessing wastes and separated plutonium

Amber R. Mason, Florent Y. Tocino, Martin C. Stennett, Neil C. Hyatt*

Immobilisation Science Laboratory, Department of Materials Science and Engineering, University of Sheffield, Sir Robert Hadfield Building, Sheffield S1 3JD, UK

**To whom correspondence should be addressed. Email n.c.hyatt@sheffield.ac.uk, phone +44 (0) 114 222 5470*

PLEASE NOTE THAT THIS CHAPTER CAN BE FOUND IN THE PUBLISHED FORMAT IN APPENDIX A.

ABSTRACT

Molten salt mediated synthesis of zirconolite $Ca_{0.9}Zr_{0.9}Ce_{0.2}Ti_2O_7$ was investigated, as a target ceramic matrix for the clean-up of waste molten salts from pyroprocessing of spent nuclear fuels and the immobilisation of separated plutonium. A systematic study of reaction variables, including, reaction temperature, time, atmosphere, reagents and composition, was made to optimise the yield of the target zirconolite phase. Zirconolite 2M and 3T polytypes were formed as the major phase (with minor perovskite) between 1000 – 1400 °C, in air, with the relative proportion of 2M polytype increasing with temperature. Synthesis under 5% H_2/N_2 or Ar increased the proportion of minor perovskite phase and reduced the yield of the zirconolite phase. The yield of zirconolite polytypes was maximised with the addition of 10 wt.% TiO_2 and 5 wt.% TiO_2, yielding 91.7 ± 2.0 wt.% zirconolite, primarily as the 2M polytype, after reaction at 1200 °C for 2 h, in air. The particle size and morphology of the zirconolite product bears a close resemblance to that of the TiO_2 precursor, demonstrating a dominant template growth mechanism. Although the molten salt mediated synthesis of zirconolite is effective at lower

reaction temperature and time, compared to reactive sintering, this investigation has demonstrated that the approach does not offer any clear advantage with over conventional reactive sintering for the envisaged application.

Keywords: nuclear applications (E), spectroscopy (B), molten salt synthesis

8.1 Introduction

Pyrochemical reprocessing (pyroprocessing) is an advanced method of recycling spent nuclear fuel (SNF) where the U, Pu and minor actinides (MA) are separated from the fission products (FP) by electrorefining in a molten salt eutectic [250]. An advantage of pyroprocessing over conventional aqueous reprocessing is that a separated Pu stream is no longer generated, which reduces the associated proliferation risk [24]. The waste stream generated via this process is typically a chloride salt eutectic with entrained MA and FP, plus trace residual Pu. Chloride rich waste streams such as these are challenging to immobilise using traditional high level waste (HLW) immobilisation methods since the chloride anion has low solubility in borosilicate glasses, which have, hitherto, been applied for HLW immobilisation [3]–[7].

Zirconolite (prototypically $CaZr_xTi_{3-x}O_7$ where $0.8<x<1.35$) is a crystalline titanate ceramic material and is the targeted actinide host phase in SYNROC C [139]. It exists in the space group C2/c and has several polytypes: 2M, 3O, 3T, 4M and 6T, with the most common being the monoclinic 2M structure [84], [139], [223], [254]. In the 2M structure, Ca and Zr adopt 8- and 7-fold coordination, respectively, as CaO_8 and ZrO_7 polyhedra; whereas, Ti adopts mixed 6-fold and 5-fold coordination, as TiO_6 and TiO_5 polyhedra, with the latter site being 50% occupied [7]. Synthetic zirconolite has natural analogue minerals retaining lanthanides and actinides dated to be millions or hundreds of millions of years old, which further demonstrates its long-term radiation stability and chemical durability over geological timescales [77], [232], [255], [256]. The lanthanide and actinide elements are usually found on the Ca site with charge balancing cations, such as Al or Mg, on the Ti site [77], [139].

Molten salt synthesis (MSS) is a method of producing ceramic materials which typically uses a chloride salt eutectic to reduce the diffusion distance of the ceramic reagents. This method generally produces a material that is homogeneous at a lower synthesis temperature and reaction time compared to traditional solid state synthesis methods [35]. The chloride salts can be

dissolved upon completion of the reaction to recover the synthesised ceramic material. Conventional solid state synthesis of zirconolite, requires reactive sintering at 1450 °C for several hours, often with several cycles of heat treatment and intermittent grinding [257]. In comparison, zirconolite can be synthesised at 1200 °C in only a few hours, in the presence of a NaCl:KCl molten salt eutectic, with a melting point of approximately 658 °C [258]. There are two bounding mechanisms observed in the MSS of ceramic materials: dissolution-precipitation and template growth [122], [259]–[263], which are dependent on the solubility of ceramic reagents in the salt eutectic. Dissolution-precipitation is favoured when all reagents are comparably soluble in the salt eutectic and subsequently react to form a product. Template growth occurs when one reagent is less soluble and acts as a template onto which the other more soluble reagents are deposited, at which point the product is formed. This mechanism allows the microstructure of the sample to be controlled resulting in uniform grain size and morphology [122].

This investigation seeks to develop the approach of decontaminating the chloride molten salt waste from pyroprocessing, by using the salt itself as a medium for the synthesis of a titanate ceramic wasteform to incorporate the long lived lanthanides, MA and trace Pu [16], [49], [52], [264], [265]. Zirconolite was selected as the titanate ceramic wasteform, with Ce utilised as a non-active structural surrogate for the actinide and lanthanide elements due to having a similar ionic radius, accessible oxidation states, and crystal chemistry [140], [141], [240]. The target composition for the wasteform was $Ca_{0.9}Zr_{0.9}Ce_{0.2}Ti_2O_7$, where Ce was substituted on both the Ca and Zr sites. This is a charge compensated composition, targeting an equal proportion of Ce^{3+} ions on the Ca and Zr sites, without the requirement of additional charge compensating species on the Ti site. The target formulation was devised to incorporate Ce, as a MA/Pu surrogate, at a realistic concentration for a conceptual ceramic wasteform.

The NaCl:KCl eutectic composition was chosen as a model system relevant to wastes arising from pyrochemical reprocessing of mixed oxide $(U,Pu)O_2$

fuels using the Dimitrovgrad Dry Process at the Research Institute for Atomic Reactors in Russia and early pyrochemical reprocessing of short cooled Experimental Reactor Breeder II metallic fuel at Argonne National Laboratory – West (now Idaho National Laboratory), USA [15], [266]. Additionally, a NaCl:KCl eutectic was used in experimental pyrochemical reprocessing of thorium high temperature reactor fuels undertaken at Joint Research Centre-Institute for Trans Uranium Elements (JRC-ITU) [267]. The UK is also undertaking strategic assessment of pyrochemical recycle of used nuclear fuels, including design and demonstration of wasteforms for decontamination and immobilisation of lanthanides and residual actinides from alkali chloride molten salts.

A further motivation for our research is management of the UK plutonium stockpile, which is projected to exceed 140 tons at the end of current reprocessing options [16]. A significant fraction of the plutonium stockpile will require immobilisation in a suitable waste form, since it is unsuitable for reuse in MOX fuel, which is the preferred management approach at the present time [15]. Some of this material is contaminated by chlorine, as a result of the degradation of the polyvinylchloride packaging used to store the material [28]. A zirconolite ceramic is the leading candidate waste form for immobilisation of this stockpile and, therefore, a rapid and low temperature MSS process could be advantageous for ceramic waste form manufacture, given the presence of chlorine as a contaminant. Gilbert previously established the NaCl:KCl eutectic to be the most advantageous for zirconolite synthesis [258], although the yield was only 86 wt.% after reaction at 1000 °C. In contrast, the yield of zirconolite was 24 wt.% in the case of $CaCl_2$:NaCl eutectic at 1000 °C, whereas zirconolite failed to form when utilising a $MgCl_2$:NaCl eutectic. Note that this work focused the synthesis of the stoichiometric parent phase but did not consider the incorporation of a MA/Pu surrogate. Our choice of NaCl:KCl eutectic composition as the MSS medium was also made with due regard to potential application to the immobilisation of chloride contaminated plutonium stockpile material in a zirconolite ceramic, using Ce as a Pu surrogate.

8.2 Materials and methods

A NaCl:KCl eutectic (1:1 molar ratio) with a salt to ceramic molar ratio of 7:1 was primarily used in this study with the aim of producing single phase Ce doped zirconolite, based upon the work of Gilbert [258] as referenced above. To optimise the yield of the target zirconolite phase, the following reaction variables were systematically investigated: salt to ceramic ratio (3:1 – 9:1), synthesis temperature (1100 °C – 1400 °C), time at synthesis temperature (2 – 8 h), atmosphere (air, Ar or 5% H_2/N_2), Ce source (CeO_2 or $CeCl_3.7H_2O$), stoichiometric or excess quantities of ZrO_2 and TiO_2 reagents (excess, respectively, of 10 wt.% and 5 wt.%).

8.2.1 Materials

CaO(Alfa Aesar purity 98%), TiO_2 (anatase) (Sigma Aldrich, 99% purity), ZrO_2 (Sigma Aldrich, purity 99%), $CeCl_3.7H_2O$ (Sigma Aldrich, >99% purity) and CeO_2 (Fisher Scientific purity >99%) were used as reagents. NaCl (Sigma Aldrich, purity 99%) and KCl (Sigma Aldrich, purity 99%) were used as the molten salt flux. All reagents, with the exception of CaO and $CeCl_3.7H_2O$, were dried overnight at 180 °C before use.

8.2.2 MSS - $Ca_{0.9}Zr_{0.9}Ce_{0.2}Ti_2O_7$

A 1:1 molar ratio of NaCl and KCl was mixed (30 Hz, 5 min) in a Fritsch Pulverisette 6 planetary mill with cyclohexane as a carrier fluid to produce the salt flux. Stoichiometric quantities of ceramic reagents were weighed according to the composition $Ca_{0.9}Zr_{0.9}Ce_{0.2}Ti_2O_7$ and mixed using the same conditions as the salt flux. A short mixing time was used to prevent size reduction of the reagents and preserve the particle morphology, to assist later assessment of the role of templating or dissolution-precipitation reaction mechanism. A 0.5 g batch with a molar ratio of 7:1 salt eutectic:ceramic was mixed in a Fritsch Mini Mill 23 with cyclohexane as a carrier fluid (30 Hz, 5 min). The resulting slurry was dried at ~95 °C, sieved through a 212 µm mesh to separate from the milling media. The powder was uniaxially pressed in a 10 mm hardened stainless-steel die with a 1 ton load and held for one minute to

produce a green pellet. The green pellets were placed in an alumina crucible and heated in a muffle furnace to 300 °C for 1 h to remove any entrained moisture and then reacted at 1200 °C for 2 h in air with a 5 °C min^{-1} heating/cooling rate. The resulting reacted pellet was crushed into a fine powder using a pestle and mortar. The powder was washed with deionised water to remove the salt flux and vacuum filtration used to recover the product.

The above method was repeated with independent changes of experimental variables as follows: salt to ceramic ratio (3:1, 5:1 and 9:1), synthesis temperature (1100 °C, 1300 °C and 1400 °C), furnace atmosphere (flowing 5% H_2/N_2 and Ar), furnace dwell duration (4 h and 8 h) and varying excess of ZrO_2 and TiO_2 reagents. Additionally, materials were produced using $CeCl_3.7H_2O$ (Sigma Aldrich, >99% purity), as the MA/Pu surrogate, replacing CeO_2 in the ceramic batch.

After refinement of the experimental parameters discussed above, the optimum synthesis conditions were used to produce Ce doped zirconolite using MSS, with the resulting powder being uniaxially pressed into a ceramic body. The ceramic body was placed into a furnace and reacted in air at 1350 °C for 20 h, and the resulting ceramic was characterised.

8.2.3 Materials characterisation

Powder X-ray diffraction of reagents and products was performed with a Bruker D2 Phaser X-ray Diffractometer with a Ni filtered Cu Kα radiation (λ = 1.5418 Å) source, operating at 30 kV and 10 mA. Diffraction patterns were collected from 10° < 2θ < 70° with a step size of 0.02° 2θ and dwell time of 38 s per step. The ICDD PDF-4+ database and ICSD sources were used to identify the phases present in each sample. The PDF numbers used for the pattern identification are: $CaZrTi_2O_7$ 2M (01-084-0163), $CaZrTi_2O_7$ 3T (01-072-7510), ZrO_2 (01-072-1669), TiO_2 (16-934), CeO_2 (01-081-0792) and $CaTiO_3$ (01-082-0228). XRD patterns were refined to provide quantitative phase analysis using the Bruker TOPAS software [216].

Secondary electron imaging of the microstructure of reagents and ceramic products was performed using a Philips XL 30 scanning electron microscope (SEM) at a working voltage of 20 kV. The powders were mixed with isopropanol in a beaker and placed in an ultrasonic bath. The resulting mixture was mounted onto aluminium pin stubs using carbon tabs, allowing for the isopropanol to evaporate before carbon coating.

The microstructure of the final sintered ceramic body was observed using a Hitachi TM3030 SEM with Oxford Instruments Swift ED3000 silicon drift detector. Energy dispersive X-ray spectroscopy (EDX) mapping was processed using the Bruker Quantax 70 software with maps collected for a minimum of 10 min. The ceramic body was mounted in epoxy resin, polished to a 1 μm optical finish and carbon coated prior to analysis.

The Ce oxidation state in each sample was determined from analysis of X-ray absorption spectroscopy data at the Ce L_3 edge (5723.0 eV). Measurements were conducted at the National Synchrotron Light Source II (NSLS-II) at Brookhaven National Laboratory (Upton, New York) on beamline 6-BM. NSLS-II operates at 3 GeV storage ring with a 400 mA current and 6-BM utilises a 3-pole wiggler to deliver X-rays in the energy range between 4.5 and 23 keV. The optical arrangement consists of a parabolic collimating mirror, a Si(111) monochromator, a toroidal focussing mirror, and a harmonic rejection mirror. For this study an unfocussed beam was used, and the beam size was limited to 0.5 mm in the vertical and 6 mm in the horizontal using slits. An ionisation chamber was used to measure the incident X-ray energy and the fluorescence signal was collected using a SII Vortex ME4 (4-element) Si drift detector. To optimise collection efficiency, the samples were mounted at 45° to both the incident X-ray beam and the vortex detector. The fluorescence signal was dead-time corrected as previously described in Woicik et al. [160]. Spectra were recorded between 5533 and 5965 eV with energy steps of 10 eV (5533 – 5693), 2 eV (5693 – 5713), 0.3 eV (5713 – 5783) and 0.05k (5783 – 5965). An accumulation time of 0.5 s $step^{-1}$ was used for the first three regions and 0.25k $step^{-1}$ for the final region. Multiple scans were collected for each sample

and averaged to improve the signal to noise ratio. To ensure energy reproducibility (± 0.05 eV) a CeO_2 standard was measured simultaneously with each sample; the CeO_2 standard was placed downstream of the sample and the transmitted intensity was measured using an ionisation chamber. Absolute energy calibration was performed by measuring a Cr foil and setting the position of the first inflection point in the derivative spectrum to 5989 eV [193]. Samples, and reference compounds, were prepared by homogenising finely powdered sample with polyethylene glycol and uniaxial pressing to form a 13 mm pellet with a thickness equivalent to 1 absorption length. Data reduction and linear combination fitting (LCF) were performed using the Athena software package [136] allowing the proportion of Ce^{3+} in each sample to be calculated.

8.3 Results

We first attempted MSS of $Ca_{0.9}Zr_{0.9}Ce_{0.2}Ti_2O_7$ at 1200 °C with a 2 h reaction time, in air, and a salt to ceramic ratio of 7:1 on a molar basis (the synthesis conditions used by Gilbert to produce the parent $CaZrTi_2O_7$ zirconolite by MSS [258]). However, secondary phases of ZrO_2 and $CaTiO_3$ were observed (Figure 8-1). Based on these results, several experimental parameters were varied to achieve a single phase ceramic product (e.g. salt to ceramic ratio, temperature, dwell duration, atmosphere, Ce source, excess reagents). It is desirable that a single phase wasteform is obtained since the accessory perovskite phase may also act as a host for Ce/Pu but has comparatively poor aqueous durability and radiation tolerance [37]. We first investigated the effect of salt to ceramic ratio (3:1, 5:1, 7:1, 9:1) on the MSS of $Ca_{0.9}Zr_{0.9}Ce_{0.2}Ti_2O_7$ at 1200 °C, with a 2 h reaction time, in air. As shown in Figure S8-1, the phase assemblage was observed to be invariant comprising a major zirconolite 2M phase, minor perovskite, and trace zirconolite 3T, residual ZrO_2 and TiO_2 reagents. Accordingly, the salt to ceramic ratio was fixed at 7:1, on a molar basis, in the middle of the range investigated for further optimisation studies.

8.3.1 Characterisation of phase assemblage by X-ray diffraction

Figure 8-1 shows powder XRD patterns of the product recovered from MSS of nominal $Ca_{0.9}Zr_{0.9}Ce_{0.2}Ti_2O_7$ over the range 1100 to 1400 °C, with a reaction time of 2 h in air. All XRD patterns show the formation of zirconolite 2M and 3T polytypes, at all temperatures, together with evidence of residual ZrO_2 and TiO_2 reagents, and an accessory perovskite phase (prototypically $CaTiO_3$). Quantitative phase analysis of the phase assemblage was undertaken, by Rietveld analysis of XRD data; the results are summarised in Table 8-1 and compared in Figure 8-2 (an example fit is shown in Figure S8-2). The quantitative phase analysis showed the overall yield of the zirconolite 2M phase to increase with reaction temperature, from 43.9 wt.% at 1100 °C, to 62.1 wt.% at 1400 °C (± 1.8 wt.%). A concomitant reduction in the fractions of residual ZrO_2 and TiO_2 reagents, accessory perovskite, and zirconolite 3T phase, were observed, with increasing reaction temperature. The combined

fraction of zirconolite 2M and 3T phases increased from 54.9 wt.% at 1100 °C, to 74.3 wt.% (± 2.0 wt.%) at 1400 °C. The reaction temperature was not increased further since single phase Ce-doped zirconolites can be produced by conventional solid state synthesis at 1400 °C [19,20], and the MSS method of interest here would offer no meaningful advantage.

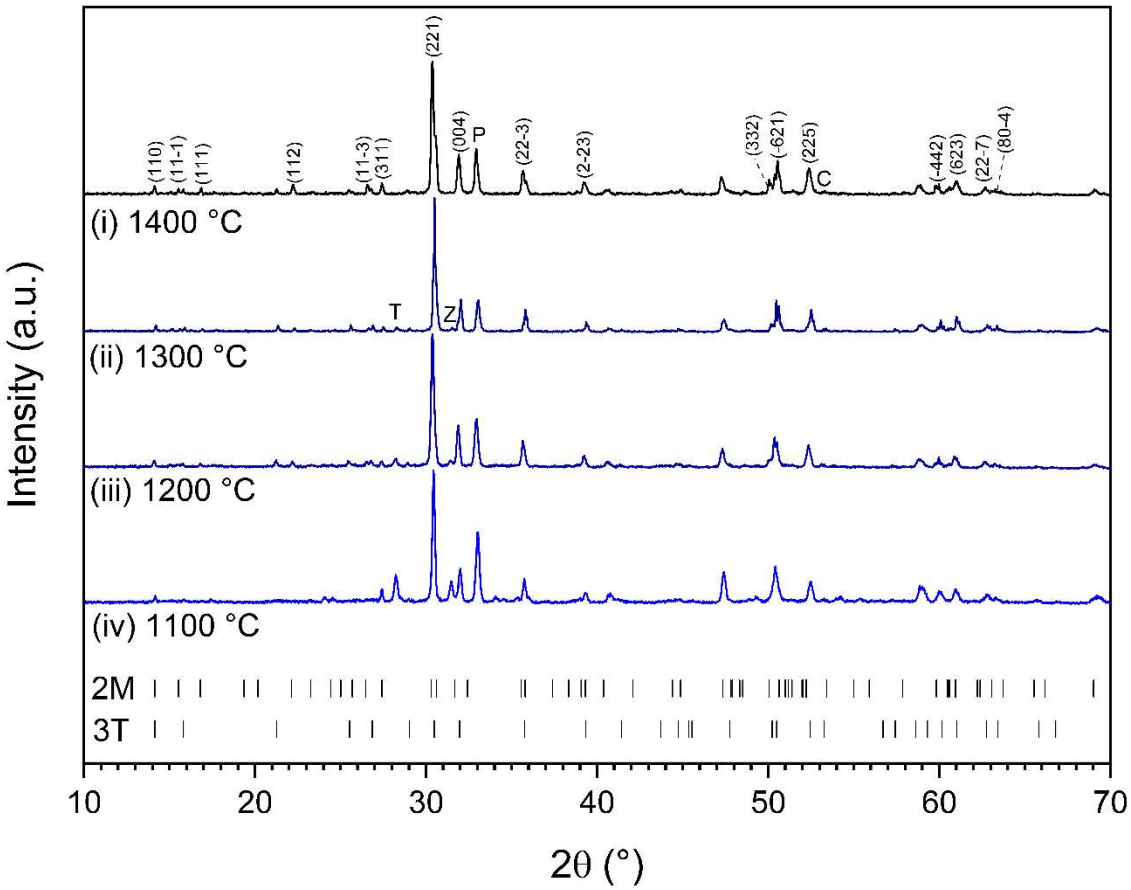

Figure 8-1 - XRD patterns of $Ca_{0.9}Zr_{0.9}Ce_{0.2}Ti_2O_7$ MSS with synthesis temperature: (i) 1400 °C (ii) 1300 °C (iii) 1200 °C (iv) 1100 °C; the reaction time was 2h in air. Miller indices highlight major reflections of the zirconolite 2M phase. Primary diagnostic reflections of reagents and accessory phases are indicated by: P, $CaTiO_3$ perovskite; T, TiO_2 rutile; Z, ZrO_2; C, CeO_2.

Overall, these data show that at 1100 °C, the yield of zirconolite 2M was hindered by slow reaction kinetics, at 1200 °C and higher temperature the yield of zirconolite 2M was increased by reaction of reagents and conversion of the

zirconolite 3T to 2M polymorph. The overall yield of zirconolite phases increased by a greater margin when the reaction temperature was increased from 1100 °C to 1200 °C, compared to 1400 °C, which may reflect increased volatilisation of the molten salt medium. For subsequent optimisation, a reaction temperature of 1200 °C was selected, given the evidence for reasonable reaction kinetics balanced against minimising the reaction temperature to reduce evaporation of the molten salt and, with a view to process implementation, potential volatile fission products.

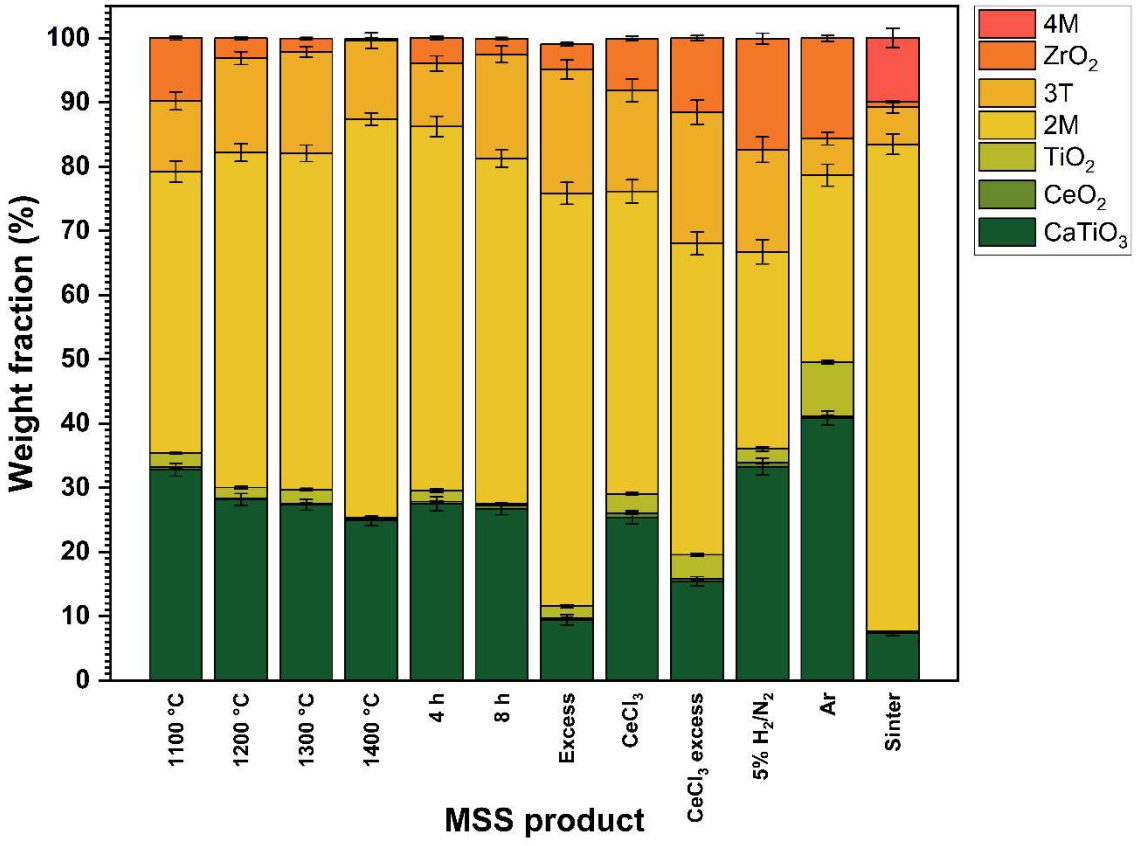

Figure 8-2 - Quantitative phase analysis of XRD data of MSS products shown in Fig.8-1 and Fig.8-3 to 8-5; "excess" denotes addition of 10 wt.% ZrO_2 and 5 wt.% TiO_2 to stoichiometric formulation. Unless otherwise stated MSS was performed at 1200 °C for 2 h in air with CeO_2 as the Ce source.

Temperature (°C)	Time (h)	Atmosphere	Reagent	Excess	Phase fraction (wt.%)						
					$CaTiO_3$ (± 1.0)	CeO_2 (± 0.07)	TiO_2 (± 0.2)	Z-2M (± 1.8)	Z-3T (± 1.5)	Z-4M (± 1.5)	ZrO_2 (± 0.4)
1100	2	air	CeO_2	-	32.8	0.40	2.1	43.9	11.0	0	9.7
1200	2	air	CeO_2	-	28.1	0.16	1.7	52.2	14.7	0	3.0
1300	2	air	CeO_2	-	27.3	0.20	2.1	52.4	15.8	0	2.1
1400	2	air	CeO_2	-	24.8	0.27	0.2	62.1	12.2	0	0.3
1200	4	air	CeO_2	-	27.5	1.11	1.7	56.7	9.8	0	3.9
1200	8	air	CeO_2	-	26.6	0.62	0.2	53.8	16.2	0	2.4
1200	2	air	CeO_2	✓	9.4	0.26	1.8	64.3	19.3	0	3.9
1200	2	air	$CeCl_3$	-	25.4	0.62	3.0	47.1	15.7	0	8.0
1200	2	air	$CeCl_3$	✓	15.4	0.33	3.7	48.5	20.4	0	11.5
1200	2	5% H_2/N_2	CeO_2	-	33.3	0.58	2.1	30.7	15.9	0	17.2
1200	2	Ar	CeO_2	-	40.9	0.28	8.4	29.1	5.7	0	15.6
1350**	20	air	CeO_2	-	7.3	0.12	0.1	75.9	5.8	10.0	0.7

Table 8-1 - Quantitative analysis using Rietveld refinement on XRD patterns in Fig. 8-1 and Fig.8-3 to 8-5; "excess" denotes addition of 10 wt.% ZrO_2 and 5 wt.% TiO_2 to stoichiometric formulation. ** Refers to the material produced after the secondary sintering of the MSS material formed at 1200 °C for 2 h in air with CeO_2 as the surrogate.

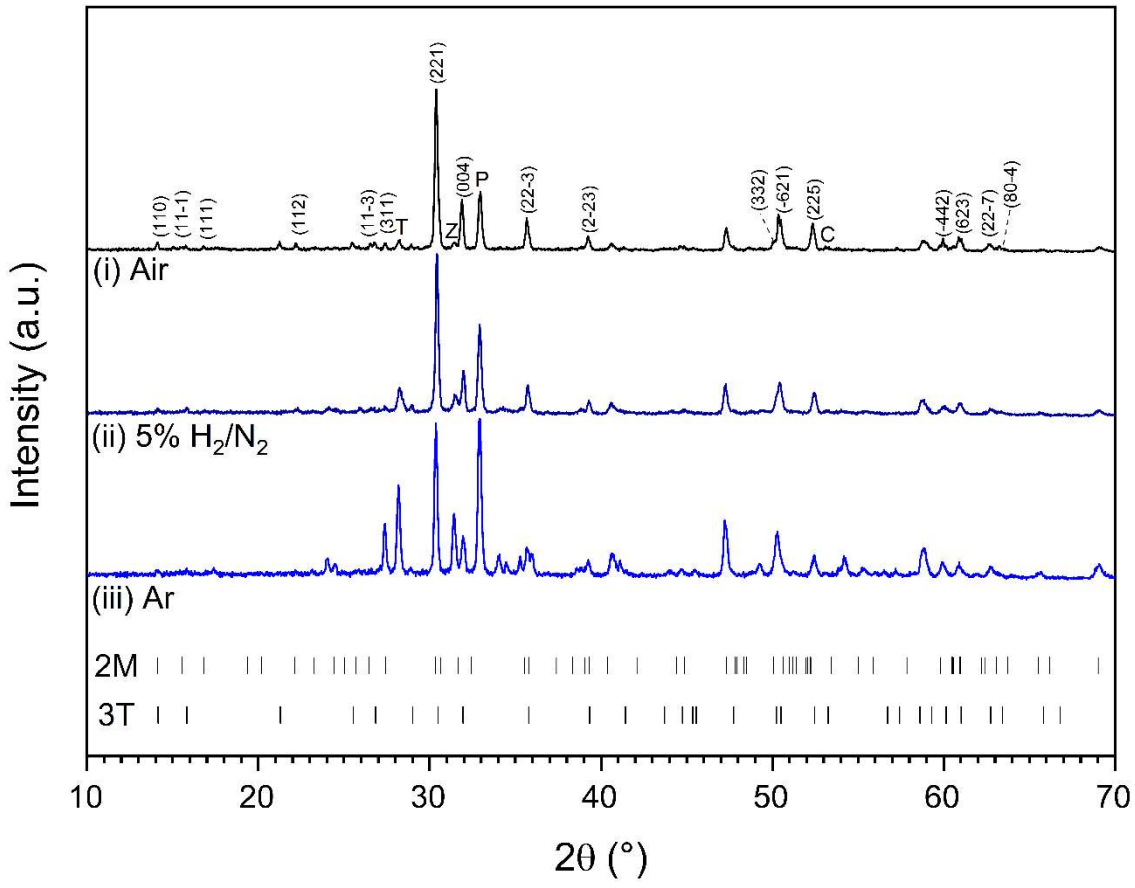

Figure 8-3 - XRD patterns of $Ca_{0.9}Zr_{0.9}Ce_{0.2}Ti_2O_7$ MSS at 1200 °C for 2 h, with synthesis atmospheres: (i) air (ii) 5% H_2/N_2 (iii) Ar. Miller indices highlight major reflections of the zirconolite 2M phase. Primary diagnostic reflections of reagents and accessory phases are indicated by: P, $CaTiO_3$ perovskite; T, TiO_2; Z, ZrO_2; C, CeO_2.

Following investigation of the phase assemblage produced by MSS as a function of reaction temperature, the effect of oxygen partial pressure was studied by imposing an atmosphere of 5% H_2/N_2 or Ar gas. Figure 3 compares the powder XRD patterns of the product recovered from MSS of nominal $Ca_{0.9}Zr_{0.9}Ce_{0.2}Ti_2O_7$ at 1200 °C, with a reaction time of 2 h in air, 5% H_2/N_2 and Ar. These data and the quantitative phase analysis summarised in Table 8-1 and Figure 8-2, show the reducing atmosphere to result in a markedly lower yield of zirconolite 2M and 3T phases. The combined yield of zirconolite 2M and 3T was 46.6 wt.% and 34.8 wt.% for the 5% H_2/N_2 and Ar atmosphere respectively, compared to 66.9 wt.% for air atmosphere (± 2.0 wt.%). Evident

from the quantitative phase analysis is a greater fraction of residual ZrO_2 (15.6 – 17.3 ± 0.4 wt.%), which suggests that the solubility of ZrO_2 in the molten salt medium is strongly dependent on effective oxygen partial pressure, resulting in a lower yield of zirconolite and increased yield of perovskite (33.3 - 40.9 ± 1.0 wt.%). Ce L_3 XANES data demonstrated Ce to be completely reduced to Ce^{3+}, which is expected to stabilise the perovskite accessory phase as discussed further in Section 8.3.3, possibly assisted by the reduction of Ti^{4+} to Ti^{3+} within the sample. Begg and Clarke reported that annealing $CaZrTi_2O_7$ under 3.5 % H_2/N_2 atmosphere results in reduction of Ti^{4+} to Ti^{3+} [259], [260], and the formation of a Zr rich zirconolite and perovskite. Our observations are consistent with this mechanism. Given the evident lower stability of the zirconolite phase under reducing conditions, further optimisation of the MSS reaction conditions applied a temperature of 1200 °C and air atmosphere.

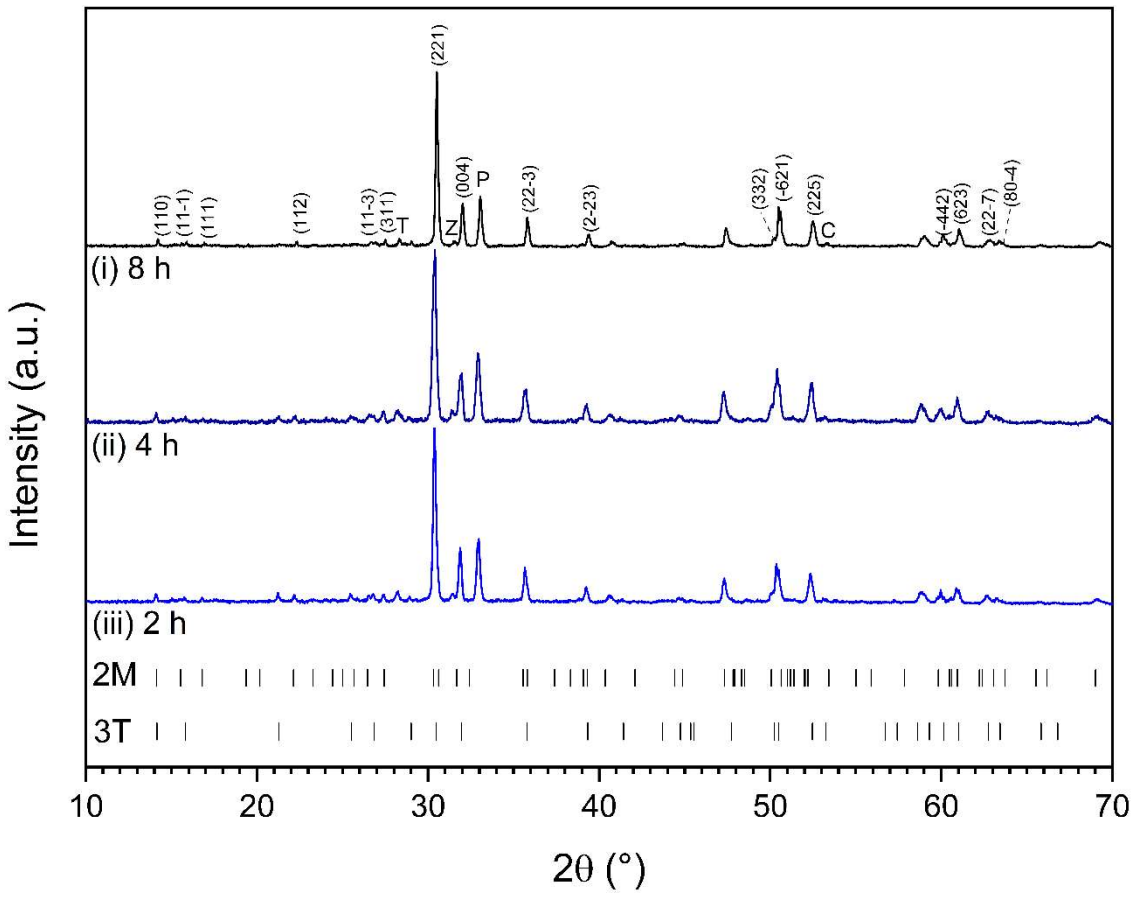

Figure 8-4 - XRD patterns of $Ca_{0.9}Zr_{0.9}Ce_{0.2}Ti_2O_7$ MSS at 1200 °C in air with furnace dwell durations: (i) 8 h (ii) 4 h (iii) 2 h. Miller indices highlight major reflections of the zirconolite 2M phase. Primary diagnostic reflections of reagents and accessory phases are indicated by: P, $CaTiO_3$ perovskite; T, TiO_2; Z, ZrO_2; C, CeO_2.

Figure 8-4 compares the powder XRD patterns of the product recovered from MSS of nominal $Ca_{0.9}Zr_{0.9}Ce_{0.2}Ti_2O_7$ after reaction at 1200 °C, with a reaction time of 2 h, 4 h or 8 h in air. These data show a broadly similar phase assemblage, with quantitative phase analysis, summarised in Table 8-1 and Figure 8-2, revealing relatively small changes in phase fraction, close to the estimated margin of precision. In particular, the total yield of zirconolite phases did not show a marked increase with reaction time, with changes being close to the estimated precision of ± 2.0 wt.%. This observation is consistent with evaporation of the molten salt medium with increased reaction time, and with

diffusion – reaction occurring primarily in the solid state, for which the reaction kinetics to yield zirconolite are known to be low at 1200 °C [19,20]. The quantitative phase analysis of the product from reaction at 1200 °C in air for 4 h showed an anomalously high fraction of residual ZrO_2 reagent, 3.9 ± 0.4 wt.%, the origin of which is unclear, but is consistent with a marginally lower yield of the target zirconolite phase. or the purpose of further optimisation of the MSS process, therefore, the reaction conditions were fixed at 1200 °C, for a duration of 2 h, under air.

With processing conditions of 1200 °C for 2 h in air, optimised from the investigations above, the addition of excess ZrO_2 and TiO_2 reagents was explored, with the aim of consuming the perovskite accessory phase. Figure 5 shows the powder XRD data pattern of the product recovered from MSS of nominal $Ca_{0.9}Zr_{0.9}Ce_{0.2}Ti_2O_7$ after reaction at 1200 °C, for 2 h, in air, with an excess of 10 wt.% ZrO_2 and 5 wt.% TiO_2 reagents. Quantitative phase analysis, Table 8-1 and Figure 8-2, showed that this adjustment of the reaction composition was successful and reduced the fraction of perovskite accessory phase to 9.4 ± 1.0 wt.%, with the yield of zirconolite 2M increased to 64.3 ± 0.8 wt.%. The overall yield of zirconolite 2M and 3T phases, combined, increased to 83.6 ± 2.0 wt.%, with ca. 5 wt.% of unreacted reagents.

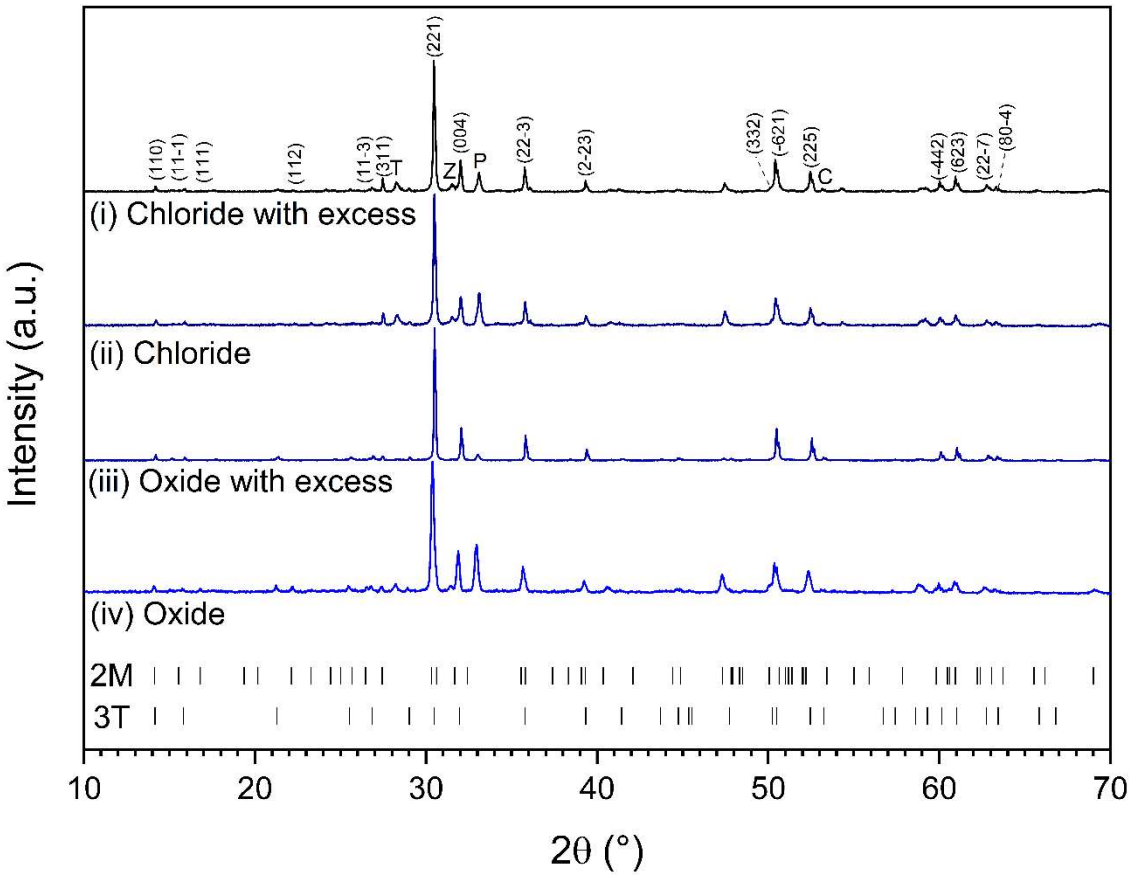

Figure 8-5 - XRD patterns of $Ca_{0.9}Zr_{0.9}Ce_{0.2}Ti_2O_7$ MSS with additional excesses of 10 wt.% ZrO_2 and 5 wt.% TiO_2, and $CeCl_3$ reagent where indicated: (i) 1200 °C, $CeCl_3$, 10 wt.% ZrO_2 and 5 wt.% TiO_2 (ii) 1200 °C, $CeCl_3$ (iii) 1200 °C,10 wt.% ZrO_2 and 5 wt.% TiO_2 (iv) 1200 °C; the reaction time was 2 h, in air. Miller indices highlight major reflections of the zirconolite 2M phase. Primary diagnostic reflections of reagents and accessory phases are indicated by: P, $CaTiO_3$ perovskite; T, TiO_2; Z, ZrO_2; C, CeO_2.

The use of $CeCl_3$ as a reagent and actinide surrogate, was also explored since MA and Pu will be incorporated as a chloride species with the molten salt in a pyroprocessing waste stream, unless precipitated as an oxide by oxygen sparging [37]. Figure 8-5 presents the powder XRD data pattern of the product recovered from MSS of nominal $Ca_{0.9}Zr_{0.9}Ce_{0.2}Ti_2O_7$ after reaction at 1200 °C, for 2 h, in air, using $CeCl_3.7H_2O$ as the Ce source, with and without an excess of 10 wt.% ZrO_2 and 5wt.% TiO_2 reagents. The overall yield of zirconolite 2M

and 3T phases, combined, was, respectively, 68.9 wt.% and 62.8 wt.% (± 2.0 wt.%) for the formulations with and without an excess of 10 wt.% ZrO_2 and 5 wt.% TiO_2. The use of $CeCl_3.7H_2O$ evidently has a detrimental effect on the phase assemblage, compared to the use of CeO_2, with a reduced yield of zirconolite. This is correlated with the residual ZrO_2 phase fraction being approximately three times greater in the products of reaction utilising $CeCl_3.7H_2O$ compared to CeO_2, suggesting the lower yield may arise from lower ZrO_2 solubility.

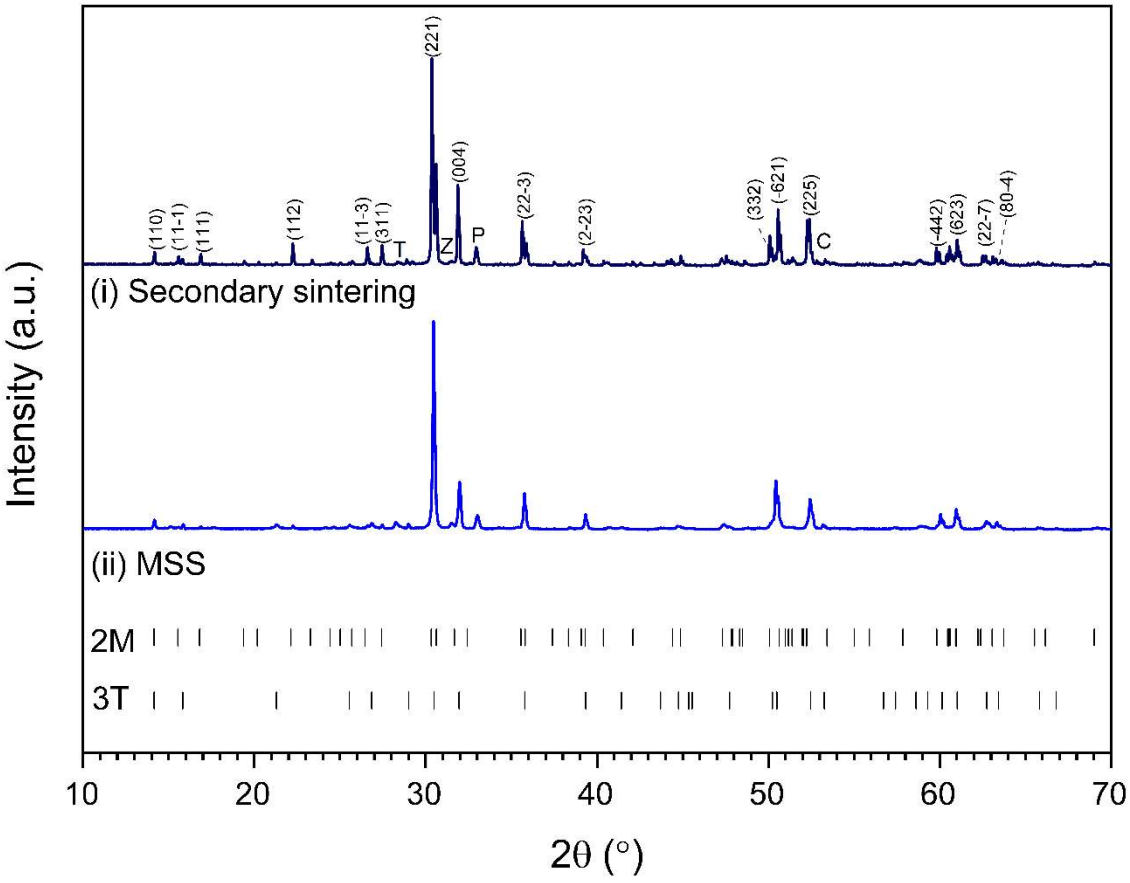

Figure 8-6 - XRD patterns to compare; (i) the product of a secondary sintering process (1350 °C, for 20 h, in air) of the MSS product in (ii), (ii) $Ca_{0.9}Zr_{0.9}Ce_{0.2}Ti_2O_7$ MSS; 1200 °C for 2 h in air. Miller indices highlight major reflections of the zirconolite 2M phase. Primary diagnostic reflections of reagents and accessory phases are indicated by: P, $CaTiO_3$ perovskite; T, TiO_2; Z, ZrO_2; C, CeO_2.

The final step in this study involved sintering of the product of $Ca_{0.9}Zr_{0.9}Ce_{0.2}Ti_2O_7$ MSS, produced at 1200 °C, for 2 h, in air with an excess of 10 wt.% ZrO_2 and 5 wt.% TiO_2, using CeO_2 as a Ce source. The sintering conditions were 1350 °C for 20 h in air, and X-ray diffraction, Figure 8-6, coupled with quantitative phase analysis, demonstrated the combined zirconolite 2M, 4M and 3T polymorphs to comprise 91.7 ± 2.0 wt.% of the phase assemblage, with the 2M polymorph (75.9 ± 1.8 wt.%) as the major component. A minor perovskite accessory phase was determined (7.3 ± 1.0 wt.%) with the trace CeO_2, ZrO_2 and TiO_2 (combined 1.0 ± 0.5 wt.%).

8.3.2 SEM/EDX characterisation

The scanning electron micrographs in Figure 8-7 show the morphology of each reagent, along with that of the $Ca_{0.9}Zr_{0.9}Ce_{0.2}Ti_2O_7$ product of MSS at 1200 °C for 2 h, in air (with CeO_2). Comparison of the particle morphology of the reagents and the product material, shows that the primary particle size and habit of the product is similar to that of the TiO_2 reagent (~ 1 μm) and clearly differentiated from the that of the CeO_2 and ZrO_2 reagents, with much larger and smaller particle size, respectively. This suggests that template growth is the mechanism by which $Ca_{0.9}Zr_{0.9}Ce_{0.2}Ti_2O_7$ was produced. The faceted nature of TiO_2 reagent (see Figure 8-7 (a)) was reflected in the habit of the $Ca_{0.9}Zr_{0.9}Ce_{0.2}Ti_2O_7$ product (Figure 8-7 (d)). However, it was evident that some growth in product particle size had occurred, relative to the TiO_2 reagent, which provides evidence for a contribution of dissolution – precipitation and/or solid state diffusion, to the overall synthesis mechanism.

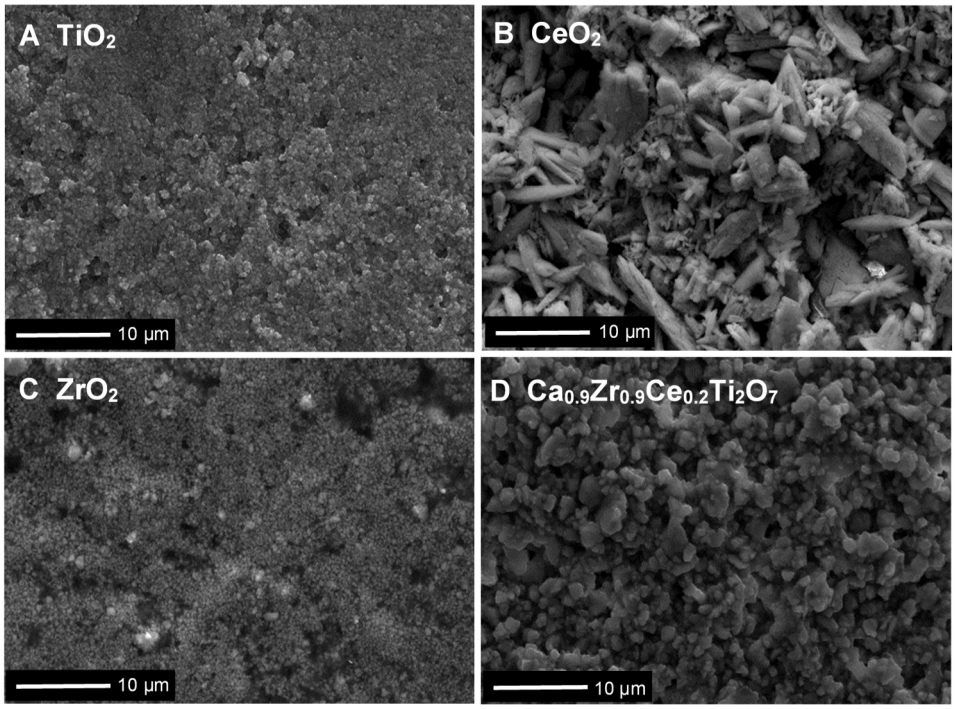

Figure 8-7 - SEM micrographs, in secondary electron mode, of: (A) TiO_2 (B) CeO_2 (C) ZrO_2 (D) $Ca_{0.9}Zr_{0.9}Ce_{0.2}Ti_2O_7$ from MSS at 1200 °C, for 2h, in air.

The microstructure of the sintered $Ca_{0.9}Zr_{0.9}Ce_{0.2}Ti_2O_7$ ceramic is shown in Figure 8-8. The material comprises a majority matrix (mid grey) of the zirconolite 2M polymorph, with inclusions of ZrO_2 (bright grey) and small isolated perovskite grains (dark grey). The zirconolite 3T polymorph cannot be differentiated from the 2M polymorph, presumably due to similar composition and hence back scattered electron contrast, combined with its low abundance. The average EDX determined composition of the combined zirconolite 2M and 3T phases, was $Ca_{0.95(3)}Zr_{0.88(3)}Ce_{0.17(2)}Ti_{2.01(2)}O_7$, in reasonable agreement with the target stoichiometry. This implies an average Ce oxidation state of $Ce^{3.2+}$, within the zirconolite phase.

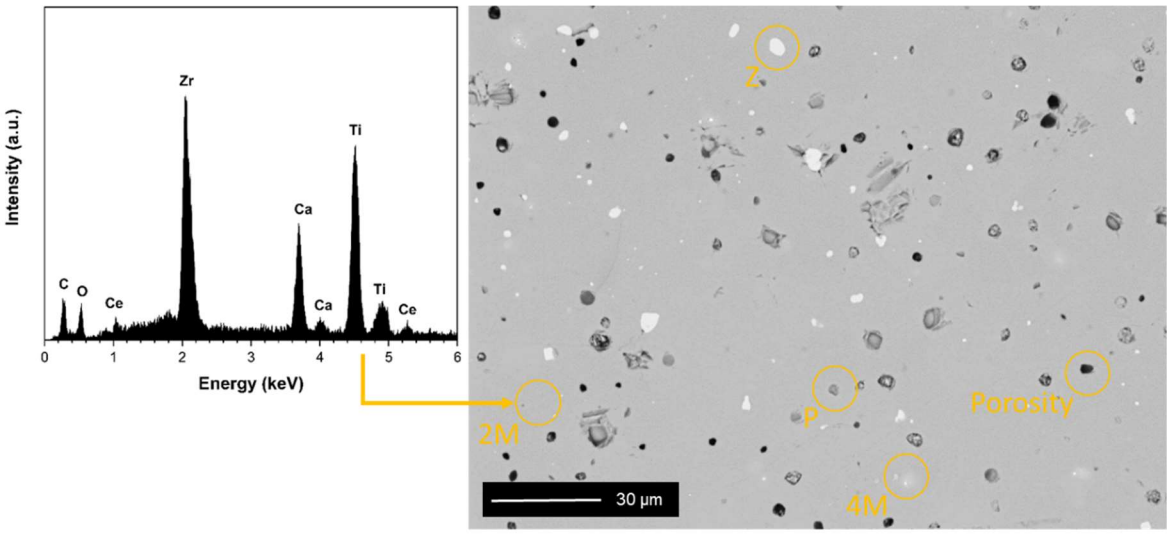

Figure 8-8 - SEM micrograph, in SE mode, of the surface of the ceramic produced after sintering of MSS product at 1350 °C for 20 h, in air, highlighting component phases: accessory phases are indicated by: P, perovskite; Z, ZrO_2; and zirconolite 2M and 4M polymorphs. Representative EDX spectrum of the zirconolite 2M phase is shown.

The zirconolite 4M phase is apparent as a small variation to the matrix contrast, which arises from a slightly higher Ce concentration as judged from EDX data. The microstructure is relatively well sintered although isolated porosity is apparent.

8.3.3 Ce L_3 XANES

Ce L_3 XANES data were acquired from product materials as a probe of the average Ce oxidation state and are shown in Figure 8-9. The spectra were analysed using linear combination fitting (LCF) to estimate the proportion of Ce^{3+} in each product, using reference spectra of CeO_2 (for 8-fold coordinated Ce^{4+}), $CeAlO_3$ (for 12-fold coordinated Ce^{3+}) and $CePO_4$ (monazite; for 9-fold coordinated Ce^{3+}). Spectra were fitted over the range 5700 – 5760 eV, under the constraint that the fractional weights of the reference spectra sum to unity; the results are summarised in Table 8-2 with an example fit shown in Figure S8-3. Note that the Ce L_3 XANES of $CePO_4$ and $CeAlO_3$ present a single intense feature on the rising absorption edge, whereas CeO_2 presents three features, of lower relative intensity, for which the corresponding final state electron configurations were previously assigned [164], [217]–[219].

The Ce L_3 XANES data and LCF analysis (Figure 8-9A; Table 8-2), showed the fraction of Ce^{3+} to increase with increasing reaction temperature (with constant reaction time of 2 h, in air), which is expected for the autoreduction of CeO_2 [212]; this was correlated with the concomitant increase in the combined fraction of major zirconolite 2M and 3T polytypes, and reduction in the perovskite fraction, in the phase assemblage (Table 8-1). In contrast, the fraction of Ce^{3+} increased only marginally when the reaction time was extended from 2 h to 8 h (Figure 8-9C; Table 8-2), consistent with only a small increase in the combined fraction of major zirconolite 2M and 3T polytypes, and reduction in perovskite phase fraction (Table 8-1). Taken together, these data show that the total yield of zirconolite and Ce^{3+} fraction increase with increasing temperature, according to the target formulation, by reaction of the perovskite accessory phase and residual TiO_2 and ZrO_2. It is evident, however, that the zirconolite product must incorporate some proportion of Ce^{4+}.

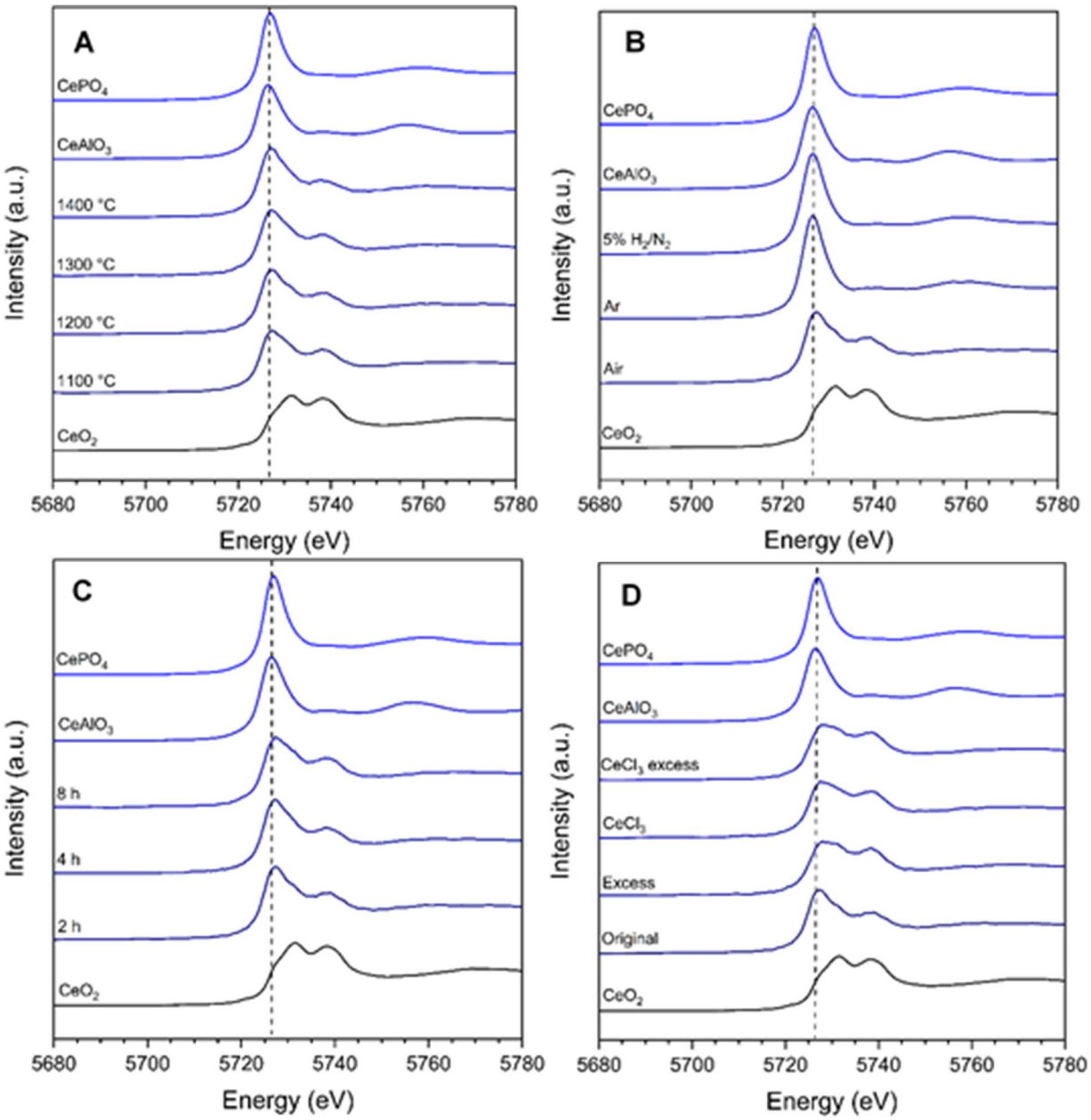

Figure 8-9 - Ce L_3 XANES spectra of recovered product of $Ca_{0.9}Zr_{0.9}Ce_{0.2}Ti_2O_7$ MSS in air, compared with $CePO_4$, $CeAlO_3$ and CeO_2 reference compounds: A) reaction at 1100 – 1400 °C for 2 h, in air; B) reaction at 1200 °C for 2 h using flowing 5% H_2/N_2, Ar or air; C) reaction at 1200 °C for 2 – 8 h, in air; D) reaction at 1200 °C for 2 h, in air, using CeO_2 or $CeCl_3.7H_2O$ as Ce source, with/without 10 wt.% ZrO_2 and 5 wt.% TiO_2 excess.

Synthesis in a reducing atmosphere showed a complete reduction of Ce with the fraction of Ce^{3+} being 100 ± 4% for both 5% H_2/N_2 and Ar products (Figure 8-9B). This was accompanied by a significant decrease in zirconolite yield in contrast with the effect of increasing temperature on phase assemblage. This implies that when the Ce^{3+} content increases above ca. 60%, the competing perovskite phase is stabilised, which provides a 12 co-ordinate site to accommodate the larger Ce^{3+} species [49]. The proportion of perovskite phase is similar to the ~ 40 wt.% observed in the phase assemblage produced from conventional reaction sintering of $CaZr_{0.6}Ce_{0.2}Ti_2O_7$ ceramics under H_2/N_2 and Ar, with a Ce^{3+} content of 80 – 100% [241].

Substituting $CeCl_3$ for CeO_2 as the Ce source, resulted in reduction of the Ce^{3+} fraction from 59 ± 3% to 38 ± 3%, in the products from reaction at 1200 °C for 2 h, in air; however, this was not accompanied by a significant change in the overall phase assemblage. The effect of addition of 10 wt.% ZrO_2 and 5 wt.% TiO_2 to the formulation resulted in marked reduction of the Ce^{3+} fraction from 59 ± 3% to 33 ± 3%, in the product from reaction at 1200 °C for 2h, in air, correlated with the maximum yield in of combined zirconolite 2M and 3T polytypes in the phase assemblage (Table 8-1); this is also the case when CeO_2 is replaced by $CeCl_3$, although to less extent. Taken together, these data demonstrate a strong effect of the addition of excess 10 wt.% ZrO_2 and 5 wt.% TiO_2 in increasing the total yield of the zirconolite product, which must incorporate a higher fraction of Ce^{4+}.

Table 8-2 - Results of linear combination fitting of spectra from Figure 8-9; "excess" denotes addition of 10 wt.% ZrO_2 and 5 wt.% TiO_2 to the stoichiometric formulation.

Temperature (°C)	Time (h)	Atmosphere	Reagent	Excess	Ce^{3+} (%)
1100	2	Air	CeO_2	-	54 ± 3
1200	2	Air	CeO_2	-	59 ± 3
1300	2	Air	CeO_2	-	62 ± 3
1400	2	Air	CeO_2	-	71 ± 3
1200	4	Air	CeO_2	-	62 ± 3
1200	8	Air	CeO_2	-	53 ± 3
1200	2	Air	CeO_2	✓	33 ± 3
1200	2	Air	$CeCl_3$	-	38 ± 3
1200	2	Air	$CeCl_3$	✓	33 ± 3
1200	2	5% H_2/N_2	CeO_2	-	100 ± 4
1200	2	Ar	CeO_2	-	100 ± 4

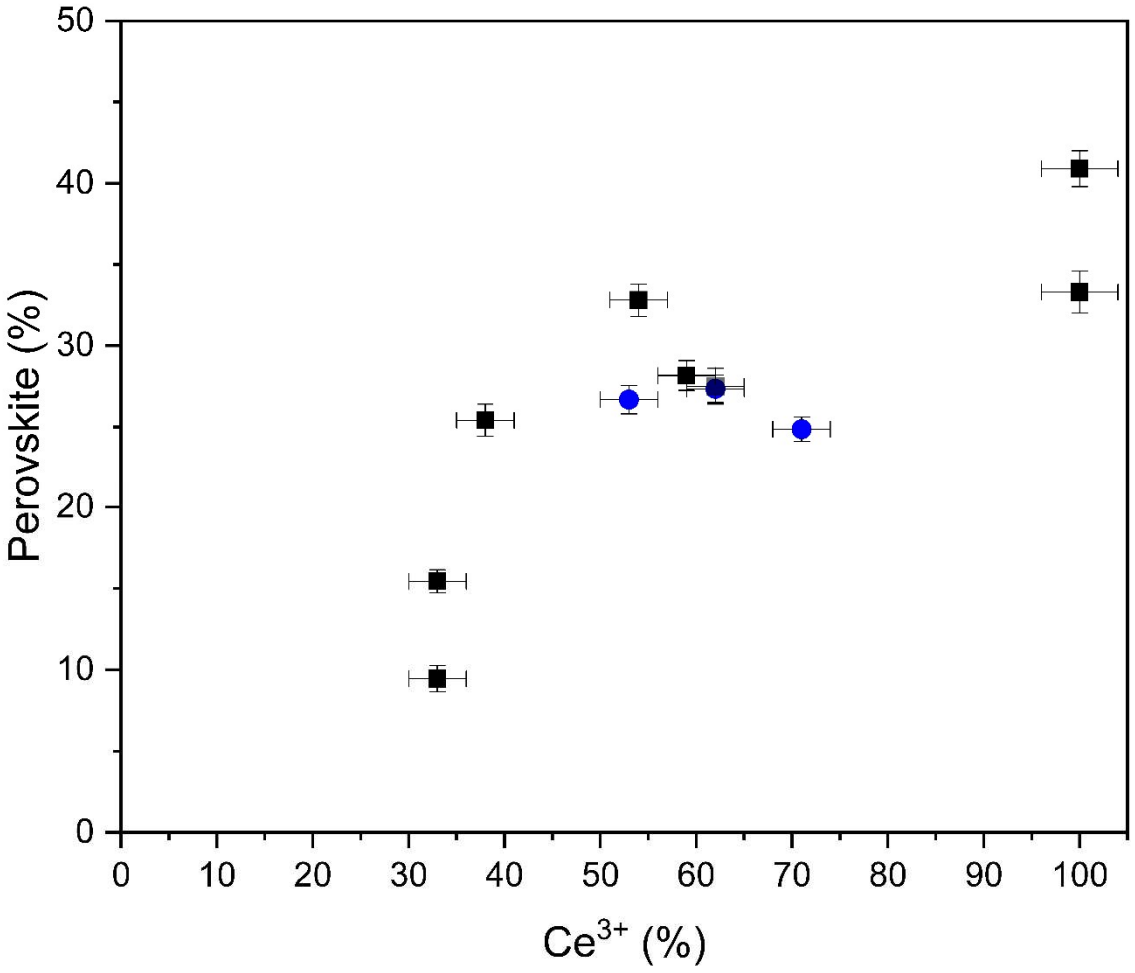

Figure 8-10 - Comparison of quantity of Ce^{3+} and perovskite weight fraction in product materials. Black squares represent all MSS zirconolite materials produced at 1200 °C. Blue circles represent MSS zirconolite materials produced at temperatures other than 1100 °C, 1300 °C and 1400 °C.

Figure 8-10 shows a comparison between the average Ce oxidation state (from Table 8-2) and the weight fraction of perovskite formed in each product. There is a general trend of increasing perovskite content associated with a greater the quantity of Ce^{3+} in the sample at a constant synthesis temperature. As noted above, the competing perovskite phase provides a 12 co-ordinate site to accommodate the larger Ce^{3+} species [90], and hence the proportion of the perovskite phase increases with increasing Ce^{3+} content, which is generally associated with a lower yield of zirconolite.

8.4 Discussion

Ce doped zirconolite was synthesised in a NaCl:KCl molten salt eutectic, as a conceptual process for decontamination of pyroprocessing molten salt wastes and immobilisation of separated plutonium. The presence of a molten salt eutectic enables synthesis of zirconolite at 1200 °C in 2 h, in air, considerably reduced compared to conventional reaction sintering which requires e.g. 1400 °C for 20 h. Interestingly, our investigation yields zirconolite 2M, 3T and 4M polytypes, with evidence for conversion of 3T to 2M, with increasing temperature. In contrast, similar compositions fabricated by conventional reactive sintering comprise only the 2M polytype, with minor 4M polytype when synthesised under air [48]. Our data are consistent with previous studies of NaCl:KCl and $CaCl_2$:NaCl molten salt synthesis of the parent $CaZrTi_2O_7$ zirconolite, which identified the formation of the 3T polytype, as the major phase after reaction at 1100 °C, giving way to formation of the 2M polytype at 1200 °C [258]. The zirconolite 3T phase therefore appears to be a low temperature metastable polytype structure.

Molten salt mediated synthesis yields products with a minimum Ce^{3+} content at least 33% greater than similar compositions synthesised by reactive sintering in air, when using CeO_2 as a reagent. Therefore, the mechanism of Ce solubility in the NaCl-KCl eutectic appears to involve reduction of Ce^{4+} to Ce^{3+}, yielding products with relatively high Ce^{3+} content. We are not aware of solubility data for Ce^{4+}/Ce^{3+} in chloride molten salts, but this conclusion is consistent with chloride molten salt mediated synthesis of CeOCl from CeO_2 [268]. Interestingly, the analogous $CaZr_{1-x}Pu_xTi_2O_7$ system is reported to yield the zirconolite 3T polytype on reduction of Pu^{4+} to Pu^{3+} and zirconolite 3T natural analogues are generally characterised by a high fraction of trivalent lanthanides [81], [89]. Hence, whilst $CaZrTi_2O_7$ can evidently be stabilised in the 3T polytype up to 1100 °C, incorporation of a significant Ce^{3+} may assist in stabilising this polytype to higher temperature as reported herein.

Perovskite is formed as an accessory phase in all products characterised in this study, with increased perovskite fraction correlated with increased Ce^{3+}

fraction at constant synthesis temperature (1200 °C). As noted in the introduction, the formation of perovskite is undesirable since it has been shown to incorporate actinides but demonstrates comparably lower radiation tolerance and durability, with respect to zirconolite [112]. Nevertheless, the perovskite phase fraction could be reduced to 7.3 ± 1.0 wt.%, by adjusting the formulation to incorporate 10 wt.% ZrO_2 and 5 wt.% TiO_2, and sintering of the product powder, which is comparable to the perovskite phase fraction in similar zirconolite compositions produced by reactive sintering in air [241].

8.5 Conclusion

Molten salt mediated synthesis of zirconolite ceramics, in the context of the decontamination of pyroprocessing molten salt wastes to yield a zirconolite ceramic, has some potential. However, this approach would not offer any clear benefit over oxygen sparging of the salt to precipitate lanthanides and minor actinides as oxides, followed by recovery and immobilisation in a glass or ceramic matrix, since both processes would require subsequent high temperature melting or reactive sintering steps to produce a wasteform monolith. Likewise, in the context of plutonium stockpile immobilisation, although molten salt mediated synthesis of zirconolite reduces the required reaction time and temperature, the subsequent requirement for a consolidation step means that the molten salt method does not offer a compelling advantage. Nevertheless, this work has served to usefully clarify mechanistic aspects of the molten salt mediated synthesis of zirconolite which should inform future application of molten salt technology in the nuclear and wider fields.

Acknowledgements

ARM is funded by the Engineering, Physical Sciences Research Council via the Next Generation Nuclear Centre for Doctoral Training (Grant EP/L015390/1). This research was supported in part by EPSRC under grant reference EP/S011935/1 and EP/R511754/1. NCH is grateful to the Royal Academy of Engineering and Nuclear Decommissioning Authority for funding. This research utilised the HADES/MIDAS facility at the University of Sheffield

established with financial support from EPSRC and BEIS, under grant EP/T011424/1 [186]. With thanks to Dr C. Shaw at the Sorby Centre for Electron Microscopy, University of Sheffield for assistance with SEM imaging. This research used beamline 6-BM of the National Synchrotron Light Source II, a U.S. Department of Energy (DOE) Office of Science User Facility Operated for the DOE office of Science by Brookhaven National Laboratory under Contract No. DE-SC0012704; the authors are grateful to Dr B. Ravel, Dr D. Bailey and Ms. L. M. Mottram for experimental assistance.

Supplementary Figures

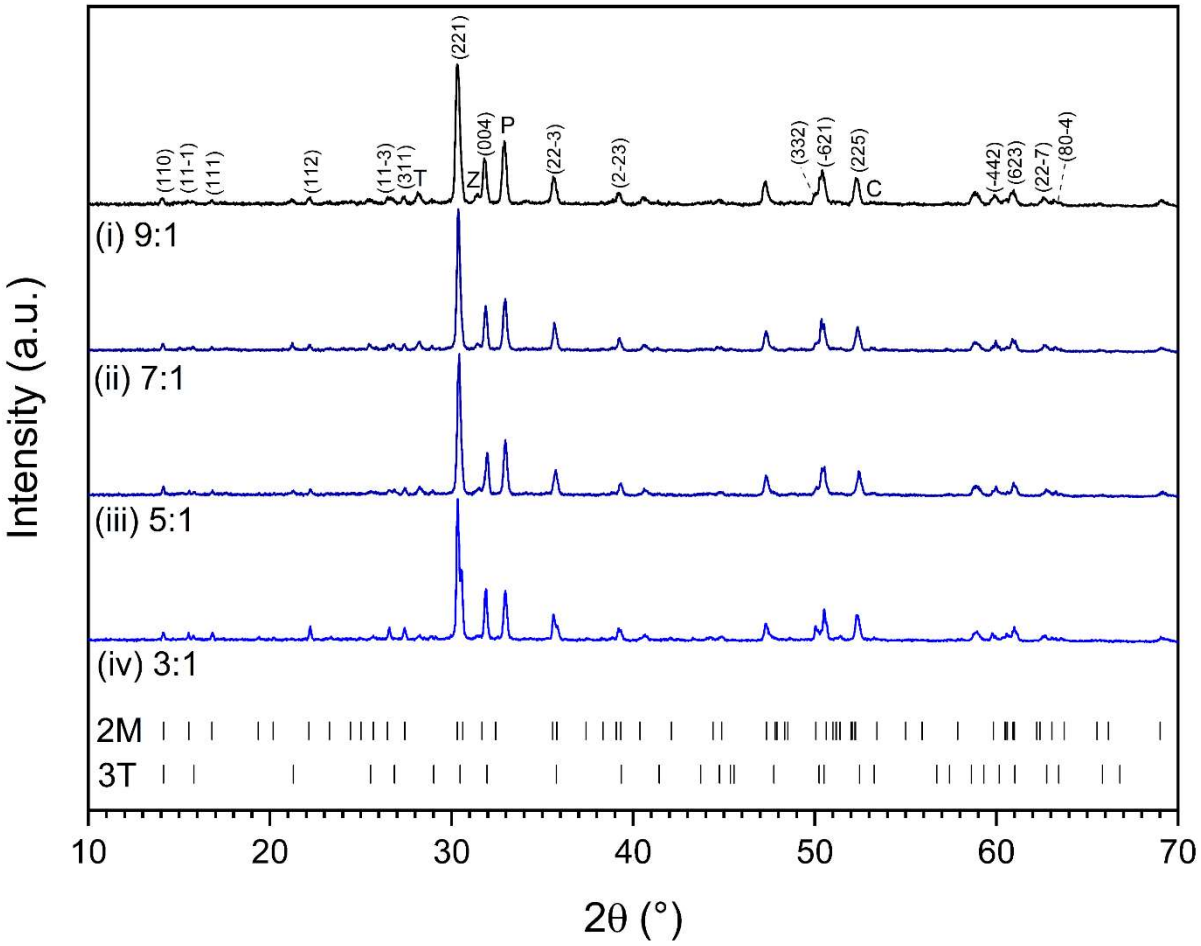

Supplementary Figure 8-1 - XRD pattern of $Ca_{0.9}Zr_{0.9}Ce_{0.2}Ti_2O_7$ MSS with salt to ceramic molar ratio: (i) 9:1 (ii) 7:1 (iii) 5:1 (iv) 3:1; the reaction was at 1200 °C for 2 h in air. Miller indices highlight major reflections of the zirconolite 2M phase. Primary diagnostic reflections of reagents and accessory phases are indicated by: P, $CaTiO_3$ perovskite; T, TiO_2 rutile; Z, ZrO_2; C, CeO_2.

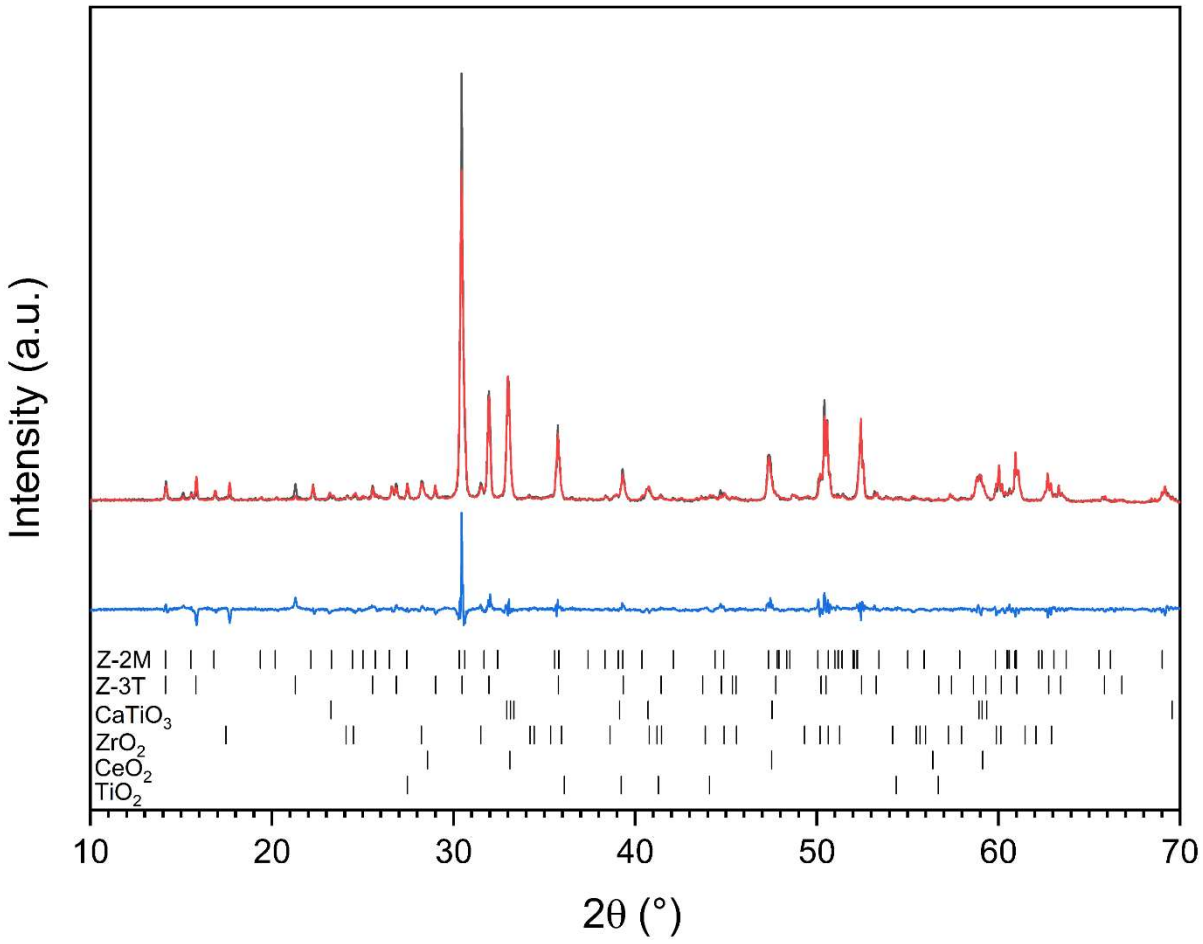

Supplementary Figure S8-2 - Rietveld fit of XRD data (black line) for QPA of the MSS $Ca_{0.9}Zr_{0.9}Ce_{0.2}Ti_2O_7$ material synthesised at 1200 °C for 2 h in air (R_p = 8.33%, R_{wp} = 11.55%, χ^2=2.85). Fitted data is shown with red line and blue is the difference profile.

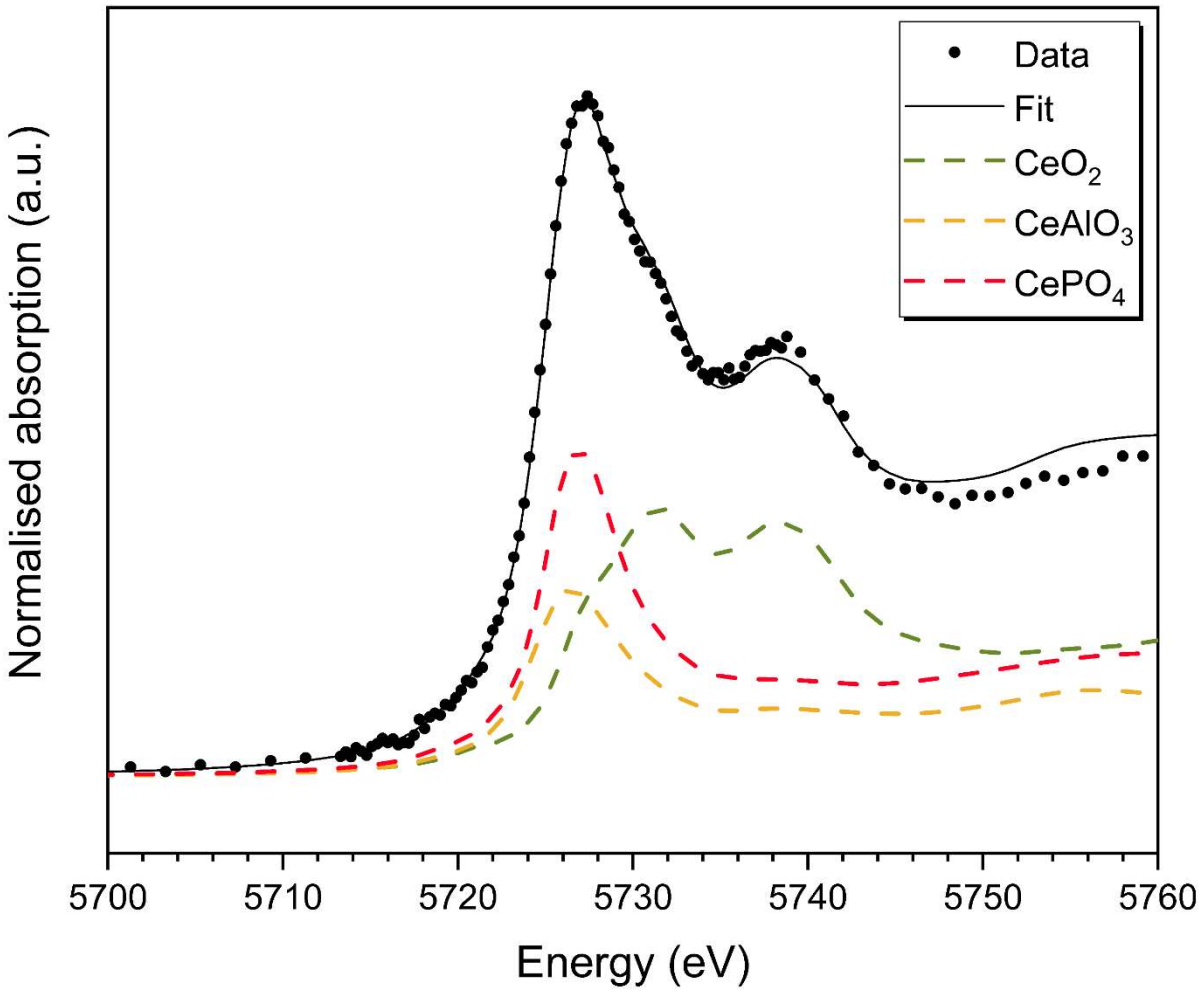

Supplementary Figure 8-3 - Example of linear combination fitting showing the Ce L_3 edge XAS of the MSS product: 1200 °C for 2 h in air. Fitted using the reference spectra: $CePO_4$, $CeAlO_3$ and CeO_2.

9 Conclusions

The primary motivation for this project was to develop and characterise wasteforms for the immobilisation of the UK PuO_2 stockpile and assess their chemical durability. Both glass and ceramic materials were selected for this purpose to assess a range of wasteforms to compare their relative advantages and disadvantages. Glasses have the advantage of technology readiness level and a flexible structure which can accommodate the incorporation of contaminants present in the waste stream. Ceramics, such as zirconolite, have improved relative long term durability with natural analogues demonstrating the retention of actinides for 10^6 – 10^9 years, when compared to glasses. The chemical durability assessment of each wasteform helped to support the safety case for the future implementation of these wasteform materials in a GDF. The viability of HIPing for the immobilisation of PuO_2 in either glass or ceramic wasteforms was demonstrated in this project, illustrating the benefits of this process particularly for the PuO_2 waste stream. The key findings from each results chapter are as follows:

Chapter 4 – Alkali tin silicate glass as a wasteform for the immobilisation of the UK Pu stockpile

ATS glass was demonstrated to be a candidate wasteform for the PuO_2 stockpile, with the wasteloading of CeO_2 maximised by utilising the increased solubility of trivalent lanthanide/actinide elements. The reduction of CeO_2 was achieved by increasing the melt temperature to induce Ce autoreduction and/or the addition of a reducing agent, Fe^0. A wasteloading of 5.6 mol.% CeO_2 was achieved at a melt temperature of 1100 °C, upon the addition of equimolar Fe^0, caused by the subsequent complete reduction of Ce^{4+} to Ce^{3+}. Caution should be exercised when interpreting these results due to the higher redox potential of Pu^{4+} when compared to Ce^{4+}. The oxidation state and local coordination environment of Fe was investigated using Fe K-edge XANES, EXAFS and Mössbauer spectroscopy, which showed that the Fe-Ce redox couple oxidised Fe^0 to a majority Fe^{3+} oxidation state in 5-fold coordination. The addition of Fe^0 was shown to improve the short term durability of the glass with the $NR_{B,\ Li,\ Na}$ reduced by an order of magnitude, compared to the

equivalent Fe-free composition. This durability is of the same order of magnitude as other glasses investigated However, Fe containing phases were predicted to precipitate from solution, which are known to induce the resumption for forward rate dissolution in borosilicate glasses.

Chapter 5 – Hot isostatic pressing of alkali tin silicate glass as a wasteform for the immobilisation of the UK Pu stockpile.

The glasses with maximum wasteloading from Chapter 4 were investigated using hot isostatic pressing as a thermal treatment method. When HIPed at 1100 °C, CeO_2 was not fully incorporated into the glass, despite the addition of Fe^0 to the melt and the reducing conditions induced by the SS HIP canister. Increasing the temperature of HIPing to 1250 °C was showed full incorporation into the glass network with and without the addition of Fe^0 to the melt. Interaction between the glass and the stainless steel (SS) HIP canister at this temperature caused the removal of Sn from the glass, and the addition of Cr. Chromite crystallites and undissolved Fe metal were observed in the melt, however upon the dissolution of these materials, similar dissolution rates were observed as for the equivalent Fe-containing composition from Chapter 4. Overall, HIPing was shown to be a viable thermal treatment method for ATS glass, offering advantages of full waste accountability throughout the process, however further investigations into the effect of scaling this process would be required.

Chapter 6 – The effect of charge compensating ions on the phase assemblage and dissolution behaviour of HIPed Ce-doped zirconolites.

An investigation into the role of three different charge compensating ions (Al, Fe and Mg) on the phase assemblage and relative dissolution rate HIPed Ce-doped zirconolite was investigated. CeO_2 was used as a surrogate for PuO_2 and substituted onto either the Ca^{2+} or Ca^{2+}/Zr^{4+} site. Zirconolite was the primary phase produced in each formulation, with a majority crystallising into the 2M polytype and small quantities of zirconolite 3T/4M also identified. Trace unreacted reagents and secondary perovskite were present in all formulations which showed to have the greatest impact on the dissolution behaviour of these materials. The substitution of Ce onto the Ca^{2+} site, and utilising the Fe^{3+}

charge compensation ion, proved to generate the most desirable phase assemblage, with 94 ± 2 wt.% zirconolite produced. This formulation also demonstrated the lowest dissolution rates (NR_{Ce} = 0.0(11) x 10^{-5} g m^{-2} d^{-1}), which was comparable to leach rates for dissolution experiments completed on similar compositions with similar leaching conditions. Further work should be completed to understand the effect of the redox environment within the HIP canister on redox active elements. This would help to establish whether secondary waste bearing phases such as perovskite would be likely to form when using PuO_2.

Chapter 7 – Hot isostatic pressing and durability testing of fluorite related ceramic wasteforms containing neutron absorbers for PuO_2 disposition.

Four Ce-doped ceramic materials based upon the fluorite structure were investigated, including *zirconolite*, *zirconate pyrochlore* and *cubic zirconia,* HIPing was used as the thermal treatment method to improve the densification of the materials, synthesised by CPS in previous work. Neutron absorbing cations (Gd/Hf) were added to each formulation provided a preliminary understanding of their role in the phase assemblage, and their relative durability compared to Ce. Ce, Hf and Gd were fully incorporated into the ceramic structure of the *zirconolite* and *cubic zirconia* formulations, however some heterogeneity was observed for the *zirconate pyrochlore* composition with the presence of a $(Ce,Gd)O_{2-x}$ solid solution identified. This heterogeneity resulted in increased the dissolution rate for Ce and Gd to three orders of magnitude above those reported in the literature. For the remaining three compositions, equilibrium was reached rapidly for the normalised mass loss of Ca, Ce, Gd and Ti, with dissolution rates comparable to those reported in the literature (when the aggressive conditions were considered). The dissolution rate of Ce and Gd was within one order of magnitude for these compositions, which suggests that subcriticality could be maintained in a post-closure GDF setting. In the literature, pyrochlore typically achieve $NR_{Ce, Gd}$ = 10^{-5} – 10^{-6} g m^{-2} d^{-1}, similar to dissolution rates measured for zirconolite and cubic zirconia in this work. Optimisation of the synthesis of the pyrochlore composition should

be completed to provide a more realistic understanding of the dissolution behaviour of this composition, compared to the others synthesised in this work.

Chapter 8 – Molten salt synthesis of Ce doped zirconolite for the immobilisation of pyroprocessing wastes and separated plutonium.

Molten salt synthesis was utilised to produce a self-compensating Ce doped zirconolite composition, $Ca_{0.9}Zr_{0.9}Ce_{0.2}Ti_2O_7$, with the aim of demonstrating the selective immobilisation of the entrained MA from pyroprocessing wastes. Several experimental parameters were adjusted to maximise the yield of zirconolite and eradicate the deleterious Ce-bearing perovskite phase. The conditions which yielded the highest quantity of zirconolite (83.6 ± 2.0 wt.%) was 1200 °C, 2h with a 10 wt.% ZrO_2 and 5 wt.% TiO_2 reagent excess. The requirement for the consolidation of the resulting powder negates the benefits afforded by these modest synthesis temperatures and dur.ations.

9.1 Future work

There are some key fundamental areas of future research identified throughout my thesis that would be beneficial to identifying an optimised wasteform for the immobilisation of PuO_2. These are:

1. The behaviour of Pu surrogates, particularly Ce, is a recurring theme throughout this project. Systematic work into how representative each surrogate is for Pu and how they behave comparatively in both glass and ceramics, would aid in selecting an appropriate surrogate for specific wasteform types and redox environment.
2. A systematic study into the substitution of Ce/Pu into the different sites of the zirconolite structure should be performed to eliminate deleterious perovskite from the phase assemblage.
3. Understanding the role of the HIP canister material on redox coupling at both laboratory scale and industrial scale should also be investigated, particularly when applied to glasses.
4. Implementation of long term durability tests for ceramic materials in conditions relevant to geological disposal in order to understand the role of the precipitation of Ti-O phases which are frequently formed upon the dissolution of zirconolite.
5. The role of different zirconolite polytypes (2M, 3T and 4M) on the PuO_2 wasteloading and the subsequent dissolution mechanisms/relative durability.
6. Optimisation of milling parameters *vs* synthesis temperature *vs* furnace dwell duration for the proposed candidate ceramic host phases to ensure an efficient synthesis route, free from unincorporated surrogates.
7. Further elucidate the relative dissolution rates of neutron absorbers and Pu surrogates to ensure that subcriticality will be maintained in a GDF environment upon water ingress.
8. Utilise the molten salt methodology from Chapter 8 with more realistic pyroprocessing waste streams to further investigate the feasibility of this immobilisation process.

10 References

[1] M. I. Ojovan and W. E. Lee, *An introduction to nuclear waste immobilisation*. Oxford, UK: Elsevier, 2005.

[2] Nuclear Decomissioning Authority and Department for Business Energy and Industrial Strategy, “UK Radioactive Waste Inventory,” p. 70, 2019.

[3] M. I. Ojovan and W. E. Lee, *New Developments in Glassy Nuclear Wasteforms*. New York, USA: Nova Science Publishers, 2007.

[4] W. E. Lee and R. W. Grimes, “Nuclear waste: a UK perspective,” *Energy Mater. Mater. Sci. Eng. Energy Syst.*, vol. 1, no. 1, pp. 22–24, 2006, doi: 10.1179/174892306X101125.

[5] West Cumbria: Managing Radioactive Waste Safely, “Geological Disposal Facility Gallery,” 2017. http://www.westcumbriamrws.org.uk/page/119/Geological-Disposal-Facility-Gallery.htm (accessed Feb. 06, 2017).

[6] Houses of Parliament: The Parliamentary Office of Science and Technology, “Managing the UK Plutonium Stockpile,” no. 531. 2016.

[7] D. Caurant, P. Loiseau, I. Bardez, and A. Quintas, *Glasses, Glass-ceramics and Ceramics for Immobilization of Highly Radioactive Nuclear Wastes*. New York, USA: Nova Science Publishers, 2009.

[8] International Atomic Energy Agency, “Classification of Radioactive Waste,” 2009. doi: ISBN:978-92-0-109209-0.

[9] International Atomic Energy Agency, “Scientific and Technical Basis for the Geological Disposal of Radioactive Wastes,” *Tech. Reports Ser. No. 413*, p. 90, 2003, [Online]. Available: http://www-pub.iaea.org/MTCD/Publications/PDF/TRS413_web.pdf.

[10] International Atomic Energy Agency, “Disposal of radioactive waste.,” 2011. doi: STI/PUB/1449 ISBN 978–92–0–103010–8.

[11] Nuclear Decommissioning Authority and Department for Business Energy and Industrial Strategy, “2019 UK Radioactive Material Inventory,” 2019.

[12] Nuclear Decomissioning Authority, “Progress on Plutonium Consolidation, Storage and Disposition,” 2019.

[13] Office for Nuclear Regulation, “UK Civil Pu Inventory,” *UK Civil Pu*

Inventory, 2018. http://www.onr.org.uk/safeguards/civilplut18.htm.

[14] Nuclear Decomissioning Authority, “Plutonium: Credible Options Analysis,” 2010.

[15] Department of Energy and Climate Change, “Management of the UK’s Plutonium Stocks: A consultation response on the proposed justification process for the reuse of plutonium,” 2013.

[16] N. C. Hyatt, “Plutonium management policy in the United Kingdom: The need for a dual track strategy,” *Energy Policy*, vol. 99, 2016, doi: 10.1016/j.enpol.2016.08.033.

[17] A. M. Macfarlane, “Another option for separated plutonium management: Storage MOX,” *Prog. Nucl. Energy*, vol. 49, no. 8, pp. 644–650, 2007, doi: 10.1016/j.pnucene.2007.02.001.

[18] N. C. Hyatt, “Safe management of the UK separated plutonium inventory : a challenge of materials degradation,” *npj Mater. Degrad.*, pp. 1–4, 2020, doi: 10.1038/s41529-020-00132-7.

[19] P. D. Wilson, *The nuclear fuel cycle : from ore to wastes*. Oxford University Press, 1996.

[20] C. L. Corkhill and N. C. Hyatt, *Nuclear Waste Management*. IOP Publishing, 2018.

[21] M. I. Ojovan and W. E. Lee, “Glassy wasteforms for nuclear waste immobilization,” *Metall. Mater. Trans. A Phys. Metall. Mater. Sci.*, vol. 42, no. 4, pp. 837–851, 2011, doi: 10.1007/s11661-010-0525-7.

[22] R. C. Ewing, W. J. Weber, and J. Lian, “Nuclear waste disposal-pyrochlore ($A_2B_2O_7$): Nuclear waste form for the immobilization of plutonium and ‘minor’ actinides,” *J. Appl. Phys.*, vol. 95, no. 11 I, pp. 5949–5971, 2004, doi: 10.1063/1.1707213.

[23] Synatom, “Nuclear Fuel Cycle,” 2017. http://synatom.be/en/our-technical-activities/back-end-of-the-nuclear-fuel-cycle// (accessed Feb. 06, 2017).

[24] National Nuclear Laboratory, “Advanced Reprocessing Research and Development Needs: Position Paper,” *Natl. Nucl. Lab.*, 2015, [Online]. Available: http://www.nnl.co.uk/media/1672/advanced-reprocessing-position-paper-final.pdf.

[25] D. Bodansky, *Nuclear Energy: Principles, Practices, and Prospects*.

New York, USA: Springer-Verlag, 2004.

[26] Department for Business Energy and Industrial Strategy, “Nuclear electricity in the UK.” 2019, [Online]. Available: www.gov.uk/government/statistics/electricity-chapter-5-.

[27] World Nuclear Association, “Nuclear Power Reactors.” https://www.world-nuclear.org/getmedia/de70ab05-7c99-4f3e-a139-fba8ad6dc786/pressurized-water-reactor-pwr.png.aspx (accessed Feb. 01, 2021).

[28] W. E. Lee, M. I. Ojovan, and C. M. Jantzen, Eds., *Radioactive waste management and contaminated site clean-up*. Cambridge, UK: Woodhead Publishing, 2013.

[29] H. Lee, G. Il Park, J. W. Lee, K. H. Kang, J. M. Hur, J. G. Kim, S. Paek, I. T. Kim, and I. J. Cho, “Current status of pyroprocessing development at KAERI,” *Sci. Technol. Nucl. Install.*, vol. 2013, 2013, doi: 10.1155/2013/343492.

[30] J. J. Laidler, J. E. Battles, W. E. Miller, J. P. Ackerman, and E. L. Carls, “Development of pyroprocessing technology,” *Prog. Nucl. Energy*, vol. 31, no. 1–2, pp. 131–140, 1997, doi: 10.1016/0149-1970(96)00007-8.

[31] H. Lee, G. Il Park, K. H. Kang, J. M. Hur, J. G. Kim, D. H. Ahn, Y. Z. Cho, and E. H. Kim, “Pyroprocessing technology development at KAERI,” *Nucl. Eng. Technol.*, vol. 43, no. 4, pp. 317–328, 2011, doi: 10.5516/NET.2011.43.4.317.

[32] M. A. Williamson and J. L. Willit, “Pyroprocessing flowsheets for recycling used nuclear fuel,” *Nucl. Eng. Technol.*, vol. 43, no. 4, pp. 329–334, 2011, doi: 10.5516/NET.2011.43.4.329.

[33] A. R. Mason, F. Y. Tocino, M. C. Stennett, and N. C. Hyatt, “Molten salt synthesis of Ce doped zirconolite for the immobilisation of pyroprocessing wastes and separated plutonium,” *Ceram. Int.*, vol. 46, no. 18, pp. 29080–29089, 2020, doi: 10.1016/j.ceramint.2020.08.080.

[34] M. R. Gilbert, “Molten salt synthesis of titanate pyrochlore waste-forms,” *Ceram. Int.*, vol. 42, no. 4, pp. 1–8, 2015, doi: 10.1016/j.ceramint.2015.12.054.

[35] M. L. Hand, M. C. Stennett, and N. C. Hyatt, “Rapid low temperature synthesis of a titanate pyrochlore by molten salt mediated reaction,” *J.*

Eur. Ceram. Soc., vol. 32, no. 12, pp. 3211–3219, 2012, doi: 10.1016/j.jeurceramsoc.2012.04.046.

[36] M. A. Lewis, D. F. Fischer, and L. J. Smith, “Salt□Occluded Zeolites as an Immobilization Matrix for Chloride Waste Salt,” *J. Am. Ceram. Soc.*, vol. 76, no. 11, pp. 2826–2832, 1993, doi: 10.1111/j.1151-2916.1993.tb04023.x.

[37] Y. Z. Cho, G. H. Park, H. C. Yang, D. S. Han, H. S. Lee, and I. T. Kim, “Minimization of eutectic salt waste from pyroprocessing by oxidative precipitation of lanthanides,” *J. Nucl. Sci. Technol.*, vol. 46, no. 10, pp. 1004–1011, 2009, doi: 10.1080/18811248.2009.9711610.

[38] Y. J. Cho, H. C. Yang, H. C. Eun, E. H. Kim, and I. T. Kim, “Characteristics of Oxidation Reaction of Rare-earth Chlorides for Precipitation in LiCl-KCl Molten Salt by Oxygen Sparging,” *J. Nucl. Sci. Technol.*, vol. 43, no. 10, pp. 1280–1286, 2006, doi: 10.1080/18811248.2006.9711221.

[39] International Atomic Energy Agency, “Spent Fuel Reprocessing Options,” no. IAEA-TECDOC-1587. 2009.

[40] W. E. Lee, M. I. Ojovan, M. C. Stennett, and N. C. Hyatt, “Immobilisation of radioactive waste in glasses, glass composite materials and ceramics,” *Adv. Appl. Ceram.*, vol. 105, no. 1, pp. 3–12, 2006, doi: 10.1179/174367606X81669.

[41] G. G. Wicks, J. M. Mckibben, and M. J. Plodinec, “Vitrification of Excess Plutonium (U),” in *Waste Management Conference*, 1995, pp. 1–10.

[42] R. C. Ewing, “Plutonium and ‘minor’ actinides: Safe sequestration,” *Earth Planet. Sci. Lett.*, vol. 229, no. 3–4, pp. 165–181, 2005, doi: 10.1016/j.epsl.2004.11.017.

[43] M. T. Harrison, C. R. Scales, and E. R. Maddrell, “Progress in the Assessment of Wasteforms for the Immobilisation of UK Civil Plutonium,” in *Waste Management Conference*, 2008, doi: 10.1017/CBO9781107415324.004.

[44] W. L. Gong, S. Naz, W. Lutze, R. Busch, A. Prinja, and W. Stoll, “Safe disposal of surplus plutonium,” *J. Nucl. Mater.*, vol. 295, no. 2–3, pp. 295–299, 2001, doi: 10.1016/S0022-3115(01)00488-3.

[45] I. Muller and W. J. Weber, “Plutonium in crystalline ceramics and

glasses," *MRS Bull.*, vol. 26, no. 9, pp. 698–706, 2001, doi: 10.1557/mrs2001.180.

[46] R. C. Ewing, W. J. Weber, and W. Lutze, "Crystalline Ceramics: Waste Forms for the Disposal of Weapons Plutonium," in *Disposal of Weapons Plutonium*, E. R. Merz and C. E. Walter, Eds. Kluwer Academic Publishers, 1996, pp. 65–83.

[47] M. C. Dixon Wilkins, M. C. Stennett, E. Maddrell, and N. C. Hyatt, "The formation of stoichiometric uranium brannerite (UTi_2O_6) glass-ceramic composites from the component oxides in a one-pot synthesis," *J. Nucl. Mater.*, vol. 542, no. January, p. 152516, 2020, doi: 10.1016/j.jnucmat.2020.152516.

[48] J. S. McCloy and A. Goel, "Glass-ceramics for nuclear-waste immobilization," *MRS Bull.*, vol. 42, no. 03, pp. 233–240, 2017, doi: 10.1557/mrs.2017.8.

[49] A. R. Mason, S. M. Thornber, M. C. Stennett, L. J. Gardner, D. Lützenkirchen-Hecht, and N. C. Hyatt, "Preliminary investigation of chlorine speciation in zirconolite glass-ceramics for plutonium residues by analysis of Cl K-edge XANES," *MRS Adv.*, pp. 1–7, 2019, doi: 10.1557/adv.2019.460.

[50] S. M. Thornber, L. M. Mottram, A. R. Mason, P. Thompson, M. C. Stennett, and N. C. Hyatt, "Solubility, speciation and local environment of chlorine in zirconolite glass–ceramics for the immobilisation of plutonium residues," *RSC Adv.*, vol. 10, pp. 32497–32510, 2020, doi: 10.1039/D0RA04938G.

[51] S. M. Thornber, M. C. Stennett, E. R. Vance, D. T. Chavara, I. Watson, M. Jovanovich, J. Davis, D. J. Gregg, and N. C. Hyatt, "A preliminary validation study of PuO_2 incorporation into zirconolite glass-ceramics," *MRS Adv.*, vol. 3, no. 20, pp. 1065–1071, 2018, doi: 10.1557/adv.2018.

[52] S. M. Thornber, P. G. Heath, G. P. Da, M. C. Stennett, and N. C. Hyatt, "The effect of pre-treatment parameters on the quality of glass-ceramic wasteforms for plutonium immobilisation, consolidated by hot isostatic pressing," *J. Nucl. Mater.*, vol. 485, 2017, doi: 10.1016/j.jnucmat.2016.12.028.

[53] E. Maddrell, S. Thornber, and N. C. Hyatt, "The influence of glass

composition on crystalline phase stability in glass-ceramic wasteforms," *J. Nucl. Mater.*, vol. 456, pp. 461–466, 2015, doi: 10.1016/j.jnucmat.2014.10.010.

[54] J. N. Cachia, X. Deschanels, C. Den Auwer, O. Pinet, J. Phalippou, C. Hennig, and A. Scheinost, "Enhancing cerium and plutonium solubility by reduction in borosilicate glass," *J. Nucl. Mater.*, vol. 352, no. 1–3, pp. 182–189, 2006, doi: 10.1016/j.jnucmat.2006.02.052.

[55] B. Grambow, "Nuclear waste glasses - How durable?," *Elements*, vol. 2, no. 6, pp. 357–364, 2006, doi: 10.2113/gselements.2.6.357.

[56] C. M. Jantzen, K. G. Brown, and J. B. Pickett, "Durable Glass for Thousands of Years," *Int. J. Appl. Glas. Sci.*, vol. 1, no. 1, pp. 38–62, 2010, doi: 10.1111/j.2041-1294.2010.00007.x.

[57] S. Gin, P. Jollivet, M. Tribet, S. Peuget, and S. Schuller, "Radionuclides containment in nuclear glasses: an overview," *Radiochim. Acta*, vol. 105, no. 11, pp. 927–959, 2017, doi: 10.1515/ract-2016-2658.

[58] J. E. Shelby, *Introduction to Glass Science and Techonology*, Second Edi. Cambridge, UK: Royal Society of Chemistry, 2005.

[59] W. H. Zachariasen, "The atomic arrangement in glass," *J. Am. Chem. Soc.*, vol. 54, no. 10, pp. 3841–3851, 1932, doi: 10.1021/ja01349a006.

[60] A. C. Wright, R. A. Hulme, D. I. Grimley, R. N. Sinclair, S. W. Martin, D. L. Price, and F. L. Galeener, "The structure of some simple amorphous network solids revisited," *J. Non. Cryst. Solids*, vol. 129, no. 1–3, pp. 213–232, 1991, doi: 10.1016/0022-3093(91)90098-Q.

[61] B. E. Warren, "Summary of Work on Atomic Arrangement in Glass," *J. Am. Ceram. Soc.*, vol. 24, no. 8, pp. 256–261, 1941, doi: 10.1111/j.1151-2916.1941.tb14858.x.

[62] G. N. Greaves, "EXAFS and the structure of glass," *J. Non. Cryst. Solids*, vol. 71, pp. 203–217, 1985.

[63] W. Vogel, *Glass Chemistry*, Second edi. Berlin: Springer-Verlag, 1994.

[64] I. W. Donald, *Waste Immobilisation in Glass and Ceramic Based Hosts*. Chichester: Wiley, 2010.

[65] A. J. G. Ellison, J. J. Mazer, and W. L. Ebert, "Effect of Glass Composition on Waste Form Durability: A Critical Review," Argonne, USA, 1994.

[66] J. K. Bates, A. J. G. Ellison, J. W. Emery, and J. C. Hoh, “Glass as a waste form for the immobilisation of plutonium,” *Mat. Res. Soc. Symp. Proc.*, vol. 412, pp. 57–64, 1996.

[67] D. C. Chamberlain, J. M. Hanchar, J. W. Emery, J. C. Hoh, S. F. Wolf, R. J. Finch, J. K. Bates, A. J. G. Ellison, and D. B. Dingwell, “Development and testing of a glass waste form for the immobilization of plutonium,” *Mater. Res. Soc. Symp. Proc.*, vol. 465, pp. 1229–1236, 1997.

[68] C. R. Scales, E. R. Maddrell, and M. T. Harrison, “Options for the Immobilisation of UK Civil Plutonium,” in *Waste Management Conference*, 2007.

[69] M. T. Harrison and C. R. Scales, “Development of Borosilicate Glass Compositions for the Immobilisation of the UK’s Separated Plutonium Stocks,” *Mater. Res. Soc. Symp. Proc.*, vol. 1107, 2008.

[70] M. T. Harrison, C. R. Scales, P. A. Bingham, and R. J. Hand, “Survey of Potential Glass Compositions for the Immobilisation of the UK’s Separated Plutonium Stocks,” *Mat. Res. Soc. Symp. Proc.*, vol. 985, pp. 151–156, 2007.

[71] P. A. Bingham, A. J. Connelly, N. C. Hyatt, and R. J. Hand, “Corrosion of glass contact refractories for the vitrification of radioactive wastes: A review,” *Int. Mater. Rev.*, vol. 56, no. 4, pp. 226–242, 2011, doi: 10.1179/1743280410Y.0000000005.

[72] P. A. Bingham, R. J. Hand, C. R. Scales, and M. Street, “Immobilisation of Simulated Plutonium-Contaminated Material in Phosphate Glass: An Initial Scoping Study,” *Mat. Res. Soc. Symp. Proc.*, vol. 932, 2006.

[73] B. E. Burakov, M. A. Yagovkina, M. V Zamoryanskaya, A. A. Kitsay, V. M. Garbuzov, E. B. Anderson, and A. S. Pankov, “Behavior of ^{238}Pu-Doped Cubic Zirconia under Self-Irradiation,” *Mat. Res. Soc. Symp. Proc.*, vol. 807, pp. 1–5, 2004.

[74] S. A. McMaster, R. Ram, N. Faris, and M. I. Pownceby, “Radionuclide disposal using the pyrochlore supergroup of minerals as a host matrix—A review,” *J. Hazard. Mater.*, vol. 360, no. March, pp. 257–269, 2018, doi: 10.1016/j.jhazmat.2018.08.037.

[75] Y. Zhang, K. P. Hart, B. D. Begg, E. A. Keegan, R. A. Day, A.

Brownscombe, and M. W. A. Stewart, “Durability of Pu-doped Titanate and Zirconate Ceramics Designed for Pu Immobilisation,” *Mat. Res. Soc. Symp. Proc.*, vol. 713, pp. 1–7, 2002, doi: 10.1557/proc-713-jj6.1.

[76] M. W. A. Stewart, D. B. Bruce, E. R. Vance, K. Finnie, H. Li, G. R. Lumpkin, K. Smith, W. J. Weber, and S. Thevuthasan, “The Replacement of Titanium by Zirconium in Ceramics for Plutonium Immobilization,” *Mater. Res.*, vol. 715, pp. 1–6, 2002.

[77] R. Gieré, C. T. Williams, and G. Lumpkin, “Chemical characteristics of natural zirconolite,” *Swiss Soc. Mineral. Petrol.*, vol. 78, pp. 433–459, 1998, doi: 10.5169/seals-59299.

[78] H. J. Rossell, “Zirconolite-a fluorite-related superstructure,” *Nature*, vol. 283. pp. 282–283, 1980, doi: 10.1038/283282a0.

[79] K. R. Whittle, N. C. Hyatt, K. L. Smith, I. Margiolaki, F. J. Berry, K. S. Knight, and G. R. Lumpkin, “Combined neutron and X-ray diffraction determination of disorder in doped zirconolite-2M,” *Am. Mineral.*, vol. 97, no. 2–3, pp. 291–298, 2012, doi: 10.2138/am.2012.3848.

[80] A. A. Coelho, R. W. Cheary, and K. L. Smith, “Analysis and Structural Determination of Nd-Substituted Zirconolite-4M,” *J. Solid State Chem.*, vol. 129, no. 2, pp. 346–359, 1997, doi: 10.1006/jssc.1996.7263.

[81] N. V. Zubkova, N. V. Chukanov, I. V. Pekov, B. Ternes, W. Schüller, D. A. Ksenofontov, and D. Y. Pushcharovsky, “The crystal structure of nonmetamict Nb-rich zirconolite-3T from the Eifel paleovolcanic region, Germany,” *Zeitschrift fur Krist. - Cryst. Mater.*, vol. 233, no. 7, pp. 463–468, 2018, doi: 10.1515/zkri-2017-2133.

[82] I. E. Grey, W. G. Mumme, T. J. Ness, R. S. Roth, and K. L. Smith, “Structural relations between weberite and zirconolite polytypes - Refinements of doped 3T and 4M $Ca_2Ta_2O_7$ and 3T $CaZrTi_2O_7$,” *J. Solid State Chem.*, vol. 174, no. 2, pp. 285–295, 2003, doi: 10.1016/S0022-4596(03)00222-6.

[83] N. V. Chukanov, N. V. Zubkova, S. N. Britvin, I. V. Pekov, M. F. Vigasina, C. Schäfer, B. Ternes, W. Schüller, Y. S. Polekhovsky, V. N. Ermolaeva, and D. Y. Pushcharovsky, “Nöggerathite-(Ce), $(Ce,Ca)_2Zr_2(Nb,Ti)(Ti,Nb)_2Fe^{2+}O_{14}$, a new zirconolite-related mineral from the Eifel volcanic region, Germany,” *Minerals*, vol. 8, no. 10, pp. 1–

14, 2018, doi: 10.3390/min8100449.

[84] T. J. White, R. L. Segall, J. L. Hutchison, and J. C. Barry, “Polytypic behaviour of zirconolite,” *Proc. R. Soc. Lond. A*, vol. 392, no. 1803, pp. 343–358, 1984, doi: 10.1098/rspa.1984.0035.

[85] A. Salamat, P. F. McMillan, S. Firth, K. Woodhead, A. L. Hector, G. Garbarino, M. C. Stennett, and N. C. Hyatt, “Structural transformations and disordering in zirconolite ($CaZrTi_2O_7$) at high pressure.,” *Inorg. Chem.*, vol. 52, no. 3, pp. 1550–8, 2013, doi: 10.1021/ic302346g.

[86] E. R. Vance, G. R. Lumpkin, M. L. Carter, D. J. Cassidy, C. J. Ball, R. A. Day, and B. D. Begg, “Incorporation of uranium in zirconolite ($CaZrTi_2O_7$),” *J. Am. Ceram. Soc.*, vol. 85, no. 7, pp. 1853–1859, 2002, doi: 10.1111/j.1151-2916.2002.tb00364.x.

[87] B. M. Clark, S. K. Sundaram, and S. T. Misture, “Polymorphic Transitions in Cerium-Substituted Zirconolite ($CaZrTi_2O_7$),” *Sci. Rep.*, vol. 7, no. 1, pp. 2–10, 2017, doi: 10.1038/s41598-017-06407-5.

[88] R. D. Shannon, “Revised effective ionic radii and systematic studies of interatomic distances in halides and chalcogenides,” *Acta Crystallogr. Sect. A*, vol. 32, no. 5, pp. 751–767, 1976, doi: 10.1107/S0567739476001551.

[89] B. D. Begg, R. A. Day, and A. Brownscombe, “Structural effect of Pu substitutions on the Zr-site in zirconolite,” *Mat. Res. Soc. Symp. Proc.*, vol. 663, 2001, doi: 10.1557/PROC-663-259.

[90] B. D. Begg, E. R. Vance, and G. R. Lumpkin, “Charge Compensation and the Incorporation of Cerium in Zirconolite and Perovskite,” *Mat. Res. Soc. Symp. Proc.*, vol. 506, pp. 79–86, 1998, doi: 10.1557/proc-506-79.

[91] E. R. Vance, C. J. Ball, R. A. Day, K. L. Smith, M. G. Blackford, B. D. Begg, and P. J. Angel, “Actinide and rare earth incorporation into zirconolite,” *J. Alloys Compd.*, vol. 213–214, no. C, pp. 406–409, 1994, doi: 10.1016/0925-8388(94)90945-8.

[92] G. R. Lumpkin, “Ceramic waste forms for actinides,” *Elements*, vol. 2, no. 6, pp. 365–372, 2006, doi: 10.2113/gselements.2.6.365.

[93] G. R. Lumpkin, K. L. Smith, M. G. Blackford, R. Giere, and C. Terry Williams, “Determination of 25 elements in the complex oxide mineral zirconolite by analytical electron microscopy,” *Micron*, vol. 25, no. 6, pp.

581–587, 1994, doi: 10.1016/0968-4328(94)90020-5.

[94] T. J. White, “The microstructure and microchemistry of synthetic zirconolite, zirkelite and related phases.,” *Am. Mineral.*, vol. 69, no. 11–12, pp. 1156–1172, 1984.

[95] R. Giere and P. Stille, *Energy, Waste and the Environment: a Geochemical Perspective*. Bath, UK: The Geological Society, 2004.

[96] G. R. Lumpkin, K. L. Smith, and M. G. Blackford, “Electron microscope study of Synroc before and after exposure to aqueous solutions,” *J. Mater. Res.*, vol. 6, no. 10, pp. 2218–2233, 1991, doi: 10.1557/JMR.1991.2218.

[97] A. E. Ringwood, S. E. Kesson, N. G. Ware, W. O. Hibberson, and A. Major, “The SYNROC process: A geochemical approach to nuclear waste immobilization,” *Geochem. J.*, vol. 13, pp. 141–165, 1979.

[98] A. E. Ringwood, V. M. Oversby, S. E. Kesson, W. Sinclair, N. Ware, W. Hibberson, and A. Major, “Immobilization of high-level nuclear reactor wastes in SYNROC: A current appraisal,” *Nucl. Chem. Waste Manag.*, vol. 2, no. 4, pp. 287–305, 1981, doi: 10.1016/0191-815X(81)90055-3.

[99] E. R. Vance, “Synroc: A Suitable Waste Form for Actinides,” *MRS Bull.*, vol. 19, no. 12, pp. 28–32, 1994, doi: 10.1557/S0883769400048661.

[100] G. A. Armantrout, L. Gray, C. C. Herman, H. F. Shaw, and R. A. Van Konynenburg, “Plutonium Immobilization Project Baseline Formulation,” 2000.

[101] ASTM International, “ASTM C1285.21: Standard Methods for Determining Chemical Durability of Nuclear, Hazardous and Mixed Waste Glasses and Multiphase Glass Ceramics: The Product Consistency Test (PCT).” 2021, doi: 10.1520/C1285-02R08.

[102] ASTM International, “ASTM C1220-20: Standard Test Method for Static Leaching of Monolithic Waste Forms for Disposal of Radioactive Waste.” 2020, doi: 10.1520/C1220-10.

[103] G. S. Frankel, J. D. Vienna, J. Lian, J. R. Scully, S. Gin, J. V. Ryan, J. Wang, S. H. Kim, W. Windl, and J. Du, “A comparative review of the aqueous corrosion of glasses, crystalline ceramics, and metals,” *npj Mater. Degrad.*, vol. 2, no. 1, 2018, doi: 10.1038/s41529-018-0037-2.

[104] ASTM International, “ASTM C1662-18: Standard Practice for

Measurement of the Glass Dissolution Rate Using the Single-Pass Flow-Through Test Method." 2018, doi: 10.1520/C1662-10.1.8.

[105] S. Gin, A. Abdelouas, L. J. Criscenti, W. L. Ebert, K. Ferrand, T. Geisler, M. T. Harrison, Y. Inagaki, S. Mitsui, K. T. Mueller, J. C. Marra, C. G. Pantano, E. M. Pierce, J. V. Ryan, J. M. Schofield, C. I. Steefel, and J. D. Vienna, "An international initiative on long-term behavior of high-level nuclear waste glass," *Mater. Today*, vol. 16, no. 6, pp. 243–248, 2013, doi: 10.1016/j.mattod.2013.06.008.

[106] T. Geisler, T. Nagel, M. R. Kilburn, A. Janssen, J. P. Icenhower, R. O. C. Fonseca, M. Grange, and A. A. Nemchin, "The mechanism of borosilicate glass corrosion revisited," *Geochim. Cosmochim. Acta*, vol. 158, pp. 112–129, 2015, doi: 10.1016/j.gca.2015.02.039.

[107] C. Lenting, O. Plümper, M. Kilburn, P. Guagliardo, M. Klinkenberg, and T. Geisler, "Towards a unifying mechanistic model for silicate glass corrosion," *npj Mater. Degrad.*, vol. 2, no. 1, 2018, doi: 10.1038/s41529-018-0048-z.

[108] S. Gin, L. Neill, M. Fournier, P. Frugier, T. Ducasse, M. Tribet, A. Abdelouas, B. Parruzot, J. Neeway, and N. Wall, "The controversial role of inter-diffusion in glass alteration," *Chem. Geol.*, vol. 440, pp. 115–123, 2016, doi: 10.1016/j.chemgeo.2016.07.014.

[109] J. D. Vienna, J. V. Ryan, S. Gin, and Y. Inagaki, "Current understanding and remaining challenges in modeling long-term degradation of borosilicate nuclear waste glasses," *Int. J. Appl. Glas. Sci.*, vol. 4, no. 4, pp. 283–294, 2013, doi: 10.1111/ijag.12050.

[110] C. A. Utton, S. W. Swanton, J. Schofield, R. J. Hand, A. Clacher, and N. C. Hyatt, "Chemical durability of vitrified wasteforms: effects of pH and solution composition," *Mineral. Mag.*, vol. 76, no. 8, pp. 2919–2930, 2012, doi: 10.1180/minmag.2012.076.8.07.

[111] B. Grambow and R. Müller, "First-order dissolution rate law and the role of surface layers in glass performance assessment," *J. Nucl. Mater.*, vol. 298, no. 1–2, pp. 112–124, 2001, doi: 10.1016/s0022-3115(01)00619-5.

[112] K. L. Smith, G. R. Lumpkin, M. G. Blackford, R. A. Day, and K. P. Hart, "The durability of Synroc," *J. Nucl. Mater.*, vol. 190, pp. 287–294, 1992,

doi: 10.1016/0022-3115(92)90092-Y.

[113] K. P. Hart, Y. Zhang, E. Loi, Z. Aly, M. W. A. Stewart, A. Brownscombe, B. Ebbinghaus, and W. Bourcier, “Aqueous durability of titanate ceramics designed to immobilise excess plutonium,” *Mater. Res. Soc. Symp. - Proc.*, vol. 608, no. 1999, pp. 353–358, 2000, doi: 10.1557/proc-608-353.

[114] K. Zhang, S. He, D. Yin, L. Peng, and J. Wu, “Self-propagating synthesis and aqueous durability of Nd-bearing zirconolite-rich composites using Ca(NO3)2 as the oxidant,” *J. Nucl. Mater.*, vol. 478, pp. 315–321, 2016, doi: 10.1016/j.jnucmat.2016.06.033.

[115] G. Wen, K. Zhang, D. Yin, and H. Zhang, “Solid-state reaction synthesis and aqueous durability of Ce-doped zirconolite-rich ceramics,” *J. Nucl. Mater.*, vol. 466, pp. 113–119, 2015, doi: 10.1016/j.jnucmat.2015.07.047.

[116] M. Tribet, N. Toulhoat, N. Moncoffre, C. Jégou, G. Leturcq, C. Corbel, and P. Toulhoat, “Leaching of a zirconolite ceramic waste-form under proton and He $^{2+}$ irradiation,” *Radiochim. Acta*, vol. 96, no. 9–11, pp. 619–624, 2008, doi: 10.1524/ract.2008.1545.

[117] S. Finkeldei, F. Brandt, K. Rozov, A. A. Bukaemskiy, S. Neumeier, and D. Bosbach, “Dissolution of ZrO_2 based pyrochlores in the acid pH range: A macroscopic and electron microscopy study,” *Appl. Geochemistry*, vol. 49, pp. 31–41, 2014, doi: 10.1016/j.apgeochem.2014.06.014.

[118] J. P. Icenhower, D. M. Strachan, B. P. McGrail, R. D. Scheele, E. A. Rodriguez, J. L. Steele, and V. L. Legore, “Dissolution kinetics of pyrochlore ceramics for the disposition of plutonium,” *Am. Mineral.*, vol. 91, no. 1, pp. 39–53, 2006, doi: 10.2138/am.2006.1709.

[119] R. B. Heimann and T. T. Vandergraaf, “Cubic zirconia as a candidate waste form for actinides: Dissolution studies,” *J. Mater. Sci. Lett.*, vol. 7, no. 6, pp. 583–586, 1988, doi: 10.1007/BF01730301.

[120] A. R. West, *Basic Solid State Chemistry*, Second Edi. John Wiley and Sons Ltd, 2003.

[121] M. N. Rahaman, *Ceramic Processing and Sintering*, Second Edi. New York, USA: Taylor & Francis, 2003.

[122] T. Kimura, “Molten Salt Synthesis of Ceramic Powders,” in *Advances in Ceramics - Synthesis and Characterization, Processing and Specific Applications*, C. Sikalidis, Ed. InTech Open, 2011, pp. 75–100.

[123] T. Kimura and T. Yamaguchi, “Morphology of Bi_2WO_6 powders obtained in the presence of fused salts,” *J. Mater. Sci.*, vol. 17, no. 7, pp. 1863–1870, 1982, doi: 10.1007/BF00540401.

[124] B. Yang, X. Yuan, and D. Chai, “A rational self-sacrificing template route to $LiMn_2O_4$ Nanotubes and Nanowires,” *J. Nanomater.*, vol. 2011, no. 20 mL, pp. 5–10, 2011, doi: 10.1155/2011/197265.

[125] S. M. Thornber, “The Development of Zirconolite Glass-Ceramics for the Disposition of Actinide Wastes,” The University of Sheffield, 2018.

[126] E. Maddrell, “Hot isostatically pressed wasteforms for future nuclear fuel cycles,” *Chem. Eng. Res. Des.*, vol. 91, no. 4, pp. 735–741, 2013, doi: 10.1016/j.cherd.2012.11.004.

[127] M. W. A. Stewart, S. Moricca, T. Eddowes, E. R. Vance, M. Dowson, M. L. Carter, Y. Zhang, G. R. Lumpkin, M. Dowson, and M. James, “The use of hot-isostatic pressing to process nuclear waste forms,” in *Proceedings of The 2009 12th International Conference on Environmental Remediation and Radioactive Waste Management*, 2009, pp. 1–6.

[128] T. Egami and S. J. L. Billinge, *Underneath the Bragg Peaks: Structural Analysis of Complex Materials*, vol. 7. Elsevier, 2003.

[129] B. D. Cullity and S. R. Stock, “Elements of X-ray diffraction, 3rd edition,” *Prentice Hall*, 2001.

[130] R. A. Young, “Introduction to the Rietveld Method,” in *The Rietveld Method*, 1995.

[131] L. B. Mccusker, R. B. Von Dreele, D. E. Cox, D. Louër, and P. Scardi, “Rietveld refinement guidelines,” *J. Appl. Crystallogr.*, vol. 32, no. 1, 1999, doi: 10.1107/S0021889898009856.

[132] P. J. Goodhew, J. Humphreys, and R. Beanland, *Electron Microscopy and Analysis*, Third Edit. London, UK: Taylor and Francis, 2001.

[133] L. Reimer, *Scanning Electron Microscopy*, Second Edi. Heidelberg, Germany: Springer-Verlag, 1998.

[134] M. Newville, “Fundamentals of XAFS,” *Rev. Mineral. Geochemistry*, vol.

78, no. 1, pp. 33–74, Jan. 2014, doi: 10.2138/rmg.2014.78.2.

[135] G. Bunker, *Introduction to XAFS*. Cambridge, UK: Cambridge University Press, 2010.

[136] B. Ravel and M. Newville, “ATHENA, ARTEMIS, HEPHAESTUS: Data analysis for X-ray absorption spectroscopy using IFEFFIT,” *J. Synchrotron Radiat.*, vol. 12, no. 4, pp. 537–541, 2005, doi: 10.1107/S0909049505012719.

[137] T. E. Cranshaw, B. W. Dale, G. O. Longworth, and C. E. Johnson, *Mossbauer spectroscopy and its applications*. Cambridge, UK: Cambridge University Press, 1985.

[138] D. G. Rancourt and K. Lagarec, “Recoil, Mossbauer Spectral Analysis Software for Windows.” 1998.

[139] B. D. Begg and E. R. Vance, “The incorporation of cerium in zirconolite,” *Mat. Res. Soc. Symp. Proc.*, vol. 465, pp. 333–340, 1997, doi: 10.1557/PROC-465-333.

[140] C. Lopez, X. Deschanels, J. M. Bart, J. M. Boubals, C. Den Auwer, and E. Simoni, “Solubility of actinide surrogates in nuclear glasses,” *J. Nucl. Mater.*, vol. 312, no. 1, pp. 76–80, 2003, doi: 10.1016/S0022-3115(02)01549-0.

[141] P. A. Bingham, R. J. Hand, M. C. Stennett, N. C. Hyatt, and M. T. Harrison, “The Use of Surrogates in Waste Immobilization Studies: A Case Study of Plutonium,” *Mater. Res. Soc. Symp. Proc.*, vol. 1107, 2008, doi: 10.1557/PROC-1107-421.

[142] M. Fournier, A. Ull, E. Nicoleau, Y. Inagaki, M. Odorico, P. Frugier, and S. Gin, “Glass dissolution rate measurement and calculation revisited,” *J. Nucl. Mater.*, vol. 476, pp. 140–154, 2016, doi: 10.1016/j.jnucmat.2016.04.028.

[143] D. L. Parkhurst and C. A. J. Appelo, “Description of input and examples for PHREEQC version 3--A computer program for speciation, batch-reaction, one-dimensional transport, and inverse geochemical calculations,” in *U.S. Geological Survey Techniques and Methods, Book 6*, 2013, p. 497.

[144] S. R. Charlton and D. L. Parkhurst, “Modules based on the geochemical model PHREEQC for use in scripting and programming languages,”

Comput. Geosci., vol. 37, no. 10, pp. 1653–1663, 2011, doi: 10.1016/j.cageo.2011.02.005.

[145] Department of Energy and Climate Change, “Management of the UK’s plutonium stocks: A consultation on the long-term management of UK owned separated civil plutonium,” 2011. doi: 10.1002/ana.22373.

[146] B. F. Dunnett, “Review of the Development of UK High Level Waste Vitrified Product,” 2007.

[147] X. Deschanels, C. Lopez, C. Denauwer, and J. M. Bart, “Solubility Of Plutonium and Surrogates in Nuclear Glass Matrices,” *AIP Conf. Proc.*, vol. 673, no. 2003, pp. 59–60, 2003, doi: 10.1063/1.1594553.

[148] J. C. Marra, C. L. Crawford, K. M. Fox, and N. E. Bibler, “Plutonium solubility in HLW alkali borosilicate glass,” 2010. [Online]. Available: http://sti.srs.gov/fulltext/SRNL-STI-2010-00766.pdf.

[149] C. Shearer, R. G. Moore, C. H. Zimmerman, C. Scafes, A. Worrall, H. E. Sims, and L. Fowler, “Options for the disposition of UK civil plutonium stocks,” *Nucl. Futur.*, vol. 4, no. 6, pp. 341–346, 2008.

[150] E. R. Vance, A. Jostsons, R. A. Day, C. J. Ball, B. D. Begg, and P. J. Angel, “Excess Pu disposition in zirconolite-rich Synroc,” *Mat. Res. Soc. Symp. Proc.*, vol. 412, pp. 41–47, 1996, doi: 10.1557/proc-412-41.

[151] I. Muller, W. J. Weber, E. R. Vance, G. Wicks, and D. Karraker, “Glass, Ceramics and Composites,” in *Advances in Plutonium Chemistry 1967-2000*, D. C. Hoffman, Ed. 2002, pp. 260–300.

[152] ASTM International, “ASTM C1663-18: Standard Test Method for Measuring Waste Glass or Glass Ceramic Durability by Vapor Hydration Test.” 2018, doi: 10.1520/C1663-09.2.

[153] M. T. Harrison and C. R. Scales, “Durability of Borosilicate Glass Compositions for the Immobilisation of the UK’s Separated Plutonium Stocks,” *Mat. Res. Soc. Symp. Proc.*, vol. 1107, pp. 1–6, 2008.

[154] A. Dietzel, “Strukturchemie des Glases,” *Naturwissenschaften*, vol. 29, pp. 537–547, 1941.

[155] X. Deschanels, J. N. Cachia, C. Lopez, and S. Peuget, “Influence of processing conditions on the glass-crystal transition into borosilicate glasses,” *Int. Conf. Nucl. Chem. Sustain. Fuel Cycles*, pp. 1–7, 2008.

[156] National Academy of Sciences, *Management and Disposition of Excess*

Weapons Plutonium. Washington, DC: The National Academies Press, 1994.

[157] M. Borsboom, W. Bras, I. Cerjak, D. Detollenaere, D. Glastra Van Loon, P. Goedtkindt, M. Konijnenburg, P. Lassing, Y. K. Levine, B. Munneke, M. Oversluizen, R. Van Tol, and E. Vlieg, "The Dutch-Belgian beamline at the ESRF," *J. Synchrotron Radiat.*, vol. 5, no. 3, pp. 518–520, 1998, doi: 10.1107/S0909049597013484.

[158] M. Wilke, F. Farges, P. E. Petit, G. E. Brown, and F. Martin, "Oxidation state and coordination of Fe in minerals: An Fe K-XANES spectroscopic study," *Am. Mineral.*, vol. 86, no. 5–6, pp. 714–730, 2001, doi: 10.2138/am-2001-5-612.

[159] D. J. Bailey, M. C. Stennett, A. R. Mason, and N. C. Hyatt, "Synthesis and characterisation of the hollandite solid solution Ba1.2-xCsxFe2.4-xTi5.6+xO16 for partitioning and conditioning of radiocaesium," *J. Nucl. Mater.*, vol. 503, pp. 164–170, 2018, doi: 10.1016/j.jnucmat.2018.03.005.

[160] J. C. Woicik, B. Ravel, D. A. Fischer, and W. J. Newburgh, "Performance of a four-element Si drift detector for X-ray absorption fine-structure spectroscopy: Resolution, maximum count rate, and dead-time correction with incorporation into the ATHENA data analysis software," *J. Synchrotron Radiat.*, vol. 17, no. 3, pp. 409–413, 2010, doi: 10.1107/S0909049510009064.

[161] S. I. Zabinsky, J. J. Rehr, A. Ankudinov, R. C. Albers, and M. J. Eller, "Multiple-scattering calculations of x-ray-absorption spectra," *Phys. Rev. B*, vol. 52, no. 4, pp. 2995–3009, 1995, doi: 10.1103/PhysRevB.52.2995.

[162] N. E. Brese and M. O'Keeffe, "Bond□valence parameters for solids," *Acta Crystallogr. Sect. B*, vol. 47, no. 2, pp. 192–197, 1991, doi: 10.1107/S0108768190011041.

[163] D. L. Parkhurst and C. a. J. Appelo, "Description of Input and Examples for PHREEQC Version 3 — A Computer Program for Speciation , Batch-Reaction , One-Dimensional Transport , and Inverse Geochemical Calculations. U.S. Geological Survey Techniques and Methods, book 6, chapter A43, 497 p.," *U.S. Geol. Surv. Tech. Methods, B. 6, chapter A43*,

pp. 6-43A, 2013.

[164] M. C. Stennett, C. L. Freeman, A. S. Gandy, and N. C. Hyatt, “Crystal structure and non-stoichiometry of cerium brannerite: $Ce_{0.975}Ti_2O_{5.95}$,” *J. Solid State Chem.*, vol. 192, pp. 172–178, 2012, doi: 10.1016/j.jssc.2012.03.057.

[165] N. C. Hyatt, R. R. Schwarz, P. A. Bingham, M. C. Stennett, C. L. Corkhill, P. G. Heath, R. J. Hand, M. James, A. Pearson, and S. Morgan, “Thermal treatment of simulant plutonium contaminated materials from the Sellafield site by vitrification in a blast-furnace slag,” *J. Nucl. Mater.*, vol. 444, no. 1–3, pp. 186–199, 2014, doi: 10.1016/j.jnucmat.2013.08.019.

[166] N. E. Bibler, W. G. Ramsey, T. F. Meaker, and J. M. Pareizs, “Durabilities and Microstructures of Radioactive Glasses for Immobilization of Excess Actinides at the Savannah River Site,” *MRS Proc.*, vol. 412, p. 65, Feb. 1995, doi: 10.1557/PROC-412-65.

[167] X. Deschanels, S. Peuget, J. N. Cachia, and T. Charpentier, “Plutonium solubility and self-irradiation effects in borosilicate glass,” *Prog. Nucl. Energy*, vol. 49, no. 8, pp. 623–634, 2007, doi: 10.1016/j.pnucene.2007.05.001.

[168] F. Farges, Y. Lefrère, S. Rossano, A. Berthereau, G. Calas, and G. E. Brown, “The effect of redox state on the local structural environment of iron in silicate glasses: A combined XAFS spectroscopy, molecular dynamics, and bond valence study,” *J. Non. Cryst. Solids*, vol. 344, no. 3, pp. 176–188, 2004, doi: 10.1016/j.jnoncrysol.2004.07.050.

[169] S. D. Kelly, D. Hesterberg, and B. Ravel, “Analysis of Soils and Minerals Using X-ray Absorption Spectroscopy,” in *Methods of Soil Analysis Part 5—Mineralogical Methods*, no. 1, A. L. Ulery and L. Richard Drees, Eds. Soil Science Society of America, 2008, pp. 387–464.

[170] M. Darby Dyar, D. G. Agresti, M. W. Schaefer, C. A. Grant, and E. C. Sklute, “Mössbauer Spectroscopy of Earth and Planetary Materials,” *Annu. Rev. Earth Planet. Sci.*, vol. 34, no. 1, pp. 83–125, 2006, doi: 10.1146/annurev.earth.34.031405.125049.

[171] M. D. Dyar, “A review of Mössbauer data on inorganic glasses: The effects of composition on iron valency and coordination,” *Am. Mineral.*,

vol. 70, no. 3, pp. 304–316, 1985.

[172] B. Cochain, D. R. Neuville, G. S. Henderson, C. A. McCammon, O. Pinet, and P. Richet, “Effects of the iron content and redox state on the structure of sodium borosilicate glasses: A Raman, Mössbauer and Boron K-edge XANES spectroscopy study,” *J. Am. Ceram. Soc.*, vol. 95, no. 3, pp. 962–971, 2012, doi: 10.1111/j.1551-2916.2011.05020.x.

[173] S. Rossano, H. Behrens, and M. Wilke, “Advanced analyses of ^{57}Fe Mössbauer data of alumino-silicate glasses,” *Phys. Chem. Miner.*, vol. 35, no. 2, pp. 77–93, 2008, doi: 10.1007/s00269-007-0200-8.

[174] B. O. Mysen, I. S. E. Carmichael, and D. Virgo, “A comparison of iron redox ratios in silicate glasses determined by wet-chemical and ^{57}Fe Mössbauer resonant absorption methods,” *Contrib. to Mineral. Petrol.*, vol. 90, no. 2–3, pp. 101–106, 1985, doi: 10.1007/BF00378253.

[175] M. Wilke, G. M. Partzsch, R. Bernhardt, and D. Lattard, “Determination of the iron oxidation state in basaltic glasses using XANES at the K-edge,” *Chem. Geol.*, vol. 213, no. 1–3, pp. 71–87, 2004, doi: 10.1016/j.chemgeo.2004.08.034.

[176] F. Farges, S. Rossano, Y. Lefrre, M. Wilke, and G. E. B. Jr, “Iron in Silicate Glasses: a Systematic Analysis of Pre-Edge, XANES and EXAFS Features,” *Phys. Scr.*, 2005, doi: 10.1238/Physica.Topical.115a00957.

[177] S. D. Forder, O. M. Hannant, P. A. Bingham, and R. J. Hand, “Concerning the use of standards for identifying coordination environments in glasses,” *J. Phys. Conf. Ser.*, vol. 217, no. 1, 2010, doi: 10.1088/1742-6596/217/1/012072.

[178] V. Magnien, D. R. Neuville, L. Cormier, J. Roux, J. L. Hazemann, O. Pinet, and P. Richet, “Kinetics of iron redox reactions in silicate liquids: A high-temperature X-ray absorption and Raman spectroscopy study,” *J. Nucl. Mater.*, vol. 352, no. 1–3, pp. 190–195, 2006, doi: 10.1016/j.jnucmat.2006.02.053.

[179] S. Gin, P. Frugier, P. Jollivet, F. Bruguier, and E. Curti, “New insight into the residual rate of borosilicate glasses: Effect of S/V and glass composition,” *Int. J. Appl. Glas. Sci.*, vol. 4, no. 4, pp. 371–382, 2013, doi: 10.1111/ijag.12048.

[180] E. Burger, D. Rebiscoul, F. Bruguier, M. Jublot, J. E. Lartigue, and S. Gin, “Impact of iron on nuclear glass alteration in geological repository conditions: A multiscale approach,” *Appl. Geochemistry*, vol. 31, pp. 159–170, 2013, doi: 10.1016/j.apgeochem.2012.12.016.

[181] D. J. Backhouse, A. J. Fisher, J. Neeway, C. L. Corkhill, N. C. Hyatt, and R. J. Hand, “Corrosion of the International Simple Glass under acidic to hyperalkaline conditions,” *npj Mater. Degrad.*, vol. 2, no. 1, 2018, doi: 10.1038/s41529-018-0050-5.

[182] A. Michelin, E. Burger, D. Rebiscoul, D. Neff, F. Bruguier, E. Drouet, P. Dillmann, and S. Gin, “Silicate glass alteration enhanced by iron: Origin and long-term implications,” *Environ. Sci. Technol.*, vol. 47, no. 2, pp. 750–756, 2013, doi: 10.1021/es304057y.

[183] P. Dillmann, S. Gin, D. Neff, L. Gentaz, and D. Rebiscoul, “Effect of natural and synthetic iron corrosion products on silicate glass alteration processes,” *Geochim. Cosmochim. Acta*, vol. 172, pp. 287–305, 2016, doi: 10.1016/j.gca.2015.09.033.

[184] M. Debure, Y. Linard, C. Martin, and F. Claret, “In situ nuclear-glass corrosion under geological repository conditions,” *npj Mater. Degrad.*, vol. 3, no. 1, pp. 1–7, 2019, doi: 10.1038/s41529-019-0100-7.

[185] S. Gin, P. Jollivet, M. Fournier, C. Berthon, Z. Wang, A. Mitroshkov, Z. Zhu, and J. V. Ryan, “The fate of silicon during glass corrosion under alkaline conditions: A mechanistic and kinetic study with the International Simple Glass,” *Geochim. Cosmochim. Acta*, vol. 151, pp. 68–85, 2015, doi: 10.1016/j.gca.2014.12.009.

[186] N. C. Hyatt, C. L. Corkhill, M. C. Stennett, R. J. Hand, L. J. Gardner, and C. L. Thorpe, “The HADES Facility for High Activity Decommissioning Engineering & Science : part of the UK National Nuclear User Facility,” *IOP Conf. Ser. Mater. Sci. Eng.*, vol. 818, pp. 1–8, 2020, doi: 10.1088/1757-899X/818/1/012022.

[187] I. Donald, B. L. Metcalfe, and R. N. J. Taylor, “The immobilization of high level radioactive wastes using ceramics and glasses,” *J. Mater. Sci.*, vol. 32, no. 22, pp. 5851–5887, 1997, doi: 10.1023/A:1018646507438.

[188] C. L. Corkhill, N. J. Cassingham, P. G. Heath, and N. C. Hyatt, “Dissolution of UK high-level waste glass under simulated hyperalkaline

conditions of a colocated geological disposal facility," *Int. J. Appl. Glas. Sci.*, vol. 4, no. 4, pp. 341–356, 2013, doi: 10.1111/ijag.12042.

[189] L. R. Blackburn, L. J. Gardner, S. K. Sun, E. R. Maddrell, M. C. Stennett, C. L. Corkhill, and N. C. Hyatt, "Hot Isostatically Pressed Zirconolite Wasteforms for Actinide Immobilisation," *IOP Conf. Ser. Mater. Sci. Eng.*, vol. 818, 2020, doi: 10.1088/1757-899X/818/1/012010.

[190] L. J. Gardner, S. A. Walling, and N. C. Hyatt, "Hot isostatic pressing : thermal treatment trials of inactive and radioactive simulant UK intermediate level waste," *IOP Conf. Ser. Mater. Sci. Eng.*, vol. 818, no. 1, 2020, doi: 10.1088/1757-899X/818/1/012009.

[191] K. Bateman, D. Wahlquist, and T. Malewitz, "Process and equipment development for hot isostatic pressing treatability study," *ASME Int. Mech. Eng. Congr. Expo. Proc.*, vol. 11, 2014, doi: 10.1115/IMECE2014-36935.

[192] A. R. Mason, M. C. Stennett, C. L. Corkhill, and N. C. Hyatt, "Alkali tin silicate glass as a wasteform the UK Pu stockpile (In preparation)," 2020.

[193] J. A. Bearden and A. F. Burr, "Reevaluation of X-ray atomic energy levels," *Rev. Mod. Phys.*, vol. 39, no. 1, pp. 125–142, 1967, doi: 10.1103/RevModPhys.39.125.

[194] P. G. Heath, C. L. Corkhill, M. C. Stennett, R. J. Hand, K. M. Whales, and N. C. Hyatt, "Immobilisation of Prototype Fast Reactor raffinate in a barium borosilicate glass matrix," *J. Nucl. Mater.*, vol. 508, pp. 203–211, 2018, doi: 10.1016/j.jnucmat.2018.05.015.

[195] H. Zhang, C. L. Corkhill, P. G. Heath, R. J. Hand, M. C. Stennett, and N. C. Hyatt, "Effect of Zn- and Ca-oxides on the structure and chemical durability of simulant alkali borosilicate glasses for immobilisation of UK high level wastes," *J. Nucl. Mater.*, vol. 462, pp. 321–328, 2015, doi: 10.1016/j.jnucmat.2015.04.016.

[196] M. T. Harrison, "The Effect of Composition on Short- and Long-term Durability of UK HLW Glass," *Procedia Mater. Sci.*, vol. 7, pp. 186–192, 2014, doi: 10.1016/j.mspro.2014.10.025.

[197] P. Frugier, S. Gin, Y. Minet, T. Chave, B. Bonin, N. Godon, J. E. Lartigue, P. Jollivet, A. Ayral, L. De Windt, and G. Santarini, "SON68 nuclear glass dissolution kinetics: Current state of knowledge and basis of the new

GRAAL model," *J. Nucl. Mater.*, vol. 380, no. 1–3, pp. 8–21, 2008, doi: 10.1016/j.jnucmat.2008.06.044.

[198] G. R. Lumpkin, "Alpha-decay damage and aqueous durability of actinide host phases in natural systems," *J. Nucl. Mater.*, vol. 289, no. 1–2, pp. 136–166, 2001, doi: 10.1016/S0022-3115(00)00693-0.

[199] T. Ringwood, "Immobilisation of Radioactive Wastes in SYNROC," *Am. Sci.*, vol. 70, no. 2, pp. 201–207, 1982.

[200] D. J. Gregg, R. Farzana, P. Dayal, R. Holmes, and G. Triani, "Synroc Technology : Perspectives and current status (Review)," *J. Am. Ceram. Soc.*, 2020, doi: 10.1111/jace.17322.

[201] G. R. Lumpkin, K. R. Whittle, C. J. Howard, Z. Zhang, F. J. Berry, G. Oates, A. N. Zaitsev, C. T. Williams, and A. N. Zaitsev, "Crystal chemistry and cation ordering in zirconolite 2M," *Mat. Res. Soc. Symp. Proc.*, vol. 932, pp. 3–9, 2006.

[202] C. Davoisne, M. C. Stennett, N. C. Hyatt, N. Peng, C. Jeynes, and W. E. Lee, "Krypton irradiation damage in Nd-doped zirconolite and perovskite," *J. Nucl. Mater.*, vol. 415, no. 1, pp. 67–73, 2011, doi: 10.1016/j.jnucmat.2011.05.043.

[203] S. Ji, M. Su, C. Liao, S. Ma, Z. Wang, K. Shih, C. K. Chang, J. F. Lee, T. S. Chan, and Y. Li, "Synchrotron x-ray spectroscopy investigation of the $Ca_{1-x}Ln_xZrTi_{2-x}(Al, Fe)_xO_7$ zirconolite ceramics (Ln = La, Nd, Gd, Ho, Yb)," *J. Am. Ceram. Soc.*, vol. 103, no. 2, pp. 1463–1475, 2020, doi: 10.1111/jace.16832.

[204] L. R. Blackburn, S. Sun, S. M. Lawson, L. J. Gardner, H. Ding, C. L. Corkhill, E. R. Maddrell, M. C. Stennett, and N. C. Hyatt, "Synthesis and Characterisation of $Ca_{1-x}Ce_xZrTi_{2-2x}Cr_{2x}O_7$: Analogue Zirconolite Wasteform for the Immobilisation of Stockpiled UK Plutonium," *J. Eur. Ceram. Soc.*, 2020, doi: 10.1016/j.jeurceramsoc.2020.05.066.

[205] F. Bellatreccia, G. Della Ventura, E. Caprilli, C. T. Williams, and G. C. Parodi, "Crystal-Chemistry of Zirconolite and Calzirtite from Jacupiranga, São Paulo (Brazil)," *Mineral. Mag.*, vol. 63, no. 5, pp. 649–660, 1999, doi: 10.1180/002646199548817.

[206] K. D. Reeve, D. M. Levins, B. W. Seatonberry, R. K. Ryan, K. P. Hart, and G. T. Stevens, "Fabrication and Leach Testing of Synroc Containing

Actinides and Fission Products," *MRS Proc.*, vol. 127, no. iv, pp. 223–230, 1988, doi: 10.1557/proc-127-223.

[207] G. R. Lumpkin, K. L. Smith, and M. G. Blackford, "Development of secondary phases on Synroc leached at 150 ºC," *Mat. Res. Soc. Symp. Proc.*, vol. 353, 1995.

[208] M. G. Blackford, K. L. Smith, and K. P. Hart, "Microstructure, partitioning and dissolution behaviour of Synroc containing actinides," *Mat. Res. Soc. Symp. Proc.*, vol. 257, pp. 243–249, 1992.

[209] G. Leturcq, P. J. McGlinn, C. Barbe, M. G. Blackford, and K. S. Finnie, "Aqueous alteration of nearly pure Nd-doped zirconolite ($Ca_{0.8}Nd_{0.2}ZrTi_{1.8}Al_{0.2}O_7$), a passivating layer control," *Appl. Geochemistry*, vol. 20, 2005, doi: 10.1016/j.apgeochem.2004.10.006.

[210] C. Meng, X. Ding, W. Li, J. Zhao, and H. Yang, "Phase structure evolution and chemical durability studies of Ce-doped zirconolite–pyrochlore synroc for radioactive waste storage," *J. Mater. Sci.*, vol. 51, no. 11, pp. 5207–5215, 2016, doi: 10.1007/s10853-016-9822-x.

[211] M. C. Stennett, C. L. Corkhill, L. A. Marshall, and N. C. Hyatt, "Preparation, characterisation and dissolution of a CeO_2 analogue for UO_2 nuclear fuel," *J. Nucl. Mater.*, vol. 432, no. 1–3, pp. 182–188, 2013, doi: 10.1016/j.jnucmat.2012.07.038.

[212] C. L. Corkhill, D. J. Bailey, F. Y. Tocino, M. C. Stennett, J. A. Miller, J. L. Provis, K. P. Travis, and N. C. Hyatt, "Role of Microstructure and Surface Defects on the Dissolution Kinetics of CeO2, a UO2 Fuel Analogue," *ACS Appl. Mater. Interfaces*, vol. 8, no. 16, pp. 10562–10571, 2016, doi: 10.1021/acsami.5b11323.

[213] K. L. Smith, G. R. Lumpkin, M. G. Blackford, M. Hambley, R. A. Day, K. P. Hart, and A. Jostsons, "Characterisation and leaching behavior of plutonium-bearing Synroc-C," *Mat. Res. Soc. Symp. Proc.*, vol. 465, pp. 1267–1272, 1997, doi: 10.1017/CBO9781107415324.004.

[214] Y. Zhang, M. W. A. Stewart, H. Li, M. L. Carter, E. R. Vance, and S. Moricca, "Zirconolite-rich titanate ceramics for immobilisation of actinides - Waste form/HIP can interactions and chemical durability," *J. Nucl. Mater.*, vol. 395, no. 1–3, pp. 69–74, 2009, doi: 10.1016/j.jnucmat.2009.09.019.

[215] S. M. Thornber, M. C. Stennett, and N. C. Hyatt, “Investigation of Ce incorporation in zirconolite glass-ceramics for UK plutonium disposition,” *MRS Adv.*, vol. 357, no. May, pp. 1–8, 2017, doi: 10.1557/adv.201.

[216] A. A. Coelho, J. Evans, I. Evans, A. Kern, and S. Parsons, “The TOPAS symbolic computation system,” *Powder Diffr.*, vol. 26, pp. 22–25, 2011, doi: 10.1154/1.3661087.

[217] D. P. Reid, M. C. Stennett, and N. C. Hyatt, “The fluorite related modulated structures of the $Gd_2(Zr_{2-x}Ce_x)O_7$ solid solution: An analogue for Pu disposition,” *J. Solid State Chem.*, vol. 191, pp. 2–9, 2012, doi: 10.1016/j.jssc.2011.12.039.

[218] A. V. Soldatov, T. S. Ivanchenko, S. Della Longa, A. Kotani, Y. Iwamoto, and A. Bianconi, “Crystal-structure effects in the Ce L_3-edge X-ray-absorption spectrum of CeO_2: Multiple-scattering resonances and many-body final states,” *Phys. Rev. B*, vol. 50, no. 8, pp. 5074–5080, 1994, doi: 10.1103/PhysRevB.50.5074.

[219] A. Bianconi, A. Marcelli, H. Dexpert, R. Karnatak, A. Kotani, T. Jo, and J. Petiau, “Specific intermediate-valence state of insulating 4f compounds detected by L_3 X-ray absorption,” *Phys. Rev. B*, vol. 35, no. 2, pp. 806–812, 1987, doi: 10.1103/PhysRevB.35.806.

[220] F. Farges, “Fivefold-coordinated Ti^{4+} in metamict zirconolite and titanite: A new occurrence shown by Ti K-edge XANES spectroscopy,” *Am. Mineral.*, vol. 82, no. 1–2, pp. 44–50, 1997, doi: 10.2138/am-1997-1-206.

[221] J. Squire, E. R. Maddrell, N. C. Hyatt, and M. C. Stennett, “Influence of lubricants and attrition milling parameters on the quality of zirconolite ceramics, consolidated by hot isostatic pressing, for immobilization of plutonium,” *Int. J. Appl. Ceram. Technol.*, vol. 12, no. S2, pp. E92–E104, 2015, doi: 10.1111/ijac.12239.

[222] Y. Zhang, H. Li, and S. Moricca, “Pyrochlore-structured titanate ceramics for immobilisation of actinides: Hot isostatic pressing (HIPing) and stainless steel/waste form interactions,” *J. Nucl. Mater.*, vol. 377, no. 3, pp. 470–475, 2008, doi: 10.1016/j.jnucmat.2008.03.022.

[223] M. R. Gilbert, C. Selfslag, M. Walter, M. C. Stennett, J. Somers, N. C. Hyatt, and F. R. Livens, “Synthesis and characterisation of Pu-doped

zirconolites - $(Ca_{1-x}Pu_x)Zr(Ti_{2-2x}Fe_{2x})O_7$," *IOP Conf. Ser. Mater. Sci. Eng.*, vol. 9, no. 1, 2010, doi: 10.1088/1757-899X/9/1/012007.

[224] S. K. Sun, M. C. Stennett, C. L. Corkhill, and N. C. Hyatt, "Reactive spark plasma synthesis of $CaZrTi_2O_7$ zirconolite ceramics for plutonium disposition," *J. Nucl. Mater.*, vol. 500, pp. 11–14, 2018, doi: 10.1016/j.jnucmat.2017.12.021.

[225] G. Deissmann, S. Nieumeier, F. Brand, G. Modolo, and D. Bosbach, "Elicitation of dissolution rate data for potential wasteform types for plutonium," *Julich Rep.*, no. October, 2011.

[226] W. Lutze, W. L. Gong, and R. C. Ewing, "Zirconia ceramics for excess weapons plutonium waste," *J. Nucl. Mater.*, vol. 277, pp. 239–249, 2000.

[227] W. J. Weber, R. C. Ewing, C. R. A. Catlow, T. D. De La Rubia, L. W. Hobbs, C. Kinoshita, H. J. Matzke, A. T. Motta, M. Nastasi, E. K. H. Salje, E. R. Vance, and S. J. Zinkle, "Radiation Effects In Crystalline Ceramics For The Immobilization Of High-level Nuclear Waste And Plutonium," *J. Mater. Res.*, vol. 13, no. 06, pp. 1434–1484, 1998, doi: 10.1557/JMR.1998.0205.

[228] B. C. Chakoumakos, "Systematics of the pyrochlore structure type, ideal A2B2X6Y," *J. Solid State Chem.*, vol. 53, no. 1, pp. 120–129, 1984, doi: 10.1016/0022-4596(84)90234-2.

[229] S. X. Wang, B. D. Begg, L. M. Wang, R. C. Ewing, W. J. Weber, and K. V. Govidan Kutty, "Radiation stability of gadolinium zirconate: A waste form for plutonium disposition," *J. Mater. Res.*, vol. 14, no. 12, pp. 4470–4473, 1999, doi: 10.1557/JMR.1999.0606.

[230] J. Wang, J. X. Wang, Y. B. Zhang, Y. F. Wei, K. B. Zhang, H. Bin Tan, and X. F. Liang, "Order-disorder phase structure, microstructure and aqueous durability of $(Gd,Sm)_2(Zr,Ce)_2O_7$ ceramics for immobilizing actinides," *Ceram. Int.*, vol. 45, no. 14, pp. 17898–17904, 2019, doi: 10.1016/j.ceramint.2019.06.006.

[231] A. E. Ringwood, "Disposal of high-level nuclear wastes : a geological perspective," *Mineral. Mag.*, vol. 49, pp. 159–176, 1985.

[232] G. R. Lumpkin, K. P. Hart, P. J. McGlinn, and T. E. Payne, "Retention of Actinides in Natural Pyrochlores and Zirconolites," *Radiochim. Acta*, vol. 66–67, no. s1, 2015, doi: 10.1524/ract.1994.6667.special-issue.469.

[233] Y. B. Zhang, J. Wang, J. X. Wang, Y. Huang, P. Luo, X. F. Liang, and H. Bin Tan, “Phase evolution, microstructure and chemical stability of $Ca_{1-x}Zr_{1-x}Gd_{2x}Ti_2O_7$ ($0.0 \leq x \leq 1.0$) system for immobilizing nuclear waste,” *Ceram. Int.*, vol. 44, no. 12, pp. 13572–13579, 2018, doi: 10.1016/j.ceramint.2018.04.191.

[234] E. R. Maddrell, “Hot isostatically pressed nuclear wasteforms for the future,” *NNL Science*, no. 2, pp. 21–24, 2014.

[235] Nuclear Decomissioning Authority, “Conditioning of Plutonium Residues by Hot Isostatic Pressing and Options for Packaging and Disposal,” 2009.

[236] M. C. Stennett, E. R. Maddrell, C. R. Scales, F. R. Livens, M. R. Gilbert, and N. C. Hyatt, “An Evaluation of Single Phase Ceramic Formulations for Plutonium Disposition,” vol. 985, pp. 1–6, 2007.

[237] M. C. Stennett, N. C. Hyatt, W. E. Lee, and E. Maddrell, “Processing and characterisation of fluorite-related ceramic wasteforms for the immobilisation of actinides,” *Environ. Issues Waste Manag. Technol. XI*, vol. 176, pp. 81–90, 2006.

[238] N. C. Hyatt, M. Stennett, A. Jenni, D. Reid, and E. R. Maddrell, “Ceramic formulation and processing design for plutonium disposition,” *Mater. Res. Soc. Symp. Proc.*, vol. 1193, 2009.

[239] B. D. Begg, E. R. Vance, and S. D. Conradson, “The incorporation of plutonium and neptunium in zirconolite and perovskite,” *J. Alloys Compd.*, vol. 271–273, pp. 221–226, 1998, doi: 10.1016/S0925-8388(98)00058-9.

[240] M. R. Gilbert and J. H. Harding, “Energetics of Ce and Pu incorporation into zirconolite waste-forms.,” *Phys. Chem. Chem. Phys.*, vol. 13, no. 28, pp. 13021–13025, 2011, doi: 10.1039/c0cp01478h.

[241] L. R. Blackburn, S. Sun, L. J. Gardner, E. R. Maddrell, C. Martin, N. C. Hyatt, M. C. Stennett, and N. C. Hyatt, “A systematic investigation of the phase assemblage and microstructure of the zirconolite $CaZr_{1-x}Ce_xTi_2O_7$ system,” *J. Nucl. Mater.*, vol. 535, pp. 1–11, 2020, doi: 10.1016/j.jnucmat.2020.152137.

[242] Y. H. Lee, H. S. Sheu, J. P. Deng, and H. C. I. Kao, “Preparation and fluorite-pyrochlore phase transformation in $Gd_2Zr_2O_7$,” *J. Alloys Compd.*,

vol. 487, no. 1–2, pp. 595–598, 2009, doi: 10.1016/j.jallcom.2009.08.021.

[243] V. Grover and A. K. Tyagi, “Phase relation studies in the CeO_2-Gd_2O_3-ZrO_2 system,” *J. Solid State Chem.*, vol. 177, no. 11, pp. 4197–4204, 2004, doi: 10.1016/j.jssc.2004.07.052.

[244] S. Finkeldei, M. C. Stennett, P. M. Kowalski, Y. Ji, E. De Visser-Týnová, N. C. Hyatt, D. Bosbach, and F. Brandt, “Insights into the fabrication and structure of plutonium pyrochlores,” *J. Mater. Chem. A*, vol. 8, no. 5, pp. 2387–2403, 2020, doi: 10.1039/c9ta05795a.

[245] U. Martin, H. Boysen, and F. Frey, “Neutron powder investigation of tetragonal and cubic stabilized zirconia, TZP and CSZ, at temperatures up to 1400 K,” *Acta Crystallogr. Sect. B*, vol. 49, no. 3, pp. 403–413, 1993, doi: 10.1107/S0108768192011297.

[246] S. Finkeldei, F. Brandt, A. Bukaemskiy, S. Neumeier, G. Modolo, and D. Bosbach, “Synthesis and dissolution kinetics of zirconia based ceramics,” *Prog. Nucl. Energy*, vol. 72, no. 3, pp. 130–133, 2014, doi: 10.1016/j.pnucene.2013.07.020.

[247] G. Leturcq, T. Advocat, K. Hart, G. Berger, J. Lacombe, and A. Bonnetier, “Solubility study of Ti, Zr-based ceramics designed to immobilize long-lived radionuclides,” *Am. Mineral.*, vol. 86, no. 7–8, pp. 871–880, 2001, doi: 10.2138/am-2001-0710.

[248] M. W. A. Stewart, B. D. Begg, E. R. Vance, K. Finnie, H. Li, G. R. Lumpkin, K. L. Smith, W. J. Weber, and S. Thevuthasan, “The replacement of titanium by zirconium in ceramics for plutonium immobilization,” *Mat. Res. Soc. Symp. Proc.*, vol. 713, 2002, doi: 10.1557/PROC-713-JJ2.5.

[249] S. K. Roberts, W. L. Bourcier, and H. F. Shaw, “Aqueous dissolution kinetics of pyrochlore, zirconolite and brannerite at 25, 50, and 75 °C,” *Radiochim. Acta*, vol. 88, no. 9–11, pp. 539–543, 2000, doi: 10.1524/ract.2000.88.9-11.539.

[250] T. Nishimura, T. Koyama, M. Iizuka, and H. Tanaka, “Development of an environmentally benign reprocessing technology - pyrometallurgical reprocessing technology,” *Prog. Nucl. Energy*, vol. 32, no. 3/4, pp. 381–387, 1998, doi: 10.1016/S0149-1970(97)00032-2.

[251] K. A. Evans, J. A. Mavrogenes, H. S. O'Neill, N. S. Keller, and L.-Y. Y. Jang, "A preliminary investigation of chlorine XANES in silicate glasses," *Geochemistry, Geophys. Geosystems*, vol. 9, no. 10, 2008, doi: 10.1029/2008GC002157.

[252] D. A. McKeown, H. Gan, I. L. Pegg, W. C. Stolte, and I. N. Demchenko, "X-ray absorption studies of chlorine valence and local environments in borosilicate waste glasses," *J. Nucl. Mater.*, vol. 408, no. 3, pp. 236–245, 2011, doi: 10.1016/j.jnucmat.2010.11.035.

[253] J. D. Webster, "The exsolution of magmatic hydrosaline chloride liquids," *Chem. Geol.*, vol. 210, no. 1–4, pp. 33–48, 2004, doi: 10.1016/j.chemgeo.2004.06.003.

[254] E. R. Vance, B. D. Begg, R. A. Day, and C. J. Ball, "Zirconolite rich ceramics for actinide wastes," *Mat. Res. Soc. Symp. Proc.*, vol. 353, pp. 767–774, 1995.

[255] G. R. Lumpkin, R. C. Ewing, B. C. Chakoumakos, R. B. Greegor, F. W. Lytle, E. M. Foltyn, F. W. Clinard, L. A. Boatner, and M. M. Abraham, "Alpha-recoil damage in zirconolite ($CaZrTi_2O_7$)," *J. Mater. Res.*, vol. 1, no. 4, pp. 564–576, 1986, doi: 10.1557/JMR.1986.0564.

[256] G. R. Lumpkin and R. C. Ewing, "Geochemical alteration of pyrochlore group minerals: Betafite subgroup," *Am. Mineral.*, vol. 81, no. 9–10, pp. 1237–1248, 1996, doi: 10.2138/am-1996-9-1022.

[257] T. Advocat, F. Jorion, T. Marcillat, G. Leturcq, X. Deschanels, J. M. Boubals, L. Bojat, P. Nivet, and S. Peuget, "Fabrication of Pu-Zirconolite Ceramic Pellets by Natural Sintering," *Mat. Res. Soc. Symp. Proc.*, vol. 807, pp. 1–5, 2004, doi: 10.1557/PROC-807-267.

[258] M. R. Gilbert, "Molten salt synthesis of zirconolite polytypes," *Mat. Res. Soc. Symp. Proc.*, vol. 1665, pp. 325–330, 2014, doi: 10.1557/opl.2014.662.

[259] Z. Li, W. E. Lee, and S. Zhang, "Low-Temperature Synthesis of $CaZrO_3$ Powder from Molten Salts," *J. Am. Ceram. Soc.*, vol. 90, no. 2, pp. 364–368, 2007, doi: 10.1111/j.1551-2916.2006.01383.x.

[260] S. Zhang, "Low Temperature Synthesis of Complex Refractory Oxide Powders From Molten Salts," *J. Pakistan Mater. Soc.*, vol. 1, no. 2, pp. 49–53, 2007.

[261] S. Zhang, D. D. Jayaseelan, G. Bhattacharya, and W. E. Lee, “Molten salt synthesis of magnesium aluminate ($MgAl_2O_4$) spinel powder,” *J. Am. Ceram. Soc.*, vol. 89, no. 5, pp. 1724–1726, 2006, doi: 10.1111/j.1551-2916.2006.00932.x.

[262] S. Hashimoto, S. Zhang, W. E. Lee, and A. Yamaguchi, “Synthesis of Magnesium Aluminate Spinel Platelets from α-Alumina Platelet and Magnesium Sulfate Precursors,” *J. Am. Ceram. Soc.*, vol. 86, no. 11, pp. 1959–1961, 2003, doi: 10.1111/j.1151-2916.2003.tb03589.x.

[263] X. Liu and S. Zhang, “Low-temperature preparation of titanium carbide coatings on graphite flakes from molten salts,” *J. Am. Ceram. Soc.*, vol. 91, no. 2, pp. 667–670, 2008, doi: 10.1111/j.1551-2916.2007.02184.x.

[264] K. Webb, R. Taylor, C. Campbell, M. Carrott, C. Gregson, J. Hobbs, F. Livens, C. Maher, R. Orr, H. Sims, H. Steele, and S. Sutherland-Harper, “Thermal Processing of Chloride-Contaminated Plutonium Dioxide,” *ACS Omega*, vol. 4, no. 7, pp. 12524–12536, 2019, doi: 10.1021/acsomega.9b00719.

[265] S. Sutherland-Harper, F. Livens, C. Pearce, J. Hobbs, R. Orr, R. Taylor, K. Webb, and N. Kaltsoyannis, “Interactions of HCl and H_2O with the surface of PuO_2,” *J. Nucl. Mater.*, vol. 518, pp. 256–264, 2019, doi: 10.1016/j.jnucmat.2019.02.036.

[266] National Reserch Council, *Electrometallurgical Techniques for DOE Spent Fuel Treatment*. Washington DC: National Academy Press, 2000.

[267] OECD Nuclear Energy Agency, “Pyrochemical Separations in Nuclear Applications, A Status Report,” 2004. [Online]. Available: http://www.oecd.org/.

[268] Y. P. Lan, H. Y. Sohn, A. Murali, J. Li, and C. Chen, “The formation and growth of CeOCl crystals in a molten KCl-LiCl flux,” *Appl. Phys. A Mater. Sci. Process.*, vol. 124, no. 10, pp. 1–6, 2018, doi: 10.1007/s00339-018-2122-3.

Appendix A: Chapter 8 Published Article

Ceramics International 46 (2020) 29080–29089

Contents lists available at ScienceDirect

Ceramics International

journal homepage: www.elsevier.com/locate/ceramint

Molten salt synthesis of Ce doped zirconolite for the immobilisation of pyroprocessing wastes and separated plutonium

Amber R. Mason, Florent Y. Tocino, Martin C. Stennett, Neil C. Hyatt*

Immobilisation Science Laboratory, Department of Materials Science and Engineering, University of Sheffield, Sir Robert Hadfield Building, Sheffield, S1 3JD, UK

ARTICLE INFO

Keywords:
Nuclear applications (E)
Spectroscopy (B)
Molten salt synthesis

ABSTRACT

Molten salt mediated synthesis of zirconolite $Ca_{0.9}Zr_{0.9}Ce_{0.2}Ti_2O_7$ was investigated, as a target ceramic matrix for the clean-up of waste molten salts from pyroprocessing of spent nuclear fuels and the immobilisation of separated plutonium. A systematic study of reaction variables, including reaction temperature, time, atmosphere, reagents and composition, was made to optimise the yield of the target zirconolite phase. Zirconolite 2M and 3T polytypes were formed as the major phase (with minor perovskite) between 1000 – 1400 °C, in air, with the relative proportion of 2M polytype increasing with temperature. Synthesis under 5% H_2/N_2 or Ar increased the proportion of minor perovskite phase and reduced the yield of the zirconolite phase. The yield of zirconolite polytypes was maximised with the addition of 10 wt.% TiO_2 and 5 wt.% TiO_2, yielding 91.7 ± 2.0 wt.% zirconolite, primarily as the 2M polytype, after reaction at 1200 °C for 2 h, in air. The particle size and morphology of the zirconolite product bears a close resemblance to that of the TiO_2 precursor, demonstrating a dominant template growth mechanism. Although the molten salt mediated synthesis of zirconolite is effective at lower reaction temperature and time, compared to reactive sintering, this investigation has demonstrated that the approach does not offer any clear advantage with over conventional reactive sintering for the envisaged application.

1. Introduction

Pyrochemical reprocessing (pyroprocessing) is an advanced method of recycling spent nuclear fuel (SNF) where the U, Pu and minor actinides (MA) are separated from the fission products (FP) by electrorefining in a molten salt eutectic [1]. An advantage of pyroprocessing over conventional aqueous reprocessing is that a separated Pu stream is no longer generated, which reduces the associated proliferation risk [2]. The waste stream generated via this process is typically a chloride salt eutectic with entrained MA and FP, plus trace residual Pu. Chloride rich waste streams such as these are challenging to immobilise using traditional high level waste (HLW) immobilisation methods since the chloride anion has low solubility in borosilicate glasses, which have, hitherto, been applied for HLW immobilisation [3–7].

Zirconolite (prototypically $CaZr_xTi_{3-x}O_7$ where $0.8 < x < 1.35$) is a crystalline titanate ceramic material and is the targeted actinide host phase in SYNROC C [8]. It exists in the space group C2/c and has several polytypes: 2M, 3O, 3T, 4M and 6T, with the most common being the monoclinic 2M structure [8–11]. In the 2M structure, Ca and Zr adopt 8-fold and 7-fold coordination, respectively, as CaO_8 and ZrO_7 polyhedra; whereas, Ti adopts mixed 6-fold and 5-fold coordination, as TiO_6 and TiO_5 polyhedra, with the latter site being 50% occupied [12]. Synthetic zirconolite has natural analogue minerals retaining lanthanides and actinides dated to be millions or hundreds of millions of years old, which further demonstrates its long-term radiation stability and chemical durability over geological timescales [13–16]. The lanthanide and actinide elements are usually found on the Ca site with charge balancing cations, such as Al or Mg, on the Ti site [8,16].

Molten salt synthesis (MSS) is a method of producing ceramic materials which typically uses a chloride salt eutectic to reduce the diffusion distance of the ceramic reagents. This method generally produces a material that is homogeneous at a lower synthesis temperature and reaction time compared to traditional solid state synthesis methods [17]. The chloride salts can be dissolved upon completion of the reaction to recover the synthesised ceramic material. Conventional solid state synthesis of zirconolite, requires reactive sintering at 1450 °C for several hours, often with several cycles of heat treatment and intermittent grinding [18]. In comparison, zirconolite can be synthesised at 1200 °C in only a few hours, in the presence of a NaCl:KCl molten salt eutectic, with a melting point of approximately 658 °C [19]. There are two bounding mechanisms observed in the MSS of ceramic materials: dissolution-precipitation and template growth [20–25], which are

* Corresponding author.
E-mail address: n.c.hyatt@sheffield.ac.uk (N.C. Hyatt).

https://doi.org/10.1016/j.ceramint.2020.08.080
Received 7 May 2020; Received in revised form 30 July 2020; Accepted 10 August 2020
Available online 21 August 2020

dependent on the solubility of ceramic reagents in the salt eutectic. Dissolution-precipitation is favoured when all reagents are comparably soluble in the salt eutectic and subsequently react to form a product. Template growth occurs when one reagent is less soluble and acts as a template onto which the other more soluble reagents are deposited, at which point the product is formed. This mechanism allows the microstructure of the sample to be controlled resulting in uniform grain size and morphology.

This investigation seeks to develop the approach of decontaminating the chloride molten salt waste from pyroprocessing, by using the salt itself as a medium for the synthesis of a titanate ceramic wasteform to incorporate the long lived lanthanides, MA and trace Pu [4,26–29]. Zirconolite was selected as the titanate ceramic wasteform, with Ce utilised as a non-active structural surrogate for the actinide and lanthanide elements due to having a similar ionic radius, accessible oxidation states, and crystal chemistry [30–32]. The target composition for the wasteform was $Ca_{0.9}Zr_{0.9}Ce_{0.2}Ti_2O_7$, where Ce was substituted on both the Ca and Zr sites. This is a charge compensated composition, targeting an equal proportion of Ce^{3+} ions on the Ca and Zr sites, without the requirement of additional charge compensating species on the Ti site. The target formulation was devised to incorporate Ce, as a MA/Pu surrogate, at a realistic concentration for a conceptual ceramic wasteform.

The NaCl:KCl eutectic composition was chosen as a model system relevant to wastes arising from pyrochemical reprocessing of mixed oxide $(U,Pu)O_2$ fuels using the Dimitrovgrad Dry Process at the Research Institute for Atomic Reactors in Russia and early pyrochemical reprocessing of short cooled Experimental Reactor Breeder II metallic fuel at Argonne National Laboratory – West (now Idaho National Laboratory), USA [33,34]. Additionally, a NaCl:KCl eutectic was used in experimental pyrochemical reprocessing of thorium high temperature reactor fuels undertaken at Joint Research Centre-Institute for Trans Uranium Elements (JRC-ITU) [35]. The UK is also undertaking strategic assessment of pyrochemical recycle of used nuclear fuels, including design and demonstration of wasteforms for decontamination and immobilisation of lanthanides and residual actinides from alkali chloride molten salts.

A further motivation for our research is management of the UK plutonium stockpile, which is projected to exceed 140 tons at the end of current reprocessing options [27]. A significant fraction of the plutonium stockpile will require immobilisation in a suitable waste form, since it is unsuitable for reuse in MOX fuel, which is the preferred management approach at the present time [34]. Some of this material is contaminated by chlorine, as a result of the degradation of the polyvinylchloride packaging used to store the material [28]. A zirconolite ceramic is the leading candidate waste form for immobilisation of this stockpile and, therefore, a rapid and low temperature MSS process could be advantageous for ceramic waste form manufacture, given the presence of chlorine as a contaminant. Gilbert previously established the NaCl:KCl eutectic to be the most advantageous for zirconolite synthesis [19], although the yield was only 86 wt.% after reaction at 1000 °C. In contrast, the yield of zirconolite was 24 wt.% in the case of $CaCl_2$:NaCl eutectic at 1000 °C, whereas zirconolite failed to form when utilising a $MgCl_2$:NaCl eutectic. Note that this work focused the synthesis of the stoichiometric parent phase but did not consider the incorporation of a MA/Pu surrogate. Our choice of NaCl:KCl eutectic composition as the MSS medium was also made with due regard to potential application to the immobilisation of chloride contaminated plutonium stockpile material in a zirconolite ceramic, using Ce as a Pu surrogate.

2. Materials and methods

A NaCl:KCl eutectic (1:1 mole ratio) with a salt to ceramic mole ratio of 7:1 was primarily used in this study with the aim of producing single phase Ce doped zirconolite. To optimise the yield of the target zirconolite phase, the following reaction variables were systematically investigated: salt to ceramic mole ratio (3:1–9:1), synthesis temperature (1100 °C–1400 °C), time at synthesis temperature (2–8 h), atmosphere (air, Ar or 5% H_2/N_2), Ce source (CeO_2 or $CeCl_3.7H_2O$), stoichiometric or excess quantities of ZrO_2 and TiO_2 reagents (excess, respectively, of 10 wt.% and 5 wt.%).

2.1. Materials

CaO (Alfa Aesar purity 98%), TiO_2 (anatase) (Sigma Aldrich, 99% purity), ZrO_2 (Sigma Aldrich, purity 99%), $CeCl_3.7H_2O$ (Sigma Aldrich, > 99% purity) and CeO_2 (Fisher Scientific purity > 99%) were used as reagents. NaCl (Sigma Aldrich, purity 99%) and KCl (Sigma Aldrich, purity 99%) were used as the molten salt flux. All reagents, with the exception of CaO and $CeCl_3.7H_2O$, were dried overnight at 180 °C before use.

2.2. MSS - $Ca_{0.9}Zr_{0.9}Ce_{0.2}Ti_2O_7$

A 1:1 mole ratio of NaCl and KCl was mixed (30 Hz, 5 min) in a Fritsch Pulverisette 6 planetary mill with cyclohexane as a carrier fluid to produce the salt flux. Stoichiometric quantities of ceramic reagents were weighed according to the composition $Ca_{0.9}Zr_{0.9}Ce_{0.2}Ti_2O_7$ and mixed using the same conditions as the salt flux. A short mixing time was used to prevent size reduction of the reagents and preserve the particle morphology, to assist later assessment of the role of templating or dissolution-precipitation reaction mechanism. A 0.5 g batch with a molar ratio of 7:1 salt eutectic:ceramic was mixed in a Fritsch Mini Mill 23 with cyclohexane as a carrier fluid (30 Hz, 5 min). The resulting slurry was dried at ~95 °C, sieved through a 212 μm mesh to separate from the milling media. The powder was uniaxially pressed in a 10 mm hardened stainless-steel die with a 1 ton load and held for 1 min to produce a green pellet. The green pellets were placed in an alumina crucible and heated in a muffle furnace to 300 °C for 1 h to remove any entrained moisture and then reacted at 1200 °C for 2 h in air with a 5 °C min^{-1} heating/cooling rate. The resulting reacted pellet was crushed into a fine powder using a pestle and mortar. The powder was washed with deionised water to remove the salt flux and vacuum filtration used to recover the product.

The above method was repeated with independent changes of experimental variables as follows: salt to ceramic mole ratio (3:1, 5:1 and 9:1), synthesis temperature (1100 °C, 1300 °C and 1400 °C), furnace atmosphere (flowing 5% H_2/N_2 and Ar), furnace dwell duration (4 h and 8 h) and varying excess of ZrO_2 and TiO_2 reagents. Additionally, materials were produced using $CeCl_3.7H_2O$ (Sigma Aldrich, > 99% purity), as the MA/Pu surrogate, replacing CeO_2 in the ceramic batch.

After refinement of the experimental parameters discussed above, the optimum synthesis conditions were used to produce Ce doped zirconolite using MSS, with the resulting powder being uniaxially pressed into a ceramic body. The ceramic body was placed into a furnace and reacted in air at 1350 °C for 20 h, and the resulting ceramic was characterised.

2.3. Materials characterisation

Powder X-ray diffraction of reagents and products was performed with a Bruker D2 Phaser X-ray Diffractometer with a Ni filtered Cu Kα radiation (λ = 1.5418 Å) source, operating at 30 kV and 10 mA. Diffraction patterns were collected from $10° < 2\theta < 70°$ with a step size of 0.02° 2θ and dwell time of 38 s $step^{-1}$. The ICDD PDF-4+ database and ICSD sources were used to identify the phases present in each sample. The PDF numbers used for the pattern identification are: $CaZrTi_2O_7$ 2M (01-084-0163), $CaZrTi_2O_7$ 3T (01-072-7510), ZrO_2 (01-072-1669), TiO_2 (16–934), CeO_2 (01-081-0792) and $CaTiO_3$ (01-082-0228). XRD patterns were refined to provide quantitative phase analysis using the Bruker TOPAS software [36].

Secondary electron imaging of the microstructure of reagents and ceramic products was performed using a Philips XL 30 scanning electron microscope (SEM) at a working voltage of 20 kV. The powders were mixed with isopropanol in a beaker and placed in an ultrasonic bath. The resulting mixture was mounted onto aluminium pin stubs using carbon tabs, allowing for the isopropanol to evaporate before carbon coating.

The microstructure of the final sintered ceramic body was observed using a Hitachi TM3030 SEM with Oxford Instruments Swift ED3000 silicon drift detector. Energy dispersive X-ray spectroscopy (EDX) mapping was processed using the Bruker Quantax 70 software with maps collected for a minimum of 10 min. The ceramic body was mounted in epoxy resin, polished to a 1 μm optical finish and carbon coated prior to analysis.

The Ce oxidation state in each sample was determined from analysis of X-ray absorption spectroscopy data at the Ce L_3 edge (5723.0 eV). Measurements were conducted at the National Synchrotron Light Source II (NSLS-II) at Brookhaven National Laboratory (Upton, New York) on beamline 6-BM. NSLS-II operates at 3 GeV storage ring with a 400 mA current and 6-BM utilises a 3-pole wiggler to deliver X-rays in the energy range between 4.5 and 23 keV. The optical arrangement consists of a parabolic collimating mirror, a Si(111) monochromator, a toroidal focussing mirror, and a harmonic rejection mirror. For this study an unfocussed beam was used, and the beam size was limited to 0.5 mm in the vertical and 6 mm in the horizontal using slits. An ionisation chamber was used to measure the incident X-ray energy and the fluorescence signal was collected using a SII Vortex ME4 (4-element) Si drift detector. To optimise collection efficiency, the samples were mounted at 45° to both the incident X-ray beam and the vortex detector. The fluorescence signal was dead-time corrected as previously described in Woicik et al. [37]. Spectra were recorded between 5533 and 5965 eV with energy steps of 10 eV (5533–5693), 2 eV (5693–5713), 0.3 eV (5713–5783) and 0.05k (5783–5965). An accumulation time of 0.5 s step^{-1} was used for the first three regions and 0.25k step^{-1} for the final region. Multiple scans were collected for each sample and averaged to improve the signal to noise ratio. To ensure energy reproducibility (± 0.05 eV) a CeO_2 standard was measured simultaneously with each sample; the CeO_2 standard was placed downstream of the sample and the transmitted intensity was measured using an ionisation chamber. Absolute energy calibration was performed by measuring a Cr foil and setting the position of the first inflection point in the derivative spectrum to 5989 eV [38]. Samples, and reference compounds, were prepared by homogenising finely powdered sample with polyethylene glycol and uniaxial pressing to form a 13 mm pellet with a thickness equivalent to 1 absorption length. Data reduction and linear combination fitting (LCF) were performed using the Athena software package [39] allowing the proportion of Ce^{3+} in each sample to be calculated.

3. Results

We first attempted MSS of $Ca_{0.9}Zr_{0.9}Ce_{0.2}Ti_2O_7$ at 1200 °C with a 2 h reaction time, in air, and a salt to ceramic mole ratio of 7:1 on a molar basis (the synthesis conditions used by Gilbert to produce the parent $CaZrTi_2O_7$ zirconolite by MSS [19]). However, secondary phases of ZrO_2 and $CaTiO_3$ were observed (Fig. 1). Based on these results, several experimental parameters were varied to achieve a single phase ceramic product (e.g. salt to ceramic ratio, temperature, dwell duration, atmosphere, Ce source, excess reagents). It is desirable that a single phase wasteform is obtained since the accessory perovskite phase may also act as a host for Ce/Pu but has comparatively poor aqueous durability and radiation tolerance [37]. We first investigated the effect of salt to ceramic mole ratio (3:1, 5:1, 7:1, 9:1) on the MSS of $Ca_{0.9}Zr_{0.9}Ce_{0.2}Ti_2O_7$ at 1200 °C, with a 2 h reaction time, in air. As shown in Fig. S1, the phase assemblage was observed to be invariant comprising a major zirconolite 2M phase, minor perovskite, and trace

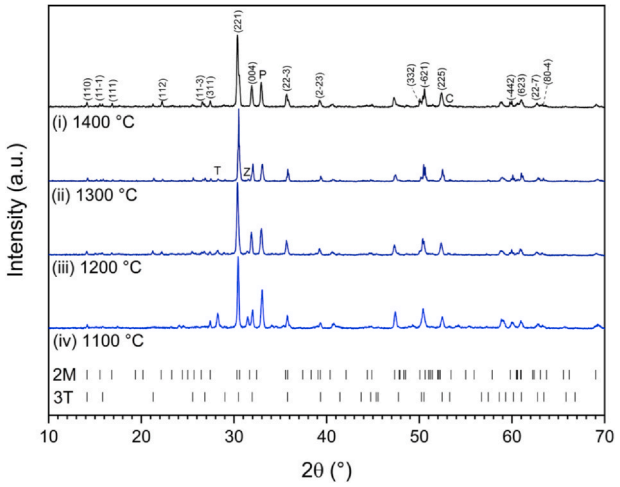

Fig. 1. XRD patterns of $Ca_{0.9}Zr_{0.9}Ce_{0.2}Ti_2O_7$ MSS with synthesis temperature: (i) 1400 °C (ii) 1300 °C (iii) 1200 °C (iv) 1100 °C; the reaction time was 2 h in air. Miller indices highlight major reflections of the zirconolite 2M phase. Primary diagnostic reflections of reagents and accessory phases are indicated by: P, $CaTiO_3$ perovskite; T, TiO_2 rutile; Z, ZrO_2; C, CeO_2.

zirconolite 3T, residual ZrO_2 and TiO_2 reagents. Accordingly, the salt to ceramic ratio was fixed at 7:1, on a molar basis, in the middle of the range investigated for further optimisation studies.

3.1. Characterisation of phase assemblage by X-ray diffraction

Fig. 1 shows powder XRD patterns of the product recovered from MSS of nominal $Ca_{0.9}Zr_{0.9}Ce_{0.2}Ti_2O_7$ over the range 1100 to 1400 °C, with a reaction time of 2 h in air. All XRD patterns show the formation of zirconolite 2M and 3T polytypes, at all temperatures, together with evidence of residual ZrO_2 and TiO_2 reagents, and an accessory perovskite phase (prototypically $CaTiO_3$). Quantitative phase analysis of the phase assemblage was undertaken, by Rietveld analysis of XRD data; the results are summarised in Table 1 and compared in Fig. 2 (an example fit is shown in Fig. S2). The quantitative phase analysis showed the overall yield of the zirconolite 2M phase to increase with reaction temperature, from 43.9 wt.% at 1100 °C, to 62.1 wt.% at 1400 °C (± 1.8 wt.%). A concomitant reduction in the fractions of residual ZrO_2 and TiO_2 reagents, accessory perovskite, and zirconolite 3T phase, were observed, with increasing reaction temperature. The combined fraction of zirconolite 2M and 3T phases increased from 54.9 wt.% at 1100 °C, to 74.3 wt.% (± 2.0 wt.%) at 1400 °C. The reaction temperature was not increased further since single phase Ce-doped zirconolites can be produced by conventional solid state synthesis at 1400 °C [19,20], and the MSS method of interest here would offer no meaningful advantage.

Overall, these data show that at 1100 °C, the yield of zirconolite 2M was hindered by slow reaction kinetics, at 1200 °C and higher temperatures the yield of zirconolite 2M was increased by reaction of reagents and conversion of the zirconolite 3T to 2M polymorph. The overall yield of zirconolite phases increased by a greater margin when the reaction temperature was increased from 1100 °C to 1200 °C, compared to 1400 °C, which may reflect increased volatilisation of the molten salt medium. For subsequent optimisation, a reaction temperature of 1200 °C was selected, given the evidence for reasonable reaction kinetics balanced against minimising the reaction temperature to reduce evaporation of the molten salt and, with a view to process implementation, potential volatile fission products.

Following investigation of the phase assemblage produced by MSS as a function of reaction temperature, the effect of oxygen partial pressure was studied by imposing an atmosphere of 5% H_2/N_2 or Ar gas. Fig. 3 compares the powder XRD patterns of the product recovered from MSS of nominal $Ca_{0.9}Zr_{0.9}Ce_{0.2}Ti_2O_7$ at 1200 °C, with a reaction

Table 1
Quantitative analysis using Rietveld refinement on XRD patterns in Figs. 1, 3 and 5; "excess" denotes addition of 10 wt.% ZrO_2 and 5 wt.% TiO_2 to stoichiometric formulation. ** Refers to the material produced after the secondary sintering of the MSS material formed at 1200 ˚C for 2 h in air with CeO_2 as the surrogate.

Temperature (˚C)	Time (h)	Atmosphere	Reagent	Excess	Phase fraction (wt.%)						
					$CaTiO_3$	CeO_2	TiO_2	Z-2M	Z-3T	Z-4M	ZrO_2
					(± 1.0)	(± 0.07)	(± 0.2)	(± 1.8)	(± 1.5)	(± 1.5)	(± 0.4)
1100	2	Air	CeO_2	–	32.8	0.40	2.1	43.9	11.0	0	9.7
1200	2	Air	CeO_2	–	28.1	0.16	1.7	52.2	14.7	0	3.0
1300	2	Air	CeO_2	–	27.3	0.20	2.1	52.4	15.8	0	2.1
1400	2	Air	CeO_2	–	24.8	0.27	0.2	62.1	12.2	0	0.3
1200	4	Air	CeO_2	–	27.5	1.11	1.7	56.7	9.8	0	3.9
1200	8	Air	CeO_2	–	26.6	0.62	0.2	53.8	16.2	0	2.4
1200	2	Air	CeO_2	✓	9.4	0.26	1.8	64.3	19.3	0	3.9
1200	2	Air	$CeCl_3$	–	25.4	0.62	3.0	47.1	15.7	0	8.0
1200	2	Air	$CeCl_3$	✓	15.4	0.33	3.7	48.5	20.4	0	11.5
1200	2	5% H_2/N_2	CeO_2	–	33.3	0.58	2.1	30.7	15.9	0	17.2
1200	2	Ar	CeO_2	–	40.9	0.28	8.4	29.1	5.7	0	15.6
1350**	20	Air	CeO_2	–	7.3	0.12	0.1	75.9	5.8	10.0	0.7

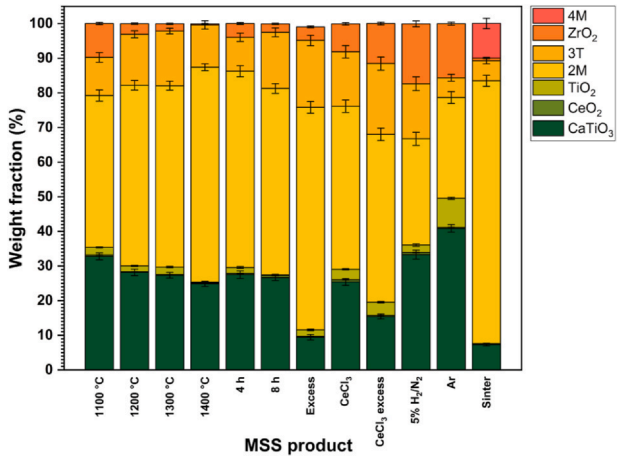

Fig. 2. Quantitative phase analysis of XRD data of MSS products shown in Figs. 1, 3 and 5; "excess" denotes addition of 10 wt.% ZrO_2 and 5 wt.% TiO_2 to stoichiometric formulation. Unless otherwise stated MSS was performed at 1200 ˚C for 2 h in air with CeO_2 as the Ce source.

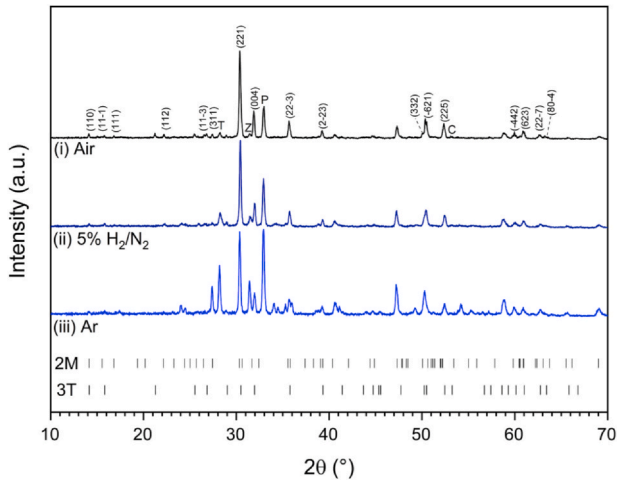

Fig. 3. XRD patterns of $Ca_{0.9}Zr_{0.9}Ce_{0.2}Ti_2O_7$ MSS at 1200 ˚C for 2 h, with synthesis atmospheres: (i) air (ii) 5% H_2/N_2 (iii) Ar. Miller indices highlight major reflections of the zirconolite 2M phase. Primary diagnostic reflections of reagents and accessory phases are indicated by: P, $CaTiO_3$ perovskite; T, TiO_2; Z, ZrO_2; C, CeO_2.

time of 2 h in air, 5% H_2/N_2 and Ar. These data and the quantitative phase analysis summarised in Table 1 and Fig. 2, show the reducing atmosphere to result in a markedly lower yield of zirconolite 2M and 3T phases. The combined yield of zirconolite 2M and 3T was 46.6 wt.% and 34.8 wt.% for the 5% H_2/N_2 and Ar atmosphere respectively, compared to 66.9 wt.% for air atmosphere (± 2.0 wt.%). Evident from the quantitative phase analysis is a greater fraction of residual ZrO_2 (15.6–17.3 ± 0.4 wt.%), which suggests that the solubility of ZrO_2 in the molten salt medium is strongly dependent on effective oxygen partial pressure, resulting in a lower yield of zirconolite and increased yield of perovskite (33.3–40.9 ± 1.0 wt.%). Ce L_3 XANES data demonstrated Ce to be completely reduced to Ce^{3+}, which is expected to stabilise the perovskite accessory phase as discussed further in Section 3.3, possibly assisted by the reduction of Ti^{4+} to Ti^{3+} within the sample. Begg and Clarke reported that annealing $CaZrTi_2O_7$ under 3.5% H_2/N_2 atmosphere results in reduction of Ti^{4+} to Ti^{3+} [21,22], and the formation of a Zr rich zirconolite and perovskite. Our observations are consistent with this mechanism. Given the evident lower stability of the zirconolite phase under reducing conditions, further optimisation of the MSS reaction conditions applied a temperature of 1200 ˚C and air atmosphere.

Fig. 4 compares the powder XRD patterns of the product recovered

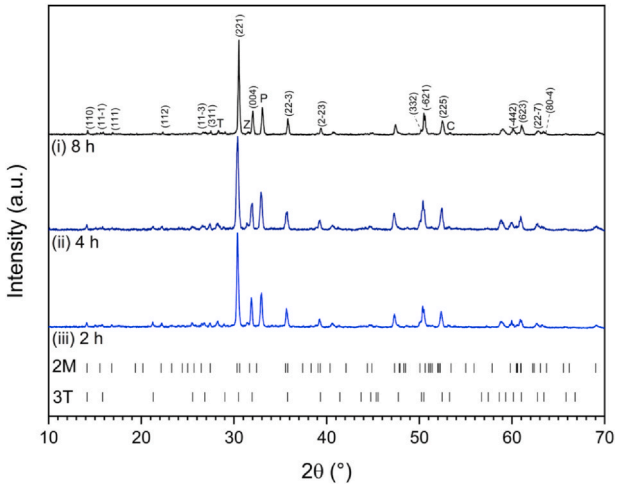

Fig. 4. XRD patterns of $Ca_{0.9}Zr_{0.9}Ce_{0.2}Ti_2O_7$ MSS at 1200 ˚C in air with furnace dwell durations: (i) 8 h (ii) 4 h (iii) 2 h. Miller indices highlight major reflections of the zirconolite 2M phase. Primary diagnostic reflections of reagents and accessory phases are indicated by: P, $CaTiO_3$ perovskite; T, TiO_2; Z, ZrO_2; C, CeO_2.

from MSS of nominal $Ca_{0.9}Zr_{0.9}Ce_{0.2}Ti_2O_7$ after reaction at 1200 °C, with a reaction time of 2 h, 4 h or 8 h in air. These data show a broadly similar phase assemblage, with quantitative phase analysis, summarised in Table 1 and Fig. 2, revealing relatively small changes in phase fraction, close to the estimated margin of precision. In particular, the total yield of zirconolite phases did not show a marked increase with reaction time, with changes being close to the estimated precision of ± 2.0 wt.%. This observation is consistent with evaporation of the molten salt medium with increased reaction time, and with diffusion – reaction occurring primarily in the solid state, for which the reaction kinetics to yield zirconolite are known to be low at 1200 °C [19,20]. The quantitative phase analysis of the product from the reaction at 1200 °C in air for 4 h showed an anomalously high fraction of residual ZrO_2 reagent, 3.9 ± 0.4 wt.%, the origin of which is unclear, but is consistent with a marginally lower yield of the target zirconolite phase. For the purpose of further optimisation of the MSS process, therefore, the reaction conditions were fixed at 1200 °C, for a duration of 2 h, under air.

With processing conditions of 1200 °C for 2 h in air, optimised from the investigations above, the addition of excess ZrO_2 and TiO_2 reagents was explored, with the aim of consuming the perovskite accessory phase. Fig. 5 shows the powder XRD data pattern of the product recovered from MSS of nominal $Ca_{0.9}Zr_{0.9}Ce_{0.2}Ti_2O_7$ after reaction at 1200 °C, for 2 h, in air, with an excess of 10 wt.% ZrO_2 and 5 wt.% TiO_2 reagents. Quantitative phase analysis, Table 1 and Fig. 2, showed that this adjustment of the reaction composition was successful and reduced the fraction of perovskite accessory phase to 9.4 ± 1.0 wt.%, with the yield of zirconolite 2M increased to 64.3 ± 0.8 wt.%. The overall yield of zirconolite 2M and 3T phases, combined, increased to 83.6 ± 2.0 wt.%, with ca. 5 wt.% of unreacted reagents.

The use of $CeCl_3$ as a reagent and actinide surrogate, was also explored since MA and Pu will be incorporated as a chloride species with the molten salt in a pyroprocessing waste stream, unless precipitated as an oxide by oxygen sparging [41]. Fig. 5 presents the powder XRD data pattern of the product recovered from MSS of nominal $Ca_{0.9}Zr_{0.9}Ce_{0.2}Ti_2O_7$ after reaction at 1200 °C, for 2 h, in air, using $CeCl_3.7H_2O$ as the Ce source, with and without an excess of 10 wt.% ZrO_2 and 5 wt.% TiO_2 reagents. The overall yield of zirconolite 2M and 3T phases, combined, was, respectively, 68.9 wt.% and 62.8 wt.% (± 2.0 wt.%) for the formulations with and without an excess of 10 wt.

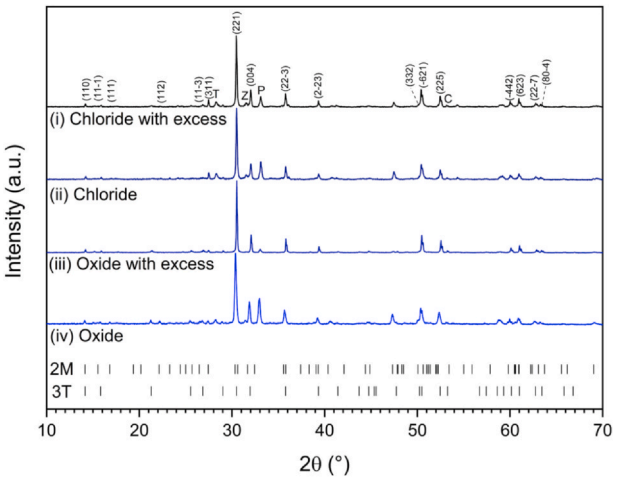

Fig. 5. XRD patterns of $Ca_{0.9}Zr_{0.9}Ce_{0.2}Ti_2O_7$ MSS with additional excesses of 10 wt.% ZrO_2 and 5 wt.% TiO_2, and $CeCl_3$ reagent where indicated: (i) 1200 °C, $CeCl_3$, 10 wt.% ZrO_2 and 5 wt.% TiO_2 (ii) 1200 °C, $CeCl_3$ (iii) 1200 °C, 10 wt.% ZrO_2 and 5 wt.% TiO_2 (iv) 1200 °C; the reaction time was 2 h, in air. Miller indices highlight major reflections of the zirconolite 2M phase. Primary diagnostic reflections of reagents and accessory phases are indicated by: P, $CaTiO_3$ perovskite; T, TiO_2; Z, ZrO_2; C, CeO_2.

% ZrO_2 and 5 wt.% TiO_2. The use of $CeCl_3.7H_2O$ evidently has a detrimental effect on the phase assemblage, compared to the use of CeO_2, with a reduced yield of zirconolite. This is correlated with the residual ZrO_2 phase fraction being approximately three times greater in the products of reaction utilising $CeCl_3.7H_2O$ compared to CeO_2, suggesting the lower yield may arise from lower ZrO_2 solubility.

The final step in this study involved sintering of the product of $Ca_{0.9}Zr_{0.9}Ce_{0.2}Ti_2O_7$ MSS, produced at 1200 °C, for 2 h, in air with an excess of 10 wt.% ZrO_2 and 5 wt.% TiO_2, using CeO_2 as a Ce source. The sintering conditions were 1350 °C for 20 h in air, and X-ray diffraction, Fig. 6, coupled with quantitative phase analysis, demonstrated the combined zirconolite 2M, 4M and 3T polymorphs to comprise 91.7 ± 2.0 wt.% of the phase assemblage, with the 2M polymorph (75.9 ± 1.8 wt.%) as the major component. A minor perovskite accessory phase was determined (7.3 ± 1.0 wt.%) with the trace CeO_2, ZrO_2 and TiO_2 (combined 1.0 ± 0.5 wt.%).

3.2. SEM/EDX characterisation

The scanning electron micrographs in Fig. 7 show the morphology of each reagent, along with that of the $Ca_{0.9}Zr_{0.9}Ce_{0.2}Ti_2O_7$ product of MSS at 1200 °C for 2 h, in air (with CeO_2). Comparison of the particle morphology of the reagents and the product material, shows that the primary particle size and habit of the product is similar to that of the TiO_2 reagent (~ 1 μm) and clearly differentiated from the that of the CeO_2 and ZrO_2 reagents, with much larger and smaller particle size, respectively. This suggests that template growth is the mechanism by which $Ca_{0.9}Zr_{0.9}Ce_{0.2}Ti_2O_7$ was produced. The faceted nature of TiO_2 reagent (see Fig. 7 (a)) was reflected in the habit of the $Ca_{0.9}Zr_{0.9}Ce_{0.2}Ti_2O_7$ product (Fig. 7 (d)). However, it was evident that some growth in product particle size had occurred, relative to the TiO_2 reagent, which provides evidence for a contribution of dissolution – precipitation and/or solid state diffusion, to the overall synthesis mechanism.

The microstructure of the sintered $Ca_{0.9}Zr_{0.9}Ce_{0.2}Ti_2O_7$ ceramic is shown in Fig. 8. The material comprises a majority matrix (mid grey) of the zirconolite 2M polymorph, with inclusions of ZrO_2 (bright grey) and small isolated perovskite grains (dark grey). The zirconolite 3T polymorph cannot be differentiated from the 2M polymorph, presumably due to similar composition and hence back scattered electron contrast, combined with its low abundance. The average EDX determined composition of the combined zirconolite 2M and 3T phases, was $Ca_{0.95(3)}Zr_{0.88(3)}Ce_{0.17(2)}Ti_{2.01(2)}O_7$, in reasonable agreement with the target stoichiometry. This implies an average Ce oxidation state of $Ce^{3.2+}$, within the zirconolite phase.

The zirconolite 4M phase is apparent as a small variation to the matrix contrast, which arises from a slightly higher Ce concentration as judged from EDX data. The microstructure is relatively well sintered although isolated porosity is apparent.

3.3. Ce L_3 XANES

Ce L_3 XANES data were acquired from product materials as a probe of the average Ce oxidation state and are shown in Fig. 9. The spectra were analysed using linear combination fitting (LCF) to estimate the proportion of Ce^{3+} in each product, using reference spectra of CeO_2 (for 8-fold coordinated Ce^{4+}), $CeAlO_3$ (for 12-fold coordinated Ce^{3+}) and $CePO_4$ (monazite; for 9-fold coordinated Ce^{3+}). Spectra were fitted over the range 5700–5760 eV, under the constraint that the fractional weights of the reference spectra sum to unity; the results are summarised in Table 2 with an example fit shown in Fig. S3. Note that the Ce L_3 XANES of $CePO_4$ and $CeAlO_3$ present a single intense feature on the rising absorption edge, whereas CeO_2 presents three features, of lower relative intensity, for which the corresponding final state electron configurations were previously assigned [42–45].

The Ce L_3 XANES data and LCF analysis (Fig. 9A; Table 2), showed

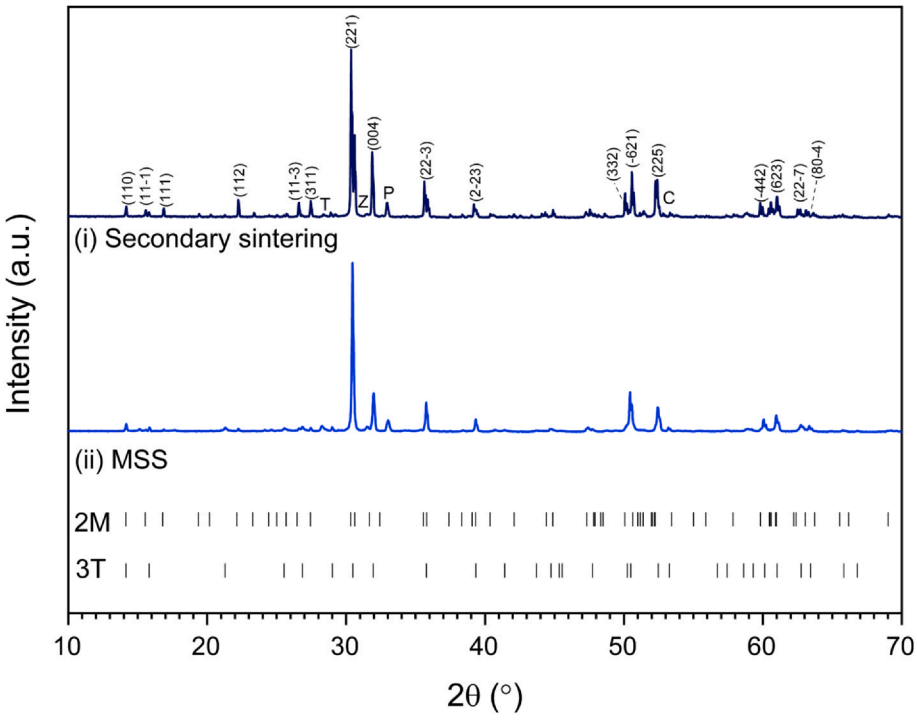

Fig. 6. XRD patterns to compare; (i) the product of a secondary sintering process (1350 °C, for 20 h, in air) of the MSS product in (ii), (ii) $Ca_{0.9}Zr_{0.9}Ce_{0.2}Ti_2O_7$ MSS; 1200 °C for 2 h in air with an excess of 10 wt.% ZrO_2 and 5 wt.% TiO_2. Miller indices highlight major reflections of the zirconolite 2M phase. Primary diagnostic reflections of reagents and accessory phases are indicated by: P, $CaTiO_3$ perovskite; T, TiO_2; Z, ZrO_2; C, CeO_2.

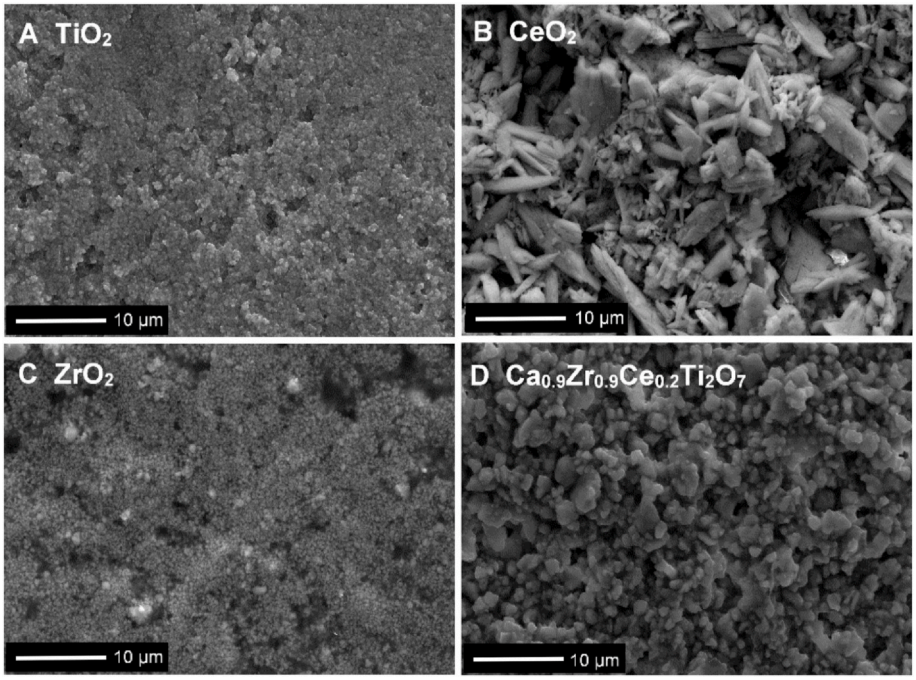

Fig. 7. SEM micrographs, in secondary electron mode, of: (A) TiO_2 (B) CeO_2 (C) ZrO_2 (D) $Ca_{0.9}Zr_{0.9}Ce_{0.2}Ti_2O_7$ from MSS at 1200 °C, for 2 h, in air.

the fraction of Ce^{3+} to increase with increasing reaction temperature (with constant reaction time of 2 h, in air), which is expected for the autoreduction of CeO_2 [46]; this was correlated with the concomitant increase in the combined fraction of major zirconolite 2M and 3T polytypes, and reduction in the perovskite fraction, in the phase assemblage (Table 1). In contrast, the fraction of Ce^{3+} increased only marginally when the reaction time was extended from 2 h to 8 h (Fig. 9C; Table 2), consistent with only a small increase in the combined fraction of major zirconolite 2M and 3T polytypes, and reduction in perovskite phase fraction (Table 1). Taken together, these data show that the total yield of zirconolite and Ce^{3+} fraction increase with increasing temperature, according to the target formulation, by reaction of the perovskite accessory phase and residual TiO_2 and ZrO_2. It is evident, however, that the zirconolite product must incorporate some proportion of Ce^{4+}.

Synthesis in a reducing atmosphere showed a complete reduction of Ce with the fraction of Ce^{3+} being 100 ± 4% for both 5% H_2/N_2 and Ar products (Fig. 9B). This was accompanied by a significant decrease in zirconolite yield in contrast with the effect of increasing temperature on phase assemblage. This implies that when the Ce^{3+} content increases above ca. 60%, the competing perovskite phase is stabilised, which provides a 12 co-ordinate site to accommodate the larger Ce^{3+}

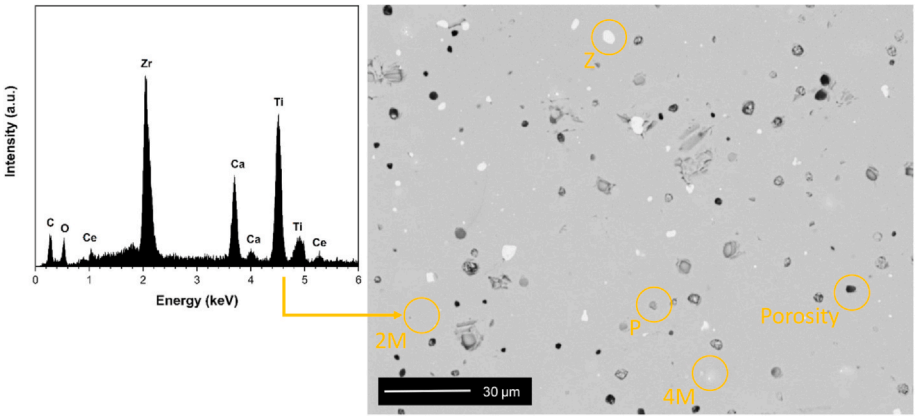

Fig. 8. SEM micrograph, in SE mode, of the surface of the ceramic produced after sintering of MSS product at 1350 °C for 20 h, in air, highlighting component phases: accessory phases are indicated by: P, perovskite; Z, ZrO_2; and zirconolite 2M and 4M polymorphs. Representative EDX spectrum of the zirconolite 2M phase is shown.

species [49]. The proportion of perovskite phase is similar to the ~ 40 wt.% observed in the phase assemblage produced from conventional reaction sintering of $CaZr_{0.6}Ce_{0.4}Ti_2O_7$ ceramics under H_2/N_2 and Ar, with a Ce^{3+} content of 80–100% [47].

Substituting $CeCl_3$ for CeO_2 as the Ce source, resulted in reduction of the Ce^{3+} fraction from 59 ± 3% to 38 ± 3%, in the products from reaction at 1200 °C for 2 h, in air; however, this was not accompanied by a significant change in the overall phase assemblage. The effect of addition of 10 wt.% ZrO_2 and 5 wt.% TiO_2 to the formulation resulted in marked reduction of the Ce^{3+} fraction from 59 ± 3% to 33 ± 3%, in the product from reaction at 1200 °C for 2 h, in air, correlated with the maximum yield in of combined zirconolite 2M and 3T polytypes in the phase assemblage (Table 1); this is also the case when CeO_2 is replaced by $CeCl_3$, although to less extent. Taken together, these data demonstrate a strong effect of the addition of excess 10 wt.% ZrO_2 and 5 wt.% TiO_2 in increasing the total yield of the zirconolite product, which must incorporate a higher fraction of Ce^{4+}.

Fig. 10 shows a comparison between the average Ce oxidation state

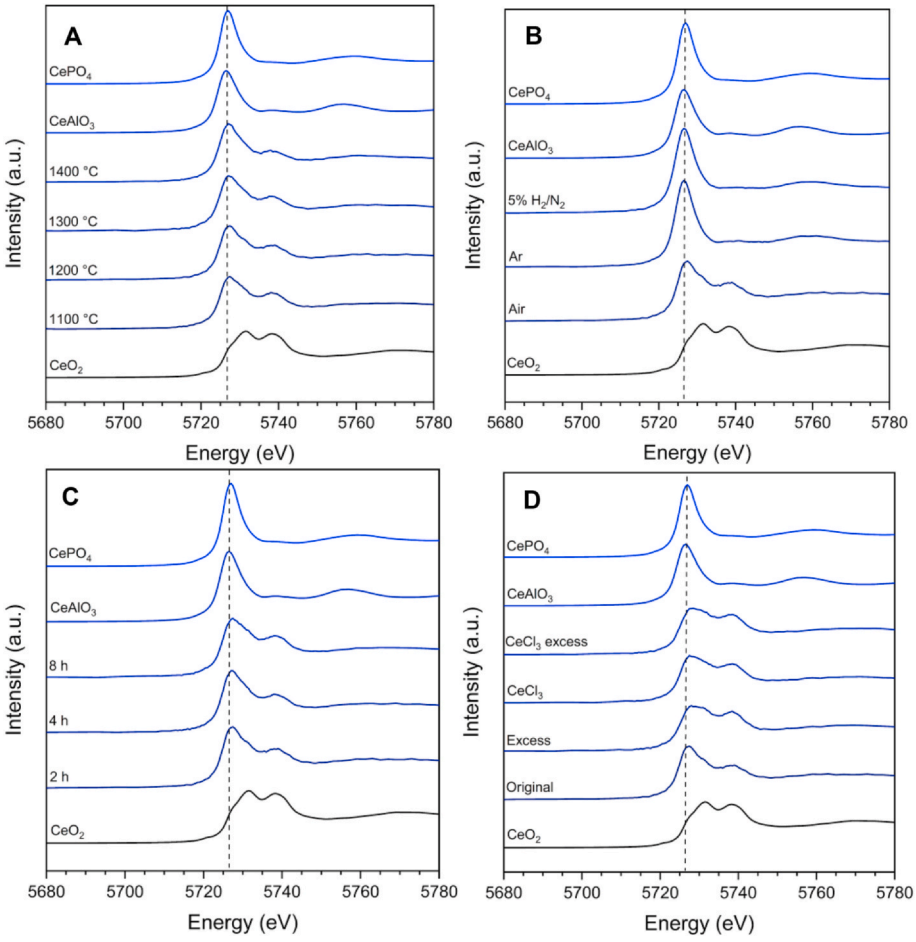

Fig. 9. Ce L_3 XANES spectra of recovered product of $Ca_{0.9}Zr_{0.9}Ce_{0.2}Ti_2O_7$ MSS in air, compared with $CePO_4$, $CeAlO_3$ and CeO_2 reference compounds: A) reaction at 1100–1400 °C for 2 h, in air; B) reaction at 1200 °C for 2 h using flowing 5% H_2/N_2, Ar or air; C) reaction at 1200 °C for 2–8 h, in air; D) reaction at 1200 °C for 2 h, in air, using CeO_2 or $CeCl_3.7H_2O$ as Ce source, with/without 10 wt.% ZrO_2 and 5 wt.% TiO_2 excess.

Table 2
Results of linear combination fitting of spectra from Fig. 9.; "excess" denotes addition of 10 wt.% ZrO_2 and 5 wt.% TiO_2 to the stoichiometric formulation.

Temperature (°C)	Time (h)	Atmosphere	Reagent	Excess	Ce^{3+} (%)
1100	2	Air	CeO_2	–	54 ± 3
1200	2	Air	CeO_2	–	59 ± 3
1300	2	Air	CeO_2	–	62 ± 3
1400	2	Air	CeO_2	–	71 ± 3
1200	4	Air	CeO_2	–	62 ± 3
1200	8	Air	CeO_2	–	53 ± 3
1200	2	Air	CeO_2	✓	33 ± 3
1200	2	Air	$CeCl_3$	–	38 ± 3
1200	2	Air	$CeCl_3$	✓	33 ± 3
1200	2	5% H_2/N_2	CeO_2	–	100 ± 4
1200	2	Ar	CeO_2	–	100 ± 4

(from Table 2) and the weight fraction of perovskite formed in each product. There is a general trend of increasing perovskite content associated with a greater the quantity of Ce^{3+} in the sample at a constant synthesis temperature. As noted above, the competing perovskite phase provides a 12 co-ordinate site to accommodate the larger Ce^{3+} species [40], and hence the proportion of the perovskite phase increases with increasing Ce^{3+} content, which is generally associated with a lower yield of zirconolite.

4. Discussion

Ce doped zirconolite was synthesised in a NaCl:KCl molten salt eutectic, as a conceptual process for decontamination of pyroprocessing molten salt wastes and immobilisation of separated plutonium. The presence of a molten salt eutectic enables synthesis of zirconolite at 1200 °C in 2 h, in air, considerably reduced compared to conventional reaction sintering which requires e.g. 1400 °C for 20 h. Interestingly, our investigation yields zirconolite 2M, 3T and 4M polytypes, with evidence for conversion of 3T to 2M, with increasing temperature. In contrast, similar compositions fabricated by conventional reactive sintering comprise only the 2M polytype, with minor 4M polytype when synthesised under air [48]. Our data are consistent with previous studies of NaCl:KCl and $CaCl_2$:NaCl molten salt synthesis of the parent $CaZrTi_2O_7$ zirconolite, which identified the formation of the 3T polytype, as the major phase after reaction at 1100 °C, giving way to formation of the 2M polytype at 1200 °C [19]. The zirconolite 3T phase therefore appears to be a low temperature metastable polytype structure.

Molten salt mediated synthesis yields products with a minimum Ce^{3+} content at least 33% greater than similar compositions synthesised by reactive sintering in air, when using CeO_2 as a reagent. Therefore, the mechanism of Ce solubility in the NaCl–KCl eutectic appears to involve reduction of Ce^{4+} to Ce^{3+}, yielding products with relatively high Ce^{3+} content. We are not aware of solubility data for Ce^{4+}/Ce^{3+} in chloride molten salts, but this conclusion is consistent with chloride molten salt mediated synthesis of CeOCl from CeO_2 [48]. Interestingly, the analogous $CaZr_{1-x}Pu_xTi_2O_7$ system is reported to yield the zirconolite 3T polytype on reduction of Pu^{4+} to Pu^{3+} and zirconolite 3T natural analogues are generally characterised by a high fraction of trivalent lanthanides [49,50]. Hence, whilst $CaZrTi_2O_7$ can evidently be stabilised in the 3T polytype up to 1100 °C, incorporation of a significant Ce^{3+} may assist in stabilising this polytype to higher temperature as reported herein.

Perovskite is formed as an accessory phase in all products characterised in this study, with increased perovskite fraction correlated with increased Ce^{3+} fraction at constant synthesis temperature (1200 °C). As noted in the introduction, the formation of perovskite is undesirable since it has been shown to incorporate actinides but demonstrates comparably lower radiation tolerance and durability, with respect to zirconolite [51]. Nevertheless, the perovskite phase fraction could be reduced to 7.3 ± 1.0 wt.%, by adjusting the formulation to incorporate 10 wt.% ZrO_2 and 5 wt.% TiO_2, and sintering of the product powder, which is comparable to the perovskite phase fraction in similar zirconolite compositions produced by reactive sintering in air [47].

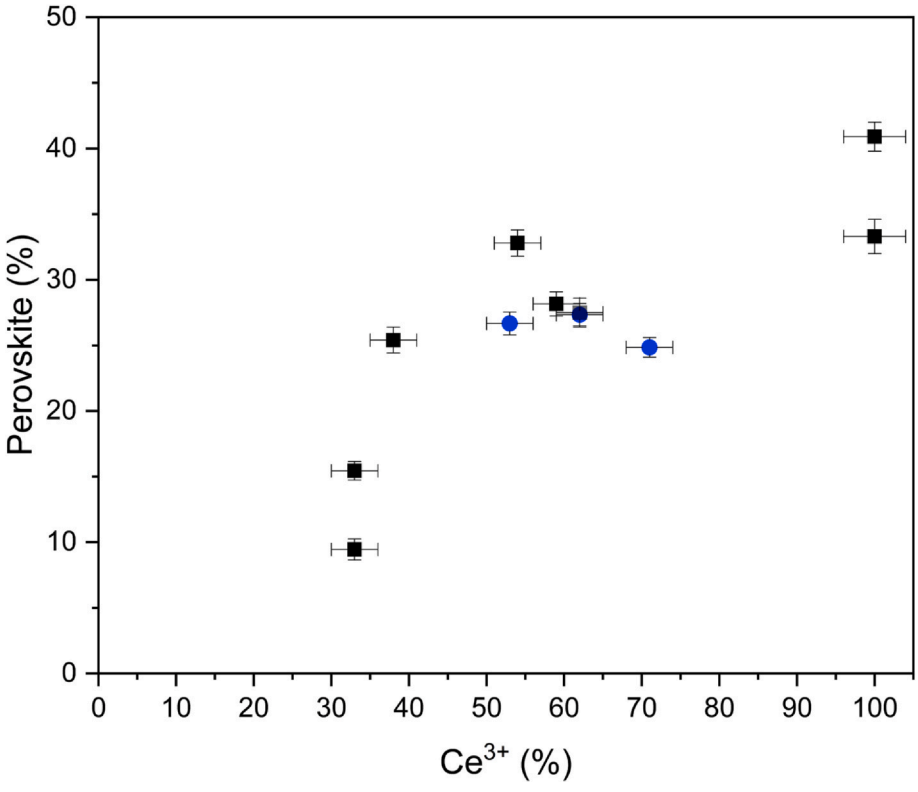

Fig. 10. Comparison of quantity of Ce^{3+} and perovskite weight fraction in product materials. Black squares represent all MSS zirconolite materials produced at 1200 °C. Blue circles represent MSS zirconolite materials produced at 1100 °C, 1300 °C and 1400 °C. (For interpretation of the references to colour in this figure legend, the reader is referred to the Web version of this article.)

5. Conclusion

Molten salt mediated synthesis of zirconolite ceramics, in the context of the decontamination of pyroprocessing molten salt wastes to yield a zirconolite ceramic, has some potential. However, this approach would not offer any clear benefit over oxygen sparging of the salt to precipitate lanthanides and minor actinides as oxides, followed by recovery and immobilisation in a glass or ceramic matrix, since both processes would require subsequent high temperature melting or reactive sintering steps to produce a wasteform monolith. Likewise, in the context of plutonium stockpile immobilisation, although molten salt mediated synthesis of zirconolite reduces the required reaction time and temperature, the subsequent requirement for a consolidation step means that the molten salt method does not offer a compelling advantage. Nevertheless, this work has served to usefully clarify mechanistic aspects of the molten salt mediated synthesis of zirconolite which should inform future application of molten salt technology in the nuclear and wider fields.

Declaration of competing interest

The authors declare that they have no known competing financial interests or personal relationships that could have appeared to influence the work reported in this paper.

Acknowledgements

ARM is funded by the Engineering, Physical Sciences Research Council via the Next Generation Nuclear Centre for Doctoral Training (Grant EP/L015390/1). This research was supported in part by EPSRC under grant reference EP/S011935/1 and EP/R511754/1, and in part by BEIS under the UK Nuclear Innovation Program. NCH is grateful to the Royal Academy of Engineering and Nuclear Decommissioning Authority for funding. This research utilised the HADES/MIDAS facility at the University of Sheffield established with financial support from EPSRC and BEIS, under grant EP/T011424/1 [52]. With thanks to Dr C. Shaw at the Sorby Centre for Electron Microscopy, University of Sheffield for assistance with SEM imaging. This research used beamline 6-BM of the National Synchrotron Light Source II, a U.S. Department of Energy (DOE) Office of Science User Facility Operated for the DOE office of Science by Brookhaven National Laboratory under Contract No. DE-SC0012704; the authors are grateful to Dr B. Ravel, Dr D. Bailey and Ms. L. M. Mottram for experimental assistance.

Appendix A. Supplementary data

Supplementary data to this article can be found online at https://doi.org/10.1016/j.ceramint.2020.08.080.

References

[1] T. Nishimura, T. Koyama, M. Iizuka, H. Tanaka, Development of an environmentally benign reprocessing technology - pyrometallurgical reprocessing technology, Prog. Nucl. Energy 32 (1998) 381–387, https://doi.org/10.1016/S0149-1970(97)00032-2.

[2] National Nuclear Laboratory, Advanced reprocessing research and development needs: position paper, Natl. Nucl. Lab. (2015), http://www.nnl.co.uk/media/1672/advanced-reprocessing-position-paper-final.pdf.

[3] I.W. Donald, Waste Immobilisation in Glass and Ceramic Based Hosts, Wiley, Chichester, 2010.

[4] A.R. Mason, S.M. Thornber, M.C. Stennett, L.J. Gardner, D. Lützenkirchen-Hecht, N.C. Hyatt, Preliminary investigation of chlorine speciation in zirconolite glass-ceramics for plutonium residues by analysis of Cl K-edge XANES, MRS Adv (2019) 1–7, https://doi.org/10.1557/adv.2019.460.

[5] K.A. Evans, J.A. Mavrogenes, H.S. O'Neill, N.S. Keller, L.-Y.Y. Jang, A preliminary investigation of chlorine XANES in silicate glasses, Geochemi. Geophys. Geosyst. 9 (2008), https://doi.org/10.1029/2008GC002157.

[6] D.A. McKeown, H. Gan, I.L. Pegg, W.C. Stolte, I.N. Demchenko, X-ray absorption studies of chlorine valence and local environments in borosilicate waste glasses, J. Nucl. Mater. 408 (2011) 236–245, https://doi.org/10.1016/j.jnucmat.2010.11.035.

[7] J.D. Webster, The exsolution of magmatic hydrosaline chloride liquids, Chem. Geol. 210 (2004) 33–48, https://doi.org/10.1016/j.chemgeo.2004.06.003.

[8] B.D. Begg, E.R. Vance, The incorporation of cerium in zirconolite, Mater. Res. Soc. Symp. Proc. 465 (1997) 333–340, https://doi.org/10.1557/PROC-465-333.

[9] M.R. Gilbert, C. Selfslag, M. Walter, M.C. Stennett, J. Somers, N.C. Hyatt, F.R. Livens, Synthesis and characterisation of Pu-doped zirconolites - $(Ca_{1-x}Pu_x)Zr(Ti_{2-2x}Fe_{2x})O_7$, IOP Conf. Ser. Mater. Sci. Eng. 9 (2010), https://doi.org/10.1088/1757-899X/9/1/012007.

[10] T.J. White, R.L.L. Segall, J.L.L. Hutchison, J.C.C. Barry, Polytypic behaviour of zirconolite, Proc. Roy. Soc. Lond. A. 392 (1984) 343–358, https://doi.org/10.1098/rspa.1984.0035.

[11] E.R. Vance, B.D. Begg, R.A. Day, C.J. Ball, Zirconolite rich ceramics for actinide wastes, Mater. Res. Soc. Symp. Proc. 353 (1995) 767–774.

[12] D. Caurant, P. Loiseau, I. Bardez, A. Quintas, Glasses, Glass-Ceramics and Ceramics for Immobilization of Highly Radioactive Nuclear Wastes, Nova Science Publishers, 2009.

[13] G.R. Lumpkin, R.C. Ewing, B.C. Chakoumakos, R.B. Greegor, F.W. Lytle, E.M. Foltyn, F.W. Clinard, L.A. Boatner, M.M. Abraham, Alpha-recoil damage in zirconolite ($CaZrTi_2O_7$), J. Mater. Res. 1 (1986) 564–576, https://doi.org/10.1557/JMR.1986.0564.

[14] G.R. Lumpkin, R.C. Ewing, Geochemical alteration of pyrochlore group minerals: betafite subgroup, Am. Mineral. 81 (1996) 1237–1248, https://doi.org/10.2138/am-1996-9-1022.

[15] G.R. Lumpkin, K.P. Hart, P.J. McGlinn, T.E. Payne, R. Gieré, C.T. Williams, Retention of actinides in natural pyrochlores and zirconolites, Radiochim. Acta 66/67 (1994) 469–474, https://doi.org/10.1524/ract.1994.6667.s1.469.

[16] R. Gieré, C.T. Williams, G. Lumpkin, Chemical characteristics of natural zirconolite, Swiss Soc. Mineral. Petrol. 78 (1998) 433–459, https://doi.org/10.5169/seals-59299.

[17] M.L. Hand, M.C. Stennett, N.C. Hyatt, Rapid low temperature synthesis of a titanate pyrochlore by molten salt mediated reaction, J. Eur. Ceram. Soc. 32 (2012) 3211–3219, https://doi.org/10.1016/j.jeurceramsoc.2012.04.046.

[18] T. Advocat, F. Jorion, T. Marcillat, G. Leturcq, X. Deschanels, J.M. Boubals, L. Bojat, P. Nivet, S. Peuget, Fabrication of Pu-zirconolite ceramic pellets by natural sintering, Mater. Res. Soc. Symp. Proc. 807 (2004) 1–5, https://doi.org/10.1557/PROC-807-267.

[19] M.R. Gilbert, Molten salt synthesis of zirconolite polytypes, Mater. Res. Soc. Symp. Proc. 1665 (2014) 325–330, https://doi.org/10.1557/opl.2014.662.

[20] T. Kimura, Molten salt synthesis of ceramic powders, in: C. Sikalidis (Ed.), Adv. Ceram. - Synth. Charact. Process. Specif. Appl. InTech Open, 2011, pp. 75–100, , https://doi.org/10.5772/20472.

[21] Z. Li, W.E. Lee, S. Zhang, Low-temperature synthesis of $CaZrO_3$ powder from molten salts, J. Am. Ceram. Soc. 90 (2007) 364–368, https://doi.org/10.1111/j.1551-2916.2006.01383.x.

[22] S. Zhang, Low temperature synthesis of complex refractory oxide powders from molten salts, J. Pakistan Mater. Soc. 1 (2007) 49–53.

[23] S. Zhang, D.D. Jayaseelan, G. Bhattacharya, W.E. Lee, Molten salt synthesis of magnesium aluminate ($MgAl_2O_4$) spinel powder, J. Am. Ceram. Soc. 89 (2006) 1724–1726, https://doi.org/10.1111/j.1551-2916.2006.00932.x.

[24] S. Hashimoto, S. Zhang, W.E. Lee, A. Yamaguchi, Synthesis of magnesium aluminate spinel platelets from α-alumina platelet and magnesium sulfate precursors, J. Am. Ceram. Soc. 86 (2003) 1959–1961, https://doi.org/10.1111/j.1151-2916.2003.tb03589.x.

[25] X. Liu, S. Zhang, Low-temperature preparation of titanium carbide coatings on graphite flakes from molten salts, J. Am. Ceram. Soc. 91 (2008) 667–670, https://doi.org/10.1111/j.1551-2916.2007.02184.x.

[26] S.M. Thornber, P.G. Heath, G.P. Da, M.C. Stennett, N.C. Hyatt, The effect of pre-treatment parameters on the quality of glass-ceramic wasteforms for plutonium immobilisation, consolidated by hot isostatic pressing, J. Nucl. Mater. 485 (2017), https://doi.org/10.1016/j.jnucmat.2016.12.028.

[27] N.C. Hyatt, Plutonium management policy in the United Kingdom: the need for a dual track strategy, Energy Pol. 99 (2016), https://doi.org/10.1016/j.enpol.2016.08.033.

[28] K. Webb, R. Taylor, C. Campbell, M. Carrott, C. Gregson, J. Hobbs, F. Livens, C. Maher, R. Orr, H. Sims, H. Steele, S. Sutherland-Harper, Thermal processing of chloride-contaminated plutonium dioxide, ACS Omega 4 (2019) 12524–12536, https://doi.org/10.1021/acsomega.9b00719.

[29] S. Sutherland-Harper, F. Livens, C. Pearce, J. Hobbs, R. Orr, R. Taylor, K. Webb, N. Kaltsoyannis, Interactions of HCl and H_2O with the surface of PuO_2, J. Nucl. Mater. 518 (2019) 256–264, https://doi.org/10.1016/j.jnucmat.2019.02.036.

[30] M.R. Gilbert, J.H. Harding, Energetics of Ce and Pu incorporation into zirconolite waste-forms, Phys. Chem. Chem. Phys. 13 (2011) 13021–13025, https://doi.org/10.1039/c0cp01478h.

[31] C. Lopez, X. Deschanels, J.M. Bart, J.M. Boubals, C. Den Auwer, E. Simoni, Solubility of actinide surrogates in nuclear glasses, J. Nucl. Mater. 312 (2003) 76–80, https://doi.org/10.1016/S0022-3115(02)01549-0.

[32] P.A. Bingham, R.J. Hand, M.C. Stennett, N.C. Hyatt, M.T. Harrison, The use of surrogates in waste immobilization studies: a case study of plutonium, Mater. Res. Soc. Symp. Proc. 1107 (2008), https://doi.org/10.1557/PROC-1107-421.

[33] National Research Council, Electrometallurgical Techniques for DOE Spent Fuel Treatment, National Academy Press, Washington DC, 2000, https://doi.org/10.17226/9883.

[34] Department of Energy and Climate Change, Management of the UK's Plutonium Stocks: A Consultation Response on the Proposed Justification Process for the Reuse of Plutonium, (2013).

[35] OECD Nuclear Energy Agency, Pyrochemical Separations in Nuclear Applications, A Status Report, (2004) http://www.oecd.org/.
[36] A.A. Coelho, J. Evans, I. Evans, A. Kern, S. Parsons, The TOPAS symbolic computation system, Powder Diffr. 26 (2011) 22–25, https://doi.org/10.1154/1.3661087.
[37] J.C. Woicik, B. Ravel, D.A. Fischer, W.J. Newburgh, Performance of a four-element Si drift detector for X-ray absorption fine-structure spectroscopy: resolution, maximum count rate, and dead-time correction with incorporation into the ATHENA data analysis software, J. Synchrotron Radiat. 17 (2010) 409–413, https://doi.org/10.1107/S0909049510009064.
[38] J.A. Bearden, A.F. Burr, Reevaluation of X-ray atomic energy levels, Rev. Mod. Phys. 39 (1967) 125–142, https://doi.org/10.1103/RevModPhys.39.125.
[39] B. Ravel, M. Newville, ATHENA, ARTEMIS, HEPHAESTUS: data analysis for X-ray absorption spectroscopy using IFEFFIT, J. Synchrotron Radiat. 12 (2005) 537–541, https://doi.org/10.1107/S0909049505012719.
[40] B.D. Begg, E.R. Vance, G.R. Lumpkin, Charge compensation and the incorporation of cerium in zirconolite and perovskite, Mater. Res. Soc. Symp. Proc. 506 (1998) 79–86, https://doi.org/10.1557/proc-506-79.
[41] Y.Z. Cho, G.H. Park, H.C. Yang, D.S. Han, H.S. Lee, I.T. Kim, Minimization of eutectic salt waste from pyroprocessing by oxidative precipitation of lanthanides, J. Nucl. Sci. Technol. 46 (2009) 1004–1011, https://doi.org/10.1080/18811248.2009.9711610.
[42] D.P. Reid, M.C. Stennett, N.C. Hyatt, The fluorite related modulated structures of the $Gd_2(Zr_{2-x}Ce_x)O_7$ solid solution: an analogue for Pu disposition, J. Solid State Chem. 191 (2012) 2–9, https://doi.org/10.1016/j.jssc.2011.12.039.
[43] M.C. Stennett, C.L. Freeman, A.S. Gandy, N.C. Hyatt, Crystal structure and non-stoichiometry of cerium brannerite: $Ce_{0.975}Ti_2O_{5.95}$, J. Solid State Chem. 192 (2012) 172–178, https://doi.org/10.1016/j.jssc.2012.03.057.
[44] A.V. Soldatov, T.S. Ivanchenko, S. Della Longa, A. Kotani, Y. Iwamoto, A. Bianconi, Crystal-structure effects in the Ce L_3-edge X-ray-absorption spectrum of CeO_2: multiple-scattering resonances and many-body final states, Phys. Rev. B 50 (1994) 5074–5080, https://doi.org/10.1103/PhysRevB.50.5074.
[45] A. Bianconi, A. Marcelli, H. Dexpert, R. Karnatak, A. Kotani, T. Jo, J. Petiau, Specific intermediate-valence state of insulating 4f compounds detected by L_3 X-ray absorption, Phys. Rev. B 35 (1987) 806–812, https://doi.org/10.1103/PhysRevB.35.806.
[46] C.L. Corkhill, D.J. Bailey, F.Y. Tocino, M.C. Stennett, J.A. Miller, J.L. Provis, K.P. Travis, N.C. Hyatt, Role of microstructure and surface defects on the dissolution kinetics of CeO_2, a UO_2 fuel analogue, ACS Appl. Mater. Interfaces 8 (2016) 10562–10571, https://doi.org/10.1021/acsami.5b11323.
[47] L.R. Blackburn, S. Sun, L.J. Gardner, E.R. Maddrell, C. Martin, N.C. Hyatt, A systematic investigation of the phase assemblage and microstructure of the zirconolite $CaZr_{1-x}Ce_xTi_2O_7$ system, J. Nucl. Mater. (2020), https://doi.org/10.1016/j.jnucmat.2020.152137.
[48] Y.P. Lan, H.Y. Sohn, A. Murali, J. Li, C. Chen, The formation and growth of CeOCl crystals in a molten KCl-LiCl flux, Appl. Phys. Mater. Sci. Process 124 (2018) 1–6, https://doi.org/10.1007/s00339-018-2122-3.
[49] B.D. Begg, R.A. Day, A. Brownscombe, Structural effect of Pu substitutions on the Zr-site in zirconolite, Mater. Res. Soc. Symp. Proc. 663 (2001), https://doi.org/10.1557/PROC-663-259.
[50] N.V. Zubkova, N.V. Chukanov, I.V. Pekov, B. Ternes, W. Schüller, D.A. Ksenofontov, D.Y. Pushcharovsky, The crystal structure of nonmetamict Nb-rich zirconolite-3T from the Eifel paleovolcanic region, Germany, Zeitschrift Fur Krist. - Cryst. Mater. 233 (2018) 463–468, https://doi.org/10.1515/zkri-2017-2133.
[51] K.L. Smith, G.R. Lumpkin, M.G. Blackford, R.A. Day, K.P. Hart, The durability of synroc, J. Nucl. Mater. 190 (1992) 287–294, https://doi.org/10.1016/0022-3115(92)90092-Y.
[52] N.C. Hyatt, C.L. Corkhill, M.C. Stennett, R.J. Hand, L.J. Gardner, C.L. Thorpe, The HADES facility for high activity decommissioning engineering & Science : part of the UK national nuclear user facility, IOP Conf. Ser. Mater. Sci. Eng. 818 (2020) 1–8, https://doi.org/10.1088/1757-899X/818/1/012022.

Appendix B – List of Figures

Appendix C – List of Tables